ulm university universität
uulm

Optimal Trajectory Planning for Multiphysics Problems Governed by Electromagnetic and Thermal Phenomena

DISSERTATION

zur Erlangung des akademischen Grades eines

DOKTOR-INGENIEURS

(Dr.-Ing.)

der Fakultät für Ingenieurwissenschaften,
Informatik und Psychologie der Universität Ulm

von

Sönke Dominik Rhein
aus Heidenheim an der Brenz

Gutachter:	Prof. Dr.-Ing. Knut Graichen
	Univ.-Prof. Dr.techn. Andreas Kugi
Amtierender Dekan:	Prof. Dr. Frank Kargl

Ulm, 9. Februar 2018

Ulm, Universität, Dissertation, 2018

Acknowledgment

This thesis was written during my time as a research assistant at the Institute of Measurement, Control, and Microtechnology at the University of Ulm. The supervision was provided by Prof. Dr.-Ing. Knut Graichen. I will always be grateful for the mentoring and for the useful suggestions and discussions forming the basis for the success of this thesis. I would like to sincerely thank Knut Graichen for allowing scope for own ideas and concepts. I am very grateful for his confidence and trust and for giving me the opportunity to devote myself to an interesting and enriching topic of research during the last years. With delight I look back on the successful time and the pleasant atmosphere in his working group.

Special thanks also goes to Dr.techn. Tilman Utz for co-supervising this work for many years. I happily remember the initial period of being a research assistant as you devoted so much effort for discussing advances and regresses in work. Thank you very much for your contribution and for the successful support. I would also like to thank Univ.-Prof. Dr.techn. Andreas Kugi for his efforts as second examiner of my thesis and for his constructive comments. Further, I would like to thank the Chairman of the Promotion Committee, Prof. Ph.D. Carl Emil Krill, and the reviewer, Prof. Dr.-Ing. Jian Xie.

I also wish to express my gratitude to all former and current colleagues from the institute. Many thanks for the friendly collaboration and interesting conversations both in professional and private matters.

Bei meiner Freundin Katharina möchte ich mich für ihre Liebe sowie für das Lesen dieser Arbeit bedanken. Der größte Dank jedoch gebührt meinen Eltern Horst und Roswitha, die mir stets helfend zur Seite stehen. Sie ermöglichten mir nicht zuletzt mein Studium und bekräftigten mich auch in schwierigeren Zeiten. Zusammen mit meinen Geschwistern boten sie mir einen Platz neben dem Studium und der Arbeit, an welchen ich jeder Zeit gerne zurückkomme. Vielen Dank!

Ulm, Februar 2018 Sönke Dominik Rhein

Meinen Eltern

Abstract

Multiphysics problems include various physical phenomena such as fluid flow, heat transfer or electromagnetism, to mention just a few. The mathematical description of this type of problem therefore requires a system of nonlinearly coupled partial differential equations (PDE – *Partial Differential Equation*), usually defined on complex spatial domains. Electromagnetic heating systems are governed by electromagnetic and thermal phenomena and are a typical example of such problems. The planning of optimal trajectories for different electromagnetic heating applications is the subject of this work.

Electromagnetic fields are used in many technical and medical applications to heat up specific spatial domains of electrically conductive objects. Examples are induction heating problems for tempering or surface hardening in the steel industry. Hyperthermia therapy constitutes another field of application of electromagnetic heating, which uses the heat source to improve conventional drug treatment techniques or to severely damage tumors caused by overheating. The good controllability of the electromagnetic field allows one to adapt the intensity and spatial distribution of the heat source to the desired heat-up behavior of a specific problem. Further advantages of electromagnetic heating are fast heat-up rates and low energy costs. However, optimal trajectory planning for such problems involves many challenges that can be divided into methodological and numerical ones.

From a methodological point of view, the nonlinear coupling effects between the electromagnetic and thermal phenomena are challenging and have to be described by a system of coupled PDEs. They are, in general, defined on complex spatial domains in order to be able to sufficiently accurate represent the real physics. In addition, many applications include temperature constraints to address technical or medical requirements. The most important degrees of freedom for planning optimal trajectories are the electrical excitation of the actuator as well as its position and shape. An effective interaction between the control strategy for the actuators in form of voltage and current sources and the specific actuator configuration allows one to tailor the intensity and spatial distribution of the electromagnetic heat source to the objectives of a heat-up process.

Another difficulty in the course of planning optimal trajectories for electromagnetic heating systems is the numerical complexity of multiphysics problems. Sophisticated algorithms and numerical solvers are required to predict the system dynamics of the multiphysics problem with sufficient accuracy. Thereby, the distinctly different temporal and spatial scales of the electromagnetic and thermal phenomena as well as complex spatial domains necessitate an adaptation of the numerical techniques and solution approaches to the specific problem. In addition, the optimization of the actuator configuration involves a change in the geometrical setup on what the PDEs are defined, which necessitates adapted strategies for the numerical solution of the multiphysics problem.

This thesis discusses optimization-based approaches to determine an optimal excitation and spatial configuration of electromagnetic actuators. The objectives of the trajectory planning problems are tailored to several induction heating processes and hyperthermia therapy. The incorporation of state constraints for the trajectory planning such as constraints on the temperature of the object to be heated or on the temperature gradient is another focus. All three problems, i. e., the optimization of the excitation of the actuator, the optimization of the actuator configuration, and the incorporation of state constraints, are tackled by formulating and numerically solving suitable optimization problems.

The primary benefit of the presented solution strategy is its wide applicability to various problems of electromagnetic heating without the necessity to overcome the numerical challenges by developing numerical algorithms and solvers. Instead, an optimization framework is presented that uses state-of-the-art simulation software to numerically solve the optimization problems. The numerical level is extended by an algorithmic level to incorporate proper optimization methods.

The optimization-based trajectory planning is based on forward and backward integrations of the multiphysics problems and its optimality conditions. In order to derive the optimality conditions, the formal Lagrangian technique and the adjoint-based sensitivity analysis is applied. The optimality condition will result in PDE systems that can be numerically solved by the optimization framework with relative ease since the numerical effort of the trajectory planning can be outsourced to FEM-based simulation software. In order to be able to tackle state constrained problems in a similar manner, an augmented Lagrangian method and a transformation approach are discussed.

The basic idea of the augmented Lagrangian method and transformation approach consists in preserving the characteristics of unconstrained state variables of the optimality conditions to guarantee that their solution can be provided by FEM-based simulation software. The augmented Lagrangian method ensures unconstrained state variables of the multiphysics problems and its optimality conditions in an algorithmic manner by adjoining the state constraints to the original problem formulation. In contrast to that, the transformation approach uses a saturation function to replace the constrained state variables by unconstrained counterparts. It is shown that this step transfers the constrained problem into an equivalent unconstrained one in which the system dynamics inherently satisfies the state constraint.

The applicability and accuracy of the optimization framework is exemplified for simulation studies ranging from induction heating processes to hyperthermia therapy. The numerical results demonstrate the optimization of the excitation and spatial configuration of the actuator for selected problems and reveal the simple adaptation of the solution strategy to other electromagnetic heating problems.

Deutsche Kurzfassung

Multiphysikprobleme umfassen unterschiedliche und in einer wechselseitigen Beziehung stehende physikalische Effekte wie zum Beispiel fluiddynamische Vorgänge, Wärmeleitung oder elektromagnetische Felder. Eine hinreichend genaue mathematische Beschreibung derartiger Probleme erfordert daher partielle Differentialgleichungen, welche häufig auf komplexen Ortsgebieten definiert sind. Ein typisches Beispiel sind elektromagnetische Heizvorgänge, die durch elektromagnetische und thermische Wechselwirkungen gekennzeichnet sind. Die Planung optimaler Trajektorien für verschiedene Anwendungen des elektromagnetischen Heizens ist Inhalt dieser Arbeit.

Elektromagnetische Felder werden in zahlreichen technischen und medizinischen Anwendungen zur Erwärmung elektrisch leitender Materialien eingesetzt. Beispielhaft seien induktive Heizvorgänge zum Anlassen oder zur Oberflächenbehandlung in der Stahlindustrie genannt. Mit dem Hyperthermieverfahren ergibt sich ein weiteres Anwendungsfeld. In diesem Fall wird die elektromagnetische Wärmequelle zur Unterstützung konventioneller Tumorbehandlungen eingesetzt. Modernere Verfahren setzen den Wärmeeintrag auch für eine direkte Abtötung des Tumors durch Überhitzung ein. Die guten Steuerbarkeitseigenschaften von elektromagnetischen Feldern ermöglicht es, die Intensität und örtliche Verteilung der Wärmequelle an ein gewünschtes Aufheizverhalten anzupassen. Weitere Vorteile sind kurze Heizzyklen bei relativ geringen Energiekosten. Die optimale Trajektorienplanung für derartige Probleme ist jedoch mit einigen methodischen und numerischen Herausforderungen verbunden.

Aus methodischer Sicht stellen vor allem die nichtlinearen Kopplungseffekte zwischen den elektromagnetischen und thermischen Vorgängen eine Herausforderung dar und müssen in Form von partiellen Differentialgleichungssystemen berücksichtigt werden. Diese sind häufig auf komplexen Ortsgebieten definiert, um das reale Systemverhalten hinreichend genau abbilden zu können. Darüber hinaus beinhalten viele Anwendungen Temperaturbeschränkungen, um technische oder medizinische Anforderungen berücksichtigen zu können. Als Stellgröße für die Trajektorienplanung steht zum einen die elektrische Aktoransteuerung zur Verfügung. Eine weitere Stellgröße ergibt sich aus der Position und Form des Aktors. Eine geeignete Wahl dieser Freiheitsgrade erlaubt es, sowohl den zeitlichen als auch den örtlichen Verlauf der Wärmequelle an ein gewünschtes Aufheizverhalten anzupassen.

Eine weitere Schwierigkeit bei der Planung optimaler Trajektorien ergibt sich aus der numerischen Komplexität des Problems. Um die Systemdynamik von elektromagnetischen Heizvorgängen hinreichend genau vorhersagen zu können werden geeignete Algorithmen und Solver benötigt. Die unterschiedlichen Orts- und Zeitskalen der elektromagnetischen und thermischen Vorgänge sowie komplexe Ortsgebiete erfordern angepasste Lösungen. Zudem verändert die Optimierung der Aktorkonfiguration den Definitionsbereich der partiellen Differentialgleichungen, was eine Adaption der numerischen Lösung des Problems erfordert.

In dieser Arbeit werden optimierungsbasierte Ansätze für die Auslegung einer optimalen Ansteuerung der Aktorik sowie einer optimale Aktorkonfiguration untersucht. Die Zielstellung der Trajektorienplanung wird auf verschiedene induktive Heizvorgänge und Formen der Hyperthermiebehandlung angepasst. Ein weiterer Schwerpunkt ist die Berücksichtigung von Zustandsbeschränkungen, um beispielsweise die Temperatur oder den Gradienten der Temperatur im Rahmen der Trajektorienplanung begrenzen zu können. Der Lösungsansatz für die unterschiedlichen Problemstellungen einer optimalen Aktoransteuerung und optimalen Aktorkonfiguration sowie für die Berücksichtigung von Zustandsbeschränkungen beruht auf der geeigneten Formulierung und numerischen Lösung von Optimierungsproblemen.

Der Vorteil des vorgestellten Lösungsansatzes zur optimalen Trajektorienplanung beruht auf dessen breiter Anwendbarkeit. Verschiedenste Problemstellungen des elektromagnetischen Heizens können bewältigt werden ohne aufwendige Erweiterungen hinsichtlich der Numerik vornehmen zu müssen. Stattdessen wird eine Optimierungsumgebung vorgestellt, die auf Basis von FEM-Software die numerische Lösung der Optimierungsprobleme ermöglicht. Die numerische Ebene wird um eine algorithmische erweitert, in welcher geeignete Optimierungsroutinen implementiert werden.

Der Ansatz zur Trajektorienplanung basiert auf einer sequentiellen Lösung der Multiphysikprobleme und deren Optimalitätsbedingungen, wobei die Optimalitätsbedingungen unter Verwendung der formalen Lagrange-Technik und einer adjungiert-basierten Sensitivitätsanalyse hergeleitet werden. Die Optimalitätsbedingungen liegen in Form von partiellen Differentialgleichungssystemen vor, deren Struktur eine numerische Lösung mit Hilfe von FEM-Software ermöglicht. Dies führt dazu, dass der numerische Aufwand der Trajektorienplanung auf FEM-basierte Simulationssoftware ausgelagert werden kann. Um auch zustandsbeschränkte Probleme auf diese Art handhaben zu können, wird ein erweiterter Lagrange-Ansatz sowie ein Transformationsansatz vorgestellt.

Die Idee des erweiterten Lagrange-Ansatzes und des Transformationsansatzes besteht in der Erhaltung der unbeschränkten Zustandsvariablen der Optimalitätsbedingungen, um somit sicherzustellen, dass das Optimalitätssystem mit Hilfe von FEM-basierter Simulationssoftware gelöst werden kann. Der erweiterte Lagrange-Ansatz beruht auf einer algorithmischen Erweiterung der Optimierungsroutinen. Die strukturelle Eigenschaft unbeschränkter Zustände bleibt dabei erhalten, indem die Zustandsbeschränkungen mit Hilfe von adjungierten Zuständen an die ursprüngliche Problemstellung gekoppelt werden. Der Transformationsansatz verwendet eine Sättigungsfunktion, um die beschränkten Zustände durch unbeschränkte zu ersetzen. Dadurch wird das beschränkte Optimierungsproblem in ein unbeschränktes transformiert, dessen Systemdynamik inhärent die Beschränkungen einhält.

Die Leistungsfähigkeit der Optimierungsumgebung wird mit Hilfe von Simulationsstudien von induktiven Heizvorgängen und Tumorbehandlungen aufgezeigt. Die Simulationsstudien führen letztendlich zu optimalen Ansteuerungen und Konfigurationen der Aktoren und verdeutlichen die breite Anwendbarkeit der Optimierungsumgebung auf verschiedene Problemstellungen des elektromagnetischen Heizens.

Contents

Chapter 1

Introduction

The major advantage of electromagnetic heating techniques over conventional technologies such as combustion, i. e., the generation of heat from coal or fuels, or electrical heating (e. g. radiant or convection heating) is the ability to localize the heat source inside the spatial domain of interest without the need for contact with the object. Typical application examples are, but are not limited to, heat treatment processes in the steel industry [118, 89] and medical sector [129, 144, 9], the manufacturing of monocrystalline silicon [78, 91], and thermal oil recovery methods [24].

In the last decades, specialized software packages were developed to simulate multiphysics problems. This formed the foundation of understanding the fundamental physics and various coupling effects of complex problems as well as to customize control strategies to a specific problem. The optimal trajectory planning of electromagnetic heating systems, however, is still a challenging task. The main reasons for this are the underlying multiphysics characteristics in combination with complex spatial domains which result in enormous methodological complexity and numerical challenges [62, 119].

The electrical excitation of electromagnetic actuators such as inductors or electrodes as well as their positions and shapes represent important degrees of freedom for an optimal trajectory planning [127, 118]. A well-balanced coordination between the control strategy for the actuators in form of voltage or current sources and appropriately selected actuator shapes and positions facilitates the adaptation of the intensity and spatial distribution of the heat source to the objectives of a heat-up process. Figure 1.1 shows typical electromagnetic heating applications in form of constant heat-up and surface hardening processes. The actuator configuration in Figure 1.1a is used to heat up the whole workpiece, whereby the actuator is excited in a way that the heat source is generated as homogeneously as possible within the workpiece. The actuator configurations in Figure 1.1b and 1.1c ensure to heat up individual areas of the surface layer of the workpiece.

In general, the major challenge of the trajectory planning stems from the objective to heat up specific regions to desired temperature profiles and is complicated by secondary objectives that are often competing [31, 38]. For example, a surface hardening process has the primary objective to heat up the surface layer without increasing the temperature of inner domains. The compliance of state constraints is a further important aspect, e. g., the workpiece must not exceed critical temperatures to prevent undesired metallurgical effects capable to downgrade the material properties.

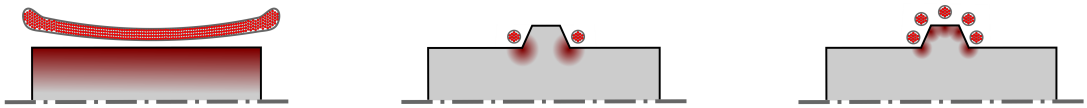

(a) Constant heat-up (b) Surface hardening (c) Surface hardening

Figure 1.1: Typical scenarios of electromagnetic heating. Different actuator configurations are used to generate the electromagnetic heat source in specific regions of the workpiece.

There are several other objectives for electromagnetic heating systems including the necessity to guarantee a homogeneous heat-up behavior, i. e. to prevent too large temperature gradients or the realization of rapid heat-up cycles that are highly accurate [118]. Moreover, the geometrical setups of electromagnetic heating systems are as manifold as the number of application examples (e. g. induction heating, hyperthermia therapy, or manufacturing of monocrystalline silicon) for which the heat-up techniques have to be customized. In turn, the trajectory planning problem will involve a great deal of effort and is computationally demanding for each individual problem.

In this thesis, a trajectory planning approach is presented to optimize the electrical excitation and the position or shape of the actuator. The approach also accounts for state constraints and is characterized by its generality to handle different problems of electromagnetic heating. The basic idea is to closely couple optimization algorithms and a software package that is specialized to the numerical solution of multiphysics problems [114, 108]. An optimization framework is developed where the methodological challenges can be separated from the numerical ones. The software package is used to numerically solve both the system dynamics of the electromagnetic heating processes and the optimality conditions to obtain optimal trajectories. The derivation of the optimality conditions and their incorporation into the optimization framework is the focus of this thesis.

This introductory chapter illustrates the multiphysics characteristics of electromagnetic heating systems and discusses the most relevant aspects for an optimal trajectory planning. Furthermore, the concept of dynamic optimization is outlined to provide an insight into the problem and theoretical basics of optimization-based trajectory planning.

1.1 Electromagnetic heating

Electromagnetic and thermal phenomena are essential physical processes that have to be taken into account when applying electromagnetic heating techniques.[1] The physical principle of electromagnetic heating and its advantages over traditional heat-up techniques are outlined in what follows, also see [56, 117].

[1] Further significant phenomena are metallurgical and thermo-mechanical effects.

1.1.1 Basic principle

A typical geometrical setup of an electromagnetic heating system consists of an actuator (e. g. an inductor in the case of induction heating or an electrode in the case of hyperthermia therapy) and the object to be heated, as illustrated in Figure 1.2. The basic principle of an electromagnetic heat-up process is as follows. One or several actuators[2] are energized with alternating electric currents $\mathcal{J}_{\text{imp}} := \mathcal{J}_{\text{imp}}(x,t)$ which in turn give rise to an electromagnetic field that propagates through the ambient area with the same frequency [130]. The characteristic of wave propagation is indicated in Figure 1.2 by means of the impressed electric currents $\mathcal{J}_{\text{imp}}$ within the actuator and the arising magnetic field $\mathcal{H} := \mathcal{H}(x,t)$ in the air. The spatial coordinates are denoted by $x := [x_1, x_2, x_3]^{\mathsf{T}}$ and the temporal coordinate by t.[3]

Objects that are penetrated by the electromagnetic field are exposed to intrinsic heat sources since the time-varying magnetic field $\mathcal{H}$ induces an electric field intensity $\mathcal{E} := \mathcal{E}(x,t)$ in electrically conductive materials [116, 57]. Thus, the temperature of the object $T := T(x,t)$ increases as a function of the intensity and spatial distribution of the heat source.

In the vast majority of electromagnetic heating scenarios, the predominant heat source is Joule heating $\mathcal{Q}_{\mathcal{J}}(\mathcal{E})$ arising from electric dissipation effects. The physical cause of this heat source lies in a combination of the resistivity of the object, respectively its electrical conductivity $\sigma := \sigma(x)$, and induced eddy currents $\mathcal{J}_{\text{ind}} := \mathcal{J}_{\text{ind}}(x,t)$ due to the electric field intensity $\mathcal{E}$. By its very nature, eddy currents flow in closed loops while they match more or less pronounced the contour of the object, cf. Figure 1.2. In the case of ferromagnetic

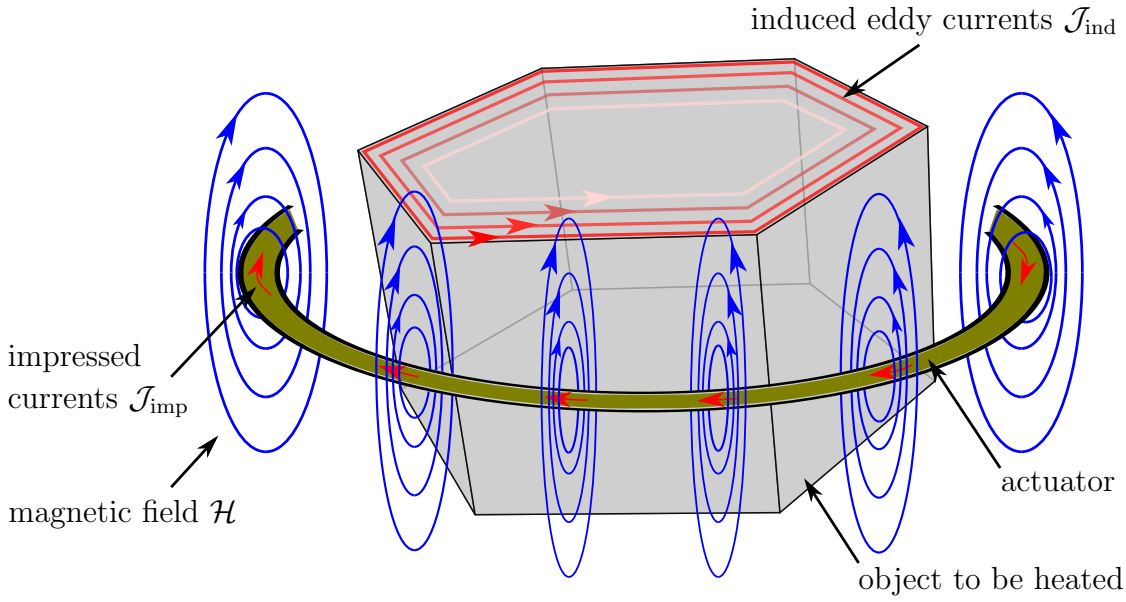

Figure 1.2: Typical setup of an electromagnetic heating application with magnetic field $\mathcal{H}$ and induced eddy currents $\mathcal{J}_{\text{ind}}$ within an electrically conductive object.

[2] In the following, the uniform description "actuator" is used also implying the plural form.

[3] After the definition of variables or physical quantities such as the magnetic field $\mathcal{H}(x,t)$ or the temperature $T(x,t)$, their arguments x and t are omitted to not further complicate the notation.

objects, the permanent magnetization and demagnetization of materials cause additional dissipation effects and a certain amount of magnetic energy is converted to heat [83]. Thus, magnetic losses may be able to generate another significant heat source $\mathcal{Q}_{\mathcal{M}}(\mathcal{H})$.

1.1.2 Advantages

Electromagnetic heat-up techniques offer several advantages over conventional heating methods. The major advantage is the possibility to localize the heat source to specific areas of the object, cf. Figure 1.1. In combination with the fast heating rates of electromagnetic fields, local areas can be heated up without significantly increasing the temperature of surrounding regions [147, 46]. In addition, the heat source can be reproduced accurately, what is particularly interesting in terms of an automation of the heat-up process [29].

Electromagnetic heating techniques are energy efficient since the heat source is directly generated in the object to be heated [20]. Moreover, the convective and radiative heat losses are kept to a minimum. The characteristic of a contactless heat transfer into the object is another advantage. Compared to external heat sources that inevitably involve contamination effects of the object, electromagnetic heating can be utilized even if the specific problem demands high standards of technical or medical cleanliness. This advantage is of particular relevance, for instance, in the course of manufacturing monocrystalline silicon [140] or hyperthermia therapy [144].

With respect to an optimal heat-up process, both the intensity and spatial distribution of the intrinsic heat source $\mathcal{Q}(\mathcal{E},\mathcal{H}) = \mathcal{Q}_{\mathcal{J}}(\mathcal{E}) + \mathcal{Q}_{\mathcal{M}}(\mathcal{H})$ are important factors. The time-dependent excitation of the actuator as well as its position and shape constitute the most important degrees of freedom to adjust the heat source.[4] There are, however, several multiphysics characteristics that influence the propagation of the electromagnetic field and hence the generation of the heat source. Thus, the intensity and spatial distribution of the heat source can be manipulated only to a certain degree. The most relevant multiphysics characteristics of electromagnetic heating applications are discussed in what follows.

1.2 Multiphysics characteristics of electromagnetic heating systems

The multiphysics characteristics of electromagnetic heating systems are complex in their nature and involve, among others, a close coupling of electromagnetic and thermal phenomena [118]. For an optimal trajectory planning, it is important to account for such multiphysics characteristics using proper mathematical models.

[4] Additional degrees of freedom are, for instance, the frequency of the electrical excitation of the actuator or stem from the application of magnetic flux concentrators, see, e. g., [118].

1.2.1 Nonlinearly coupled partial differential equations

From a mathematical point of view, a sufficiently precise description of the electromagnetic and thermal phenomena requires a set of coupled partial differential equations (PDE – *Partial Differential Equation*). The Maxwell equations and the heat equation can be used to model the temporal and spatial dynamics of electromagnetic heating systems [57, 87]. For the sake of compactness, the system dynamics and the associated challenges for an optimal trajectory planning are discussed, for the time being, on the basis of the PDE system

$$e_{\mathrm{sys}}(y, v) = 0 \qquad \text{in } \Omega \times (0, t_{\mathrm{f}}) \qquad \text{(system dynamics)} \tag{1.1a}$$

$$e_{\mathrm{bc}}(y, v) = 0 \qquad \text{on } \Gamma \times (0, t_{\mathrm{f}}) \qquad \text{(boundary condition)} \tag{1.1b}$$

$$e_{\mathrm{ic}}(y) = 0 \qquad \text{in } \Omega \text{ at } t = 0 \qquad \text{(initial condition)} \tag{1.1c}$$

with state $y := y(x, t)$ and input $v := v(x, t)$. The electromagnetic and thermal phenomena are represented by the model $e_{\mathrm{sys}}(y, v) = 0$ on the space-time cylinder $\Omega \times (0, t_{\mathrm{f}})$ with t_{f} as the final time of the heat-up cycle. The boundary condition on Γ and the initial condition within the region of interest Ω at $t = 0$ are described by $e_{\mathrm{bc}}(y, v) = 0$ and $e_{\mathrm{ic}}(y) = 0$, respectively. The input v represents the available degrees of freedom to actuate the electromagnetic heating system such as the electrical excitation or the position and shape of the actuator. A detailed description of the PDE system (1.1) is presented in Chapter 2.

The planning of optimal trajectories for problems governed by PDEs is challenging in its own [19, 27]. In the case of electromagnetic heating, the problem is complicated by the fact that the PDE constraints involve nonlinear coupling effects [11]. For example, the mathematical model (1.1) must be able to describe the temporal and spatial distribution of the electric field intensity $\mathcal{E}$ according to Faraday's law of induction

$$\nabla \times \mathcal{E} = -\mu \, \partial_t \mathcal{H} \qquad \text{in } \Omega \times (0, t_{\mathrm{f}}) \tag{1.2}$$

with $\mu := \mu(x)$ denoting the magnetic permeability.[5] Depending on the knowledge about the temporal and spatial distribution of the electric field intensity, the Joule heat source

$$\mathcal{Q}_{\mathcal{J}} = \sigma \, \mathcal{E} \cdot \mathcal{E} \qquad \text{in } \Omega \times (0, t_{\mathrm{f}}) \tag{1.3}$$

can be used to describe the density of electrical power converted to heat.[6] The Joule heat source $\mathcal{Q}_{\mathcal{J}}$ allows one to describe the thermal behavior of the object by expanding the mathematical model (1.1) by the well known heat equation

$$\rho C \partial_t T - \nabla \cdot (k \, \nabla T) = \mathcal{Q}_{\mathcal{J}} \qquad \text{in } \Omega \times (0, t_{\mathrm{f}}) \ , \tag{1.4}$$

whereby the material parameters $\rho := \rho(x)$, $C := C(x)$, and $k := k(x)$ specify the density, the heat capacity, and the thermal conductivity of the object.

[5] The temporal operator $\partial_t(\cdot)$ denotes the partial derivative with respect to time t. The spatial operators $\nabla \times (\cdot)$ and $\nabla \cdot (\cdot)$ denote the curl and divergence operator, also see Appendix B.5.

[6] In the remainder, the operator '$\cdot$' is used to formulate the scalar product of two vectors.

The computational effort that is associated with the simulation of multiphysics problems, not to mention their optimization, is another crucial point [76, 119]. The solution of the system dynamics (1.1) requires sophisticated algorithms and solvers to cope with distinctly different temporal and spatial scales of the electromagnetic and thermal phenomena [65, 116, 95]. In addition, the geometrical setup on which the system dynamics is formulated often exhibits complex spatial domains and structures by which its numerical treatment becomes a tedious and costly procedure [118].

In principle, the numerical effort for the trajectory planning can be reduced by assuming more simple spatial domains as they really are. This results in mathematical models with symmetry planes and reduced space dimensions. In turn, the numerical load decreases and the application of semi-analytical approaches for the trajectory planning is facilitated, see, e. g., [17, 125]. On the other hand, non-uniform shapes and structures of the object may have a major impact on the propagation of the electromagnetic field, and thus on the spatial distribution of the electromagnetic heat source. A discussion of such distortion effects and its influence on the heat-up behavior of the object is the subject of the following section.

1.2.2 Distortion effects of the electromagnetic field

The intensity of the electromagnetic heat source depends on, among other things, the strength and frequency of the electromagnetic field, cf. Equation (1.3) in the case of Joule heating. By adjusting the power supply of the actuator in form of impressed current or voltage sources of sinusoidal type

$$u := u(t) = \hat{u}(t)\cos(\omega t) \tag{1.5}$$

with time-dependent peak-value $\hat{u}(t)$ and angular frequency ω, both the intensity and frequency of the electric field can be changed. In turn, the control strategy (1.5) allows one to temporally adapt the electromagnetic heat source to the desired heat-up behavior of a specific problem. The spatial distribution of the electromagnetic heat source, however, may be highly non-uniform. The most pronounced distortion effects leading to an uneven spatial distribution of the heat source are the skin, end, and edge effect, which will be discussed in the following lines, also see [31, 116].

Skin and damping effects

The time-varying electromagnetic field induces a further time-varying field in electrically conductive objects that opposes the former one due to Lenz's law, see, e. g., [130, 118]. As a result, the eddy currents $\mathcal{J}_{\text{ind}}$ decreases from the surface layer of the object towards its core. This phenomenon is known in the literature as skin effect and is illustrated in Figure 1.3 by the induced eddy currents, which are concentrated to the surface layer of the object. The impact of the skin effect is more pronounced as the frequency of the electromagnetic field is increased, also see [118].

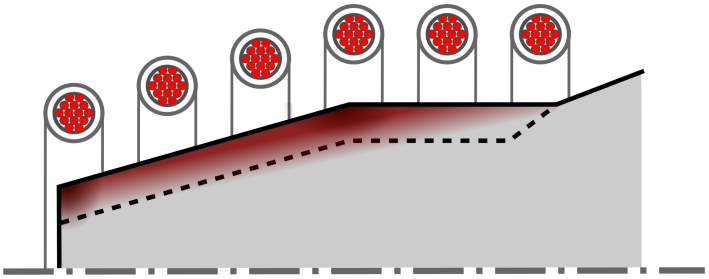

Figure 1.3: Illustration of the skin, end, and edge effect in the course of surface hardening. A darker coloration of the red-marked surface layer corresponds to a higher intensity of the electromagnetic heat source.

There are also damping effects when the electromagnetic field propagates through space. Roughly speaking, the skin and damping effects cause an exponential decrease of the eddy current distribution from the surface layer of the object towards its core. Taking into account Ohm's law

$$\mathcal{J}_{\mathrm{ind}} = \sigma \mathcal{E} \qquad \text{in } \Omega \times (0, t_{\mathrm{f}}) \ , \tag{1.6}$$

it becomes clear that also the Joule heat source $\mathcal{Q}_{\mathcal{J}}(\mathcal{E})$ decreases in an exponential manner, cf. Equation (1.3). Thus, the Joule heat source is predominant in the surface layer of the object [118]. Similar conclusions apply to heat losses due to magnetic hysteresis effects.

End effect

A further distortion of the electromagnetic field is evoked by the end effect, which eventually result in a spatially uneven heat source along the surface of the object. The end effect occurs in areas between the object and the ambient air or at the boundary of different materials. The electromagnetic field lines are contracted or stretched in these areas depending on the material parameters, the geometrical setup of the problem, and the severity of the skin effect, see, e. g., [118]. The spatial distribution of the heat source is affected by these distortions of the electromagnetic field and may vary from very intensive to less pronounced. Figure 1.3 illustrates the end effect by a darker color at the left end of the surface layer, which has a higher heat source intensity.

Edge effect

Another important effect that can significantly distort the electromagnetic field in some areas is the edge effect. Here, the electromagnetic field and its associated heat source is affected in areas with sharp edges and non-uniform shapes, as shown in Figure 1.3 in the middle region of the surface layer of the object. The edge effect strongly depends on the severity of the

skin effect. Because a more pronounced skin effect leads to a better alignment of the eddy currents to the contour of the object, the three-dimensional edge layers represent regions in which more eddy currents can penetrate, see, e. g., [118]. In consequence, such areas may be exposed to a much higher electromagnetic heat source than other domains.

Depending on the geometrical setup of the object to be heated, the impact of the edge effect can be inverse and the corresponding regions of the surface layer are submitted to a much lower intensity of induced currents. This phenomenon is illustrated in Figure 1.3 by the non-existent coloration at the right hand side of the surface layer of the object, where the intensity of the electromagnetic heat source is less pronounced.

1.2.3 Temperature-dependent material parameters

The material properties of the object can significantly vary with temperature, so that the intensity and spatial distribution of the electromagnetic heat source can also change during a heat-up cycle. The temperature dependence of the material influences, for example, how strongly the electromagnetic field penetrates into the object. Depending on the temperature increase and heating rate, the system dynamics of the electromagnetic phenomena change with time. Similarly, the phenomenon of heat propagation is also affected by changes of the material parameters.

The handling of temperature-dependent materials is a crucial point when planning trajectories for electromagnetic heating systems, see, for instance, [11, 23]. Both the temporal and spatial dynamics of the electromagnetic and thermal phenomena may significantly change during a heat-up cycle. For instance, the thermal conductivity of commonly used steels of induction heat-up and surface hardening processes is a function of temperature

$$k := k(T) \qquad \text{in } \Omega \times (0, t_\mathrm{f}) \ , \tag{1.7}$$

cf., e. g., [87, 118]. Thus, the intensity of diffusive heat propagation depends on the current temperature of the object and therefore on the spatial coordinate x, cf. Equation (1.4). Note that the temperature-dependent and hence space-dependent thermal conductivity k in combination with the locally concentrated heat source intensifies the issue of an uneven heat-up behavior.

Similar to the thermal conductivity in Equation (1.7), the density and heat capacity depend on the temperature

$$\rho := \rho(T) \qquad \text{in } \Omega \times (0, t_\mathrm{f}) \tag{1.8a}$$

$$C := C(T) \qquad \text{in } \Omega \times (0, t_\mathrm{f}) \ , \tag{1.8b}$$

which causes a change of the thermal dynamics of electromagnetic heating systems. Typical application examples of temperature-dependent material parameters influencing the thermal phenomena are discussed in [118, 75] and [23] in the case of heating up various types of

metals and tumour cells. The dependency of the electrical conductivity and the magnetic permeability on temperature, i. e.,

$$\sigma := \sigma(T) \qquad \text{in } \Omega \times (0, t_\mathrm{f}) \tag{1.9a}$$

$$\mu := \mu(T) \qquad \text{in } \Omega \times (0, t_\mathrm{f}) \ , \tag{1.9b}$$

does not affect the thermal dynamics, but rather the propagation of the electromagnetic field itself. In this case, both the intensity and the spatial distribution of the heat source can change considerably during the heat-up process, see, e. g. [11, 64].

The intensity of the temperature dependency as well as the temperature increase during a heat-up cycle influences the severity of the impact of temperature-dependent materials on the heat-up behavior. A decision must be made as to whether the effects of temperature-dependent material parameters are significant or whether they can be neglected for planning optimal trajectories of an electromagnetic heating system. In the following, the issue of temperature-dependent material parameters is not further discussed, but it is referred to the above-mentioned contributions. Moreover, there are simulation tools for multiphysics problems such as Comsol Multiphysics [28] or Ansys [5] which offer comprehensive material databases.

1.3 Optimal trajectory planning for multiphysics problems

The objective of electromagnetic heating systems is either to heat up the entire object to a constant temperature profile or to heat only a portion of it without increasing the temperature of surrounding regions [118, 38]. Control strategies can tackle such problems by appropriately matching the position and shape of the actuator and its electrical excitation, but are confronted with a number of methodological and numerical challenges. Besides this, the trajectory planning approach often should lead to an optimal heat-up behavior in terms of being highly accurate and rapid or energy efficient. To be able to meet these additional criteria, the exploitation of input and state constraints is inevitable.

Optimization-based techniques constitute a promising approach to overcome the challenges of planning optimal trajectories of PDE constrained problems [88, 40, 62, 101]. The discussion below provides an introduction to PDE constrained optimization to address the trajectory planning of electromagnetic heating systems. For the moment, however, the discussion is limited to a simplified problem formulation before the optimization-based approach is adapted in the following chapters for determining optimal excitation strategies and spatial configurations of electromagnetic actuators.

1.3.1 Problem formulation

Optimization-based trajectory planning relies on the formulation and numerical solution of an optimization problem. The general procedure for handling such a problem is discussed in the following by means of the time-independent motivating example

$$\min_{v} \; J(y,v) = \int_{\Omega} \frac{q_1}{2} \left(y - y_\mathrm{d}\right)^2 \; \mathrm{d}x + \int_{\Gamma_0} \frac{q_2}{2} \left(v - v_\mathrm{d}\right)^2 \; \mathrm{d}x \tag{1.10a}$$

$$\text{s.t.} \quad -\Delta y = f \qquad \text{in } \Omega \tag{1.10b}$$

$$n \cdot \nabla y = v \qquad \text{on } \Gamma_0 \tag{1.10c}$$

$$n \cdot \nabla y = 0 \qquad \text{on } \Gamma_1 \tag{1.10d}$$

with state variable $y := y(x)$ and control variable v. The cost functional $J(y,v)$ is used to define the objectives of the trajectory planning. Here, the quadratic error of the state and input variable is penalized with respect to desired profiles $y_\mathrm{d} := y_\mathrm{d}(x)$ and v_d, respectively. The non-negative weights q_1 and q_2 are used to balance the two control tasks against each other.[7] The discussion on handling optimization problem (1.10) is simplified by considering a one-dimensional spatial domain $\Omega = (0,1)$ with boundary $\Gamma = \Gamma_0 \cup \Gamma_1$, whereby $\Gamma_0 = 0$ and $\Gamma_1 = 1$. Neither input nor state constraints are considered for the time being.

The cost functional (1.10a) is minimized with respect to the optimization variable v taking into account the linear PDE constraint defined by the Poisson equation (1.10b) and the Neumann boundary conditions (1.10c)–(1.10d). The infinite-dimensional system dynamics of stationary type is specified by the Laplacian $\Delta(\cdot)$, the gradient $\nabla(\cdot)$, a given right hand side $f := f(x)$, and the outward unit normal vector n. For the minimization of the cost functional, the dynamics of the PDE constraint have to be affected in an optimal manner by taking advantage of the boundary control v on Γ_0. The homogeneous Neumann boundary condition on Γ_1 models perfect thermal insulation.

The numerical solution of optimization problem (1.10) results in the optimal design variable v^* and state variable y^*, which minimize the cost functional

$$J(y^*, v^*) \leq J(y,v) \qquad \forall v \; . \tag{1.11}$$

A common approach to cope with the optimization problem relies on the algorithmic treatment of a set of optimality conditions. The formulation of the optimality conditions, however, is challenging, even in the case of the rather simple problem (1.10). The following section presents suitable approaches to tackle such optimization problems from a mathematical point of view before introducing a formal approach that offers a promising alternative.

[7] For an overall scaling, both parts of the cost functional are weighted by individual parameter q_1 and q_2.

1.3.2 Typical optimization approaches

A major contribution to the treatment of optimization problems with PDE constraints goes back to the research activities of J. L. Lions in the early seventies [88]. In this connection, analytical and numerical foundations for linear problems were developed, see, e. g., [88, 1]. Research activity was continuously intensified to cope with problems governed by nonlinear PDEs leading to a rapidly growing mathematical field [40, 62]. This is particularly the case for the problem of proving the existence and uniqueness of a solution [62, 8] as well as for developing methods that are able to derive proper optimality conditions [55, 33, 62, 133].

Research activity also focused on the efficient numerical solution of PDEs. Probably the most important method is the finite element method (FEM – *Finite Element Method*) because of its flexibility to deal with complex spatial domains [88, 146, 8]. The continuous increase in computational power favors this development to this day. However, the proper handling of PDE constrained optimization problems is still a challenging task. This is especially true if nonlinear coupling effects or state constraints are present [62, 96, 101].

Generally speaking, methods to tackle PDE constrained optimization problems can be divided into the two approaches "first discretize then optimize" (FDTO – *First Discretize Then Optimize*) and "first optimize then discretize" (FOTD – *First Optimize Then Discretize*), see, e. g., [62, 63]. Both approaches have advantages and disadvantages, and the choice for one of them depends largely on the complexity of the PDE constraints and the spatial domains for which the infinite-dimensional system dynamics is defined [119].

First discretize then optimize (FDTO)

The idea of an FDTO approach is to first discretize the temporal and spatial coordinates of the infinite-dimensional system dynamics before suitable optimization techniques are applied [62]. The prior discretization step allows to derive the optimality conditions in finite-dimensional spaces. There are two different techniques concerning the discretization step, known as semi-discretization and full-discretization [146, 124, 84]. The former one discretizes either the temporal or spatial coordinate whereas the latter discretizes both.

The FDTO approach is demonstrated for optimization problem (1.10). Since this problem is stationary, there is no difference between full and semi-discretization. First of all, the spatial coordinate x is discretized on $\Omega \in (0, 1)$ at N grid nodes

$$x_h = [x^1 = 0,\, x^2, \ldots,\, x^N = 1]^\mathsf{T} \;, \quad x^j < x^{j+1} \tag{1.12}$$

with the subscript h indicating the discretization of the spatial domain, i. e., $h = x^{j+1} - x^j$. The discrete grid nodes facilitate the evaluation of the infinite-dimensional state variable

$$y_h = [y^1,\, y^2, \ldots,\, y^N]^\mathsf{T} \;. \tag{1.13}$$

The discretized state variables $y^j \approx y(x)|_{x=x^j}$ can be used to approximate the spatial operators of the system dynamics (1.10b)–(1.10d) using finite difference, finite element, or finite

volume techniques, see, e. g., [131, 146, 138]. Eventually, the discretization step results in the finite-dimensional optimization problem

$$\min_{v} \; J_h(y_h, v) \tag{1.14a}$$

$$\text{s.t.} \quad K y_h = f_h \tag{1.14b}$$

that approximates the infinite-dimensional counterpart (1.10), also see [63]. The new cost functional to be minimized $J_h(y_h, v)$ represents (1.10a). The algebraic equation (1.14b) approximates the PDE constraints (1.10b)–(1.10d), whereby $K := K(y_h, v)$ and $f_h := f_h(y_h, v)$ denote the stiffness matrix and the load vector, respectively.

The second step of an FDTO approach deals with the numerical solution of the discretized optimization problem (1.14). In the vast majority, the numerical solution relies on the formulation and evaluation of optimality conditions, see, e. g., [21, 98]. Commonly used approaches to derive the optimality conditions are adjoint-based methods. To this end, the discretized system dynamics (1.14b) is adjoined to the cost functional (1.14a) using adjoint states. An analysis of the extended cost functional eventually reveals the optimality conditions. In order to numerically solve them, approaches such as (conjugate) gradient methods, sequential quadratic programming, (quasi-)Newton methods, or interior point methods can be applied, also see [22, 21, 98].

First optimize then discretize (FOTD)

An FOTD approach offers an alternative to cope with optimization problems such as (1.10). In this case, the optimality conditions are formulated directly in infinite-dimensional spaces without applying prior discretization techniques. The discretization step is solely required to numerically solve the optimality conditions. A detailed discussion on FOTD approaches can be found in [55, 63, 62].

For a number of reasons (e. g., infinite-dimensional system dynamics, nonlinearly coupled PDEs, or presence of state constraints), the major challenge of an FOTD approach is to formulate a well-defined control-to-state operator

$$y = G(v) \qquad \text{in } \Omega \,, \tag{1.15}$$

which maps each control variable v to a unique state variable y. Thereby, the side constraints of the optimization problem in form of PDE systems or input and state constraints have to taken into account [62]. For the sake of simplicity, the discussion of the main steps of an FOTD approach are exemplified for optimization problem (1.10).

A sophisticated analysis of optimization problem (1.10) shows that a unique control-to-state operator $y = G(v)$ exists [2]. The reduced problem reads as

$$\min_{v} \; J(G(v), v) = \int_{\Omega} \frac{q_1}{2} \left(G(v) - y_\mathrm{d}\right)^2 \, \mathrm{d}x + \int_{\Gamma_0} \frac{q_2}{2} \left(v - v_\mathrm{d}\right)^2 \, \mathrm{d}x \tag{1.16}$$

and solely depends on the optimization variable v but not on the state variable y. The directional derivative of the reduced cost functional with respect to the optimization variable v can be used to formulate a set of optimality conditions. The reformulation of the directional derivative eventually yields the so-called adjoint dynamics

$$\Delta p^* = q_1 \left(y^* - y_\mathrm{d}\right) \qquad \text{in } \Omega \tag{1.17a}$$

$$n \cdot \nabla p^* = 0 \qquad \text{on } \Gamma \tag{1.17b}$$

as a necessary optimality condition. Roughly speaking, the adjoint dynamics reflects the impact of the cost functional (1.10a) on the system dynamics (1.10b)–(1.10d) in terms of an optimal solution.

The optimality conditions of problem (1.10) also comprise the gradient condition

$$g_v = \int_{\Gamma_0} q_2 \left(v^* - v_\mathrm{d}\right) - p^* \, \mathrm{d}x = 0 \tag{1.18}$$

with $g_v := g_v(v, p)$ relating the control input v to an optimal solution (p^*, v^*). The negative gradient $-g_v$ can be interpreted as a descent direction for the optimization variable v in order to reduce the cost functional, which is particularly interesting from an algorithmic point of view, see, e. g., [74, 62, 58].

The second step of an FOTD approach uses the optimality system, described by the system dynamics (1.10b)–(1.10d), the adjoint dynamics (1.17), and the gradient condition (1.18), to determine a numerical solution of the optimization problem in an algorithmic manner [58]. To this end, the system dynamics and the adjoint dynamics, also referred to as canonical equations, are discretized using finite difference, finite element, or finite volume techniques, see, e. g., [146, 138, 132]. On the basis of the discretized optimality conditions, (conjugate) gradient methods, sequential quadratic programming or (quasi-)Newton methods are typically used to determine an optimal solution [62, 58].

Comparison of FDTO and FOTD approaches

Generally, one can say that multiphysics problems give rise to severe difficulties in the course of planning optimal trajectories regardless whether an FDTO or FOTD approach is applied, see, e. g., [62, 133, 119]. The crucial points can be divided into methodological issues (e. g., derivation of optimality conditions, incorporation of state constraints) and numerical issues (e. g., numerical solution of nonlinear coupled PDEs, handling of complex spatial domains), whose degree of severity varies for the two different approaches.

The major issues of an FDTO approach are numerical ones and are linked to the discretization step. The approximation of the PDE constrained optimization problem by an finite-dimensional counterpart necessitates tailored discretization techniques and problem specific workarounds [146, 132]. Various subdomains, on which the cost functional is defined, or the adequate implementation of the degrees of freedom for shape optimization, to name just a few aspects, necessitate customized and tedious discretization techniques.

The lack of freedom to employ different grids for discretizing and numerically solving the canonical equations is another disadvantage of FDTO approaches [55]. The crucial point is that the system dynamics and adjoint dynamics often need different spatial grids. For example, the surface layer of typical induction heating processes as shown in Figure 1.3, is subject to the steepest temperature gradients and should therefore be discretized sufficiently fine. The adjoint dynamics, however, requires a rather fine spatial grid in the region of the actuator in order to precisely reflect its sensitivity for shape optimization [55].

The advantage of FDTO approaches lies in well-developed methods and algorithms to cope with optimization problems governed by ODEs or algebraic equations. There exists a variety of software packages to derive and numerically solve the optimality conditions. Examples include, but are not limited to, the software packages QPOPT [48], ACADO Toolkit [66], IPOPT [139], and GRAMPC [54]. Such numerical frameworks also make it possible to cope with state constraints by means of interior point methods [143], augmented Lagrangian methods [16, 69], or transformation techniques [53, 52]. Another advantage of FDTO approaches is a consistent gradient condition (1.18). In contrast, the optimality conditions of an FOTD approach need a rather fine spatial grid to guarantee their numerical validity.

Most of the numerical issues discussed above can be avoided by applying an FOTD approach that is closely coupled to state-of-the-art FEM software [108, 109]. Thereby, it is important to keep in mind that the discretization step of an FOTD approach is solely required to numerically solve the optimality conditions. An elaborate representation of the discretized system dynamics for deriving the optimality conditions is not necessary. By its very nature, FOTD approaches provide the possibility to discretize the system dynamics and adjoint dynamics on different spatial grids [133, 63]. This allows one to suit the fineness of the grid to the expected dynamics of the canonical equations, by which the numerical effort for solving them can be kept to a minimum without introducing noticeable discretization errors [55]. Furthermore, the possibility to influence the spatial discretization with relative ease allows to deal with changing geometries during shape optimization [111].

As already mentioned, an FOTD approach follows the idea to formulate the optimality conditions in infinite-dimensional spaces and requires a deep mathematical insight into the optimization problem [40, 133, 62]. Another challenging aspect concerns the proper treatment of state constraints when deriving the optimality conditions, see, e. g., [16, 14, 96]. In general, the state constraints lead to complementarity conditions to handle active and inactive state constraints. This not only complicates the formulation of the optimality system but also its numerical solution. In order to achieve a well-defined problem formulation, the complementarity conditions can be handled numerically by means of proper regularization techniques [60, 134, 96]. Another way to deal with active and inactive state constraints follows from a transformation method that reformulates the inequality constrained problem as an equality constrained counterpart [52].

1.3.3 Mathematical "inexact" optimization approaches

This thesis takes the opportunity of an FOTD approach to outsource the numerical effort of the trajectory planning of electromagnetic heating systems to FEM-based simulation software. However, a more formal approach is pursued to cope with the challenging task of deriving the optimality conditions. The basic idea of formally deriving the optimality conditions is exemplified for optimization problem (1.10) using the formal Lagrangian technique [133] and the calculus of variations [120]. This provides the methodological basis for optimizing the excitation and the position or shape of electromagnetic actuators.

Formal Lagrangian technique

The formal Lagrangian technique tackles optimization problems such as (1.10) by analyzing a so-called Lagrangian that eliminates side constraints (e. g. PDE systems or state constraints) in a first step. The Lagrangian $\mathcal{L} := \mathcal{L}(y, v, p)$ for optimization problem (1.10) reads

$$\begin{aligned}\mathcal{L} = &\int_\Omega \frac{q_1}{2}\left(y - y_\mathrm{d}\right)^2 \,\mathrm{d}x + \int_{\Gamma_0} \frac{q_2}{2}\left(v - v_\mathrm{d}\right)^2 \,\mathrm{d}x \\ &- \int_\Omega p\left(\Delta y + f\right) \,\mathrm{d}x + \int_{\Gamma_0} p\left(n \cdot \nabla y - v\right) \,\mathrm{d}x + \int_{\Gamma_1} p\left(n \cdot \nabla y\right) \,\mathrm{d}x \;, \end{aligned} \tag{1.19}$$

where the side constraints (1.10b)–(1.10d) are coupled to the cost functional (1.10a) by means of the adjoint state $p := p(x)$, cf., e. g., [133, 119]. The Lagrangian $\mathcal{L}$ can be interpreted, roughly speaking, as the counterpart of the reduced cost functional (1.16). Thereby, the Lagrangian only accounts for the system dynamics by means of the adjoint state p instead of a control-to-state operator $G(v)$, cf. Equation (1.15).

The Lagrangian (1.19) allows one to derive the optimality conditions of minimization problem (1.10) in a classical sense. To this end, the directional derivatives of first order

$$\left.\frac{\partial \mathcal{L}}{\partial p}\right|_{a^*} h_p = 0 \qquad \forall h_p \tag{1.20a}$$

$$\left.\frac{\partial \mathcal{L}}{\partial y}\right|_{a^*} h_y = 0 \qquad \forall h_y \tag{1.20b}$$

$$\left.\frac{\partial \mathcal{L}}{\partial v}\right|_{a^*} h_v = 0 \qquad \forall h_v \tag{1.20c}$$

are considered to interrelate an optimal solution $a^* = (y^*, v^*, p^*)$ to vanishing partial derivatives of the Lagrangian $\mathcal{L}$ with respect to the adjoint state p, the state y, and the optimization variable v, respectively.[8] Thereby, the admissible directions $h_p = p - p^*$, $h_y = y - y^*$, and $h_v = v - v^*$ represent the rate of change of the Lagrangian $\mathcal{L}$ as the optimal solution a^* varies, also see [133, 55].

[8] The notation $(\cdot)|_{a^*}$ is used in short for $(\cdot)|_{a=a^*}$ to not further complicate the notation.

In order to be able to analyze the directional derivatives (1.20) with respect to an optimal solution, the formal Lagrangian technique accepts a negligence of mathematical strictness in the sense that spatial operators such as the Laplacian $\Delta(\cdot)$ or the gradient $\nabla(\cdot)$ are treated formally.[9] The function space of the adjoint state p is not properly defined either. Instead, it is assumed that both the state y and the adjoint state p are at least twice continuous differentiable with respect to the spatial coordinate x.

The simplifying assumptions mentioned above shall facilitate the derivation of an optimality system by reformulating the directional derivatives (1.20). Actually, suitable integral identities can be applied to the directional derivatives to interchange the arguments (h_y, h_p) with the arguments (y, p) of the spatial operators $\Delta(\cdot)$ and $\nabla(\cdot)$. The following lines demonstrate this reformulation step. A detailed discussion of the formal Lagrangian technique can be found in [133].

An evaluation of the directional derivative (1.20a) yields the variational equation

$$\left.\frac{\partial \mathcal{L}}{\partial p}\right|_{a^*} h_p = -\int_\Omega (\Delta y^* + f)\, h_p \,\mathrm{d}x + \int_{\Gamma_0} (n \cdot \nabla y^* - v^*)\, h_p \,\mathrm{d}x + \int_{\Gamma_1} (n \cdot \nabla y^*)\, h_p \,\mathrm{d}x = 0 \qquad \forall h_p \quad (1.21)$$

from which the first of three required conditions for the optimality of the state y, the optimization variable v, and the adjoint state p can be deduced. To guarantee that the variational equation (1.21) vanishes for all admissible directions h_p, the system dynamics

$$-\Delta y^* = f \qquad \text{in } \Omega \quad (1.22a)$$

$$n \cdot \nabla y^* = v^* \qquad \text{on } \Gamma_0 \quad (1.22b)$$

$$n \cdot \nabla y^* = 0 \qquad \text{on } \Gamma_1 \quad (1.22c)$$

has to be satisfied by an optimal solution. Note that this PDE system ensures that the variational equation (1.21) vanishes in a distributional manner, implying optimality in terms of the first-order optimality condition (1.20a).

The directional derivative (1.20b) allows to derive the adjoint dynamics, which, as already discussed in Section 1.3.2, reflects the impact of the system dynamics on the cost functional. In view of a formal treatment of spatial operators, the directional derivative (1.20b) can be evaluated and results in the variational equation

$$\left.\frac{\partial \mathcal{L}}{\partial y}\right|_{a^*} h_y = \int_\Omega q_1 (y^* - y_\mathrm{d})\, h_y \,\mathrm{d}x - \int_\Omega p^* \,\Delta h_y \,\mathrm{d}x + \int_\Gamma p^* \, n \cdot \nabla h_y \,\mathrm{d}x = 0 \qquad \forall h_y \,. \quad (1.23)$$

Thereby, the arguments of the Laplacian and gradient operator swap from the state y to the admissible directions h_y.

[9] The term "formal" refers to the fact that spatial operators are treated as constants when evaluating directional derivatives such as (1.20). It is also assumed that the arguments of the spatial operators are interchangeable between the state and adjoint variables in the sense of suitable integral identities [133].

Integration by parts is applied to the second integral of the variational equation (1.23). This allows one to analyze the variational equation for all admissible directions h_y. A suitable integral identity to shift the spatial operator from the admissible directions h_y to the adjoint state p is given by Green's second identity

$$\int_\Omega p^* \, \Delta h_y \, \mathrm{d}x = \int_\Omega \Delta p^* \, h_y \, \mathrm{d}x - \int_\Gamma n \cdot (\nabla p^*) \, h_y \, \mathrm{d}x + \int_\Gamma p^* \, n \cdot \nabla h_y \, \mathrm{d}x \; . \tag{1.24}$$

Finally, the application of the integral identity (1.24) to the variational equation (1.23) yields the formulation

$$\left.\frac{\partial \mathcal{L}}{\partial y}\right|_{a^*} h_y = \int_\Omega \Big[q_1 \, (y^* - y_\mathrm{d}) - \Delta p^* \Big] h_y \, \mathrm{d}x + \int_\Gamma n \cdot \nabla p^* h_y \, \mathrm{d}x = 0 \qquad \forall h_y \tag{1.25}$$

that no longer contains admissible directions h_y that are subject to spatial operators.

The reformulated variational equation (1.25) is used to define the adjoint dynamics

$$\Delta p^* = q_1 \, (y^* - y_\mathrm{d}) \qquad \text{in } \Omega \tag{1.26a}$$

$$n \cdot \nabla p^* = 0 \qquad \text{on } \Gamma \tag{1.26b}$$

by which the directional derivative (1.20b) vanishes for all admissible directions h_y in a distributional manner. Consequently, the adjoint dynamics (1.26) can be used to determine the optimal adjoint state p^* depending on the optimal state y^*.

Two of three necessary optimality conditions of optimization problem (1.10) are already known in form of the system dynamics (1.22) and the adjoint dynamics (1.26). In order to derive the third condition, the directional derivative (1.20c) is evaluated

$$\left.\frac{\partial \mathcal{L}}{\partial v}\right|_{a^*} h_v = \int_{\Gamma_0} q_2 \, (v^* - v_\mathrm{d}) \, h_v \, \mathrm{d}x - \int_{\Gamma_0} p^* \, h_v \, \mathrm{d}x = 0 \qquad \forall h_v \; . \tag{1.27}$$

This variational equation can be used to formulate the gradient condition

$$g_v = \int_{\Gamma_0} q_2 \, (v^* - v_\mathrm{d}) - p^* \, \mathrm{d}x = 0 \; , \tag{1.28}$$

whereby the negative gradient $-g_v$ minimizes the cost functional (1.10a) in terms of a steepest descent approach. In conclusion, the optimality conditions described by the system dynamics (1.22), the adjoint dynamics (1.26), and the gradient condition (1.28) can be used to determine an optimal solution of optimization problem (1.10).

The procedure of deriving the optimality conditions by means of the formal Lagrangian technique benefits to a great extent from the negligence of mathematical strictness. This allows, in the absence of state constraints, to both formulate and evaluate the directional derivatives (1.20) with relative ease. It is for this reason, that, for the time being, no state constraints

are considered. A detailed discussion about the incorporation of state constraints is given in Chapter 5 and Appendix A. The situation is different with regard to input constraints

$$v \in \mathcal{V}_{\mathrm{ad}} := \{v \in \mathbb{R} \,|\, v^- \leq v \leq v^+\} \tag{1.29}$$

with bounds $v^- < v^+$. It is straightforward to show that in this case the optimality conditions coincide with the unconstrained case apart from the variational inequality

$$\left.\frac{\partial \mathcal{L}}{\partial v}\right|_{a^*} h_v = \int_{\Gamma_0} q_2 \,(v^* - v_{\mathrm{d}})\; h_v \;\mathrm{d}x - \int_{\Gamma_0} p^*\, h_v \;\mathrm{d}x \geq 0 \qquad \forall v \in \mathcal{V}_{\mathrm{ad}} \tag{1.30}$$

replacing the variational equation (1.27), see, e. g., [133, 62]. On the basis of the variational inequality and the definition of the unconstrained gradient (1.28), the conditional expression

$$g_v \begin{cases} > 0 & \text{if } v^* = v^- \\ = 0 & \text{if } v^* \in (v^-, v^+) \\ < 0 & \text{if } v^* = v^+ \end{cases} \tag{1.31}$$

allows one to adapt the optimality conditions for the input constraints (1.29), also see [1].

Calculus of variations

The calculus of variations copes with optimization problem (1.10) by analyzing the stationary of the Lagrangian (1.19) in a slightly different way than the formal Lagrangian technique [120]. First of all, the non-optimal trajectories are introduced

$$p = p^* + \epsilon\, \delta p \tag{1.32a}$$
$$y = y^* + \epsilon\, \delta y \tag{1.32b}$$
$$v = v^* + \epsilon\, \delta v \tag{1.32c}$$

with ϵ as a variational parameter for the variations $(\delta p, \delta y, \delta v)$, whereby $\delta p := \delta p(x)$ and $\delta y := \delta y(x)$. The variational parameter ϵ is used as a scaling factor to defect the optimal solution (p^*, y^*, v^*) in the direction of $(\delta p, \delta y, \delta v)$.

The calculus of variations derives the first-order optimality conditions of optimization problem (1.10) by reformulating the derivatives

$$\lim_{\epsilon \to 0} \left(\frac{\mathcal{L}(y^*, v^*, p^* + \epsilon\, \delta p) - \mathcal{L}(y^*, v^*, p^*)}{\epsilon} \right) = \left. \frac{\mathrm{d}\mathcal{L}(y^*, v^*, p^* + \epsilon\, \delta p)}{\mathrm{d}\epsilon} \right|_{\epsilon = 0} = 0 \qquad \forall \delta_p \tag{1.33a}$$

$$\lim_{\epsilon \to 0} \left(\frac{\mathcal{L}(y^* + \epsilon\, \delta y, v^*, p^*) - \mathcal{L}(y^*, v^*, p^*)}{\epsilon} \right) = \left. \frac{\mathrm{d}\mathcal{L}(y^* + \epsilon\, \delta y, v^*, p^*)}{\mathrm{d}\epsilon} \right|_{\epsilon = 0} = 0 \qquad \forall \delta_y \tag{1.33b}$$

$$\lim_{\epsilon \to 0} \left(\frac{\mathcal{L}(y^*, v^* + \epsilon\, \delta v, p^*) - \mathcal{L}(y^*, v^*, p^*)}{\epsilon} \right) = \left. \frac{\mathrm{d}\mathcal{L}(y^*, v^* + \epsilon\, \delta v, p^*)}{\mathrm{d}\epsilon} \right|_{\epsilon = 0} = 0 \qquad \forall \delta_v \;, \tag{1.33c}$$

which show a close similarity to the directional derivatives (1.20) in the case of the formal Lagrangian technique.

The variation of the Lagrangian with respect to the adjoint state (1.33a) again results in the system dynamics (1.22) representing one part of the optimality conditions. Similarly, the analysis of the variation of the Lagrangian with respect to the state (1.33b) will result in an adjoint dynamics. To this end, the non-optimal state trajectory (1.32b) is substituted into the Lagrangian (1.19) yielding

$$\begin{aligned}\mathcal{L}(y^* + \epsilon\,\delta y, v^*, p^*) = &\int_\Omega \frac{q_1}{2}\,(y^* + \epsilon\,\delta y - y_\mathrm{d})^2\ \mathrm{d}x + \int_{\Gamma_0} \frac{q_2}{2}\,(v^* - v_\mathrm{d})^2\ \mathrm{d}x \\ &- \int_\Omega p^*\,(\Delta\, y^* + \epsilon\,\Delta\,\delta y + f)\ \mathrm{d}x \\ + \int_{\Gamma_0} p^*\,(n\cdot\nabla\, y^* + \epsilon\, n\cdot\nabla\,\delta y - v^*)\ \mathrm{d}x &+ \int_{\Gamma_1} p^*\,(n\cdot\nabla\, y^* + \epsilon\, n\cdot\nabla\,\delta y)\ \mathrm{d}x\ . \quad (1.34)\end{aligned}$$

The total differentiation of the modified Lagrangian (1.34) with respect to the variational parameter ϵ according to (1.33b) gives

$$\begin{aligned}\left.\frac{\mathrm{d}\mathcal{L}(y^* + \epsilon\,\delta y, v^*, p^*)}{\mathrm{d}\epsilon}\right|_{\epsilon=0} = &\int_\Omega q_1\,(y^* - y_\mathrm{d})\,\delta y\ \mathrm{d}x \\ &- \int_\Omega p^*\Delta\,\delta y\ \mathrm{d}x + \int_\Gamma p^* n\cdot\nabla\,\delta y\ \mathrm{d}x = 0 \qquad \forall\delta_y\ . \quad (1.35)\end{aligned}$$

Note that the variational equation (1.35) exhibits an identical structure as its counterpart (1.23) obtained from the directional derivative (1.20b) in the course of applying the formal Lagrangian technique. Hence, the calculus of variations confirms that an optimal solution of optimization problem (1.10) has to satisfy the adjoint dynamics (1.26).[10]

The first-order optimality condition (1.33c) relating the optimization variable v to an optimal solution results in the variational equation

$$\left.\frac{\mathrm{d}\mathcal{L}(y^*, v^* + \epsilon\,\delta v, p^*)}{\mathrm{d}\epsilon}\right|_{\epsilon=0} = \int_{\Gamma_0} q_2\,(v^* - v_\mathrm{d})\,\delta v - p^*\delta v\ \mathrm{d}x = 0 \quad \forall\delta_v\ . \qquad (1.36)$$

This variational equation allows again to define the gradient (1.28) that completes with the system dynamics (1.22) and the adjoint dynamics (1.26) the optimality system of optimization problem (1.10). In the case of a constrained optimization variable (1.29), the gradient condition is subject to the conditional expression (1.31).

[10] The adjoint dynamics (1.26) can be derived from the variational equation (1.35) by applying a modified version of Green's second identity (1.24) by which the spatial operators $\Delta\,(\cdot)$ and $\nabla\,(\cdot)$ can be shifted from the variation δy to the adjoint state p.

1.4 Overview on trajectory planning methods for electromagnetic heating systems

The various methodological and numerical issues discussed so far are the reason why there are only few approaches in the literature that optimize electromagnetic heating systems in a holistic manner. Usually, the trajectory planning problem is confined to optimizing the electrical excitation of the actuator [135, 122] or its position/shape [3, 36]. Furthermore, most of the contributions use mathematical models of reduced space dimension [140, 41, 45] and pursue semi-analytical approaches or simplify the problem formulation for the trajectory planning [125, 17]. State constraints are also often neglected [65, 41, 45]. The majority of contributions cope with the numerical challenges by means of frameworks that are adapted to the specific problem, see, e. g., [122, 3, 140].

The following lines address the most relevant contributions concerning the trajectory planning of electromagnetic heating systems. The review is not restricted to optimization-based techniques but includes other commonly used approaches. The discussion is divided into two parts. The first part gives an overview on existing solution approaches from a more methodological point of view. The second part discusses how the numerical solution of the trajectory planning problem is carried out in literature.

1.4.1 Methodological approaches

A variety of methods has been proposed in literature that cope with the trajectory planning for electromagnetic heating systems with different emphasis. The methods can be divided into trial-and-error approaches, genetic algorithms, and optimization-based techniques.

Trial-and-error approaches

An intuitive way to cope with trajectory planning of electromagnetic heating systems are trial-and-error approaches [118]. Thereby, simulation studies or experiments are used to investigate the impact of the available degrees of freedom on the objectives of a problem, see, e. g., [64, 73, 29]. The contribution [91] uses a trial-and-error approach to relate the impact of the electrical excitation of individual actuators on the heat-up behavior of a semiconductor wafer. The knowledge of the actuated system dynamics is used to formulate an actuation strategy in terms of a superposition method. A similar approach is presented by the authors of the contribution [103]. Here, the superposition method takes the law of conservation of energy into account to describe the relationship between the actuator excitation and the spatial distribution of the heat source in a more realistic manner.

A trial-and-error approach is discussed in [38] for the temperature control in hyperthermia therapy. The authors investigate the impact of some design parameters (e. g. Curie temperature of magnetic nanoparticles, excitation of the actuator) to plan trajectories that overheat the tumor without increasing the temperature of healthy tissue too much. There are also

trial-and-error approaches that adapt the actuator position and shape to obtain an optimal heat-up behavior for induction heating processes and hyperthermia therapy [147, 26, 75, 44]. However, in particular the shape optimization problem becomes manifold and has to be restricted to few parameters (e. g. length and width of the actuator).

Genetic algorithms

Genetic algorithms provide a more systematic approach to optimize the electrical excitation and the position or shape of the actuator, see, e. g., [49, 35]. The adaptive and heuristic search algorithms allow to find at least a suboptimal solution of the trajectory planning problem.[11] A further advantage of genetic algorithms over trial-and-error approaches is the fact that the adaptation of the optimization variables can be automated. The optimization of the actuator excitation by means of genetic algorithms is presented in [36, 23] for an induction heat-up process and hyperthermia therapy. The contributions [36, 82] simultaneously optimize the excitation and position of an actuator for induction heating and hyperthermia therapy problems of axisymmetrical type. An approach that is based on genetic algorithms and optimizes the shape of an actuator for a surface hardening process is presented in [81].

The bottleneck of genetic algorithms is the necessity to test a sequence of suitable candidates of optimization variables. Thereby, the test sequence has to be sufficiently large to ensure that the algorithm converges to an optimal solution. This confines the applicability of genetic algorithms to only few optimization variables and rather simple actuator shapes. In addition, genetic algorithms are zero-order methods that do not employ gradient information and the algorithm converges for practical reasons only to a suboptimal solution.

Optimization-based techniques

Optimization-based techniques constitute a promising approach to cope with the trajectory planning problem in a more systematic manner. Once the crucial task of discretizing the infinite-dimensional system dynamics is overcome, the optimization step of an FDTO approach can be carried out by means of nonlinear programming techniques. The contribution [59] considers an induction heating process and uses sequential quadratic programming to optimize the length and width of the actuator. Similarly, the contributions [34, 122, 23] discretize the infinite-dimensional system dynamics of hyperthermia processes to optimize the actuator excitation. The nonlinear programming problems are tackled by the simplex algorithm, an interior point method, and sequential quadratic programming.

The discretization of the infinite-dimensional system dynamics also facilitates to use other control design methods than optimization-based techniques. As the PDE constraints reduce to a set of ODEs or algebraic equations, the control design can benefit from well-established

[11] Theoretically, genetic algorithms converge to the global optimum. However, the implementation of the algorithm often relies on an approximated problem formulation since they do not scale well with the complexity of the problem [35].

methods. For instance, the authors of [125] apply a flatness-based feedforward design method to a thixoforming process to determine a suitable control strategy for exciting the actuator. The concept of eigenvalue optimization, see, e. g., [85], is used in [80, 97] to optimize the excitation of some actuators for hyperthermia therapy.

The application of FOTD approaches is investigated by some authors to cope with the optimization of electromagnetic heating problems. The contributions [145, 37, 135] determine an optimal excitation strategy for actuators in the course of induction heating. The optimality conditions in the infinite-dimensional function spaces are derived by analyzing suitable control-to-state operators such as (1.15). Similar optimization problems are considered by the authors of [17, 90], where the formal Lagrangian technique is used to derive the optimality conditions with respect to an optimal excitation strategy for the actuator.

In literature, there are relatively few FOTD approaches that deal with the optimization of the position and shape of electromagnetic actuators. The optimization of actuator positions of a hyperthermia process is presented in [3]. In [17], the infinite-dimensional problem of shape optimization is reformulated to incorporate the corresponding design variables in an explicit form. It is assumed that the geometrical setup of the induction heating process is infinite in the direction perpendicular to a sufficiently thin actuator. The optimality conditions are derived formally on the basis of the reformulated optimization problem.

The concept of shape sensitivities is used in [65] to optimize the actuator shape in the course of surface hardening. An analysis of the shape sensitivities reveals a descent direction for the boundary of the actuator. The authors of the contribution [77] present a similar approach. Here, the shape sensitivity analysis is combined with level-set methods to simultaneously optimize the actuator shape and its structure and topology. The method is based on the proper definition of transformation approaches which, roughly speaking, comply with the control-to-state operator (1.15) in the case of optimizing the excitation of the actuator. Thus, the above optimization techniques require a deep mathematical insight into the problem.

Although state constraints complicate the derivation of optimality conditions, optimization-based techniques are the preferred choice for state constrained trajectory planning. An FDTO approach can benefit from interior point methods, augmented Lagrangian methods or transformation approaches to tackle state constraints both from an algorithmic and a numerical point of view, cf. Section 1.3.2, also see [16, 98].

The research activity of PDE constrained optimization has focused on handling state constraints in the last years providing a solid theoretical foundation [69, 33, 61, 96]. In general, the optimality conditions of state constrained problems are of Karush-Kuhn-Tucker type [25, 62, 61, 96] that can, for instance, be numerically solved using augmented Lagrangian methods [13, 14, 69]. The systematic incorporation of state constraints for the trajectory planning is presented in [145, 37, 135]. The problem formulation, however, concerns the optimization of either the excitation or the shape of the actuator.

A more straightforward procedure to handle state constraints is given by inner and outer barrier methods [90, 123]. Here, the violation of the state constraint is penalized by means of a sufficiently large additional cost value. The contribution [90] proposes such a barrier

method for an induction heating process. Most of the contributions, however, disregard state constraints when planning optimal trajectories for electromagnetic heating systems, see, for instance, [17, 36, 65, 41, 90, 77].

1.4.2 Numerical frameworks

Trial-and-error approaches and genetic algorithms cope with optimal trajectory planning problems on the basis of a repetitive solution of the system dynamics. The characteristic of such zero-order methods offers the opportunity to outsource the numerical effort that is related with multiphysics problems to simulation software. The authors of [36, 82, 97, 81, 23] present numerical frameworks relying on this idea and plan optimal trajectories for induction heating or hyperthermia therapy. To this end, genetic algorithms are combined with simulation software such as Comsol Multiphysics [28] or Ansys [5]. This allows to get rid of the crucial tasks of numerically solving the system dynamics without developing own numerical tools and frameworks.

The numerical FDTO and FOTD frameworks used in the literature to cope with optimal trajectory planning are commonly adapted to the specific problem. The discretization step of an FDTO approach must result in a proper representation of the specific problem for the subsequent optimization step, which makes it impractical to transfer the results to other problems. The contributions [80, 59, 122] apply discretization techniques such as finite differences, finite elements, or finite difference time domain methods to cope with the numerical issues. However, the problems are often restricted to more simple geometrical setups and axisymmetrical problems to reduce the numerical effort, see, e. g., [34, 59, 125].

An FOTD approach is faced with similar numerical issues as an FDTO approach, which is reflected not only by the fact that existing contributions adapt the discretization step to the problem at hand. The contributions [77, 3] develop and adapt frameworks to numerically solve the optimality conditions. Here again, the trajectory planning is often restricted to rather simple geometrical setups and axisymmetrical problems [17, 90, 77]. Some contributions minimize the numerical effort by applying specialized optimization techniques which ensure that the optimality conditions are inherently simple to solve. For instance, the authors of the contribution [135] define a control-to-state operator that leads to optimality conditions that comprise the system dynamics but not any additional PDE system.

1.5 Goals and outline of the thesis

The overview on trajectory planning approaches reveals that there is a lack of holistic optimization approaches for electromagnetic heating problems. There are many contributions that either optimize the electrical excitation or the position or shape of the actuator, but do not handle both aspects simultaneously. It can also be noticed that existing approaches are often restricted to explicit geometrical setups including simple shapes and structures. The contributions are also mainly customized for individual problems such as induction heating or hyperthermia therapy and often disregard constraints for the trajectory planning.

In this thesis, an optimal trajectory planning approach is proposed that simultaneously optimizes the excitation and position or shape of electromagnetic actuators. The systematic incorporation of state constraints for the trajectory planning is another focus of this work. The presented approach is capable to handle typical electromagnetic heating systems such as induction heating or hyperthermia therapy including geometries of arbitrary complexity. To this end, an optimization framework is developed that combines FOTD approaches with software tools that are specialized on simulating multiphysics problems. Thereby, the separation of the numerical issues from the methodological ones allows to cover different application domains and geometrical setups in a straightforward manner.

The crucial point of deriving the optimality conditions of the PDE constrained optimization problems is attacked formally. It is shown that the problem of optimizing the electrical excitation of the actuator can be tackled by means of the formal Lagrangian technique resulting in a set of suitable optimality conditions. The problem of optimizing the position and shape of the actuator is handled in a separate step. To this end, the adjoint-based sensitivity analysis is applied to the optimization problems to derive the corresponding optimality conditions. However, both sets of optimality conditions are combined to simultaneously optimize the excitation and position or shape of the actuator. In order to incorporate state constraints, both a transformation approach and an augmented Lagrangian method are investigated.

The key role in the numerical solution of the trajectory planning problems plays the structure of the optimality conditions, ensuring a sequential solution by means of tailored gradient methods. Because of this characteristic, both the system dynamics and adjoint dynamics can be iteratively solved forward and backward in time. This structural advantage can be preserved even if state constraints are present. The development of an optimization framework picks up this idea and couples the software packages MATLAB and COMSOL MULTIPHYSICS. Thus, the algorithmic treatment of the optimality conditions benefits from well known methods of optimization problems governed by ODEs or algebraic equations. On the other hand, the numerical solution of the multiphysics problems and its optimality conditions is outsourced to COMSOL MULTIPHYSICS. The applicability and accuracy of the optimization framework is investigated for various applications from induction heating and hyperthermia therapy.

The goals of this thesis reflect the structure of the individual chapters. Chapter 2 addresses the mathematical description of electromagnetic heating systems in form of coupled PDEs. The Maxwell equations and the heat equation form the system dynamics of the electromagnetic heating processes and are equipped with suitable boundary conditions to complete its mathematical description.

The optimal excitation of electromagnetic actuators is investigated in Chapter 3. The trajectory planning problem is tackled by formulating and numerically solving suitable optimization problems. Thereby, the formal Lagrangian technique is used to derive the corresponding optimality conditions following an FOTD approach. Chapter 3 also presents an optimization framework that involves the primary benefit to handle various kinds of electromagnetic heating systems with relative ease. The optimization framework closely couples FEM software with a tailored gradient method.

Chapter 4 deals with the problem of optimizing the position and shape of electromagnetic actuators. A coupled optimization problem is formulated in order to simultaneously optimize the actuator configuration and excitation. Similar to Chapter 3, the optimality conditions are derived on the basis of FOTD approaches. It is shown that a combination of the formal Lagrangian technique and adjoint-based sensitivity analysis is applicable to derive the optimality conditions of the coupled problem. The numerical solution of the optimality conditions is provided by a modified version of the optimization framework from Chapter 3 to still benefit from the capabilities of FEM software.

The trajectory planning approaches from Chapter 3 and 4 are extended in Chapter 5 to account for state constraints in a systematic manner. To this end, an augmented Lagrangian method is introduced, where special emphasis is put on maintaining the structural benefits of the optimality conditions to facilitate the numerical solution of the constrained problem by means of FEM software. The augmented Lagrangian method ensures this by adjoining the state constraints to the cost functional. From an algorithmic point of view, the reformulated problem is unconstrained and can be numerically solved similar to Chapter 3 and 4 by outsourcing the numerical effort to FEM software. Finally, the results of this thesis and an outlook on potential future work are summarized in Chapter 6.

In Appendix A, a transformation approach is discussed to handle state constraints in a more analytical manner compared to the augmented Lagrangian method in Chapter 5. Saturation functions are used to transform the constrained optimization problem into an unconstrained one that can be numerically solved by means of the optimization frameworks presented in this thesis. Appendix B summarizes abbreviations and symbols that are used throughout the text.

Chapter 2

Modeling of electromagnetic heating systems

The trajectory planning of electromagnetic heating systems requires mathematical models that represent at least the electromagnetic and thermal phenomena of the real physics.[1] In order to optimize the electrical excitation as well as the position and shape of the actuator on the basis of a highly accurate mathematical model, the Maxwell equations and the heat equation are introduced. This chapter follows the idea to describe the multiphysics problem of electromagnetic heating in a general setting.

2.1 Model requirements

The governing equations of electromagnetic heating systems are formulated for the geometrical setups shown in Figure 2.1. The left hand side illustrates an induction heating process as it typically arises in steel industry when conducting tempering, surface hardening, or shrinking processes for electrically conductive objects Ω_o, see, e. g., [31, 118, 32]. In short, the objective of the trajectory planning consists of heating up either the whole object or only individual parts of it. To this end, the actuator with spatial domain Ω_c is energized with alternating currents $i := i(t)$, $t \in (0, t_\mathrm{f})$ to generate the electromagnetic heat source, cf. Figure 2.1a. From a mathematical point of view, the spatial domain of air Ω_a is required to model the electromagnetic field in the surrounding area.[2]

In order to address the problem of planning optimal trajectories for interstitial hyperthermia therapy, see, e. g., [9, 144], the geometrical setup from Figure 2.1b is considered. In this case, the spatial domain Ω_o represents a region of the human body that is affected by a tumor and includes the infected and healthy tissue as well as blood vessels and nerves. Hyperthermia therapy uses the electromagnetic heat source for overheating the tumor or making the cancer cells more susceptible to conventional drug treatments [144, 46, 73].

The objective of the trajectory planning in the case of hyperthermia therapy is to realize specific temperature profiles that guarantee optimal therapeutic success. A needle-like actuator acts as a coaxial cable and is sticked into the diseased tissue to guide the electric energy

[1] Further phenomena are, e. g., metallurgical effects, mechanical stresses, and deformations of the object to be heated and can be taken into account by extending the mathematical model by suitable PDEs.

[2] A description of the subscripts of spatial domains can be found in Appendix B.4.

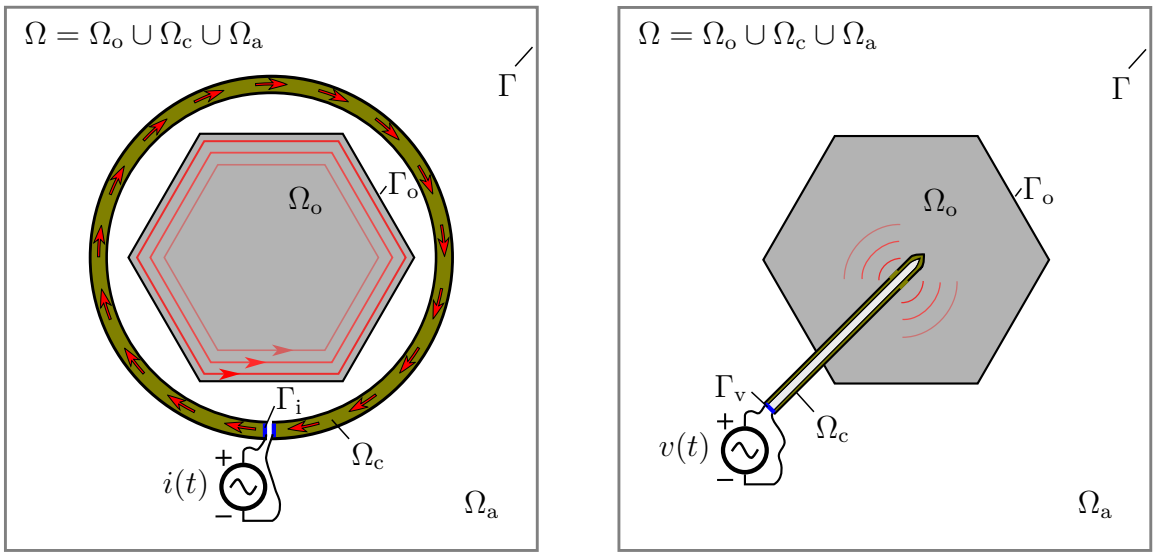

(a) Induction heating

(b) Hyperthermia therapy

Figure 2.1: Geometrical setups of induction heating and hyperthermia processes with spatial domain $\Omega = \Omega_o \cup \Omega_c \cup \Omega_a$ including the object, actuator, and ambient air (not to scale).

from a voltage source $v := v(t)$, $t \in (0, t_f)$ via an air gap to the tumor, cf. Figure 2.1b. This generates the electromagnetic heat source as close as possible in the region of the tumor and avoids a hazardous overheating of healthy tissue.

In what follows, the electromagnetic phenomena are mathematically described on the spatial domain $\Omega = \Omega_o \cup \Omega_c \cup \Omega_a$ with boundary Γ. The impact of confining the spatial domain to a smaller region is accommodated by the formulation of boundary conditions. The thermal phenomena of the induction heating and hyperthermia processes, however, are modeled solely on the spatial domain of the object Ω_o. The formulation of boundary conditions on Γ_o is used to account for the thermal interaction between the object and its surrounding.

2.2 Electromagnetic phenomena

The Maxwell equations are used to incorporate the electromagnetic phenomena for the trajectory planning. A time-dependent as well as a time-harmonic formulation is introduced, whereby the latter requires considerably lower numerical effort for solving the system dynamics. The Maxwell equations are adapted according to whether current or voltage sources are used to generate the electromagnetic field. This ensures that the corresponding optimization variable occurs explicitly in the optimization problem for the trajectory planning.

A set of boundary conditions completes the mathematical formulation of the electromagnetic phenomena. Conditions for symmetry planes are introduced to reduce the region of interest Ω if circumstances permit. Finally, the electromagnetic heat source is mathematically described and interlinked to the thermal phenomena.

2.2.1 Maxwell's equations in time-dependent form

The electromagnetic phenomena are described by the time-dependent Maxwell equations in differential form, see, for instance, [130],

$$\nabla\cdot\mathcal{D} = \hat{\rho} \qquad \text{in } \Omega\times(0,t_\mathrm{f}) \tag{2.1a}$$
$$\nabla\cdot\mathcal{B} = 0 \qquad \text{in } \Omega\times(0,t_\mathrm{f}) \tag{2.1b}$$
$$\nabla\times\mathcal{E} = -\partial_t\mathcal{B} \qquad \text{in } \Omega\times(0,t_\mathrm{f}) \tag{2.1c}$$
$$\nabla\times\mathcal{H} = \mathcal{J}+\partial_t\mathcal{D} \qquad \text{in } \Omega\times(0,t_\mathrm{f})\ . \tag{2.1d}$$

Gauss' law (2.1a) relates the electric charge density $\hat{\rho} := \hat{\rho}(x,t)$ to the electric flux density $\mathcal{D} := \mathcal{D}(x,t)$ using the divergence operator $\nabla\cdot(\cdot)$. Gauss' law of magnetism (2.1b) states that the divergence of the magnetic flux density $\mathcal{B} := \mathcal{B}(x,t)$ is zero. Note that the quantities of the electromagnetic field are vectors depending both on space x and time t, whereby vectors are distinguished from scalars using capital letters.

The wave propagation effects of the electromagnetic field stem from a close coupling between Faraday's law of induction (2.1c) and Ampere's law (2.1d) with $\nabla\times(\cdot)$ denoting the curl operator. Faraday's law of induction describes the generation of an electric field intensity $\mathcal{E}$ due to a time-varying magnetic field. On the other hand, Ampere's law states that the current density $\mathcal{J} := \mathcal{J}(x,t)$ creates a magnetic field intensity $\mathcal{H}$ in addition to a temporally changing electric field. Ampere's law (2.1d) in combination with Gauss' law (2.1a) implies the equation of continuity

$$\nabla\cdot\mathcal{J}+\partial_t\hat{\rho} = 0 \qquad \text{in } \Omega\times(0,t_\mathrm{f})\ , \tag{2.2}$$

since the divergence of the curl of any vector field is zero. A more detailed discussion on the Maxwell equations (2.1) can be found, for instance, in [130, 57].

As a result of the bilateral coupling effects between Faraday's law of induction (2.1c) and Ampere's law (2.1d), electromagnetic waves travel through space. With respect to an optimal trajectory planning, the electrical charge density $\hat{\rho}$ and the current density $\mathcal{J}$ are the degrees of freedom to manipulate the temporal and spatial distribution of the electromagnetic field quantities [147, 118]. For example, if the actuator is energized by a current source i as illustrated in Figure 2.1a, the current density $\mathcal{J}$ can be assumed to be impressed within the spatial domain of the actuator Ω_c. Accordingly, the current density in total is

$$\mathcal{J} = \mathcal{J}_\mathrm{imp}+\mathcal{J}_\mathrm{ind} \qquad \text{in } \Omega\times(0,t_\mathrm{f}) \tag{2.3}$$

summarizing externally impressed current densities $\mathcal{J}_\mathrm{imp}$ and induced current densities $\mathcal{J}_\mathrm{ind}$ due to Ohm's law. Thus, the objective of the trajectory planning to heat up specific regions of the object Ω_o can be tackled by modifying the excitation and the position or shape of the actuator in a way that the electromagnetic field generates an appropriate heat source.

The Maxwell equations (2.1) need to be extended by the constitutive relationships $\mathcal{B} = \mathcal{B}(\mathcal{H})$ and $\mathcal{D} = \mathcal{D}(\mathcal{E})$ to model how the electromagnetic field interacts in a macroscopic manner with materials. For isotropic linear materials, the constitutive relationships read as

$$\mathcal{B} = \mu\mathcal{H} \qquad \text{in } \Omega \times (0, t_\mathrm{f}) \tag{2.4a}$$

$$\mathcal{D} = \epsilon\mathcal{E} \qquad \text{in } \Omega \times (0, t_\mathrm{f}) \tag{2.4b}$$

with $\mu = \mu_0\mu_\mathrm{r}$ denoting the magnetic permeability and $\epsilon = \epsilon_0\epsilon_\mathrm{r}$ the electrical permittivity. The permeability and permittivity of free space is denoted by μ_0 and ϵ_0, the relative magnetic permeability by $\mu_\mathrm{r} := \mu_\mathrm{r}(x)$, and the relative electric permittivity by $\epsilon_\mathrm{r} := \epsilon_\mathrm{r}(x)$. The induced current densities $\mathcal{J}_\mathrm{ind}$ are modeled by means of Ohm's law

$$\mathcal{J}_\mathrm{ind} = \sigma\mathcal{E} \qquad \text{in } \Omega \times (0, t_\mathrm{f}) \tag{2.5}$$

forming another constitutional relation, whereby σ denotes the electrical conductivity.

2.2.2 Maxwell's equations in time-harmonic form

Costly power electronics or restrictions to specific hardware platforms means that the electromagnetic actuator is typically excited by current and voltage sources of sinusoidal type with constant frequency. Thus, the electromagnetic field quantities are time-harmonic and the mathematical analysis of the Maxwell equations (2.1) becomes simpler [57]. For example, the instantaneous magnetic field intensity $\mathcal{H}$ can be expressed in the frequency domain by defining the complex-valued phasor $H := H(x)$ as

$$\mathcal{H}(x,t) = \mathrm{Re}\{H(x)e^{j\omega t}\} \ , \tag{2.6}$$

whereby the phasor H solely depends on space but not on time. The angular frequency of the sinusoidal variation is denoted by ω and the operator $\mathrm{Re}\{\cdot\}$ evaluates the real part of its argument. The imaginary unit is denoted by j. The spatial components of $\mathcal{H}$ and H in the direction of x_i are related as follows

$$\mathcal{H}_i(x,t) = \mathrm{Re}\{H_i(x)e^{j\omega t}\} = |H_i(x)|\cos(\omega t + \Phi_i) \tag{2.7}$$

with peak-value $|H_i(x)|$ and phase Φ_i. Thus, the complex-valued phasor of $\mathcal{H}$ is defined as the time-independent vector $H(x) := |H(x)|e^{j\Phi}$ with $|H(x)| = [|H_1(x)|, |H_2(x)|, |H_3(x)|]^\mathsf{T}$ and $\Phi = [\Phi_1, \Phi_2, \Phi_3]^\mathsf{T}$. Equivalently, the electromagnetic field quantities $(\mathcal{B}, \mathcal{D}, \mathcal{E}, \mathcal{J})$ and the electrical charge density $\hat{\rho}$ can be formulated on the basis of the complex-valued phasors (B, D, E, J) and ρ, see, e. g., [57].

Using the complex-valued phasors introduced above, the Maxwell equations (2.1) can be formulated in time-harmonic form

$$\nabla\cdot D = \rho \qquad \text{in } \Omega \tag{2.8a}$$

$$\nabla\cdot B = 0 \qquad \text{in } \Omega \tag{2.8b}$$

$$\nabla\times E = -j\omega B \qquad \text{in } \Omega \tag{2.8c}$$

$$\nabla\times H = J + j\omega D \qquad \text{in } \Omega \ , \tag{2.8d}$$

which no longer contains any temporal dynamics. Thereby, the time-harmonic version (2.8) is derived by means of the phasor arithmetic

$$\mathrm{Re}\{A\} + \mathrm{Re}\{B\} = \mathrm{Re}\{A + B\} \tag{2.9a}$$

$$\mathrm{Re}\{\alpha A\} = \alpha\, \mathrm{Re}\{A\} \tag{2.9b}$$

$$\partial_x\, \mathrm{Re}\{A\} = \mathrm{Re}\{\partial_x A\} \tag{2.9c}$$

$$\int_\Omega \mathrm{Re}\{A\}\ \mathrm{d}x = \mathrm{Re}\{\int_\Omega A\ \mathrm{d}x\} \tag{2.9d}$$

with complex-valued vectors A and B and scalar α. In addition, the transformation from the time-dependent to the time-harmonic form of the Maxwell equations relies on the relation

$$\mathrm{Re}\{Ae^{j\omega t}\} = \mathrm{Re}\{Be^{j\omega t}\}\ \ \forall t \quad \Leftrightarrow \quad A = B\ \ \forall t \tag{2.10}$$

that can be deduced from the phasor arithmetic, see, for instance, [57].

The time-independent formulation of the Maxwell equations (2.8) favors a numerically more efficient treatment of the trajectory planning problem compared to the case of using the time-dependent counterpart (2.1). The time-harmonic form avoids the handling of distinctly different temporal scales of the electromagnetic and thermal phenomena that would lead to a stiff system dynamics [116]. In what follows, two different PDE formulations are presented to incorporate the optimization variables for the case of exciting the actuator with both current and voltage sources.

Governing equations for current sources

A suitable representation of the time-harmonic Maxwell equations is presented for the case of using current sources to generate the electromagnetic field, cf. Figure 2.1a. The displacement currents in Ampere's law (2.8d) are neglected since the estimation

$$j\omega D \ll J_{\mathrm{ind}} \qquad \text{in } \Omega \tag{2.11}$$

holds true for typical induction heating problems, see, e. g., [11, 64]. This is also referred to as the quasi-stationary case, where coupling effects between the electric and magnetic field occur solely within electrically conductive materials [118, 95].

To bring the time-harmonic Maxwell equations (2.8) in a more suitable form for the trajectory planning, the magnetic vector potential $\mathcal{A} := \mathcal{A}(x,t)$ and the scalar electric potential $\hat{v} := \hat{v}(x,t)$ with associated phasors $A := A(x)$ and $v := v(x)$ are introduced, see, for instance, [130, 57]. The governing equations of the potentials are

$$B = \nabla \times A \qquad \text{in } \Omega \tag{2.12a}$$

$$E = -\nabla v - j\omega A \qquad \text{in } \Omega \tag{2.12b}$$

and describe its relation to the magnetic and electric field quantities. The governing equation of the magnetic vector potential (2.12a) follows from Gauss' law of magnetism (2.8b)

and the fact that the divergence of the curl of any vector is zero. The validity of the second relation (2.12b) can be verified by Faraday's law of induction (2.8c) and the phasor arithmetic (2.9c). Note that relation (2.12b) corresponds to the definition of the electric field intensity E for stationary problems with $\omega = 0$.

Ampere's law (2.8d) is reformulated using the magnetic vector potential A and its governing equation (2.12a) as follows

$$\nabla\times(\mu^{-1}\nabla\times A) = J \qquad \text{in } \Omega\ , \tag{2.13}$$

whereby the constitutive equation (2.4a) is used to express the magnetic field intensity H by B, respectively A. The displacement currents $j\omega D$ are neglected due to quasi-stationary field quantities. The total current density

$$J = \sigma E + J_{\text{imp}} \qquad \text{in } \Omega \tag{2.14}$$

consists of the induced currents σE due to Ohm's law (2.5) and externally impressed currents J_{imp} within the spatial domain of the actuator Ω_{c}.

The impressed current density

$$J_{\text{imp}} = -\sigma\chi_{\Omega_{\text{c}}}\nabla v \qquad \text{in } \Omega \tag{2.15}$$

models the flow of electric charge resulting from the current source i, cf. Figure 2.1a, also see, e. g., [11, 102]. The characteristic function $\chi_{\Omega_{\text{c}}}$ is defined by

$$\chi_{\Omega_{\text{c}}} = \begin{cases} 1 & \text{if } x \in \Omega_{\text{c}} \\ 0 & \text{else} \end{cases}\ . \tag{2.16}$$

The proper representation of the real current density within the spatial domain of the actuator is commonly based on measurements [11].

The description of the impressed current density (2.15) provides different perspectives for modeling the direction of flow and amplitude of the impressed currents i within the spatial domain of the actuator Ω_{c}. An analytical function can be used to describe the excitation of the electromagnetic field [135, 102]. This modeling approach is particularly suited for circular or straight-lined actuator shapes as well as for axisymmetrical setups where the flow direction of the impressed currents is identical to the out-of-plane vector [108, 115].

Alternatively, the direction of flow and amplitude of the currents can be described by a PDE system such as

$$\nabla\cdot(-\sigma\nabla v) = 0 \qquad \text{in } \Omega_{\text{c}} \tag{2.17a}$$

$$n\cdot\sigma\nabla v = J_{\text{ext}} \qquad \text{on } \Gamma_{\text{i}} \tag{2.17b}$$

$$n\cdot\sigma\nabla v = 0 \qquad \text{on } \Gamma_0 \tag{2.17c}$$

following from the equation of continuity (2.2), see, for instance, [64]. The inhomogeneous Neumann boundary condition (2.17b) models the flow of currents through the cross section Γ_i due to the external power supply, cf. Figure 2.1a. Its right hand side is specified by

$$\int_{\Gamma_\mathrm{i}} n \cdot J_\mathrm{ext} \, \mathrm{d}x = i \tag{2.18}$$

with J_ext denoting the current density from the external source. The homogeneous Neumann boundary condition (2.17c) describes an electrical insulation of the actuator.

The set of PDEs (2.13)–(2.14) forms a suitable basis to model the electromagnetic phenomena that arise from current sources i, whereby the magnetic vector potential A serves as the state variable. The electric field intensity E within Equation (2.14) can be reformulated as a function of A, i. e.,

$$E = -j\omega A \qquad \text{in } \Omega \ , \tag{2.19}$$

using Faraday's law of induction (2.12b) and the phasor arithmetic (2.9c). Eventually, the time-harmonic PDE of second order

$$\nabla\times(\mu^{-1}\nabla\times A) + j\omega\sigma A = J_\mathrm{imp} \qquad \text{in } \Omega \tag{2.20}$$

is obtained.

The time-harmonic PDE of second order (2.20) complies both with Faraday's law of induction (2.8c) and Ampere's law (2.8d). The validity of the remaining Maxwell equations (2.8a)–(2.8b) is guaranteed through the definition of the vector potentials (2.12). Furthermore, the PDE system (2.20) is extended by the gauging condition

$$\nabla\cdot A = 0 \qquad \text{in } \Omega \ , \tag{2.21}$$

also referred to as Coulomb gauging, since the magnetic vector potential A is not uniquely defined by Equation (2.12a), see, e. g., [4, 93].

Governing equations for voltage sources

The following lines address the problem that some actuators generate the electromagnetic field not by prescribing a current source within Ω_c. The actuator rather serves as a transmission line for the electric energy of the power supply. Such a scenario is typical for interstitial hyperthermia therapy where the heat is generated as close as possible to the tumor, cf. Figure 2.1b, also see [73, 38]. The voltage source v induces an electromagnetic field at the end of the coaxial cable with boundary Γ_v. The other end of the actuator comprises an air gap by which the electromagnetic field penetrates the region of the tumor.

A different formulation of the time-harmonic Maxwell equations (2.8) is considered to model the electromagnetic behavior of problems governed by boundary controlled voltage sources. In this case, the assumption of quasi-stationary field quantities is no longer admissible since

the electromagnetic wave propagation effects in the actuator have to be mathematically described using the full set of the Maxwell equations.

The electromagnetic phenomena arising from the boundary controlled voltage sources are mathematically described using the electric field intensity E as a state variable. The time-harmonic Maxwell equations (2.8) are reformulated by considering a modified version of Faraday's law of induction

$$\mu_{\mathrm{r}}^{-1}\nabla\times E = -j\omega\mu_0 H \qquad \text{in } \Omega\ . \tag{2.22}$$

To incorporate Ampere's law (2.8d) into the modified version of Faraday's law of induction, the curl operator is applied to both sides of Equation (2.22) resulting in

$$\nabla\times(\mu_{\mathrm{r}}^{-1}\nabla\times E) = -j\omega\mu_0\nabla\times H \qquad \text{in } \Omega\ . \tag{2.23}$$

The phasor arithmetic (2.9c) guarantees that Equation (2.23) still coincides with Faraday's law of induction (2.22). The electric flux density D and the current density J within Ampere's law (2.8d) are formulated as a function of the electric field intensity E yielding

$$\nabla\times H = j\omega\epsilon_0\left(\epsilon_{\mathrm{r}} - j\tfrac{\sigma}{\omega\epsilon_0}\right)E \qquad \text{in } \Omega\ , \tag{2.24}$$

whereby Ohm's law (2.5) and the constitutive equation (2.4b) were used.

Based on the modified versions of Faraday's law of induction (2.23) and Ampere's law (2.24), the time-harmonic PDE of second order

$$\nabla\times(\mu_{\mathrm{r}}^{-1}\nabla\times E) - k_0^2\left(\epsilon_{\mathrm{r}} - j\tfrac{\sigma}{\omega\epsilon_0}\right)E = 0 \qquad \text{in } \Omega \tag{2.25}$$

is obtained with $k_0 = \omega\sqrt{\epsilon_0\mu_0}$ denoting the wave number. The additional side constraint

$$\nabla\cdot E = 0 \qquad \text{in } \Omega \tag{2.26}$$

is formulated to ensure that the time-harmonic PDE system (2.25) complies with the Maxwell equations (2.8).[3] The PDE system (2.25)–(2.26) allows one to mathematically describe the electromagnetic phenomena of interstitial hyperthermia processes. The voltage sources of the actuator are taken into account by means of suitable boundary conditions.

2.2.3 Interface conditions, symmetry planes, and boundary conditions

The formulation of internal and external boundary conditions is required to complete the mathematical description of the PDE system (2.20) and (2.25). The introduction of boundary conditions will also make it possible to model the generation of the electromagnetic field by means of a boundary controlled voltage source, cf. Figure 2.1b. They also allows one to cope with the truncated electromagnetic field due to the closed spatial domain Ω.

[3] The generation of the electric field by means of a prescribed electrical charge density ρ is not considered.

Interface conditions

For several reasons (e. g. variations of material parameters, objects placed next to each other), the region of interest Ω comprises internal boundaries, also referred to as interfaces, where the relative magnetic permeability μ_r and the relative electric permittivity ϵ_r may be discontinuous. A classical solution of the PDE systems (2.20) and (2.25) does not exist in these regions since the electromagnetic field quantities have to be well-behaved, i. e., they have to be continuous functions involving continuous derivatives. This problem can be tackled numerically by deducing interface conditions from the integral forms of the Maxwell equations (2.8), see, for instance, [130].

The theorems of Gauss and Stokes are applied to the Maxwell equations resulting in the interface conditions for the electric field quantities[4]

$$n_{12} \times (E_2 - E_1) = 0 \qquad \text{on } \Gamma_{12} \tag{2.27a}$$

$$n_{12} \cdot (D_2 - D_1) = 0 \qquad \text{on } \Gamma_{12} \tag{2.27b}$$

with the normal vector n_{12} that points from the spatial domain of material 1 to material 2 with corresponding interface Γ_{12}, also see [57]. Equation (2.27a) implies that the tangential component of the electric field intensity E has to be continuous on Γ_{12} in contrast to its normal component which can jump between two materials. On the other hand, Equation (2.27b) requires that the normal components of the electric flux density D are continuous on Γ_{12}. The interface conditions for the magnetic field quantities are

$$n_{12} \times (H_2 - H_1) = 0 \qquad \text{on } \Gamma_{12} \tag{2.28a}$$

$$n_{12} \cdot (B_2 - B_1) = 0 \qquad \text{on } \Gamma_{12}\ . \tag{2.28b}$$

The interpretation of Equation (2.28) is similar to its electric counterpart (2.27).

The overall set of interface conditions (2.27)–(2.28) results in an overdetermined system of equations of the electromagnetic subsystem. Either the interface conditions (2.27) or (2.28) have to be considered to complete the mathematical description of the Maxwell equations. As the PDE system (2.20) comprises the state variable A, it is advantageous to use the interface condition (2.28) for this problem formulation. For this purpose, the magnetic field quantities (H, B) are reformulated as functions of the magnetic vector potential

$$n_{12} \times \left(\mu_2^{-1} \nabla\times A_2 - \mu_1^{-1} \nabla\times A_1\right) = 0 \qquad \text{on } \Gamma_{12} \tag{2.29a}$$

$$n_{12} \cdot (\nabla\times A_2 - \nabla\times A_1) = 0 \qquad \text{on } \Gamma_{12}\ . \tag{2.29b}$$

The interface conditions of the PDE system (2.25) are reformulated as a function of the electric field intensity E as follows

$$n_{12} \times (E_2 - E_1) = 0 \qquad \text{on } \Gamma_{12} \tag{2.30a}$$

$$n_{12} \cdot (\epsilon_2 E_2 - \epsilon_1 E_1) = 0 \qquad \text{on } \Gamma_{12}\ . \tag{2.30b}$$

As will be shown later, this interface conditions facilitates to mathematically describe the generation of the electromagnetic field due to a voltage source v, cf. Figure 2.1b.

[4] The interface conditions (2.27) do not account for surface charges on the interface Γ_{12}. Similarly, Equation (2.28) neglects surface current densities on the interface.

Symmetry planes

Materials with a perfect electric or magnetic conduction offer the basis to introduce symmetry planes confining the region of interest Ω to a smaller one. In turn, the numerical effort for solving the PDE system (2.20) or (2.25) can be reduced. Under the assumption that material 1 is a perfect electric conductor (PEC – *Perfect Electric Conductor*), the interface condition (2.27a) reduces to the homogeneous Dirichlet boundary condition

$$n_{12} \times E_2 = 0 \qquad \text{on } \Gamma_{12} \qquad \text{(PEC)} \tag{2.31}$$

in view of a vanishing electric field intensity E_1. This is a direct consequence of Ohm's law (2.5) and the perfect electric conduction implying $\sigma_1 = \infty$. Otherwise, a non-zero electric field intensity E_1 would produce an infinite current density. For a perfect magnetic conductor (PMC – *Perfect Magnetic Conductor*), Equation (2.28a) degenerates to

$$n_{12} \times H_2 = 0 \qquad \text{on } \Gamma_{12} \qquad \text{(PMC)} \ . \tag{2.32}$$

The homogeneous Dirichlet boundary condition (2.31) can be used to model symmetry planes, where the normal component of the magnetic field quantities B and H, respectively the tangential component of D and E, vanish [130]. From a numerical point of view, the PDE systems (2.20) and (2.25) can benefit from such symmetry planes by means of the homogeneous Dirichlet boundary conditions

$$n_\mathrm{s} \times A = 0 \qquad \text{on } \Gamma_\mathrm{s} \qquad \text{(PEC–A)} \tag{2.33a}$$

$$n_\mathrm{s} \times E = 0 \qquad \text{on } \Gamma_\mathrm{s} \qquad \text{(PEC–E)} \tag{2.33b}$$

with n_s denoting the outward unit normal vector of the symmetry plane Γ_s. In contrast, the condition of a perfect magnetic conduction (2.32) facilitates to model symmetry planes where the tangential component of the magnetic field quantities B and H or respectively the normal component of D and E vanish. The homogeneous Neumann boundary conditions

$$n_\mathrm{s} \times \left(\mu^{-1} \nabla \times A\right) = 0 \qquad \text{on } \Gamma_\mathrm{s} \qquad \text{(PMC–A)} \tag{2.34a}$$

$$n_\mathrm{s} \times \left(\mu^{-1} \nabla \times E\right) = 0 \qquad \text{on } \Gamma_\mathrm{s} \qquad \text{(PMC–E)} \tag{2.34b}$$

model this symmetric behavior of the electromagnetic field depending on whether the PDE system (2.20) or (2.25) is considered for the trajectory planning.

Boundary conditions

A modified formulation of the interface condition (2.30a) is considered to model the generation of the electromagnetic field due to a voltage source v, cf. Figure 2.1b. It is assumed that the voltage source prescribes the electric field intensity $E_\mathrm{imp}(v)$ between the inner and outer conductors of the coaxial cable, cf. Figure 3.3. This facilitates to model the generation of the electromagnetic field by means of the inhomogeneous Dirichlet boundary condition

$$n \times E = E_\mathrm{imp}(v) \qquad \text{on } \Gamma_\mathrm{v} \tag{2.35}$$

with the boundary Γ_v as the electrical connection to the power supply [130, 44].

As shown in Figure 2.1, the boundary Γ confines the region of interest Ω to a closed area. To mathematically describe the electromagnetic phenomena on Γ, it is assumed that the boundary is divided into Neumann and Dirichlet boundary conditions with the disjunct segments Γ_{N} and Γ_{D}, i. e.,

$$\Gamma = \Gamma_{\mathrm{N}} \cup \Gamma_{\mathrm{D}} \ , \tag{2.36}$$

also see [8]. The correct formulation of such boundary conditions is, however, a crucial point since the electromagnetic field actually extends into an infinite spatial domain [57, 11].

One possibility to mathematically describe the electromagnetic field on boundary segments of Γ are homogeneous Dirichlet boundary conditions

$$n \times A = 0 \qquad \text{on } \Gamma_{\mathrm{D}} \tag{2.37a}$$

$$n \times E = 0 \qquad \text{on } \Gamma_{\mathrm{D}} \ . \tag{2.37b}$$

In order to avoid artificial disturbance effects, it is assumed that the tangential component of the magnetic vector potential A, respectively of the electric field intensity E, vanishes towards an infinite point in view of the radial propagation of electromagnetic waves, see, e. g., [92, 57, 64]. Thus, the boundary segment Γ_{D} has to be chosen sufficiently far away from the sources of the electromagnetic field [11, 135].

The first-order absorbing boundary conditions

$$n \times (\nabla \times A) = F_A(A) \qquad \text{on } \Gamma_{\mathrm{N}} \tag{2.38a}$$

$$n \times \left(\mu^{-1} \nabla \times E\right) = F_E(E) \qquad \text{on } \Gamma_{\mathrm{N}} \tag{2.38b}$$

constitute another modeling approach to prevent disturbance effects, whereby the right hand sides $F_A(A)$ and $F_E(E)$ are specified for a specific problem [11, 6, 67]. The inhomogeneous Neumann boundary conditions (2.38) are used to make the boundary Γ_{N} as transparent as possible to incident electromagnetic waves. The advantage over the Dirichlet boundary conditions (2.37) is the possibility to place the boundary Γ_{N} closer to the electromagnetic source. This decreases the numerical effort for solving the PDE systems (2.20) and (2.25).

2.2.4 Electromagnetic heat source

In general, the physical cause of electromagnetic heating are electric and magnetic energy dissipation effects. The electromagnetic heating applications considered in this work, however, are restricted to problems where the electric losses are considerably greater than the magnetic ones, see, e. g., [118].

The electromagnetic heat source is modeled by the instantaneous power density

$$\mathcal{Q} = \mathcal{J} \cdot \mathcal{E} \qquad \text{in } \Omega_{\mathrm{o}} \times (0, t_{\mathrm{f}}) \tag{2.39}$$

and describes the conversion of electric energy into thermal energy as electromagnetic waves propagate through space. To describe the electromagnetic heat source by means of the time-harmonic PDE systems (2.20) and (2.25), the instantaneous power density $\mathcal{Q}$ is transformed

into the frequency domain, cf. Section 2.2.2. To this end, Equation (2.39) is averaged over one time period $\Delta t = 2\pi\omega^{-1}$ yielding

$$Q = \tfrac{\sigma\omega^2}{2}|A|^2 \qquad \text{in } \Omega_\mathrm{o} \tag{2.40a}$$

$$Q = \tfrac{\sigma}{2}|E|^2 \qquad \text{in } \Omega_\mathrm{o} \tag{2.40b}$$

with $Q := Q(x;t)$ and $|F|^2 = F \cdot F^*$ for any complex-valued vector F with complex conjugate F^*, see, for instance, [57, 95]. Note that both formulations of the electromagnetic heat source neglect displacement currents and are linked to each other by Equation (2.19).

A sufficiently precise representation of the electromagnetic heat source generally requires a fine local discretization of the spatial domain of the object Ω_o. Thereby, the fineness of the spatial grid should facilitate to numerically resolve the highly uneven spatial distribution of the electromagnetic heat source due to the distortion effects of the electromagnetic field, also see the discussion about the skin, end, and edge effect in Section 1.2.2.

2.3 Thermal phenomena

Heat propagation is another relevant physical process in the course of electromagnetic heating. Its essential driving force is the heat source (2.40) as well as the temporal temperature profile of the object. The well known heat equation is introduced to mathematically describe the temporal and spatial dynamics of the thermal phenomena. This allows one to predict the evolution of temperature within the object to be heated.

2.3.1 Heat equation

The thermal phenomena of the induction heating processes and hyperthermia therapy are mathematically described by a common PDE system. The modifications and extensions that are required for a sufficiently precise description of problem specific features are customized to different application examples in the following chapters. To begin with, the heat equation

$$\rho C \partial_t T - \nabla\cdot(k\,\nabla T) = Q \qquad \text{in } \Omega_\mathrm{o} \times (0, t_\mathrm{f}) \tag{2.41}$$

is introduced with the temperature T serving as the state variable of the parabolic PDE of second order, see, e. g., [141, 87].

The dynamics of the heat equation (2.41) is described on the spatial domain of the object Ω_o in contrast to the electromagnetic subsystems (2.20) and (2.25) which are defined on the whole spatial domain Ω. The heat-up process is considered on the time interval $(0, t_\mathrm{f})$ and it is assumed that the control strategy of the actuator gives rise to an electromagnetic heat source $Q(x;t)$, cf. Section 2.2.4. The final time of the heat-up cycles is denoted by $t_\mathrm{f} > 0$. The material parameters of the heat equation (2.41) are specified by the density ρ, the heat capacity C, and the thermal conductivity k.

The heat flux by conduction, also referred to as Fourier's law of heat conduction, is

$$q = -k \nabla T \qquad \text{in } \Omega_\mathrm{o} \times (0, t_\mathrm{f}) \tag{2.42}$$

and allows to interpret the heat equation (2.41) from a physical point of view [87]. The heat flow q relates the temperature gradient ∇T to the thermal conductivity k serving as a proportionality constant. Thus, the left hand side of the heat equation models the rate of change of the temperature T over time and space due to diffusion.

2.3.2 Boundary conditions, symmetry planes, and initial conditions

In an analogous manner to the electromagnetic phenomena, a set of boundary conditions and symmetry planes is formulated to complete the mathematical description of the thermal dynamics and to confine the spatial domain for which the heat equation (2.41) is numerically solved. In addition, an initial condition is formulated to take the fact into account that the heat equation is instationary.

Boundary conditions

The thermal interaction between the object Ω_o and its surrounding is modeled by means of a set of boundary conditions. For this purpose, the boundary of the object Γ_o is divided into the disjunct boundary segments $\Gamma_\mathrm{o,N}$ and $\Gamma_\mathrm{o,D}$, i. e.,

$$\Gamma_\mathrm{o} = \Gamma_\mathrm{o,N} \cup \Gamma_\mathrm{o,D} \ , \tag{2.43}$$

to account for Neumann boundary conditions and Dirichlet boundary conditions.

The inhomogeneous Neumann boundary condition

$$n \cdot (k \nabla T) = f(T) \qquad \text{on } \Gamma_\mathrm{o,N} \times (0, t_\mathrm{f}) \tag{2.44}$$

models the heat flow in the direction of the outward unit normal vector n subject to Fourier's law of heat conduction (2.42). Heat losses of the object by convection and radiation to the constant ambient temperature T_a are taken into account by setting the function $f := f(T)$ to

$$f = \alpha \left(T_\mathrm{a} - T\right) \qquad \text{on } \Gamma_\mathrm{o,N} \times (0, t_\mathrm{f}) \qquad \text{(convection)} \tag{2.45a}$$

$$f = \epsilon \sigma_\mathrm{SB} \left(T_\mathrm{a}^4 - T^4\right) \qquad \text{on } \Gamma_\mathrm{o,N} \times (0, t_\mathrm{f}) \qquad \text{(radiation)} \ , \tag{2.45b}$$

respectively. The convective heat losses are parametrized by the surface heat transfer coefficient α, the heat losses due to radiation by the emissivity of the surface ϵ and the Stefan-Boltzmann constant σ_SB, see, e. g., [87, 11]. Note that the set of equations (2.44)–(2.45) facilitates to model a combination of convective and radiative heat losses. A thermal insulation of the object Ω_o against its surrounding is modeled by

$$f = 0 \qquad \text{on } \Gamma_\mathrm{o,N} \times (0, t_\mathrm{f}) \ , \tag{2.46}$$

which is equivalent to a vanishing heat flow at the boundary segment $\Gamma_\mathrm{o,N}$.

Typical electromagnetic heating systems involve, in some situations, boundary segments that are subject to external cooling strategies. To this end, the inhomogeneous Dirichlet boundary condition

$$T = g \qquad \text{on } \Gamma_{\mathrm{o,D}} \times (0, t_{\mathrm{f}}) \tag{2.47}$$

is formulated, where the function $g := g(t)$ facilitates to specify the prescribed temperature.

Symmetry planes

The boundary condition for thermal insulation, i. e., the Neumann boundary condition (2.44) with the function f specified by (2.46), can be used to model symmetry planes. This allows to confine the spatial domain Ω_{o} for which the thermal dynamics has to be numerically solved. To model the thermal phenomenon on a symmetry plane Γ_{s}, the boundary condition

$$n_{\mathrm{s}} \cdot (k \nabla T) = 0 \qquad \text{on } \Gamma_{\mathrm{s}} \times (0, t_{\mathrm{f}}) \tag{2.48}$$

is introduced, where n_{s} denotes the outward unit normal vector of the symmetry plane. The essential prerequisite to confine the spatial domain in this way is that the electromagnetic heat source is symmetric with respect to the symmetry plane. Note that this implies that the same symmetry plane can be applied to the PDE system of the electromagnetic phenomena (2.20) and (2.25).

Initial conditions

The mathematical description of the thermal phenomena is completed by the initial condition

$$T(\cdot, 0) = T_0 \qquad \text{in } \Omega_{\mathrm{o}} \text{ at } t = 0 \ . \tag{2.49}$$

The temperature profile $T_0 := T(x, 0)$ is used to describe the temperature at the beginning of a heat-up cycle. Alternatively, the temperature profile T_0 allows to represent a specific temperature profile resulting from a prior heat treatment process.

2.4 Numerical solution

FE methods are widely used techniques to numerically solve PDE systems [146, 132, 93]. Similar to finite difference methods, the FE methods calculate a solution of the PDEs at discrete places of the spatial domain, also referred to as the grid nodes. The spatial domain is covered by a mesh to discretize the functions of the infinite-dimensional state variables. Thus, the yet unknown functions of the state variables can be approximated at the grid nodes by a finite set of basis functions and coefficients. Depending on whether the discretization is applied only to the spatial domain or to space and time coordinates, the original problem reduces to a system of ordinary differential equations (ODE – *Ordinary Differential Equation*) or algebraic equations with the coefficients as its states and variables, respectively.

The approximation of the infinite-dimensional functions of the state variables by a finite set of basis functions and coefficients relies on the method of variational calculus [8]. The reformulation of the PDE system as a variational equation makes it possible to divide the spatial domain Ω into several subdomains with relative ease and offers several additional advantages. The requirement of a solution to be pointwise differentiable can be mitigated. A solution of the finite-dimensional problem calls solely for functions that are differentiable in an integral manner.

The variational principle also provides the flexibility to deduce the system of ODEs or algebraic equations not on the basis of the original variational equation but on a weak formulation [2]. Thus, the necessary degree of regularity of the solution can be reduced by half, since the temporal and spatial derivatives can be spread over the state variables and the test functions used to formulate the variational equation. The following lines discuss the numerical solution of the coupled PDEs of the electromagnetic and thermal phenomena by means of FE methods. This includes the derivation of the weak formulations, its discretization to convert the infinite-dimensional problem into a finite-dimensional counterpart as well as the numerical solution of the latter one.

2.4.1 Weak formulation of the electromagnetic subsystem

To determine a numerical solution of the electromagnetic subsystems (2.20) and (2.25), the function space of the magnetic vector potential A and electric field intensity E is defined as the Banach space

$$X = \left\{ K \in H\left(curl;\Omega\right) \cap H\left(div;\Omega\right) \;\middle|\; \nabla\cdot K = 0 \text{ in } \Omega, \quad K \times n = 0 \text{ on } \Gamma_{\mathrm{D}} \right\} \tag{2.50}$$

with $K \in \{A, E\}$, see, e. g., [8, 92, 135]. The function space X allows one to incorporate Dirichlet boundary conditions on Γ_{D}. The curl and div spaces in Equation (2.50) are defined as follows

$$H\left(curl;\Omega\right) = \left\{ K \in L^2\left(\Omega;\mathbb{C}\right)^3 \;\middle|\; \nabla\times K \in L^2\left(\Omega;\mathbb{C}\right)^3 \right\} \tag{2.51a}$$

$$H\left(div;\Omega\right) = \left\{ K \in L^2\left(\Omega;\mathbb{C}\right)^3 \;\middle|\; \nabla\cdot K \in L^2\left(\Omega;\mathbb{C}\right) \right\} \tag{2.51b}$$

with $L^2\left(\Omega;\mathbb{C}\right)$ as the Lebesgue space of complex-valued square-integrable functions [4].

The weak formulation of the electromagnetic subsystem (2.20) is obtained by multiplying its governing equation on both sides with the test function $\Lambda := \Lambda(x;t)$. A subsequent integration over the spatial domain Ω results in the variational equation

$$\int_{\Omega} \nabla\times(\mu^{-1}\nabla\times A)\cdot\Lambda + j\omega\sigma A\cdot\Lambda \,\mathrm{d}x = \int_{\Omega} J_{\mathrm{imp}}\cdot\Lambda \,\mathrm{d}x \qquad \forall\Lambda \in X \tag{2.52}$$

that complies with (2.20) in accordance with the variational principle. In order to shift the outer curl operator to the test function Λ, the formula of partial integration

$$\int_{\Omega} \nabla\times U\cdot V \,\mathrm{d}x = \int_{\Omega} U\cdot\nabla\times V \,\mathrm{d}x - \int_{\Gamma} (U\times n)\cdot V \,\mathrm{d}x \;, \tag{2.53}$$

also referred to as Green's formula, is applied to (2.52) with U and V denoting complex-valued vectors [4, 57]. Thus, the weak formulation of the electromagnetic subsystem

$$\int_\Omega (\mu^{-1}\nabla\times A)\cdot(\nabla\times\Lambda)\ \mathrm{d}x - \int_\Gamma \big((\mu^{-1}\nabla\times A)\times n\big)\cdot\Lambda\ \mathrm{d}x + \int_\Omega j\omega\sigma A\cdot\Lambda\ \mathrm{d}x = \int_\Omega J_{\mathrm{imp}}\cdot\Lambda\ \mathrm{d}x \qquad \forall\Lambda\in X \quad (2.54)$$

is obtained. Note that the new boundary integral of Equation (2.54) follows from the formula of partial integration (2.53) that is applied to (2.52).

The boundary integral in the weak formulation (2.54), i. e.,

$$\int_\Gamma \big((\mu^{-1}\nabla\times A)\times n\big)\cdot\Lambda\ \mathrm{d}x\ , \quad (2.55)$$

is used to take the boundary conditions of a specific problem into account. In the case of homogeneous Dirichlet boundary conditions, the boundary integral vanishes on Γ_{D} since the test function Λ is set to zero for numerical reasons. Note that inhomogeneous Dirichlet boundary conditions can be taken into account by adapting the solution space X as defined by Equation (2.50), also see, for instance, [8]. The structure of the boundary integral (2.55) allows one to incorporate Neumann boundary conditions of the type

$$n\times(\mu^{-1}\nabla\times A) = g_A \qquad \text{on } \Gamma_{\mathrm{N}}\times(0,t_{\mathrm{f}}) \quad (2.56)$$

in a straightforward manner. In summary, the weak formulation corresponding to the electromagnetic subsystem (2.20) is specified by

$$\int_\Omega (\mu^{-1}\nabla\times A)\cdot(\nabla\times\Lambda) + j\omega\sigma A\cdot\Lambda\ \mathrm{d}x + \int_{\Gamma_{\mathrm{N}}} g_A\cdot\Lambda\ \mathrm{d}x = \int_\Omega J_{\mathrm{imp}}\cdot\Lambda\ \mathrm{d}x \qquad \forall\Lambda\in X\ . \quad (2.57)$$

Similar to the electromagnetic subsystem (2.20) used to describe the electrical excitation of the actuator by means of a current source i, the weak formulation of the electromagnetic subsystem (2.25) can be formulated as

$$\int_\Omega (\mu_{\mathrm{r}}^{-1}\nabla\times E)\cdot(\nabla\times\Lambda) - k_0^2\left(\epsilon_{\mathrm{r}} - j\tfrac{\sigma}{\omega\epsilon_0}\right)E\cdot\Lambda\ \mathrm{d}x + \int_{\Gamma_{\mathrm{N}}} g_E\cdot\Lambda\ \mathrm{d}x = 0 \qquad \forall\Lambda\in X \quad (2.58)$$

in order to deal with boundary controlled voltage sources v, cf. Figure 2.1. The function g_E denotes the right hand side of a Neumann boundary condition of the type (2.56).

2.4.2 Weak formulation of the thermal subsystem

The weak formulation of the thermal subsystem (2.41) is derived in an analogous manner to the procedure presented for the electromagnetic subsystem in Section 2.4.1. The function space of the temperature T is defined by

$$W\left(0,t_\mathrm{f}\right) = \left\{ T \in L^2\left(0,t_\mathrm{f};H^1(\Omega_\mathrm{o})\right) \;\middle|\; \partial_t T \in L^2\left(0,t_\mathrm{f};H^1(\Omega_\mathrm{o})^*\right), \quad T=0 \text{ on } \Gamma_{\mathrm{o,D}} \right\}, \tag{2.59}$$

see, for instance, [132, 135], with the Sobolev space

$$H^1(\Omega_\mathrm{o}) = \left\{ T \in L^2\left(\Omega_\mathrm{o}\right) \;\middle|\; \nabla T \in L^2\left(\Omega_\mathrm{o}\right) \right\} \tag{2.60}$$

encompassing weak derivatives in the Lebesgue space $L^2\left(\Omega_\mathrm{o}\right)$. The dual space of $H^1(\Omega_\mathrm{o})$ is denoted by $H^1(\Omega_\mathrm{o})^*$, see, e. g., [2, 8]. Here, the Lebesgue space $L^2\left(\Omega_\mathrm{o}\right)$ comprises real-valued square-integrable functions.

The test function $p := p(x,t)$ with function space (2.59) is used to derive the weak formulation of the thermal subsystem. The heat equation (2.41) is multiplied with the test function p and subsequently integrated over the space-time cylinder $\Omega_\mathrm{o} \times (0,t_\mathrm{f})$, i. e.,

$$\iint\limits_{\Omega_\mathrm{o}\times(0,t_\mathrm{f})} \rho C \partial_t T p + (k\,\nabla T)\cdot(\nabla p)\;\mathrm{d}x\,\mathrm{d}t - \iint\limits_{\Gamma_{\mathrm{o,N}}\times(0,t_\mathrm{f})} g_T p\;\mathrm{d}x\,\mathrm{d}t = \iint\limits_{\Omega_\mathrm{o}\times(0,t_\mathrm{f})} Q p\;\mathrm{d}x\,\mathrm{d}t \quad \forall p \in W\left(0,t_\mathrm{f}\right)\;. \tag{2.61}$$

Thereby, Green's first identity was used to divide the spatial operators between the temperature T and the test function p. The function g_T denotes the inhomogeneous part of a Neumann boundary condition on the boundary segment $\Gamma_{\mathrm{o,N}}$ of following type

$$n\cdot(k\,\nabla T) = g_T \qquad \text{on } \Gamma_{\mathrm{o,N}} \times (0,t_\mathrm{f})\;. \tag{2.62}$$

2.4.3 Approximation of the infinite-dimensional problem

The weak formulations of the electromagnetic and thermal subsystems allows one to approximate the infinite-dimensional functions of the corresponding state variables. For this purpose and in a first step, the spatial domain on which the system dynamics is formulated is divided into finite elements. There are several types of finite elements to cover the spatial domain of one-dimensional, two-dimensional, and three-dimensional problems as illustrated in Figure 2.2, also see [146, 92, 106]. The subdivision of the spatial domain into non-overlapping finite elements is based on grid points that coincide with the vertices of the finite elements.

The main steps of representing the infinite-dimensional problem by a finite-dimensional counterpart is outlined for the weak formulation of the thermal subsystem (2.61). For the sake of compactness, a one-dimensional spatial domain is considered and the problem is assumed to be stationary in time with homogeneous Dirichlet boundary conditions. First of

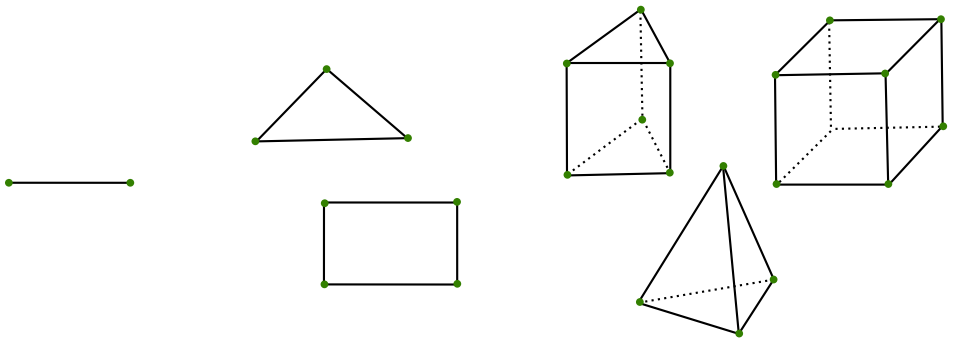

Figure 2.2: Typical finite elements to discretize spatial domains of different dimensions: 1D (line), 2D (triangular, quadrilateral), and 3D (pentrahedron, tetrahedron, hexahedron).

all, a mesh is generated to discretize the spatial domain of the system dynamics. The spatial coordinate x is subdivided into the finite elements e_i and its associated grid points i and $i+1$, also referred to as nodes, cf. Figure 2.3. For each node, a basis function $\Psi_i := \Psi_i(x)$ and coefficient T_i is introduced to approximate the temperature $T := T(x)$ linearly over each element e_i according to

$$T \approx T_h = \sum_i T_i \Psi_i(x) \ . \tag{2.63}$$

The basis functions have compact support, meaning that they are non-zero only in close proximity to its belonging node. The test function of the weak formulation is approximated in an analogous manner

$$p \approx p_h = \sum_j \Psi_j(x) \ . \tag{2.64}$$

The solution space of the finite-dimensional approximations T_h and p_h is adapted from the infinite-dimensional counterparts T and p in form of the subspace $V_h \subset H^1(\Omega_\mathrm{o})$, cf. Equation (2.60), also see, for instance, [132].

The finite-dimensional representation of the weak formulation is obtained by approximating the infinite-dimensional state T and the test function p according to Equation (2.63) and (2.64). This eventually leads to the system of algebraic equations

$$\sum_i T_i \int_{\Omega_\mathrm{o}} (k \nabla \Psi_i) \cdot (\nabla \Psi_j) \ \mathrm{d}x = \int_{\Omega_\mathrm{o}} Q \Psi_j \ \mathrm{d}x \qquad \forall j \tag{2.65}$$

with T_i as the only dependent variables since both the basis functions Ψ_i and the test functions Ψ_j are known. Similarly, the FE method can be applied to the weak formulation of the electromagnetic subsystems (2.57) and (2.58). A detailed discussion of FE methods can be found in the literature, see, for instance, [146, 92, 7, 30].

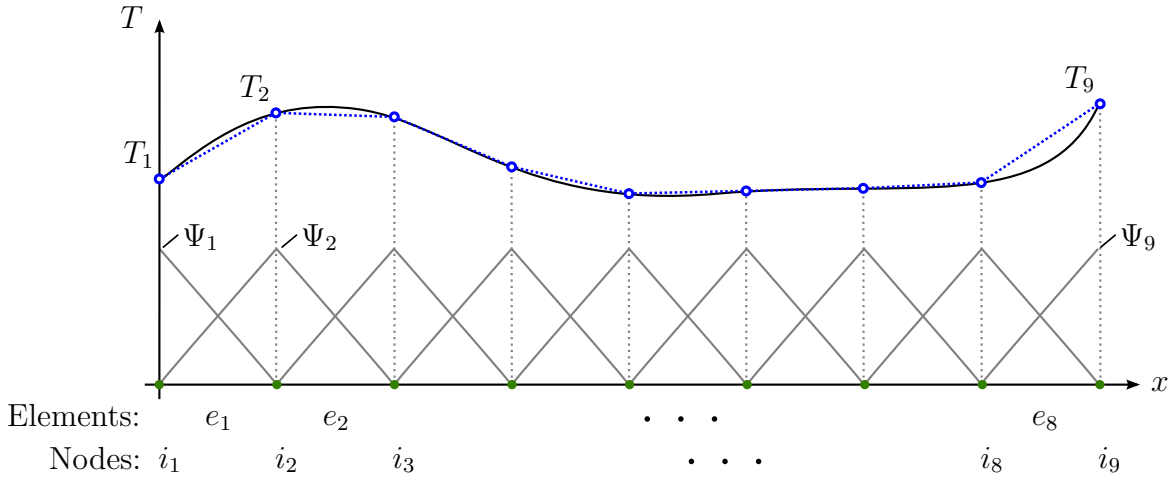

Figure 2.3: Approximation of the infinite-dimensional function of temperature T by a finite set of basis functions $\Psi_i(x)$ and coefficients T_i (inspired by Zienkiewicz [146]).

2.4.4 Numerical solution of the finite-dimensional problem

The reformulation of PDEs as a system of ODEs in the non-stationary case or as algebraic equations in the stationary case paves the way to numerically solve the system dynamics of electromagnetic heating systems. Examples of numerical techniques are Runge-Kutta, Adam-Bashford, and Newton-Raphson methods. A detailed discussion on these techniques goes beyond the scope of this thesis. Instead, the idea of this work to outsource the numerical effort to state-of-the-art FEM software is emphasized here.

Software packages such as Comsol Multiphysics [28] or Ansys [5] provide highly adapted FE methods that allow to numerically handle multiphysics problems and especially electromagnetic heating systems. Crucial points such as the design of the geometrical setup, the formulation of the governing equations, and the numerical solution of the multiphysics problem can be mastered regardless of the complexity of both the geometrical setup and the governing equations. For example, the mathematical description of the geometrical setup can benefit from computer-aided design tools (CAD – *Computer-Aided Design*) that are included in the software packages.

In addition, software packages such as Comsol Multiphysics or Ansys include sophisticated algorithms for discretizing the spatial domain of almost any complexity. The freedom to choose between different mesh types and element sizes facilitates the adaptation of the discretization step to a specific problem. Different types of basis and test functions such as linear, quadratic, or cubic interpolation functions provide further flexibility to modify the discretization of the spatial domain, see, e. g., [146, 92, 102]. In this regard, the interaction of several physical phenomena can be tackled in an optimal manner by adapting the type and order of the basis functions to the individual state variables. Finally, the numerical solution of the electromagnetic heating systems can benefit from mesh refinement techniques that automatically adapt the accuracy of the solution.

2.5 Conclusions

The governing equations of electromagnetic and thermal phenomena presented in this chapter enable a flexible handling of various types of electromagnetic heating systems and provide the basis for an optimization-based trajectory planning. The time-harmonic PDE (2.20) is applicable to describe situations, where the electromagnetic field is generated by a prescribed current source within the spatial domain of the actuator. The generation of the electromagnetic field by means of a needle-like actuator with boundary controlled voltage source can be mathematically described by the time-harmonic PDE (2.25). The thermal phenomena of electromagnetic heating systems are modeled by the heat equation (2.41). The PDE systems of the electromagnetic and thermal phenomena are equipped with various types of boundary conditions to deal with different situations and needs of problems such as induction heating or hyperthermia therapy.

The diversity of FEM-based simulation software makes it possible to overcome the challenging task of numerically solving the system dynamics of electromagnetic heating systems. This also offers a promising approach to meet the numerical challenges of optimization-based trajectory planning for electromagnetic heating systems. The proper combination of FOTD approaches and FEM software will provide the foundation for separating methodological challenges from numerical ones, as discussed in the following chapters.

Chapter 3

Optimal excitation of actuators

The electrical excitation of the actuator affects the intensity of the electromagnetic field and therefore the intensity of the heat source. In turn, electrically conductive materials that are placed in the region of the electromagnetic field can be heated up. This chapter presents a trajectory planning approach that optimizes the current and voltage sources of electromagnetic actuators. Special emphasis is laid on coping with a wide variety of electromagnetic heating systems including complex shapes.

The proposed trajectory planning approach relies on the formulation of a PDE constrained optimization problem that is solved by a software framework in a straightforward manner. To this end, the optimality conditions are derived in the function space of the original problem formulation to ensure that not only the system dynamics but rather the whole optimality system can be solved by FEM-based simulation software. The trajectory planning approach for optimizing the electrical excitation of electromagnetic actuators is exemplified for induction heating processes [118] and hyperthermia therapy [144]. Both problems represent typical scenarios of electromagnetic heating and illustrate the generality of the presented trajectory planning approach.

3.1 Optimal control strategies for induction heating

Induction heating is a widely used heat treatment process in which the electromagnetic heat source facilitates to alter mechanical properties of a workpiece such as hardness, strength, ductility, or wear resistance [31, 118, 20]. A transformation process of the crystalline structure of the workpiece is enforced through metallurgical effects that highly depend on the temperature and heating rate. To prevent undesired retransformation processes during the time of workpiece cooling, final quenching is carried out in some induction heating processes. Further applications of induction heating are brazing, melting, or welding, to name just a few. For an overview, also see, e. g., [147, 118].

3.1.1 Geometrical setup and control tasks

In general, a distinction is made between the two types of induction heating applications shown in Figure 3.1. The constant heat-up process in Figure 3.1a is performed to alter the mechanical properties of the whole workpiece. Examples are tempering and stress relieving processes as well as the preheating for forging and thixoforming operations. The other type of induction heating applications are surface hardening processes, cf. Figure 3.1b. Here, the objective is to increase the hardness of the workpiece in specific surface layers.[1] A subsequent quenching process ensures the formation of a martensitic microstructure, which leads to the hardness of the surface layer [32, 29].

Figure 3.1a shows a constant heat-up process of a gear wheel with spatial domain Ω_o and boundary Γ_o. The electromagnetic field and its associated heat source is generated by means of a time-dependent excitation of the actuator Ω_c. The spatial domain of the ambient air is denoted by Ω_a. The region of interest is described by $\Omega = \Omega_\mathrm{o} \cup \Omega_\mathrm{c} \cup \Omega_\mathrm{a}$ with boundary Γ. Figure 3.1b shows a surface hardening process with the surface layer to be hardened $\tilde{\Omega}_\mathrm{o}$. In this case, the spatial domain of the actuators is denoted by $\Omega_\mathrm{c} = \cup \Omega_{\mathrm{c}_j},\ j \in \{1, 2, \ldots, 6\}$.

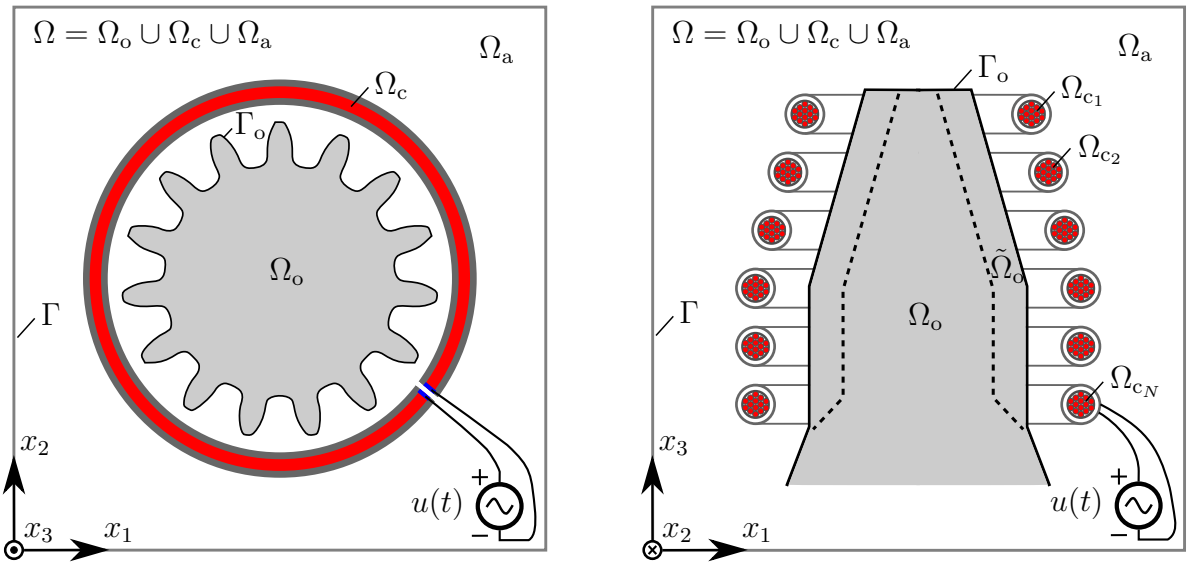

(a) Constant heat-up process

(b) Surface hardening process

Figure 3.1: Geometrical setups of induction heating processes (not to scale): a) constant heat-up process of a gear wheel and b) surface hardening process of an axisymmetrical workpiece with spatial domain Ω_o. The flow of currents in the actuator Ω_c, respectively in the actuators $\Omega_{\mathrm{c}_j},\ j \in \{1, 2, \ldots, N\}$, generates the electromagnetic heat source.

[1] It is assumed that the phase transitions leading to the hardening effects, i. e., the transformation of ferrite, pearlite, and bainite into martensite, can be represented for the trajectory planning by suitable temperature profiles (isothermal transformation diagrams), see, e. g., [118, 11, 64]. A more accurate description of the phase transition effects is presented in [42, 64] and the references therein.

For both constant heating and surface hardening, the control trajectory $u := u(t)$ is used to describe the electrical excitation of the actuator by means of the flow of currents, cf. the red marked regions in Figure 3.1. The position and shape of the actuators are fixed and cannot be modified for the time being.[2] The frequency of the current source is also fixed in view of the accompanying expensive power electronics [118]. Similarly, the actuators are excited by an identical current source u, if several of them are used to generate the heat source.

Besides the primary objective of the trajectory planning to heat up either the whole workpiece or solely parts of it, the limitation of the current source has to be taken into account due to physical restrictions. In addition, the workpiece temperature is not allowed to exceed the bound T^+. This should prevent undesired metallurgical effects during the heat-up process that would lead to poor mechanical properties of the workpiece [118]. The trajectory planning accounts for the input and state constraints by means of the admissible sets

$$u(t) \in \mathcal{U}_{\text{ad}} := \{u(t) \in \mathbb{R} \,|\, u^- \leq u(t) \leq u^+\} \tag{3.1a}$$

$$T(x,t) - T^+ \leq 0 \quad \text{in } \Omega_{\text{o}} \times (0, t_{\text{f}}) \tag{3.1b}$$

with the bounds $0 \leq u^- < u^+$ and $T^+ > 0$.

3.1.2 Governing equations of induction heating processes

The constant heat-up and surface hardening processes are mathematically described by the coupled PDE system

$$\rho C \partial_t T - \nabla \cdot (k \nabla T) = \tfrac{\sigma\omega^2}{2}|A|^2 \qquad \text{in } \Omega_{\text{o}} \times (0, t_{\text{f}}) \tag{3.2a}$$

$$n \cdot (k \nabla T) = f(T) \qquad \text{on } \Gamma_{\text{o}} \times (0, t_{\text{f}}) \tag{3.2b}$$

$$T(\cdot, 0) = T_0 \qquad \text{in } \Omega_{\text{o}} \text{ at } t = 0 \tag{3.2c}$$

$$\nabla \times (\mu^{-1} \nabla \times A) + j\omega\sigma A = J_{\text{imp}}(u) \qquad \text{in } \Omega \times (0, t_{\text{f}}) \tag{3.2d}$$

$$n \times A = 0 \qquad \text{on } \Gamma \times (0, t_{\text{f}}) \ , \tag{3.2e}$$

whereby the thermal subsystem (3.2a)–(3.2c) is defined for the workpiece with the spatial domain Ω_{o}. The electromagnetic subsystem (3.2d)–(3.2e) is taken into account for the whole region of interest Ω.

The heat equation (3.2a) describes the thermal phenomena of the considered heat-up processes with the temperature T serving as the state variable. The boundary condition (3.2b) models heat losses due to convection and radiation against the surrounding. Its right hand side is specified by

$$f(T) = \alpha\,(T_{\text{a}} - T) + \epsilon\sigma_{\text{SB}}\left(T_{\text{a}}^4 - T^4\right) \qquad \text{on } \Gamma_{\text{o}} \times (0, t_{\text{f}}) \tag{3.3}$$

with the heat transfer coefficient α, the emissivity of the surface ϵ, the Stefan-Boltzmann constant σ_{SB} and the temperature of air T_{a}. A more accurate description of heat losses due

[2] The optimization of the position and shape of electromagnetic actuators is the subject of Chapter 4.

to radiation effects can be achieved by introducing view factors, also referred to as shape factors. This allows one to model the radiative heat transfer between different surfaces, see, e. g., [87, 37]. The initial workpiece temperature is specified by Equation (3.2c).

The electromagnetic phenomena of induction heating are described by the time-harmonic PDE (3.2d) with the magnetic vector potential A as the state variable. The PDE is formulated on the space-time cylinder $\Omega \times (0, t_\mathrm{f})$ to reflect the time-dependent excitation of the actuator. It is assumed that the sinusoidal current source u prescribes a time-harmonic current density within the spatial domain of the actuator. To this end, the phasor

$$J_\mathrm{imp}(u) = \tfrac{N_\mathrm{c}}{A_\mathrm{c}} u \chi_{\Omega_\mathrm{c}} e_\mathrm{c} \qquad \text{in } \Omega \times (0, t_\mathrm{f}) \tag{3.4}$$

is introduced with N_c and A_c as the coil windings and cross section surface of the actuator, see, e. g., [135, 102].[3] The direction of the flow of currents is described by the vector

$$e_\mathrm{c} = \left(\frac{-\tilde{x}_2}{\sqrt{\tilde{x}_1^2 + \tilde{x}_2^2}}, \frac{\tilde{x}_1}{\sqrt{\tilde{x}_1^2 + \tilde{x}_2^2}}, 0 \right)^\mathsf{T} \tag{3.5}$$

with $(\tilde{x}_1, \tilde{x}_2)$ following from a suitable coordinate transformation. Note that the electrical excitation of the actuator can be modeled more precisely by a PDE system such as (2.17), if the trajectory planning approach requires a higher accuracy.

The boundary condition (3.2e) models a vanishing electromagnetic field on Γ. Thereby, the boundary Γ is chosen sufficiently far away from the current source within the actuator, cf. the discussion in Section 2.2.3, also see [11, 135]. For a more compact notation, the gauging condition (2.21) as well as interface conditions of the magnetic vector potential A such as (2.29) are not explicitly formulated in what follows. A detailed explanation of the system dynamics (3.2) is presented in Section 2.2 and 2.3, respectively.

3.1.3 Formulation of a cost functional

The objectives of the induction heating processes are represented for the trajectory planning by a cost functional of the following type

$$J(u) = \int_\Omega V(T(\cdot, t_\mathrm{f}))\, \mathrm{d}x + \iint_{\Omega \times (0, t_\mathrm{f})} l(T, u)\, \mathrm{d}x\, \mathrm{d}t \ , \tag{3.6}$$

whereby the Mayer and Lagrange terms $V(T(\cdot, t_\mathrm{f}))$ and $l(T, u)$ are specified for both the constant heat-up and surface hardening process as follows

$$V(T(\cdot, t_\mathrm{f})) = \frac{q_1}{2} \chi_{\Omega_\mathrm{d}} \left(T(\cdot, t_\mathrm{f}) - T_\mathrm{d} \right)^2 \tag{3.7a}$$

$$l(T, u) = \frac{q_2}{2} \chi_{\Omega_\mathrm{d}} \left(T - T_\mathrm{d} \right)^2 + \frac{q_3}{2} \chi_{\Omega_\mathrm{o}} \max\left(0, T - T^+\right)^2 + \frac{q_4}{2} \chi_{\Omega_\mathrm{c}} u^2 \ . \tag{3.7b}$$

In fact, the three weights (q_1, q_2, q_3) are sufficient to balance the four objectives of the Mayer and Lagrange terms (3.7). For an overall scaling of the cost functional, however, all parts are weighted by individual parameters.

[3] The characteristic function χ_{Ω_c} is defined by Equation (2.16).

The primary objective of heating up the workpiece is taken into account for the trajectory planning by penalizing the quadratic error between the temperature T and the desired temperature T_d with the non-negative weights (q_1, q_2) within the Mayer and Lagrange terms (3.7). Depending on whether a constant heat-up or a surface hardening process is considered, the quadratic error $(T - T_\mathrm{d})^2$ is penalized on the spatial domain

$$\Omega_\mathrm{d} = \Omega_\mathrm{o} \qquad \text{(constant heat-up)} \tag{3.8a}$$

$$\Omega_\mathrm{d} = \tilde{\Omega}_\mathrm{o} \qquad \text{(surface hardening)} \ , \tag{3.8b}$$

whereby χ_{Ω_d} is the characteristic function of the spatial domain Ω_d, cf. Equation (2.16).

In the case of surface hardening, the control task of preventing an undesired heat-up of inner domains of the workpiece is taken into account by choosing the final time of the heat-up process t_f sufficiently short. Note that unavoidable diffusive heat transport phenomena can not be suppressed completely in view of the limited influence of the control trajectory u on the system dynamics of the induction heating processes (3.2).

At this current stage, the cost functional to be minimized (3.6) is also used to incorporate the state constraint (3.1b). To this end, the Lagrange term $l(T, u)$ is amended by an outer penalty function that is weighted with $q_3 \geq 0$. This not only reduces the numerical effort for solving the optimization problem specified in what follows, but also simplifies the derivation of its optimality conditions.[4] The last part of the Lagrange term weights the control action by means of the parameter $q_4 \geq 0$. This part of the cost functional also prevents, to some degree, the heat-up of inner domains of the workpiece in the case of surface hardening.

3.2 Optimal control strategies for hyperthermia therapy

Hyperthermia therapy is another typical example in which the energy of electromagnetic fields is used to heat up electrically conductive materials. The electromagnetic heat source is localized to cancer cells to make them more susceptible to conventional drug treatments, see, e. g., [144, 46]. A further type of hyperthermia therapy uses the electromagnetic heat source to significantly damage and kill the tumor by inducing biological effects including coagulation and necrosis [3].

Especially for tumors located deep within the human body, interstitial hyperthermia therapy facilitates optimal therapeutic success not to say making a cancer treatment possible. The particular challenges for the trajectory planning are to adapt the electrical excitation of the actuator to the size of the tumor, to the thermal behavior of healthy tissue, and to prevent adverse effects of the electromagnetic field to the human body.

[4] A more systematic incorporation of state constraints is devoted to Chapter 5 and Appendix A, where an augmented Lagrangian method and a transformation approach is discussed.

3.2.1 Geometrical setup and control tasks

The optimal trajectory planning for hyperthermia therapy is exemplified for the minimally invasive methods microwave ablation (MWA – *Micro-Wave Ablation*) and radio frequency ablation (RFA – *Radio Frequency Ablation*). MWA is often applied to treat tumors Ω_t in the region of the breast or liver Ω_h, as illustrated in Figure 3.2a for an axisymmetrical setup, see, e. g., [43, 107]. An alternating voltage source u is applied to the boundary Γ_c of a needle-like actuator, also referred to as electrode or applicator, with spatial domain Ω_c. The induced electromagnetic field penetrates through an air gap into the tumor and surrounding tissue. By sticking the actuator directly into the diseased tissue, the electromagnetic heat source is generated as close as possible to the spatial domain which should be heated up.

Figure 3.2b shows a typical scenario of RFA, where a tumor Ω_t close to the dorsal vertebra Ω_b and spinal canal Ω_s is heat-treated [15, 46]. The healthy tissue is denoted by Ω_h.[5] Alternating voltages u are applied to the boundary segment of the actuators $\Gamma_\mathrm{c} = \Gamma_{\mathrm{c},1} \cup \Gamma_{\mathrm{c},2}$ to guide the electromagnetic field through air gaps into the region of the diseased tissue. As a result, the tumor Ω_t as well as surrounding healthy tissue heats up. The intensity of the heat source can be controlled as in the case of MWA by the specific choice of the voltage source u.

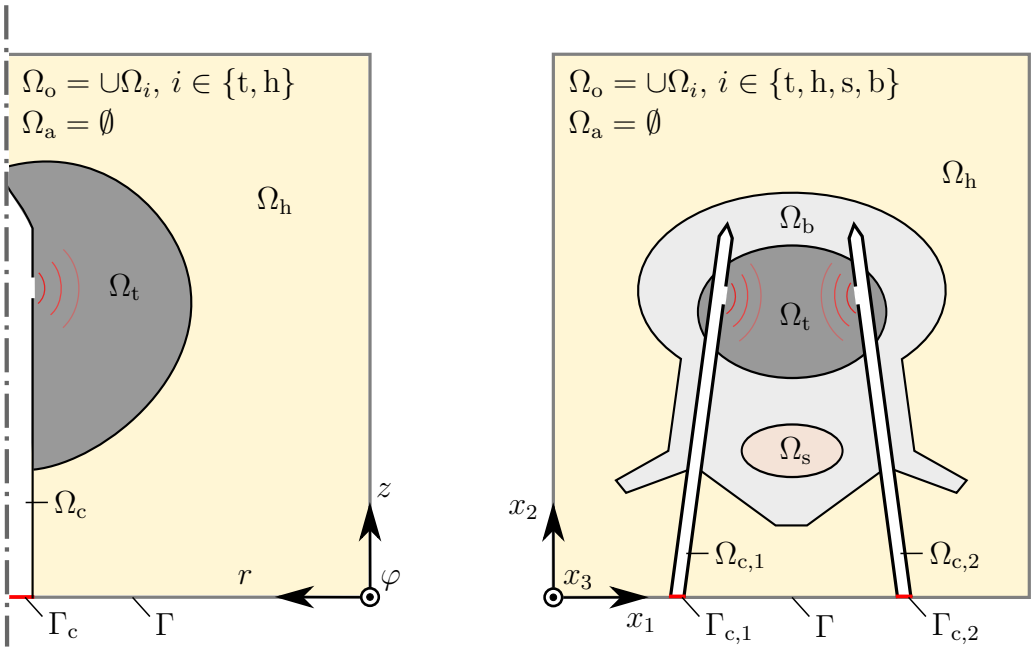

(a) MWA setup

(b) RFA setup

Figure 3.2: MWA and RFA setup (not to scale) with actuator Ω_c, respectively $\Omega_{\mathrm{c},1}$ and $\Omega_{\mathrm{c},2}$, to generate the electromagnetic heat source in close proximity to the tumor Ω_t. MWA is typically applied to treat tumors in the region of the breast or liver Ω_h. RFA is a preferred cancer therapy for tumors close to the dorsal vertebra Ω_b and spinal canal Ω_s.

[5] A description of the subscripts of the individual spatial domains is presented in Appendix B.4.

The electrically conductive materials of MWA and RFA are summarized as follows

$$\Omega_{\mathrm{o}} = \Omega_{\mathrm{t}} \cup \Omega_{\mathrm{h}} \qquad \text{(MWA)} \tag{3.9a}$$

$$\Omega_{\mathrm{o}} = \Omega_{\mathrm{t}} \cup \Omega_{\mathrm{h}} \cup \Omega_{\mathrm{s}} \cup \Omega_{\mathrm{b}} \qquad \text{(RFA)}\ , \tag{3.9b}$$

whereby Γ_{o} denotes the corresponding boundary, cf. Figure 3.3, also see Appendix B.4. The definition of the region of interest Ω_{o} facilitates a consistent description of the spatial domain for which the electromagnetic and thermal phenomena have to be taken into account in the case of MWA and RFA, respectively. In RFA, the spatial domain of the actuators is denoted by $\Omega_{\mathrm{c}} = \Omega_{\mathrm{c},1} \cup \Omega_{\mathrm{c},2}$. Note that the spatial coordinates are either specified by $x = [r, \varphi, z]^{\mathsf{T}}$ or $x = [x_1, x_2, x_3]^{\mathsf{T}}$, according to whether MWA or RFA is considered, cf. Figure 3.2.

The electromagnetic phenomena of MWA and RFA are modeled not only on the spatial domain of the diseased and healthy tissue Ω_{o}, but also on the spatial domain of the actuator Ω_{c} in view of the boundary control u. For numerical reasons, the geometrical setups of hyperthermia therapy contain no ambient air Ω_{a} in contrast to the induction heating scenarios in Section 3.1. Consequently, the spatial domain for which the electromagnetic phenomena of hyperthermia therapy has to be solved is $\Omega = \Omega_{\mathrm{o}} \cup \Omega_{\mathrm{c}}$.

The control tasks of hyperthermia therapy are similar to those of induction heating processes. Both the objective to make the tumor more susceptible to conventional drugs and the required necrosis effects to severely damage the tumor can be reduced to desired temperature profiles T_{d}, see, e. g., [23, 45, 38]. For example, to achieve a complete destruction of the tumor caused by necrosis effects, the tumor temperature has to exceed a critical value T_{d} for a certain time interval. Further criteria to account for is the limitation of the voltage source as described by the input constraints (3.1a). To prevent a health-damaging overheating, the temperature T is subject to the state constraint (3.1b).

3.2.2 Governing equations of hyperthermia processes

The PDE (2.25) allows one to describe the connection between the boundary control u and the generation of the electromagnetic heat source. The thermal phenomena are modeled by means of a modified version of the heat equation (2.41). Overall, the PDE system

$$\rho C \partial_t T - \nabla \cdot (k \nabla T) = \tfrac{\sigma}{2}|E|^2 - \rho_{\mathrm{b}} C_{\mathrm{b}} \omega_{\mathrm{b}} (T - T_{\mathrm{b}}) \qquad \text{in } \Omega_{\mathrm{o}} \times (0, t_{\mathrm{f}}) \tag{3.10a}$$

$$n \cdot (k \nabla T) = 0 \qquad \text{on } \Gamma_{\mathrm{o}} \times (0, t_{\mathrm{f}}) \tag{3.10b}$$

$$T(\cdot, 0) = T_{\mathrm{b}} \qquad \text{in } \Omega_{\mathrm{o}} \text{ at } t = 0 \tag{3.10c}$$

$$\nabla \times (\mu_{\mathrm{r}}^{-1} \nabla \times E) - k_0^2 (\epsilon_{\mathrm{r}} - j \tfrac{\sigma}{\omega \epsilon_0}) E = 0 \qquad \text{in } \Omega \times (0, t_{\mathrm{f}}) \tag{3.10d}$$

$$n \times E = E_{\mathrm{imp}}(u) \qquad \text{on } \Gamma_{\mathrm{c}} \times (0, t_{\mathrm{f}}) \tag{3.10e}$$

$$n \times E = 0 \qquad \text{on } \Gamma_{\mathrm{PEC}} \times (0, t_{\mathrm{f}}) \tag{3.10f}$$

$$n \times (\nabla \times E) = j k_0 E_{\mathrm{out}} \qquad \text{on } \Gamma \times (0, t_{\mathrm{f}}) \tag{3.10g}$$

facilitates to model the system dynamics of hyperthermia therapy. The PDE (3.10a) is also referred to as Pennes' bioheat equation [100].

The right hand side of the heat equation (3.10a) includes the Joule heat source (2.40b) and a heat sink to model heat transfer effects due to blood perfusion. The thermal behavior of different kinds of tissue and bones is taken into account by the density $\rho_\mathrm{b} := \rho_\mathrm{b}(x)$ and the specific heat capacity $C_\mathrm{b} := C_\mathrm{b}(x)$. The temperature of blood penetrating the tumor and surrounding tissue with perfusion rate $\omega_\mathrm{b} := \omega_\mathrm{b}(x)$ is specified by T_b, see, e. g., [15, 3].

The Neumann boundary condition (3.10b) models a vanishing heat flow on the boundary segment Γ_o including the outer boundary of the region of interest and the boundary of the actuator, cf. Figure 3.3. This is an appropriate assumption since the predominant heat sink due to blood perfusion has the effect that regions away from the heat source rapidly reach the temperature of blood [3]. The assumption of a vanishing heat flow on the boundary of the actuator is justified by a heat transfer coefficient close to zero for the catheter that is used as an insulating layer to human tissue [15, 46]. The initial temperature of hyperthermia therapy is specified by Equation (3.10c).

The time-harmonic PDE (3.10d) models the electromagnetic phenomena of MWA and RFA, whereby $k_0 = \omega\sqrt{\epsilon_0\mu_0}$ denotes the wave number. The Dirichlet boundary condition (3.10e) comprises the voltage source u that acts as the degree of freedom for an optimal trajectory planning. The control trajectory u prescribes the electric field intensity at the boundary of the actuator on the time interval $(0, t_\mathrm{f})$ according to

$$E_\mathrm{imp}(u) = \frac{u e_\mathrm{r}}{r \ln\left(r_2/r_1\right)} \qquad \text{on } \Gamma_\mathrm{c} \times (0, t_\mathrm{f}) \tag{3.11}$$

with e_r denoting the unit vector in the direction of r, also see [44]. Consequently, electromagnetic waves travel through the dielectric $\Omega_\mathrm{c,d}$ of the actuator of coaxial type, cf. Figure 3.3. It is assumed that only the fundamental TEM mode (TEM – *Transverse Electro-Magnetic*) is present by which the most part of the energy of the electromagnetic field radiates through the air gap $\Omega_\mathrm{c,a}$ into the tumor, see, e. g., [107].

The homogeneous Dirichlet boundary condition (3.10f) models a perfect electric conduction on the boundary of the dielectric and catheter Γ_PEC. The first-order absorbing boundary condition (3.10g) makes the boundary Γ transparent for outgoing waves

$$E_\mathrm{out} = n \times (n \times E) \qquad \text{on } \Gamma \times (0, t_\mathrm{f}) \ , \tag{3.12}$$

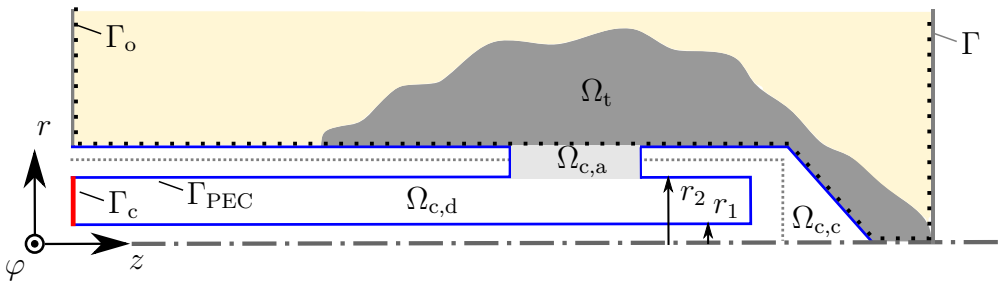

Figure 3.3: Detail view of an actuator of coaxial type (not to scale) with the dielectric $\Omega_\mathrm{c,d}$, the air gap $\Omega_\mathrm{c,a}$ and the catheter $\Omega_\mathrm{c,c}$ as an insulating layer to human tissue.

cf. Figure 3.2, also see [11, 6, 67].[6] This takes into account the fact that electromagnetic waves in reality propagate outside the region of interest Ω. A more detailed description of the electromagnetic and thermal phenomena is presented in Chapter 2.

3.2.3 Formulation of a cost functional

A cost functional similar to that of induction heating (3.6) is formulated for the trajectory planning in the case of hyperthermia therapy

$$J(u) = \int_{\Omega} V(T(\cdot, t_\mathrm{f}))\ \mathrm{d}x + \iint_{\Omega\times(0,t_\mathrm{f})} l(T)\ \mathrm{d}x\,\mathrm{d}t + \iint_{\Gamma\times(0,t_\mathrm{f})} l_\Gamma(u)\ \mathrm{d}x\,\mathrm{d}t\ . \tag{3.13}$$

To convert the various objectives of hyperthermia therapy into a suitable form for the optimization-based trajectory planning approach, the Mayer term $V(T(\cdot, t_\mathrm{f}))$ and the Lagrange terms $l(T)$ and $l_\Gamma(u)$ are specified as follows

$$V(T(\cdot, t_\mathrm{f})) = \frac{q_1}{2}\chi_{\Omega_\mathrm{t}}\left(T(\cdot, t_\mathrm{f}) - T_\mathrm{d}\right)^2 \tag{3.14a}$$

$$l(T) = \frac{q_2}{2}\chi_{\Omega_\mathrm{t}}\left(T - T_\mathrm{d}\right)^2 + \frac{q_3}{2}\chi_{\Omega_\mathrm{o}}\max\left(0, T - T^+\right)^2 \tag{3.14b}$$

$$l_\Gamma(u) = \frac{q_4}{2}\chi_{\Gamma_\mathrm{c}}\left(u - u_\mathrm{d}\right)^2\ . \tag{3.14c}$$

Note that all four parts of the Mayer and Lagrange terms are weighted by an individual parameter instead of the minimum required number of three.

The primary objective of heating up the tumor is taken into account by penalizing the quadratic error between the temperature T and the desired temperature T_d on the spatial domain Ω_t. The Mayer term $V(T(\cdot, t_\mathrm{f}))$ and the Lagrange term $l(T)$ weight this control task by $q_1 \geq 0$ and $q_2 \geq 0$. The second part of the Lagrange term is an outer penalty function to incorporate the state constraint (3.1b). The corresponding weight is $q_3 \geq 0$. The Lagrange term $l_\Gamma(u)$ penalizes the quadratic error between the control trajectory u and a set point u_d using the weight $q_4 \geq 0$.

3.3 Optimization problem for electromagnetic heating systems

The optimization-based trajectory planning for the induction heating processes and hyperthermia therapy described in Section 3.1 and 3.2 relies on the formulation of a common PDE constrained optimization problem. This offers the possibility to derive the optimality conditions of both problems in a more compact form. This will also ensure that the trajectory planning approach will be able to address other electromagnetic heating applications in a straightforward manner.

[6] Except for the segment Γ_PEC which is not included in Γ, the boundary Γ corresponds to the boundary Γ_o, i. e., $\Gamma = \Gamma_\mathrm{o} \setminus \Gamma_\mathrm{PEC}$, also see Figure 3.2 and 3.3.

3.3.1 Definition of differential operators

The governing equations of the induction heating and hyperthermia processes (3.2) and (3.10) contain the same differential operators. It is therefore feasible to represent both problems by a PDE system exhibiting a generic structure. For reformulating the thermal subsystems (3.2a)–(3.2c) and (3.10a)–(3.10c) in the following lines, the temporal and spatial operators

$$e_{\nabla,\,t}\,(\alpha, T) = \alpha \partial_t T \qquad \text{in } \Omega_\mathrm{o} \times (0, t_\mathrm{f}) \tag{3.15a}$$

$$e_{\Delta}\,(\alpha, T) = \nabla\cdot\,(\alpha\,\nabla\, T) \qquad \text{in } \Omega_\mathrm{o} \times (0, t_\mathrm{f}) \tag{3.15b}$$

$$e_{\nabla,\,x}\,(\alpha, T) = n\cdot\,(\alpha\,\nabla\, T) \qquad \text{on } \Gamma_\mathrm{o} \times (0, t_\mathrm{f}) \tag{3.15c}$$

are introduced. The parameter α is used to address different material parameters.

The electromagnetic subsystems (3.2d)–(3.2e) and (3.10d)–(3.10g) are reformulated on the basis of the spatial operators

$$e_{\nabla\times,\nabla\times}\,(\alpha, K) = \nabla\times(\alpha\nabla\times K) \qquad \text{in } \Omega \times (0, t_\mathrm{f}) \tag{3.16a}$$

$$e_{\nabla\times}\,(\alpha, K) = n \times (\alpha\nabla\times K) \qquad \text{on } \Gamma \times (0, t_\mathrm{f}) \tag{3.16b}$$

$$e_{\times}\,(K) = n \times K \qquad \text{on } \Gamma \times (0, t_\mathrm{f}) \tag{3.16c}$$

with the phasor $K := K(x;t),\ K \in \{A, E\}$ as the corresponding state variable. The generalizations of the differential operators (3.15) and (3.16) facilitate to define optimality conditions for both induction heating and hyperthermia processes in a holistic way.

3.3.2 Problem formulation

The differential operators defined in the last section are used to express optimal control problems for electromagnetic heating systems in the generalized form

$$\min_{u(\cdot)\in\mathcal{U}_\mathrm{ad}} J(u) = \int_{\Omega} V(T(\cdot, t_\mathrm{f}))\ \mathrm{d}x + \iint_{\Omega\times(0,t_\mathrm{f})} l(T, u)\ \mathrm{d}x\,\mathrm{d}t + \iint_{\Gamma\times(0,t_\mathrm{f})} l_\Gamma(u)\ \mathrm{d}x\,\mathrm{d}t \tag{3.17a}$$

$$\text{s.t.} \quad e_{\nabla,\,t}\,(\rho C, T) - e_{\Delta}\,(k, T) = f_{\Omega_\mathrm{o}}(T, K) \qquad \text{in } \Omega_\mathrm{o} \times (0, t_\mathrm{f}) \tag{3.17b}$$

$$e_{\nabla,\,x}\,(k, T) = f_{\Gamma_{\mathrm{o,N}}}(T) \qquad \text{on } \Gamma_{\mathrm{o,N}} \times (0, t_\mathrm{f}) \tag{3.17c}$$

$$T = f_{\Gamma_{\mathrm{o,D}}} \qquad \text{on } \Gamma_{\mathrm{o,D}} \times (0, t_\mathrm{f}) \tag{3.17d}$$

$$T(\cdot, 0) = T_0 \qquad \text{in } \Omega_\mathrm{o} \text{ at } t = 0 \tag{3.17e}$$

$$e_{\nabla\times,\nabla\times}\,(\mu^{-1}, K) = f_{\Omega}(K, u) \qquad \text{in } \Omega \times (0, t_\mathrm{f}) \tag{3.17f}$$

$$e_{\nabla\times}\,(\mu^{-1}, K) = f_{\Gamma_\mathrm{N}}(K, u) \qquad \text{on } \Gamma_\mathrm{N} \times (0, t_\mathrm{f}) \tag{3.17g}$$

$$e_{\times}\,(K) = f_{\Gamma_\mathrm{D}}(u) \qquad \text{on } \Gamma_\mathrm{D} \times (0, t_\mathrm{f})\ . \tag{3.17h}$$

The cost functional (3.17a) consists of the Mayer term $V(T(\cdot, t_\mathrm{f}))$ and the Lagrange terms $l(T, u)$ and $l_\Gamma(u)$. The individual parts are specified by Equation (3.7) or (3.14), according to whether an induction heating or hyperthermia problem is considered.

The formulation of optimization problem (3.17) includes both Dirichlet boundary conditions and Neumann boundary conditions for the thermal and electromagnetic phenomena. Thereby, the functions

$$f_{\Omega_\mathrm{o}}(T,K) \qquad \text{in } \Omega_\mathrm{o}\times(0,t_\mathrm{f}) \tag{3.18a}$$
$$f_{\Gamma_{\mathrm{o,N}}}(T) \qquad \text{on } \Gamma_{\mathrm{o,N}}\times(0,t_\mathrm{f}) \tag{3.18b}$$
$$f_{\Gamma_{\mathrm{o,D}}} \qquad \text{on } \Gamma_{\mathrm{o,D}}\times(0,t_\mathrm{f}) \tag{3.18c}$$

facilitate to adapt the right hand sides of the heat equation (3.17b), the Neumann boundary condition (3.17c), and the Dirichlet boundary condition (3.17d) to a specific electromagnetic heating problem. Similarly, the electromagnetic subsystem (3.17f)–(3.17h) is described in general form with the functions

$$f_\Omega(K,u) \qquad \text{in } \Omega\times(0,t_\mathrm{f}) \tag{3.19a}$$
$$f_{\Gamma_\mathrm{N}}(K,u) \qquad \text{on } \Gamma_\mathrm{N}\times(0,t_\mathrm{f}) \tag{3.19b}$$
$$f_{\Gamma_\mathrm{D}}(u) \qquad \text{on } \Gamma_\mathrm{D}\times(0,t_\mathrm{f})\ . \tag{3.19c}$$

The induction heating processes described in Section 3.1 can be addressed by optimization problem (3.17) by setting the right hand sides (3.18)–(3.19) as follows

$$f_{\Omega_\mathrm{o}}(T,A) = \tfrac{\sigma\omega^2}{2}|A|^2 \qquad \text{in } \Omega_\mathrm{o}\times(0,t_\mathrm{f}) \tag{3.20a}$$
$$f_{\Gamma_{\mathrm{o,N}}}(T) = \alpha\left(T_\mathrm{a}-T\right)+\epsilon\sigma_\mathrm{SB}\left(T_\mathrm{a}^4-T^4\right) \qquad \text{on } \Gamma_{\mathrm{o,N}}\times(0,t_\mathrm{f}) \tag{3.20b}$$

$$f_\Omega(A,u) = \tfrac{N_\mathrm{c}}{A_\mathrm{c}}u\chi_{\Omega_\mathrm{c}}e_\mathrm{c}-j\omega\sigma A \qquad \text{in } \Omega\times(0,t_\mathrm{f}) \tag{3.20c}$$
$$f_{\Gamma_\mathrm{D}}(u) = 0 \qquad \text{on } \Gamma_\mathrm{D}\times(0,t_\mathrm{f})\ , \tag{3.20d}$$

cf. Equation (3.2). The undefined functions $f_{\Gamma_{\mathrm{o,D}}}$ and $f_{\Gamma_\mathrm{N}}(A,u)$ in (3.20) reflect the fact that the thermal subsystem (3.2a)–(3.2b) and electromagnetic subsystem (3.2d)–(3.2e) comprises no Dirichlet boundary condition, respectively no Neumann boundary condition.

To deal with the optimal trajectory planning problem in the course of hyperthermia therapy, the right hand sides (3.18)–(3.19) are set to

$$f_{\Omega_\mathrm{o}}(T,E) = \tfrac{\sigma}{2}|E|^2-\rho_\mathrm{b}C_\mathrm{b}\omega_\mathrm{b}(T-T_\mathrm{b}) \qquad \text{in } \Omega_\mathrm{o}\times(0,t_\mathrm{f}) \tag{3.21a}$$
$$f_{\Gamma_{\mathrm{o,N}}}(T) = 0 \qquad \text{on } \Gamma_{\mathrm{o,N}}\times(0,t_\mathrm{f}) \tag{3.21b}$$

$$f_\Omega(E,u) = k_0^2(\epsilon_\mathrm{r}-j\tfrac{\sigma}{\omega\epsilon_0})E \qquad \text{in } \Omega\times(0,t_\mathrm{f}) \tag{3.21c}$$
$$f_{\Gamma_\mathrm{N}}(E,u) = jk_0E_\mathrm{out} \qquad \text{on } \Gamma_\mathrm{N}\times(0,t_\mathrm{f}) \tag{3.21d}$$
$$f_{\Gamma_\mathrm{D}}(u) = E_\mathrm{imp}(u) \qquad \text{on } \Gamma_\mathrm{D}\times(0,t_\mathrm{f})\ . \tag{3.21e}$$

For reasons of consistency, however, only the Dirichlet boundary condition (3.10e) is incorporated into optimization problem (3.17) using Equation (3.21e) to avoid an adaptation of the structure of the optimization problem.

3.4 Derivation of optimality conditions

The formal Lagrangian technique provides a promising approach to deal with the nonlinear PDEs when deriving the optimality conditions of optimization problem (3.17), see [133], as well as the discussion in Section 1.3.3. First of all, the Lagrangian $\mathcal{L} := \mathcal{L}(T, K, u, p, \Lambda)$ is defined as follows

$$\begin{aligned}\mathcal{L} = &\int_{\Omega} V(T(\cdot, t_\mathrm{f}))\,\mathrm{d}x + \iint_{\Omega\times(0,t_\mathrm{f})} l(T,u)\,\mathrm{d}x\,\mathrm{d}t + \iint_{\Gamma\times(0,t_\mathrm{f})} l_\Gamma(u)\,\mathrm{d}x\,\mathrm{d}t \\ &+ \iint_{\Omega_\mathrm{o}\times(0,t_\mathrm{f})} p\left[e_{\nabla,t}\left(\rho C, T\right) - e_\Delta\left(k, T\right) - f_{\Omega_\mathrm{o}}(T, K)\right]\,\mathrm{d}x\,\mathrm{d}t \\ &+ \iint_{\Gamma_{\mathrm{o,N}}\times(0,t_\mathrm{f})} p\left[e_{\nabla,x}\left(k, T\right) - f_{\Gamma_{\mathrm{o,N}}}(T)\right]\,\mathrm{d}x\,\mathrm{d}t + \iint_{\Gamma_{\mathrm{o,D}}\times(0,t_\mathrm{f})} p\left[T - f_{\Gamma_{\mathrm{o,D}}}\right]\,\mathrm{d}x\,\mathrm{d}t \\ &+ \iint_{\Omega\times(0,t_\mathrm{f})} \Lambda\cdot\left[e_{\nabla\times,\nabla\times}\left(\mu^{-1}, K\right) - f_\Omega(K,u)\right]\,\mathrm{d}x\,\mathrm{d}t \\ &+ \iint_{\Gamma_\mathrm{N}\times(0,t_\mathrm{f})} \Lambda\cdot\left[f_{\Gamma_\mathrm{N}}(K,u) - e_{\nabla\times}\left(\mu^{-1}, K\right)\right]\,\mathrm{d}x\,\mathrm{d}t + \iint_{\Gamma_\mathrm{D}\times(0,t_\mathrm{f})} \Lambda\cdot\left[e_\times\left(K\right) - f_{\Gamma_\mathrm{D}}(u)\right]\,\mathrm{d}x\,\mathrm{d}t \end{aligned} \tag{3.22}$$

to couple the PDE system (3.17b)–(3.17h) to the cost functional (3.17a) by means of adjoint states.[7] The scalar-valued adjoint state $p := p(x,t)$ accounts for the thermal subsystem (3.17b)–(3.17d) within the Lagrangian $\mathcal{L}$ and depends on space and time. The adjoint state $\Lambda := \Lambda(x;t)$ is a phasor, which takes the electromagnetic subsystem (3.17f)–(3.17h) into account. In this case, however, the adjoint state Λ is a vector that depends on time only implicitly, since the electromagnetic phenomena are assumed to be time-harmonic.

The first-order optimality conditions of optimization problem (3.17) are deduced from the directional derivatives

$$\left.\frac{\partial\mathcal{L}}{\partial T}\right|_{y^*} h_T = 0 \qquad \forall h_T \tag{3.23a}$$

$$\left.\frac{\partial\mathcal{L}}{\partial K}\right|_{y^*} \cdot H_K = 0 \qquad \forall H_K \tag{3.23b}$$

$$\left.\frac{\partial\mathcal{L}}{\partial u}\right|_{y^*} h_u \geq 0 \qquad \forall u \in \mathcal{U}_\mathrm{ad}\ , \tag{3.23c}$$

whereby $y^* = (T^*, K^*, u^*, p^*, \Lambda^*)$ denotes optimal state, adjoint state, and control trajectories, also see [133, 119]. The admissible directions of the temperature T are specified by $h_T = T - T^*$, of the state variable of the electromagnetic subsystem K by $H_K = K - K^*$, and of the control trajectory u by $h_u = u - u^*$, respectively.[8] With respect to an optimal

[7] To simplify the following discussion, the left and right hand side of the boundary condition (3.17g) is multiplied by minus one before being incorporated into the Lagrangian.

[8] Contrary to the notation to distinguish vectors from scalars by capital letters, the temperature is denoted by T despite it is scalar. Accordingly, the admissible directions h_T have a capital letter as subscript.

solution y^*, the directional derivatives (3.23a) and (3.23b) have to be equal to zero for all admissible directions h_T and H_K. On the contrary, the third directional derivative (3.23c) is formulated as an inequality constraint to take the input constraints (3.1a) into account, also see, for instance, [1, 62].

The basic idea of the formal Lagrangian technique to treat temporal and spatial operators formally makes it possible to evaluate and analyze the partial derivatives of the Lagrangian $\mathcal{L}$ with respect to the states (T, K) and the control trajectory u. Consequently, the first-order optimality conditions (3.23a) and (3.23b) can be mathematically handled with relative ease and will result in adjoint PDE systems, cf. Section 1.3. The same applies to the first-order optimality condition (3.23c) that results in a gradient condition. The derivation of the adjoint PDE systems and gradient condition is the subject of the following sections.

3.4.1 Adjoint dynamics of the thermal subsystem

The following lines analyze the directional derivative (3.23a), which eventually results in an adjoint dynamics related to the thermal subsystem (3.17b)–(3.17e). The partial derivative of the Lagrangian $\mathcal{L}$ with respect to the state T yields the variational equation

$$\begin{aligned}\left.\frac{\partial \mathcal{L}}{\partial T}\right|_{y^*} h_T = &\int_{\Omega} \partial_T V(T(\cdot,t_\mathrm{f}))|_{y^*}\, h_T(\cdot,t_\mathrm{f})\,\mathrm{d}x + \iint_{\Omega\times(0,t_\mathrm{f})} \partial_T l(T,u)|_{y^*}\, h_T\,\mathrm{d}x\,\mathrm{d}t \\ &+ \iint_{\Omega_\mathrm{o}\times(0,t_\mathrm{f})} p^*\left[e_{\nabla,t}\left(\rho C, h_T\right) - e_\Delta\left(k, h_T\right) - \partial_T f_{\Omega_\mathrm{o}}(T,K)|_{y^*}\, h_T\right]\,\mathrm{d}x\,\mathrm{d}t \\ + \iint_{\Gamma_{\mathrm{o,N}}\times(0,t_\mathrm{f})} p^*\left[e_{\nabla,x}\left(k, h_T\right) - \partial_T f_{\Gamma_{\mathrm{o,N}}}(T)\big|_{y^*}\, h_T\right]\,\mathrm{d}x\,\mathrm{d}t &+ \iint_{\Gamma_{\mathrm{o,D}}\times(0,t_\mathrm{f})} p^* h_T\,\mathrm{d}x\,\mathrm{d}t = 0 \qquad \forall h_T\ ,\end{aligned} \tag{3.24}$$

whereby the derivatives concerning the temporal and spatial operators (3.15) are treated formally. The arguments of the temporal and spatial operators swap from the state T to the admissible directions h_T, i. e.,

$$\partial_T e_{\nabla,t}\left(\rho C, T\right)|_{y^*}\, h_T = e_{\nabla,t}\left(\rho C, h_T\right) \qquad \text{in } \Omega_\mathrm{o}\times(0,t_\mathrm{f}) \tag{3.25a}$$

$$\partial_T e_\Delta\left(k, T\right)|_{y^*}\, h_T = e_\Delta\left(k, h_T\right) \qquad \text{in } \Omega_\mathrm{o}\times(0,t_\mathrm{f}) \tag{3.25b}$$

$$\partial_T e_{\nabla,x}\left(k, T\right)|_{y^*}\, h_T = e_{\nabla,x}\left(k, h_T\right) \qquad \text{on } \Gamma_\mathrm{o}\times(0,t_\mathrm{f})\ , \tag{3.25c}$$

what can also be observed by comparing the Lagrangian (3.22) with the variational equation (3.24), also see [133].

In order to be able to analyze the variational equation (3.24) for all admissible directions h_T, the temporal and spatial operators involving h_T as an argument, i. e., the parts $e_{\nabla,t}\left(\rho C, h_T\right)$, $e_\Delta\left(k, h_T\right)$, and $e_{\nabla,x}\left(k, h_T\right)$, are applied to proper integral identities. This reformulation step eventually allows one to replace the arguments h_T of the temporal and spatial operators in Equation (3.24) by the adjoint state p.

First of all, the formula of partial integration

$$\iint\limits_{\Omega_\mathrm{o}\times(0,t_\mathrm{f})} p^* e_{\nabla,\,t}\left(\rho C, h_T\right)\,\mathrm{d}x\,\mathrm{d}t = \int\limits_{\Omega_\mathrm{o}} p^*\rho C h_T\big|_0^{t_\mathrm{f}}\,\mathrm{d}x - \iint\limits_{\Omega_\mathrm{o}\times(0,t_\mathrm{f})} e_{\nabla,\,t}\left(\rho C, p^*\right) h_T\,\mathrm{d}x\,\mathrm{d}t \tag{3.26}$$

is applied to the first part of the second line of the variational equation (3.24). This integral identity allows to get rid of the temporal derivative affecting the admissible directions h_T. Moreover, Green's second identity

$$\begin{aligned} -\iint\limits_{\Omega_\mathrm{o}\times(0,t_\mathrm{f})} p^* e_{\Delta}\left(k, h_T\right)\,\mathrm{d}x\,\mathrm{d}t = &-\iint\limits_{\Omega_\mathrm{o}\times(0,t_\mathrm{f})} e_{\Delta}\left(k, p^*\right) h_T\,\mathrm{d}x\,\mathrm{d}t \\ &+ \iint\limits_{\Gamma_{\mathrm{o,N}}\times(0,t_\mathrm{f})} e_{\nabla,\,x}\left(k, p^*\right) h_T\,\mathrm{d}x\,\mathrm{d}t - \iint\limits_{\Gamma_{\mathrm{o,N}}\times(0,t_\mathrm{f})} p^* e_{\nabla,\,x}\left(k, h_T\right)\,\mathrm{d}x\,\mathrm{d}t \end{aligned} \tag{3.27}$$

is applied to the second part of the second line of the variational equation (3.24) to cope with the spatial derivative that is subject to the admissible directions h_T, see, e. g., [133, 119]. This substitution also cancels out the spatial derivative of the admissible directions h_T within the boundary integral on the segment $\Gamma_{\mathrm{o,N}}$.

By applying both the formula of partial integration (3.26) and Green's second identity (3.27) to the variational equation (3.24), the modified counterpart

$$\begin{aligned} \left.\frac{\partial \mathcal{L}}{\partial T}\right|_{y^*} h_T = &\iint\limits_{\Omega_\mathrm{o}\times(0,t_\mathrm{f})} \left[-e_{\nabla,\,t}\left(\rho C, p^*\right) - e_{\Delta}\left(k, p^*\right) - \partial_T f_{\Omega_\mathrm{o}}(T,K)\big|_{y^*} p^* + \partial_T l(T,u)\big|_{y^*}\right] h_T\,\mathrm{d}x\,\mathrm{d}t \\ &+ \iint\limits_{\Gamma_{\mathrm{o,N}}\times(0,t_\mathrm{f})} \left[e_{\nabla,\,x}\left(k, p^*\right) - \partial_T f_{\Gamma_{\mathrm{o,N}}}(T)\big|_{y^*} p^*\right] h_T\,\mathrm{d}x\,\mathrm{d}t + \iint\limits_{\Gamma_{\mathrm{o,D}}\times(0,t_\mathrm{f})} p^* h_T\,\mathrm{d}x\,\mathrm{d}t \\ &+ \int\limits_{\Omega_\mathrm{o}} \left[\rho C p^*(\cdot,t_\mathrm{f}) + \partial_T V(T(\cdot,t_\mathrm{f}))\big|_{y^*}\right] h_T(\cdot,t_\mathrm{f})\,\mathrm{d}x = 0 \qquad \forall h_T \end{aligned} \tag{3.28}$$

is obtained.[9] The new variational equation (3.28) no longer contains admissible directions h_T which are subject to temporal or spatial derivatives. This allows one to specify a condition for an optimal solution y^*. The parts within the squared brackets must vanish in a distributional manner, since the admissible directions h_T are arbitrary. The adjoint PDE system

$$e_{\nabla,\,t}\left(\rho C, p^*\right) + e_{\Delta}\left(k, p^*\right) = \partial_T l(T,u)\big|_{y^*} - \partial_T f_{\Omega_\mathrm{o}}(T,K)\big|_{y^*} p^* \qquad \text{in } \Omega_\mathrm{o}\times(0,t_\mathrm{f}) \tag{3.29a}$$

$$e_{\nabla,\,x}\left(k, p^*\right) = \partial_T f_{\Gamma_{\mathrm{o,N}}}(T)\big|_{y^*} p^* \qquad \text{on } \Gamma_{\mathrm{o,N}}\times(0,t_\mathrm{f}) \tag{3.29b}$$

$$p^* = 0 \qquad \text{on } \Gamma_{\mathrm{o,D}}\times(0,t_\mathrm{f}) \tag{3.29c}$$

$$\rho C p^*(\cdot,t_\mathrm{f}) = -\,\partial_T V(T(\cdot,t_\mathrm{f}))\big|_{y^*} \qquad \text{in } \Omega_\mathrm{o} \text{ at } t = t_\mathrm{f} \tag{3.29d}$$

[9] For the sake of compactness, the part $\partial_T l(T,u)$ is now only integrated over Ω_o as the temperature T is just defined for the object to be heated, see Equation (3.24) and (3.28).

guarantees this necessary optimality condition, cf., e. g., [17, 3]. The adjoint dynamics (3.29a) ensures that the first line of the variational equation (3.28) vanishes for all admissible directions h_T. The same applies to the Neumann boundary condition (3.29b) and the Dirichlet boundary condition (3.29c) which cancels out the second line of Equation (3.28). The third line of the variational equation (3.28) vanishes in view of the final condition (3.29d).

3.4.2 Adjoint dynamics of the electromagnetic subsystem

The directional derivative (3.23b) is analyzed in the following lines to derive the adjoint dynamics of the electromagnetic subsystem of optimization problem (3.17). After substituting the Lagrangian (3.22) into Equation (3.23b), the partial derivative of (3.23b) is carried out and results in the variational equation

$$\begin{aligned}\left.\frac{\partial \mathcal{L}}{\partial K}\right|_{y^*} \cdot H_K = &- \iint\limits_{\Omega_\mathrm{o}\times(0,t_\mathrm{f})} p^* \, \partial_K f_{\Omega_\mathrm{o}}(T,K)\big|_{y^*} \cdot H_K \, \mathrm{d}x \, \mathrm{d}t \\ &+ \iint\limits_{\Omega\times(0,t_\mathrm{f})} \Lambda^* \cdot \Big[e_{\nabla\times,\nabla\times}\left(\mu^{-1}, H_K\right) - \partial_K f_\Omega(K,u)\big|_{y^*} \cdot H_K \Big] \, \mathrm{d}x \, \mathrm{d}t \\ &+ \iint\limits_{\Gamma_\mathrm{N}\times(0,t_\mathrm{f})} \Lambda^* \cdot \Big[\partial_K f_{\Gamma_\mathrm{N}}(K,u)\big|_{y^*} \cdot H_K - e_{\nabla\times}\left(\mu^{-1}, H_K\right) \Big] \, \mathrm{d}x \, \mathrm{d}t \\ &+ \iint\limits_{\Gamma_\mathrm{D}\times(0,t_\mathrm{f})} \Lambda^* \cdot e_\times\left(H_K\right) \, \mathrm{d}x \, \mathrm{d}t = 0 \qquad \forall H_K \ . \end{aligned} \tag{3.30}$$

The partial derivatives of spatial operators are formally treated similar to the derivation of the adjoint dynamics of the thermal subsystem in Section 3.4.1, i. e.,

$$\partial_K e_{\nabla\times,\nabla\times}\left(\mu^{-1}, K\right)\big|_{y^*} \cdot H_K = e_{\nabla\times,\nabla\times}\left(\mu^{-1}, H_K\right) \qquad \text{in } \Omega\times(0,t_\mathrm{f}) \tag{3.31a}$$

$$\partial_K e_{\nabla\times}\left(\mu^{-1}, K\right)\big|_{y^*} \cdot H_K = e_{\nabla\times}\left(\mu^{-1}, H_K\right) \qquad \text{on } \Gamma\times(0,t_\mathrm{f}) \tag{3.31b}$$

$$\partial_K e_\times\left(K\right)\big|_{y^*} \cdot H_K = e_\times\left(H_K\right) \qquad \text{on } \Gamma\times(0,t_\mathrm{f}) \ , \tag{3.31c}$$

also see Section 3.3.1 for a definition of the differential operators.

The spatial operators of the variational equation (3.30) that involve admissible directions H_K as arguments are submitted to proper integral identities to be able to formulate the adjoint dynamics. This applies to the parts $e_{\nabla\times,\nabla\times}\left(\mu^{-1}, H_K\right)$, $e_{\nabla\times}\left(\mu^{-1}, H_K\right)$, and $e_\times\left(H_K\right)$. To this end, the formula of partial integration

$$\int\limits_\Omega U \cdot \nabla\times V \, \mathrm{d}x = \int\limits_\Omega \nabla\times U \cdot V \, \mathrm{d}x + \int\limits_\Gamma \left(U \times n\right) \cdot V \, \mathrm{d}x \ , \tag{3.32}$$

also referred to as Green's formula [4, 130], as well as the vector identities

$$U \cdot (V \times W) = V \cdot (W \times U) = W \cdot (U \times V) \qquad \text{in } \Omega\times(0,t_\mathrm{f}) \tag{3.33a}$$

$$U \times V = -V \times U \qquad \text{in } \Omega\times(0,t_\mathrm{f}) \tag{3.33b}$$

are introduced, whereby U, V, and W denote some vectors, see, e. g., [57].

Applying the formula of partial integration (3.32) twice as well as the vector identities (3.33) to the part $e_{\nabla\times,\nabla\times}\left(\mu^{-1}, H_K\right)$ yields the integral identity

$$\iint\limits_{\Omega\times(0,t_\mathrm{f})} \Lambda^* \cdot e_{\nabla\times,\nabla\times}\left(\mu^{-1}, H_K\right) \,\mathrm{d}x\,\mathrm{d}t = \iint\limits_{\Omega\times(0,t_\mathrm{f})} e_{\nabla\times,\nabla\times}\left(\mu^{-1}, \Lambda^*\right) \cdot H_K \,\mathrm{d}x\,\mathrm{d}t - \iint\limits_{\Gamma\times(0,t_\mathrm{f})} e_{\nabla\times}\left(\mu^{-1}, \Lambda^*\right) \cdot H_K \,\mathrm{d}x\,\mathrm{d}t + \iint\limits_{\Gamma\times(0,t_\mathrm{f})} \Lambda^* \cdot e_{\nabla\times}\left(\mu^{-1}, H_K\right) \,\mathrm{d}x\,\mathrm{d}t \;, \quad (3.34)$$

which is also referred to as the vector analogue of Green's second identity [130]. Using the integral identity (3.34), the admissible directions H_K of the spatial operator $e_{\nabla\times,\nabla\times}\left(\mu^{-1}, H_K\right)$ can be shifted to the adjoint state Λ. The last part of the integral identity (3.34) also cancels out the spatial operator $e_{\nabla\times}\left(\mu^{-1}, H_K\right)$ within the variational equation (3.30). The vector identity (3.33a) is used to replace the admissible directions H_K with the adjoint state Λ within the part $e_\times\left(H_K\right)$, i. e., the reformulation

$$\iint\limits_{\Gamma_\mathrm{D}\times(0,t_\mathrm{f})} \Lambda^* \cdot e_\times\left(H_K\right) \,\mathrm{d}x\,\mathrm{d}t = -\iint\limits_{\Gamma_\mathrm{D}\times(0,t_\mathrm{f})} e_\times\left(\Lambda^*\right) \cdot H_K \,\mathrm{d}x\,\mathrm{d}t \quad (3.35)$$

holds true in a distributional manner.

The integral identities (3.34)–(3.35) facilitate to reformulate the variational equation (3.30) into the equivalent counterpart

$$\left.\frac{\partial \mathcal{L}}{\partial K}\right|_{y^*} \cdot H_K = \iint\limits_{\Omega\times(0,t_\mathrm{f})} \left[e_{\nabla\times,\nabla\times}\left(\mu^{-1}, \Lambda^*\right) - \partial_K f_\Omega(K,u)\big|_{y^*} \cdot \Lambda^* - \chi_{\Omega_\mathrm{o}} p^* \,\partial_K f_{\Omega_\mathrm{o}}(T,K)\big|_{y^*}\right] \cdot H_K \,\mathrm{d}x\,\mathrm{d}t + \iint\limits_{\Gamma_\mathrm{N}\times(0,t_\mathrm{f})} \left[\partial_K f_{\Gamma_\mathrm{N}}(K,u)\big|_{y^*} \cdot \Lambda^* - e_{\nabla\times}\left(\mu^{-1}, \Lambda^*\right)\right] \cdot H_K \,\mathrm{d}x\,\mathrm{d}t - \iint\limits_{\Gamma_\mathrm{D}\times(0,t_\mathrm{f})} e_\times\left(\Lambda^*\right) \cdot H_K \,\mathrm{d}x\,\mathrm{d}t = 0 \qquad \forall H_K \;, \quad (3.36)$$

whereby the characteristic function χ_{Ω_o} is introduced for the sake of compactness, cf. Equation (2.16). Similar to the procedure in Section 3.4.1, the variational equation (3.36) facilitates the formulation of the adjoint PDE system

$$e_{\nabla\times,\nabla\times}\left(\mu^{-1}, \Lambda^*\right) - \partial_K f_\Omega(K,u)\big|_{y^*} \cdot \Lambda^* = \chi_{\Omega_\mathrm{o}} p^* \,\partial_K f_{\Omega_\mathrm{o}}(T,K)\big|_{y^*} \qquad \text{in } \Omega\times(0,t_\mathrm{f}) \quad (3.37a)$$

$$e_{\nabla\times}\left(\mu^{-1}, \Lambda^*\right) = \partial_K f_{\Gamma_\mathrm{N}}(K,u)\big|_{y^*} \cdot \Lambda^* \qquad \text{on } \Gamma_\mathrm{N}\times(0,t_\mathrm{f}) \quad (3.37b)$$

$$e_\times\left(\Lambda^*\right) = 0 \qquad \text{on } \Gamma_\mathrm{D}\times(0,t_\mathrm{f}) \;, \quad (3.37c)$$

which eliminates the various parts of the modified directional derivative (3.36).

The first-order optimality condition (3.23b) is satisfied for all admissible directions H_K since the adjoint dynamics (3.37a) cancels out the first line of the variational equation (3.36). The Neumann boundary condition (3.37b) and the Dirichlet boundary condition (3.37c) ensure that the second and the third line vanishes for all admissible directions H_K.

3.4.3 Gradient condition for optimal control trajectory

An optimal solution of optimization problem (3.17) also requires the compliance of the first-order optimality condition (3.23c). The evaluation of this optimality condition yields the variational inequality

$$\begin{aligned}\left.\frac{\partial \mathcal{L}}{\partial u}\right|_{y^*} h_u = &\iint\limits_{\Omega\times(0,t_\mathrm{f})} \left[\partial_u l(T,u)|_{y^*} - \Lambda^* \cdot \partial_u f_\Omega(K,u)|_{y^*}\right] h_u \,\mathrm{d}x\,\mathrm{d}t \\ &\iint\limits_{\Gamma\times(0,t_\mathrm{f})} \left[\partial_u l_\Gamma(u)|_{y^*} + \Lambda^* \cdot \left(\chi_{\Gamma_\mathrm{N}}\, \partial_u f_{\Gamma_\mathrm{N}}(K,u)|_{y^*} - \chi_{\Gamma_\mathrm{D}}\, \partial_u f_{\Gamma_\mathrm{D}}(u)|_{y^*}\right)\right] h_u \,\mathrm{d}x\,\mathrm{d}t \\ &\geq 0 \quad \forall u \in \mathcal{U}_\mathrm{ad}\ , \end{aligned} \tag{3.38}$$

which can be used to define a gradient condition with respect to an optimal control trajectory u, see, e. g., [133, 62]. To simplify matters, the characteristic functions χ_{Γ_N} and χ_{Γ_D} are used to formulate the variational inequality (3.38).

In view of a time-dependent excitation of electromagnetic heating systems, the variational inequality (3.38) is used to define the reduced gradient

$$\begin{aligned} g_u = &\int\limits_\Omega \partial_u l(T,u)|_{y^*} - \Lambda^* \cdot \partial_u f_\Omega(K,u)|_{y^*} \,\mathrm{d}x \\ &+ \int\limits_\Gamma \partial_u l_\Gamma(u)|_{y^*} + \Lambda^* \cdot \left(\chi_{\Gamma_\mathrm{N}}\, \partial_u f_{\Gamma_\mathrm{N}}(K,u)|_{y^*} - \chi_{\Gamma_\mathrm{D}}\, \partial_u f_{\Gamma_\mathrm{D}}(u)|_{y^*}\right) \mathrm{d}x\ , \end{aligned} \tag{3.39}$$

also see [62, 17]. Note that the reduced gradient $g_u := g_u(T,K,u)$ is a time-dependent function, whereby its evaluation requires the numerical solution of the adjoint PDE systems (3.29) and (3.37). The reduced gradient has to comply with the conditional expression

$$g_u(t) \begin{cases} > 0 & \text{if } u^*(t) = u^- \\ = 0 & \text{if } u^*(t) \in (u^-, u^+)\ , \\ < 0 & \text{if } u^*(t) = u^+ \end{cases} \qquad \forall t \in (0, t_\mathrm{f}) \tag{3.40}$$

to take the input constraints (3.1a) into account, see, e. g., [1, 133].

As an alternative to a time-dependent control strategy, electromagnetic actuators are often excited with a constant intensity of the current or voltage source over the optimization horizon $(0, t_\mathrm{f})$. To this end, the gradient

$$\bar{g}_u = \int\limits_0^{t_\mathrm{f}} g_u \,\mathrm{d}t \tag{3.41}$$

is defined instead of its time-dependent counterpart (3.39). With respect to an optimal solution, the modified gradient $\bar{g}_u := \bar{g}_u(T,K,u)$ has also to comply with the conditional expression (3.40) but is constant over time.

3.4.4 Analysis of the optimality conditions

The optimality conditions for optimizing the electrical excitation of electromagnetic actuators are described by a set of coupled PDEs, whose structure is analyzed in the following lines. An optimal solution y^* of optimization problem (3.17) has to comply with the system dynamics $e_{\text{sys}}(T, K, u) = 0$ specified by the PDE system (3.17b)–(3.17h). In addition, an optimal solution must comply with the adjoint dynamics $e_{\text{adj}}(p, \Lambda, T, K, u) = 0$ comprising the PDE systems (3.29) and (3.37). The system dynamics and adjoint dynamics are also referred to as the canonical equations. The gradient defined by Equation (3.39), respectively by Equation (3.41), and the conditional expression (3.40) complete the optimality system of optimization problem (3.17).

The left hand sides of the system dynamics and adjoint dynamics are almost identical but differ in some algebraic signs. The canonical equations consist of the same temporal and spatial operators (3.15)–(3.16), which determine mostly the specific type of the PDE and its underlying boundary conditions. For example, the temporal and spatial operators $e_{\nabla,t}(\alpha, T)$ and $e_{\Delta}(\alpha, T)$, as occurring in the heat equation (3.17b), are also present in the adjoint counterpart (3.29a). The same applies to the left hand sides of the Neumann and Dirichlet boundary conditions (3.17c) and (3.17d), which are represented by boundary conditions of identical type in the adjoint counterparts (3.29b) and (3.29c). This structural similarity can also be observed in the electromagnetic subsystem and its adjoint dynamics. Consequently, the adjoint PDE system $e_{\text{adj}}(p, \Lambda, T, K, u) = 0$ can be numerically solved in a similar way as the system dynamics $e_{\text{sys}}(T, K, u) = 0$, if proper optimization algorithms are applied.[10]

The structural similarity of the canonical equations allows one to physically interpret the adjoint PDE system $e_{\text{adj}}(p, \Lambda, T, K, u) = 0$. To this end, the right hand sides of the adjoint dynamics are analyzed, which depend on, among other, the individual parts of the cost functional (3.17a). Additionally, the sinks and sources of the PDE system $e_{\text{sys}}(T, K, u) = 0$ that are described by the functions (3.18)–(3.19) influence the right hand sides of the adjoint dynamics. Thus, the adjoint PDE systems (3.29) and (3.37) reflect, roughly speaking, the energy that is required by the system dynamics to minimize the cost functional and to compensate existing sinks and sources. The temporal and spatial propagation of energy is represented by the left hand side of the adjoint dynamics.

3.5 Numerical solution of the optimality conditions

The following lines discuss the numerical solution of the optimality conditions of induction heating processes and hyperthermia therapy. An optimization framework is presented that combines a gradient method in MATLAB with the FEM software COMSOL MULTIPHYSICS. This allows one to outsource the numerical issues of multiphysics problems (e. g. description and discretization of complex spatial domains or numerical solution of coupled PDE systems, also see Section 2.4.4) to the FEM software.

[10] A discussion of the algorithmic treatment of the optimality conditions is the subject of Section 3.5.

3.5.1 Gradient method

The gradient method shown in Algorithm 3.1, see, for instance, [21, 1, 58, 62], is used to numerically solve optimization problem (3.17). The gradient method takes advantage of the structure of the optimality conditions from Section 3.4 comprising the system dynamics $e_{\text{sys}}(T, K, u) = 0$, the adjoint dynamics $e_{\text{adj}}(p, \Lambda, T, K, u) = 0$, and the gradient condition (3.39) and (3.40).

The separated initial and final time conditions of the canonical equations (3.17e) and (3.29d) allow for a sequential solution of the optimality conditions. Algorithm 3.1 starts with the solution of the canonical equations $e_{\text{sys}}(T, K, u^{(j)}) = 0$ and $e_{\text{adj}}(p, \Lambda, T^{(j)}, K^{(j)}, u^{(j)}) = 0$ in the steps II.i)–II.ii) after the initialization step I). Thereby, the current iteration index of the gradient method is denoted by j. The basic idea is to numerically solve the canonical equations as a function of a specific control trajectory $u^{(j)}$, generally a non-optimal one, to be able to determine the direction of steepest descent $-g_u^{(j)}$ in step II.iii).

Algorithm 3.1 Gradient method for solving optimization problem (3.17).

I. **Initialization**

i) Choice of initial control trajectory $u^{(1)}$.

ii) Select termination criterion (3.55) or (3.56) with threshold $\epsilon_u > 0$ or $\epsilon_J > 0$.

II. **Gradient iteration $j = 1, 2, \ldots$**

i) Forward integration of system dynamics $e_{\text{sys}}(T, K, u^{(j)}) = 0$ specified by PDE system (3.17b)–(3.17h) to obtain state trajectories $(T^{(j)}, K^{(j)})$.

ii) Backward integration of adjoint dynamics $e_{\text{adj}}(p, \Lambda, T^{(j)}, K^{(j)}, u^{(j)}) = 0$ specified by PDE system (3.29) and (3.37) to obtain adjoint state trajectories $(p^{(j)}, \Lambda^{(j)})$.

iii) Evaluation of gradient (3.39) to obtain direction of steepest descent $-g_u^{(j)}$.

iv) Numerical solution of line search problem

$$\alpha^{(j)} = \arg\min_{\alpha > 0} J\left(\psi_u(u^{(j)} - \alpha g_u^{(j)})\right) \tag{3.42}$$

with projection function ψ_u, cf. Equation (3.44).

v) Update of control trajectory

$$u^{(j+1)} = \psi_u(u^{(j)} - \alpha^{(j)} g_u^{(j)}) \tag{3.43}$$

following a steepest descent approach.

vi) Quit gradient method, if termination criterion (3.55) respectively (3.56) is fulfilled. Otherwise, set $j \leftarrow j + 1$ and return to step II.i).

The steps II.iv) and II.v) of Algorithm 3.1 deal with the update of the control trajectory $u^{(j)}$ following a steepest descent approach. To this end, the line search problem (3.42) is numerically solved to determine the step size in the direction of steepest descent $\alpha^{(j)}$. The projection function

$$\psi_u(u(t)) = \begin{cases} u^- & \text{if } u(t) < u^- \\ u^+ & \text{if } u(t) > u^+ \\ u(t) & \text{else} \end{cases}, \qquad \forall t \in (0, t_\mathrm{f}) \tag{3.44}$$

takes the input constraints (3.1a) into account, cf. the conditional expression (3.40) and Pontryagin's maximum principle [105].[11] An improved control trajectory $u^{(j+1)}$ can then be obtained by correcting the current one in the direction of the steepest descent $-g_u^{(j)}$, what eventually decreases the value of the cost functional (3.17a), see Equation (3.43). Figure 3.4 illustrates the individual steps of the gradient method.

Since the direction of steepest descent $-g_u^{(j)}$ depends on the numerical solution of the canonical equations $e_\mathrm{sys}(T, K, u^{(j)}) = 0$ and $e_\mathrm{adj}(p, \Lambda, T^{(j)}, K^{(j)}, u^{(j)}) = 0$ and hence on the current control trajectory $u^{(j)}$, several gradient iterations are needed to approach the optimal solution y^*. The proper determination of the step size $\alpha^{(j)}$ ensures stability of Algorithm 3.1 and guarantees convergence to at least a local minimum of optimization problem (3.17), see, e. g., [1, 62, 51].

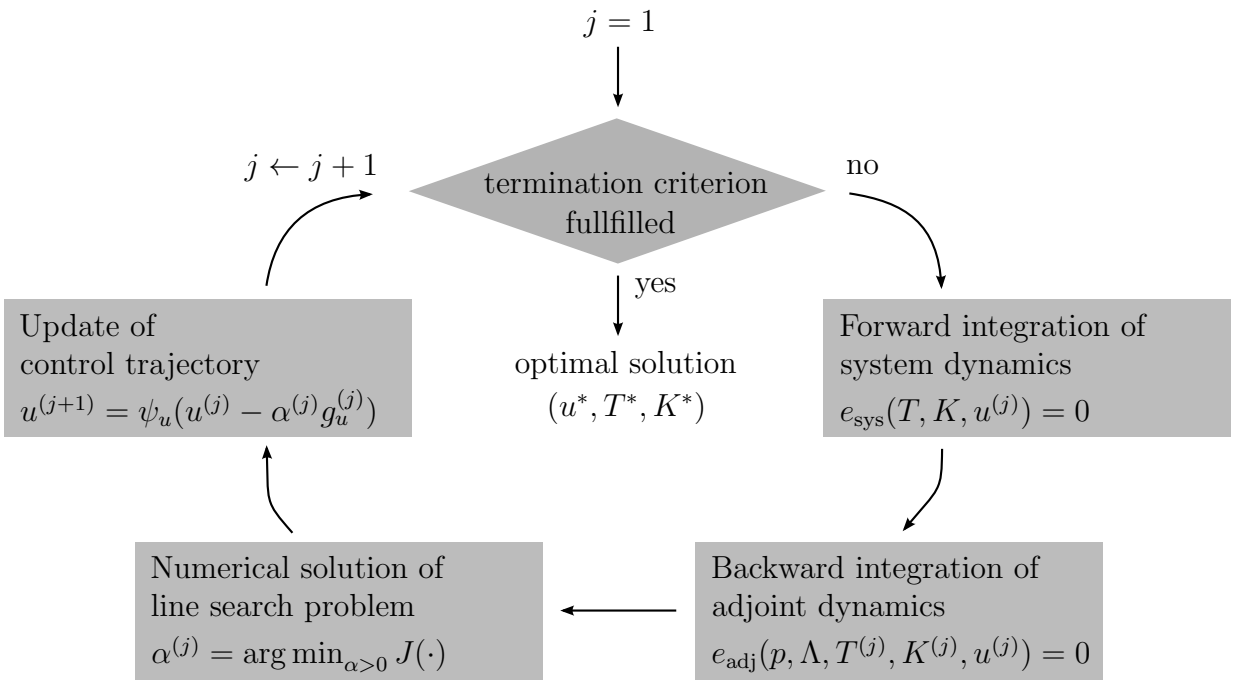

Figure 3.4: Illustration of the gradient method.

[11] In PDE constrained optimization, the applicability of Pontryagin's maximum principle has only been proven for specific problem classes such as semi-linear parabolic PDEs with boundary control [25].

Line search strategies

In order to achieve a sufficiently large decrease in the cost functional (3.17a) when updating the control trajectory $u^{(j)}$ in the direction of steepest descent $-g_u^{(j)}$, the line search problem (3.42) is numerically solved. There are two important issues with respect to numerically solving this scalar minimization problem. Firstly, the numerical solution has to be determined sufficiently accurate to satisfy convergence and stability conditions for the sequence of control and state trajectories $u^{(j)}$ and $(T^{(j)}, K^{(j)})$. Secondly, the solution of line search problem (3.42) is accompanied by a high numerical effort since each candidate of the step size α used for determining $\alpha^{(j)}$ requires the evaluation of the cost functional (3.17a). Thus, the PDE system $e_{\mathrm{sys}}(T, K, u^{(j)}) = 0$ has to be numerically solved several times.

Different types of line search strategies are known in literature, see, e. g., [74, 98]. A very simple strategy is to use a fixed step size

$$\alpha^{(j)} = \text{const.} \qquad \forall j \tag{3.45}$$

in each gradient iteration j to circumvent expensive numerical computations. However, the fixed step size has to be chosen sufficiently small to guarantee stability of Algorithm 3.1. Thus, a slow convergence behavior will be obtained in general by which the numerical effort in total increases despite the costless determination of the step size.

More sophisticated line search strategies solve the line search problem (3.42) approximately. To this end, a sequence of candidates of the step size $\alpha^{(j)}$ is tested. The Armijo rule is a typical inexact line search strategy using the update rule

$$\alpha^{(j)} = \bar{\alpha}\, 2^{-l(j)} \tag{3.46}$$

for determining the test sequence. A commonly used stopping criteria reads

$$l(j) = \min \left\{ k \in \mathbb{Z}_0 \mid J\left(T^{(j)}, u^{(j)} - \bar{\alpha} 2^{-k} \tilde{g}_u^{(j)}\right) \leq J\left(T^{(j)}, u^{(j)}\right) - \sigma\, \bar{\alpha}\, 2^{-k} \left\| \tilde{g}_u^{(j)} \right\|^2_{L_2(0,t_\mathrm{f})} \right\} \tag{3.47}$$

with the iteration index k and the parameters $\bar{\alpha} > 0$ and $\sigma \in (0, 1)$ to adapt the line search to a specific problem [74, 70]. The stopping criteria (3.47) is formulated with the projected gradient $\tilde{g}_u^{(j)}$ to take the input constraints (3.1a) into account and uses the norm

$$\|a\|^2_{L_2(0,t_\mathrm{f})} := \int_0^{t_\mathrm{f}} a^2 \, \mathrm{d}t \tag{3.48}$$

with $a := a(t)$. The initial guess of the first candidate $\alpha^{(0)}$ is successively reduced until the new iterate complies with the stopping criterion (3.47). This leads to a reduction of the cost functional in each gradient iteration j and therefore to stability of the gradient method [70]. Improved convergence properties can be achieved by applying Wolfe or Goldstein conditions, which consider a modified version of the stopping criteria (3.47), see, for instance, [98, 70, 58]. The number of required iterations for testing the stopping criteria, however, can be very large and may lead to an expensive line search.

A good trade-off between an accurate determination of the step size $\alpha^{(j)}$ and the related numerical effort can be achieved by applying an adaptive line search strategy [50, 51]. Here, the cost functional to be minimized (3.42) is evaluated at three sample points $\alpha \in \{\alpha_1, \alpha_2, \alpha_3\}$ with $\alpha_1 < \alpha_3$ and mid-point $\alpha_2 = (\alpha_1 + \alpha_3)/2$. This allows one to approximate the cost functional (3.17a) by means of a quadratic polynomial

$$J\left(\psi_u\left(u^{(j)} - \alpha g_u^{(j)}\right)\right) \approx \gamma(\alpha) = c_0 + c_1\alpha + c_2\alpha^2 \,, \qquad \alpha \in [\alpha_1, \alpha_3] \tag{3.49}$$

whose minimum can be solved analytically as $\hat{\alpha} = -c_1/(2c_2)$. The step size for updating the control trajectory according to (3.43) can then be determined as follows

$$\alpha^{(j)} = \begin{cases} \hat{\alpha} & \text{if } c_2 > 0 \text{ and } \hat{\alpha} \in [\alpha_1, \alpha_3] \\ \min\{J(\alpha_1), J(\alpha_3)\} & \text{else} \end{cases} \tag{3.50}$$

with $\min\{J(\alpha_1), J(\alpha_3)\}$ selecting the step size α_1 or α_3 which leads to a smaller value of the approximated cost functional (3.49).

To track the minimum of the approximated cost functional (3.49) for forthcoming gradient iterations, the interval $[\alpha_1, \alpha_3]$ is adapted if the step size $\alpha^{(j)}$ is close to the boundaries α_1 or α_3. The update of the interval reads as

$$[\alpha_1, \alpha_3] \leftarrow \begin{cases} \kappa[\alpha_1, \alpha_3] & \text{if } \hat{\alpha} \geq \alpha_3 - \epsilon_\alpha(\alpha_3 - \alpha_1) \text{ and } \alpha_3 \leq \alpha_{\max} \\ {}^1\!/\!_\kappa[\alpha_1, \alpha_3] & \text{if } \hat{\alpha} \leq \alpha_1 + \epsilon_\alpha(\alpha_3 - \alpha_1) \text{ and } \alpha_3 \leq \alpha_{\min} \\ [\alpha_1, \alpha_3] & \text{else} \end{cases} \tag{3.51}$$

with the adaptation factor $\kappa > 1$, the interval tolerance $\epsilon_\alpha \in (0, 1)$, and the maximal and minimal interval bounds $\alpha_{\max} > \alpha_{\min} > 0$, also see [51].

A further reduction of the computational effort for determining the step size $\alpha^{(j)}$ can be achieved by using an explicit line search strategy [10, 71]. This approach is motivated by minimizing the distance between two consecutive control trajectories $u^{(j)}$ and $u^{(j+1)}$ with the same step size $\alpha^{(j)}$ and is mathematically described as

$$\alpha^{(j)} = \arg\min_{\alpha>0} \left\| \left(u^{(j)} - \alpha g_u^{(j)}\right) - \left(u^{(j-1)} - \alpha g_u^{(j-1)}\right) \right\|^2_{L_2(0,t_\mathrm{f})} \tag{3.52a}$$

$$= \arg\min_{\alpha>0} \left\| \underbrace{\left(u^{(j)} - u^{(j-1)}\right)}_{=:\Delta u^{(j)}} - \alpha \underbrace{\left(g_u^{(j)} - g_u^{(j-1)}\right)}_{=:\Delta g_u^{(j)}} \right\|^2_{L_2(0,t_\mathrm{f})} . \tag{3.52b}$$

The function to be minimized (3.52) is used to approximate the secant equation, similar to quasi-Newton methods. A detailed analysis of (3.52) can be found in [10, 71] and eventually results in the two similar rules

$$\alpha^{(j)} = \frac{\int_0^{t_\mathrm{f}} \Delta u^{(j)} \Delta g_u^{(j)} \,\mathrm{d}t}{\int_0^{t_\mathrm{f}} \Delta g_u^{(j)} \Delta g_u^{(j)} \,\mathrm{d}t} \qquad \text{and} \qquad \alpha^{(j)} = \frac{\int_0^{t_\mathrm{f}} \Delta u^{(j)}, \Delta u^{(j)} \,\mathrm{d}t}{\int_0^{t_\mathrm{f}} \Delta u^{(j)}, \Delta g_u^{(j)} \,\mathrm{d}t} \tag{3.53}$$

for determining the step size $\alpha^{(j)}$ in explicit form. For numerical reasons, the calculated step size (3.53) is constrained to an interval

$$\alpha^{(j)} \leftarrow \min\left(\alpha_{\max}, \max\left(\alpha^{(j)}, \alpha_{\min}\right)\right) \tag{3.54}$$

specified by maximal and minimal step sizes.

The explicit line search strategy (3.53) requires only the control trajectories $(u^{(j)}, u^{(j-1)})$ and the gradients $(g_u^{(j)}, g_u^{(j-1)})$ to determine the step size $\alpha^{(j)}$ but no evaluations of the cost functional (3.17a). This leads to a very efficient line search strategy. The convergence and stability behavior of an explicit line search strategy depends on the specific problem, whereby practical use shows very good and robust results [72, 115, 39]. The choice of which of the two equations in (3.53) is used to calculate the step size $\alpha^{(j)}$ depends on the problem.

Termination criterion

There are several choices for terminating the gradient method in Algorithm 3.1, see, e. g., [74, 21, 1]. An obvious termination criterion is to check if the change of the control trajectory between two consecutive iterations is smaller than a specific value $\epsilon_u > 0$. In view of the time-dependent control trajectory, the gradient method is terminated after achieving

$$\frac{\left\|u^{(j+1)} - u^{(j)}\right\|^2_{L_2(0,t_\mathrm{f})}}{\left\|u^{(1)}\right\|^2_{L_2(0,t_\mathrm{f})}} \leq \epsilon_u \ , \tag{3.55}$$

whereby the norm $\|\cdot\|^2_{L_2(0,t_\mathrm{f})}$ is specified by Equation (3.48).

A further termination criterion can be deduced from the objective of the optimization problem to minimize the cost functional (3.17a). The demand for a sufficiently large reduction of the cost functional between two consecutive iterations can be used to terminate the gradient method after achieving

$$\frac{J^{(j+1)} - J^{(j)}}{J^{(1)}} \leq \epsilon_J \ . \tag{3.56}$$

In this case, the stopping criteria is specified by $\epsilon_J > 0$.

3.5.2 Optimization framework

The optimization framework shown in Figure 3.5 uses the software package MATLAB to implement the gradient method from Algorithm 3.1. However, the numerical solution of the canonical equations $e_{\mathrm{sys}}(T, K, u) = 0$ and $e_{\mathrm{adj}}(p, \Lambda, T, K, u) = 0$ in step II.i) and II.ii) is outsourced to the FEM software COMSOL MULTIPHYSICS. This makes it possible to separate the numerical issues of the trajectory planning of electromagnetic heating systems from the algorithmic ones. The FEM software provides the simulation results to MATLAB, which allows one to both numerically solve the line search problem (3.42) and perform the control update (3.43) with relative ease.

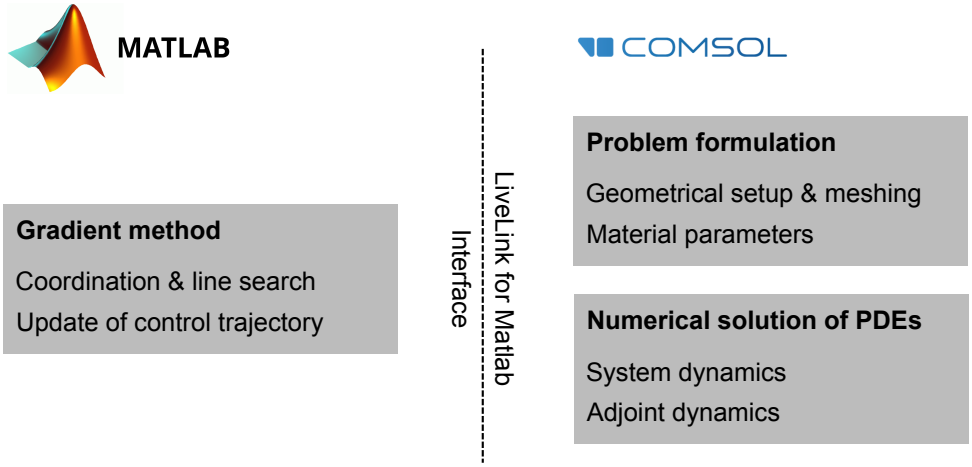

Figure 3.5: Optimization framework for solving optimization problem (3.17).

The canonical equations $e_{\text{sys}}(T, K, u) = 0$ and $e_{\text{adj}}(p, \Lambda, T, K, u) = 0$ are represented in COMSOL MULTIPHYSICS by means of their weak formulations using the PHYSICSBUILDER module, cf. Section 2.4.1–2.4.2. The COMSOL module LIVELINK FOR MATLAB is applied to establish a software interface between MATLAB and COMSOL, cf. Figure 3.5. This makes it possible to start the forward and backward integrations of the canonical equations as well as to provide their simulation results for the line search and control update within MATLAB. The control trajectory $u^{(j)}$ is written to an ASCII file at the beginning of each gradient iteration to synchronize the workspaces of MATLAB and COMSOL.

The optimization framework separates the challenging task of numerically solving the canonical equations from the algorithmic treatment of the optimality conditions. This allows one, among others, to benefit from extensive modeling capabilities of the FEM software. The enclosed CAD tools simplify the description of the geometrical setup of a specific problem, cf. Figure 3.5. Furthermore, the FEM software offers the possibility to import geometrical setups from third-party CAD software or from magnetic resonance imaging systems (MRI – *Magnetic Resonance Imaging*).

A further advantage of the optimization framework concerns the application of state-of-the-art FEM techniques to numerically solve the canonical equations. This also applies to the generation of meshes for complex geometries and to the choice of suitable classes of basis and test functions for discretizing the weak formulations of PDEs. The weak formulations can be transformed into finite-dimensional counterparts without leading to significant discretization errors. In addition, the FEM software provides well-developed time stepping algorithms of explicit and implicit type to numerically solve the discretized canonical equations.

In conclusion, the primary benefit of the optimization framework consists in the interaction of MATLAB and COMSOL MULTIPHYSICS to cope with the trajectory planning of electromagnetic heating problems including complex geometries. The specification of the cost functional allows one to handle different control tasks such as preheating for forging and thixoforming operations or surface hardening processes in the case of induction heating. The optimization framework also facilitates to cope with various kinds of hyperthermia therapy.

3.6 Numerical results

The optimization of the electrical excitation of electromagnetic actuators is presented in simulation studies for induction heating processes and hyperthermia therapy. The spatial domains of the application examples range from axisymmetrical setups to three-dimensional ones involving complex structures. The numerical results of the trajectory planning verify the applicability of the optimality conditions as derived in Section 3.4.

3.6.1 Constant heat-up process of a gear wheel

The first simulation study applies the trajectory planning approach to a constant heat-up process of a gear wheel made of steel (high tensile steel, EN steel name 34CrNiMo6) with 16 teeth, cf. Figure 3.6. The outside diameter of the gear wheel $d_1 = 38\,\mathrm{mm}$ is measured from the tops of the teeth, its root diameter $d_2 = 32\,\mathrm{mm}$ from the base of the teeth. The inner and outer diameter of the inductor is $d_3 = 44\,\mathrm{mm}$ and $d_4 = 54\,\mathrm{mm}$. The spatial dimensions result in a minimal air gap between inductor boundary and workpiece of $r_{\mathrm{ag}} = 3\,\mathrm{mm}$. The ambient air is modeled by a sphere with diameter $d_5 = 1\,\mathrm{m}$.

The amplitude of the impressed currents within the inductor with cross section surface $A_{\mathrm{c}} = 2.5\pi \cdot 10^{-5}\,\mathrm{m}^2$ and coil windings $N_{\mathrm{c}} = 100$ is described by the control trajectory u serving as the optimization variable. The inductor current is bounded by $[0\,\mathrm{A}, 200\,\mathrm{A}]$ in terms of the input constraints (3.1a). The angular frequency of the sinusoidal excitation of the inductor

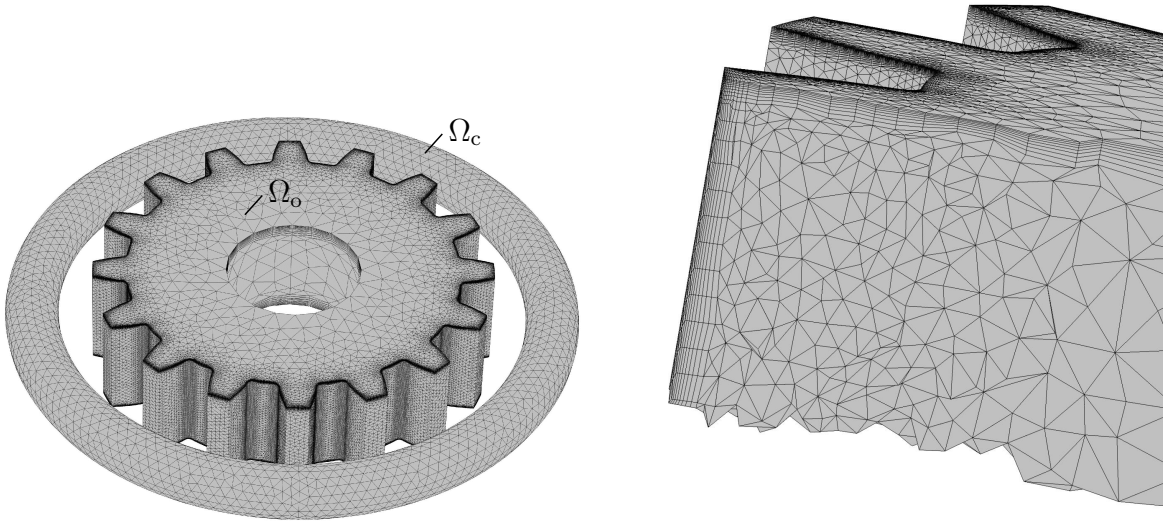

(a) Gear wheel and inductor

(b) Detail view of gear wheel

Figure 3.6: Geometrical setup of the constant heat-up process with discretized spatial domain of the gear wheel Ω_{o} and inductor Ω_{c}. The boundary layers of the gear wheel are covered by much finer finite elements to numerically resolve the highly uneven spatial distribution of the heat source due to distortion effects of the electromagnetic field.

Table 3.1: Material parameters of the heat-up process of the gear wheel.

	gear wheel Ω_o	inductor Ω_c	air Ω_a	
rel. magnetic permeability μ_r	200	1	1	$[-]$
electrical conductivity σ	$5.26 \cdot 10^6$	10^2	10^2	[S/m]
density ρ	$7.85 \cdot 10^3$	-	-	$[\mathrm{kg/m^3}]$
heat capacity C	460	-	-	$[\mathrm{J/(kg\,K)}]$
thermal conductivity k	42	-	-	$[\mathrm{W/(m\,K)}]$
heat transfer coefficient α	7.9	-	-	$[\mathrm{W/(m^2\,K)}]$
emissivity of the surface ϵ	0.5	-	-	$[-]$

is $\omega = 1\,\mathrm{kHz}$. The material parameters of the thermal and electromagnetic subsystem are shown in Table 3.1. For numerical reasons, the electrical conductivity of the spatial domain of the inductor Ω_c and air Ω_a is set to a value greater than zero.

The cost functional (3.17a) is specified by the Mayer and Lagrange terms (3.7). The primary objective of the trajectory planning consists in heating up the gear wheel to the desired temperature $T_\mathrm{d} = 773\,\mathrm{K}$ as it is typically the case for annealing or stress relieving processes.[12] The corresponding weights of the Mayer and Lagrange terms are set to $q_1 = 10^2$ and $q_2 = 10^6$. The temperature of the gear wheel is bounded by $T^+ = 853\,\mathrm{K}$. To incorporate the state constraint $T \leq T^+$ for the trajectory planning, the outer penalty function in the Lagrange term (3.7b) is weighted by $q_3 = 10^9$. The control action u^2 is weighted by $q_4 = 10^3$. Table 3.2 gives an overview of the weights. The right hand sides of the thermal and electromagnetic subsystem (3.17b)–(3.17e) and (3.17f)–(3.17h) are specified as follows

$$f_{\Omega_\mathrm{o}}(T, A) = \tfrac{\sigma\omega^2}{2}|A|^2 \qquad \text{in } \Omega_\mathrm{o} \times (0, t_\mathrm{f}) \tag{3.57a}$$

$$f_{\Gamma_\mathrm{o,N}}(T) = \alpha\,(T_\mathrm{a} - T) + \epsilon\sigma_\mathrm{SB}\left(T_\mathrm{a}^4 - T^4\right) \qquad \text{on } \Gamma_\mathrm{o,N} \times (0, t_\mathrm{f}) \tag{3.57b}$$

$$f_\Omega(A, u) = \tfrac{N_\mathrm{c}}{A_\mathrm{c}} u \chi_{\Omega_\mathrm{c}} e_\mathrm{c} - j\omega\sigma A \qquad \text{in } \Omega \times (0, t_\mathrm{f}) \tag{3.57c}$$

$$f_{\Gamma_\mathrm{D}}(u) = 0 \qquad \text{on } \Gamma_\mathrm{D} \times (0, t_\mathrm{f})\ . \tag{3.57d}$$

The geometrical setup of the gear wheel neither takes into account symmetry planes for the thermal nor for the electromagnetic subsystem to demonstrate the ability of the optimization framework to handle large scale problems.[13] The region of interest $\Omega = \Omega_\mathrm{o} \cup \Omega_\mathrm{c} \cup \Omega_\mathrm{a}$ is covered by finite elements as shown in Figure 3.6b for a detail view of the gear wheel. The boundary layers of the gear wheel are discretized much finer. This allows one to accurately represent the distortion effects of the electromagnetic field such as the skin, end, and edge effect.

The numerical solution of the trajectory planning problem specified above is provided by the optimization framework from Section 3.5. Thereby, the explicit line search strategy (3.53) is used for updating the optimization variable u in each gradient iteration, cf. Algorithm 3.1. The threshold of the termination criterion (3.55) is set to $\epsilon_u = 10^{-6}$.

[12] The initial temperature of the gear wheel T_0 is specified by the ambient temperature $T_\mathrm{a} = 293\,\mathrm{K}$.
[13] A problem setting that accounts for symmetry planes is presented in [114].

Table 3.2: Weights of the Mayer and Lagrange term (3.7) for heating up the gear wheel.

weight	objective
$q_1 = 10^2$	minimization of state error $(T - T_\mathrm{d})^2$ in Ω_o (Mayer term)
$q_2 = 10^6$	minimization of state error $(T - T_\mathrm{d})^2$ in Ω_o (Lagrange term)
$q_3 = 10^9$	violation of state constraint $T \leq T^+$ in Ω_o (Lagrange term)
$q_4 = 10^3$	penalization of control action u^2 in Ω_c (Lagrange term)

As can be seen in Figure 3.7, the numerical solution of optimization problem (3.17) leads to the desired heat-up of the gear wheel by accounting for the input and state constraints (3.1). The control trajectory u harmonizes the average temperature of the gear wheel $T_\mathrm{avg}(t)$ with the desired temperature $T_\mathrm{d} = 773\,\mathrm{K}$. Moreover, the maximum temperature of the gear wheel $T_\mathrm{max}(t)$ does not significantly violate the constraint $T^+ = 853\,\mathrm{K}$. The relatively slow heat-up behavior of the gear wheel, represented in Figure 3.7 by the minimum temperature $T_\mathrm{min}(t)$, stems from the concentration of the heat source to boundary layers caused by the skin effect, cf. Figure 3.8. Consequently, the dynamically slower process of heat conduction is necessary to heat up inner domains of the gear wheel.

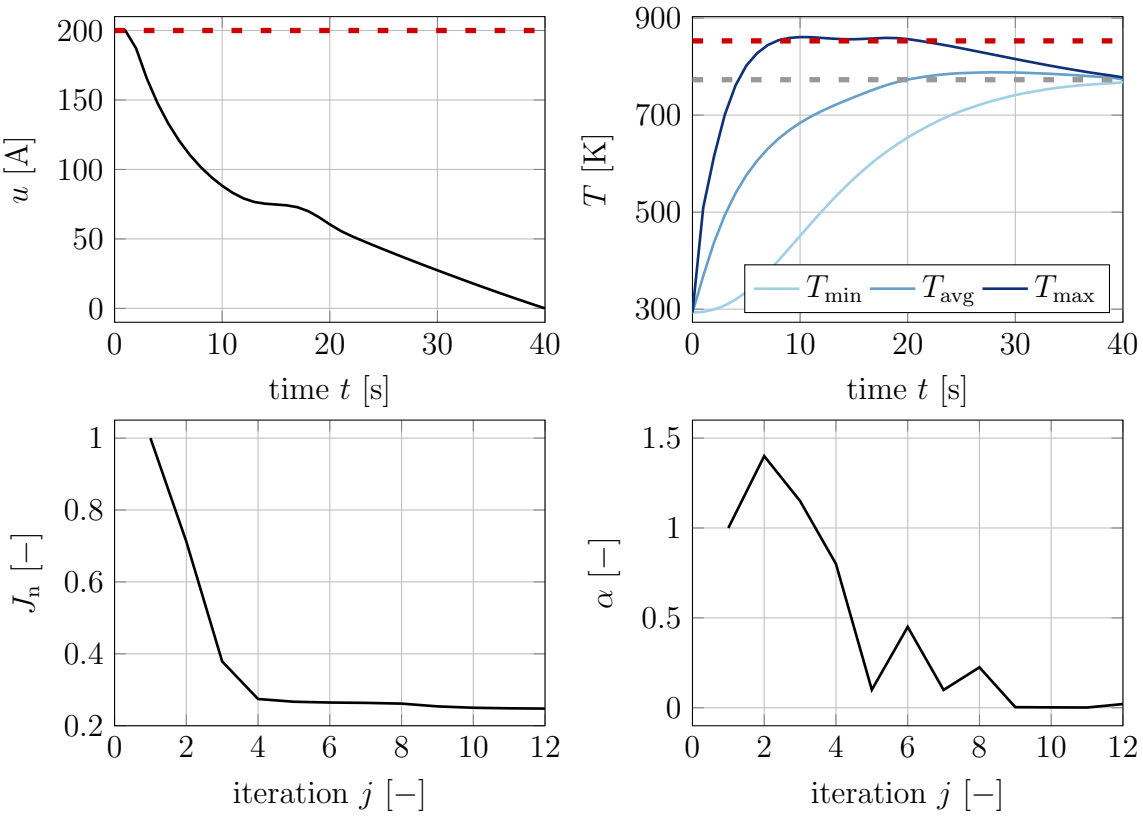

Figure 3.7: Control trajectory u and minimum T_min, average T_avg, and maximum temperature T_max of the gear wheel. The normalized cost functional J_n and the step size α during the gradient iterations show the fast convergence behavior of Algorithm 3.1.

Figure 3.7 also shows the fast convergence of Algorithm 3.1 to the optimal solution by means of the normalized cost functional

$$J_{\mathrm{n}}^{(j)} = \frac{J^{(j)}}{J^{(1)}} \tag{3.58}$$

and the step size $\alpha^{(j)}$ during the gradient iterations j. It can be observed that $j = 10$ gradient iterations are already sufficient to achieve a good control performance and that the optimization framework is capable to deal with the large scale problem. The average required CPU time for one gradient iteration is 19 h, whereby the canonical equations $e_{\mathrm{sys}}(T, A, u) = 0$ and $e_{\mathrm{adj}}(p, \Lambda, T, K, u) = 0$ are discretized by $2.5 \cdot 10^7$ degrees of freedom within the region of interest Ω, cf. Figure 3.6.[14]

Figure 3.8 shows the electromagnetic heat source of the gear wheel at the time instant $t = 0\,\mathrm{s}$. The end and edge effects in combination with the skin effect cause the heat source to be unevenly distributed along the surface layer of the gear wheel. As a result, local areas of the workpiece tend to overheat. Nevertheless, the optimized control trajectory u guarantees that the trajectories of the minimum, average, and maximum temperature of the gear wheel reach the desired temperature T_{d} as fast as possible, while complying with the formulated input and state constraints, cf. Figure 3.7.

The uneven spatial distribution of the electromagnetic heat source results in local hot spots of the temperature of the gear wheel as can be seen in Figure 3.9 for selected time instants of the heat-up process. However, the trajectory planning approach adjusts the intensity of the electromagnetic heat source in a way that the temperature of the gear wheel does not excessively violate the state constraint (3.1b), cf. Figure 3.7. Indeed, the control trajectory u adapts the intensity of the heat source to the current temperature and diffusive heat propagation effects to heat up the gear wheel in an optimal manner.

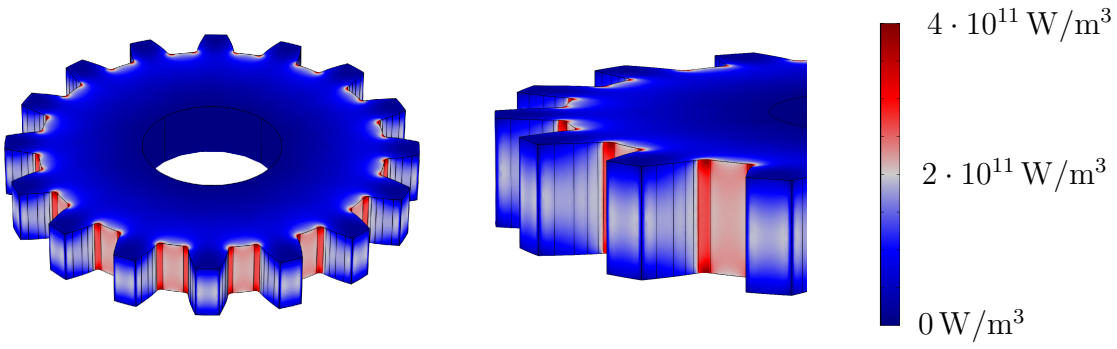

Figure 3.8: Electromagnetic heat source of the gear wheel $\frac{\sigma\omega^2}{2}|A|^2$ at time instant $t = 0\,\mathrm{s}$.

[14] In this thesis, the simulation studies are carried out on an Intel Core i7-7700 processor with 3.6 GHz and 64 GB RAM.

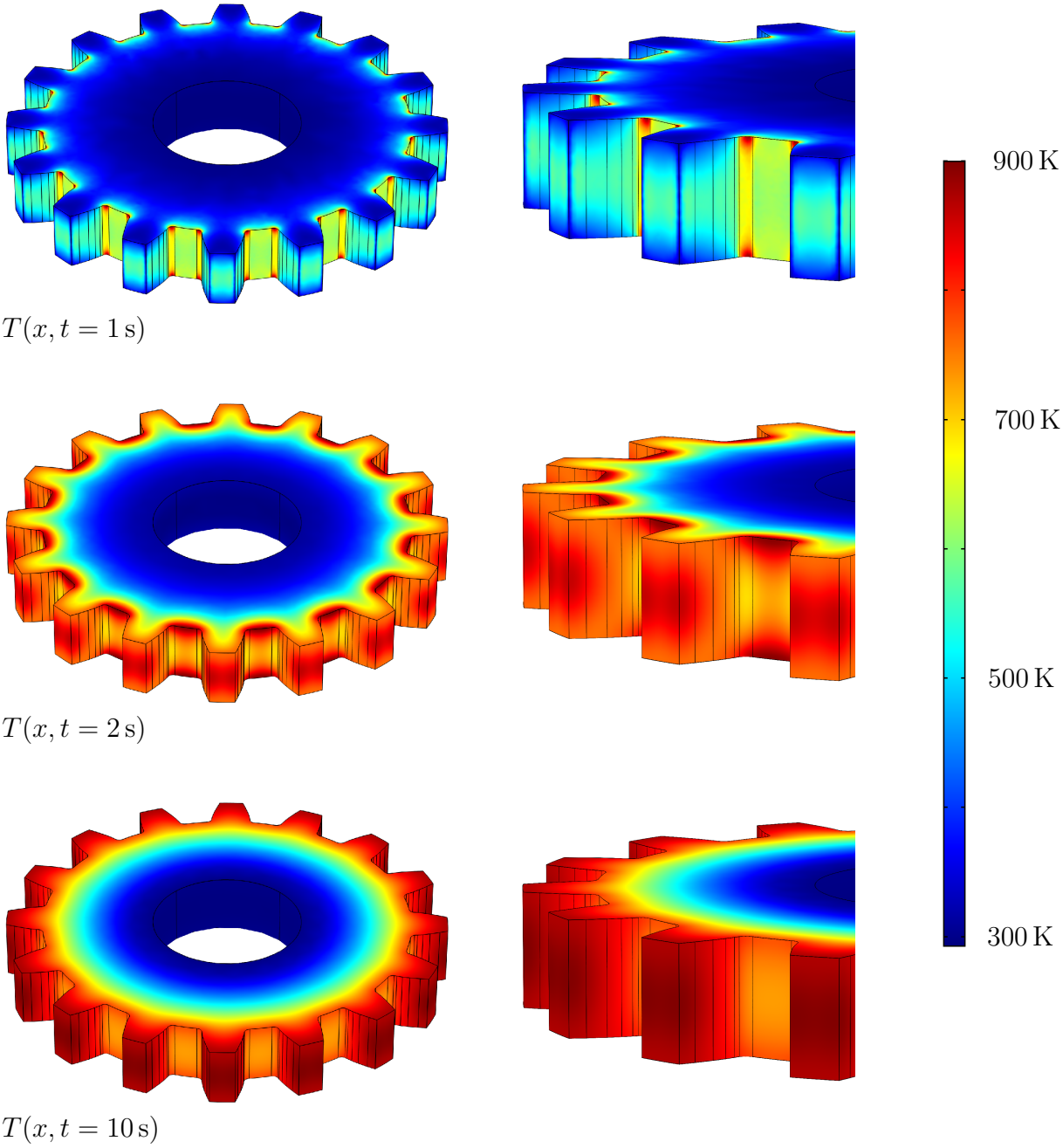

Figure 3.9: Temperature profiles of the gear wheel T at $t \in \{1\,\mathrm{s}, 2\,\mathrm{s}, 10\,\mathrm{s}\}$.

3.6.2 Surface hardening process of an axisymmetrical workpiece

The trajectory planning approach is presented in a second simulation study for the surface hardening process from Figure 3.10. The considered scenario consists of heating up the surface layer $\tilde{\Omega}_\mathrm{o}$ from the initial temperature $T_0 = 293\,\mathrm{K}$ to the desired temperature $T_\mathrm{d} = 1023\,\mathrm{K}$ as homogeneously as possible. The bounds of the inductor current u and workpiece temperature T are specified by $[0\,\mathrm{A}, 30\,\mathrm{A}]$ and $T^+ = 1173\,\mathrm{K}$.

The material parameters for a workpiece made of low-carbon steel (EN steel name C18D) are shown in Table 3.3. Similar to the heat-up process of the gear wheel, the trajectory planning relies on the numerical solution of optimization problem (3.17). The right hand sides of the thermal and electromagnetic subsystem (3.17b)–(3.17h) are specified by Equation (3.57). The direction of the flow of currents within the inductor is described by $e_\varphi = [0, 1, 0]^\mathsf{T}$. Note that the surface hardening process is modeled using an axisymmetrical setup with spatial coordinates $x = [r, \varphi, z]^\mathsf{T}$.

In order to be able to heat up the surface layer without increasing the temperature of inner domains too much, the angular frequency of the impressed currents u is set to $\omega = 50\,\mathrm{kHz}$, which is much higher compared to the previous constant heat-up process. In addition, the time period of the heat-up process is shortened to $t_\mathrm{f} = 6\,\mathrm{s}$ to alleviate the propagation of heat from the surface layer to inner domains of the workpiece. The most important dimensions of the workpiece are the radii $r_1 = 20\,\mathrm{mm}$ and $r_2 = 40\,\mathrm{mm}$ as well as the lengths $z_1 = 70\,\mathrm{mm}$ and $z_2 = 50\,\mathrm{mm}$. The depth of the surface layer is $\delta = 4\,\mathrm{mm}$. The electromagnetic heat source is generated by six inductors with spatial domain $\Omega_\mathrm{c} = \cup\,\Omega_{\mathrm{c}_j},\ j \in \{1, 2, \ldots, 6\}$.

An obvious choice for the actuator configuration to generate the electromagnetic heat source predominantly within the surface layer is to place the inductors equidistantly along the corresponding segment in the direction of z, cf. Figure 3.10a. The air gap between the boundary of the individual inductors and workpiece is chosen as $r_\mathrm{ag} = 5\,\mathrm{mm}$. The cross

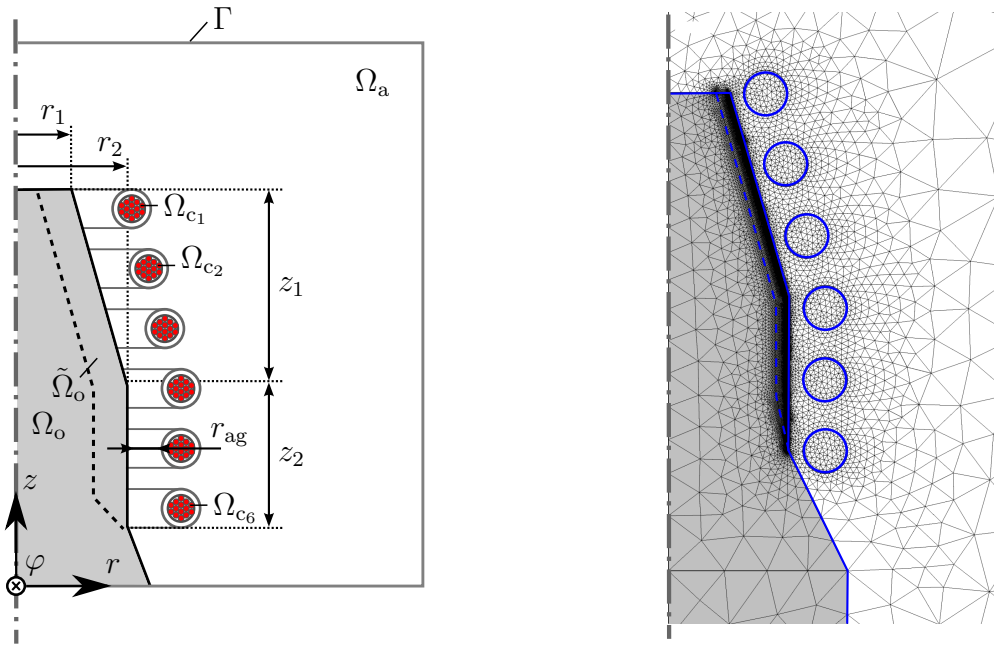

(a) Geometrical setup (not to scale)

(b) Meshed spatial domain (detail view)

Figure 3.10: Geometrical setup of the surface hardening process with axisymmetrical workpiece Ω_o and inductors $\Omega_{\mathrm{c}_j},\ j \in \{1, 2, \ldots, 6\}$. The mesh as used for numerically solving the optimality conditions is adapted to the skin, end, and edge effects.

Table 3.3: Material parameters of the surface hardening process.

	workpiece Ω_o	inductor Ω_c	air Ω_a	
rel. magnetic permeability μ_r	100	1	1	[−]
electrical conductivity σ	$6.29 \cdot 10^6$	0	0	[S/m]
density ρ	$7.78 \cdot 10^3$	-	-	[kg/m^3]
heat capacity C	486	-	-	[J/(kg K)]
thermal conductivity k	51.9	-	-	[W/(m K)]
heat transfer coefficient α	1.54	-	-	[W/(m^2 K)]
emissivity of the surface ϵ	0.75	-	-	[−]

section surface and the coil windings of each inductor is $A_\mathrm{c} = 7.5^2\,\pi\,10^{-6}\,\mathrm{m}^2$ and $N_\mathrm{c} = 75$. The ambient air is described by a rectangle with length $r = 1\,\mathrm{m}$ and height $h = 2\,\mathrm{m}$. Figure 3.10b shows a detail view of the discretized spatial domain Ω as used for numerically solving optimization problem (3.17).

The optimization framework from Figure 3.5 uses the adaptive line search strategy to approximately solve the line search problem (3.42), cf. Section 3.5.1. The cost functional of optimization problem (3.17) is specified by the Mayer and Lagrange terms (3.7) with the weights shown in Table 3.4. The gradient method uses termination criterion (3.55) with bound $\epsilon_u = 10^{-9}$ to quit Algorithm 3.1.

Table 3.4: Weights of the Mayer and Lagrange terms (3.7) for the surface hardening process.

weight	objective
$q_1 = 10^1$	minimiz. of state error $(T - T_\mathrm{d})^2$ in surface layer $\tilde{\Omega}_\mathrm{o}$ (Mayer term)
$q_2 = 10^4$	minimiz. of state error $(T - T_\mathrm{d})^2$ in surface layer $\tilde{\Omega}_\mathrm{o}$ (Lagrange term)
$q_3 = 10^8$	violation of state constraint $T \leq T^+$ in Ω_o (Lagrange term)
$q_4 = 10^1$	penalization of control action u^2 in Ω_c (Lagrange term)

The optimized control trajectory u and the resulting trajectories of the minimum $\tilde{T}_\mathrm{min}(t)$, average $\tilde{T}_\mathrm{avg}(\mathrm{t})$, and maximum temperature $\tilde{T}_\mathrm{max}(t)$ within the surface layer $\tilde{\Omega}_\mathrm{o}$ are shown in Figure 3.11. The difference between the desired temperature T_d and the temperature in the surface layer $\tilde{\Omega}_\mathrm{o}$ is minimized in a quadratic manner. Moreover, the optimized control trajectory ensures the compliance of the state constraint $T \leq T^+$ with bound $T^+ = 1173\,\mathrm{K}$ according to the outer penalty function approach.

Figure 3.11 also shows the directions of steepest descent $-g_u^{(j)}$ during the gradient iterations. With respect to an optimal solution, the gradient $g_u^{(j)}$ converges over the entire time interval to zero except for the first 2.4 s where the control trajectory u hits its upper bound, cf. the conditional expression (3.40). The fast convergence of Algorithm 3.1 to the optimal solution is illustrated in Figure 3.11 by means of the normalized cost functional (3.58) during the

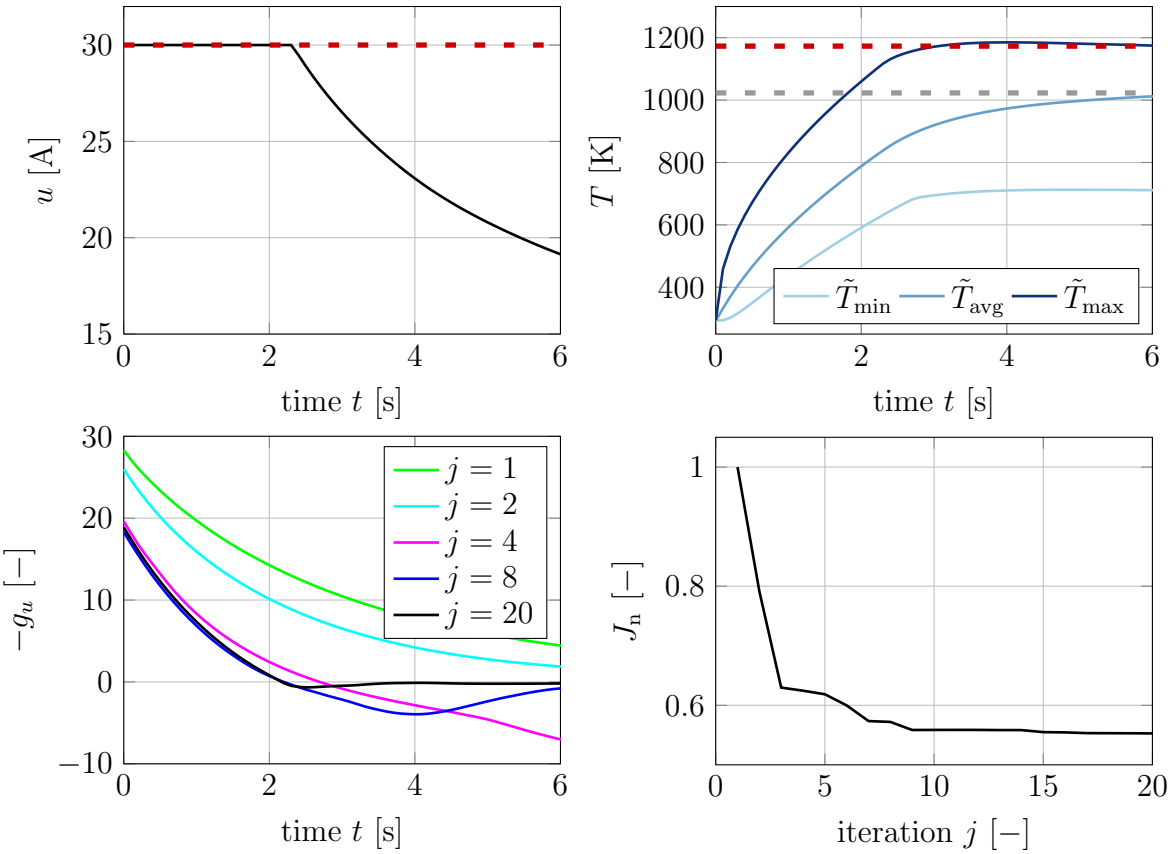

Figure 3.11: Control trajectory u that leads to an optimal heat-up behavior of the surface layer with minimum $\tilde{T}_{\min}$, average $\tilde{T}_{\text{avg}}$, and maximum temperature $\tilde{T}_{\max}$. The normalized cost functional J_{n} reveals the fast convergence behavior of Algorithm 3.1.

gradient iterations. Thereby, already $j = 16$ gradient iterations are sufficient to achieve a good control performance. Note that the number of gradient iterations can be reduced to $j = 10$ without downgrading the control performance too much.

The formulated state constraint $T \leq T^{+}$ in combination with the inhomogeneous distribution of the electromagnetic heat source prevents a complete heat-up of the surface layer to the desired temperature $T_{\text{d}} = 1023\,\text{K}$, cf. Figure 3.11. However, the intensity of the electromagnetic heat source is continuously decreased by the control trajectory u to ensure that the heat transfer due to diffusion heats up the surface layer as good as possible to the desired temperature without violating the state constraint too much.

The very pronounced end and edge effects leading to the inhomogeneous distribution of the electromagnetic heat source can be observed in the temperature profiles of the workpiece in Figure 3.12. Especially the temperature profile at the time instant $t = 2\,\text{s}$ reveals the highly non-uniform heat source within the surface layer by means of pronounced hot spots of the temperature. The temperature profiles also reflect the optimal heat-up behavior of the surface layer to the desired temperature $T_{\text{d}} = 1023\,\text{K}$. The inevitable heat-up of inner

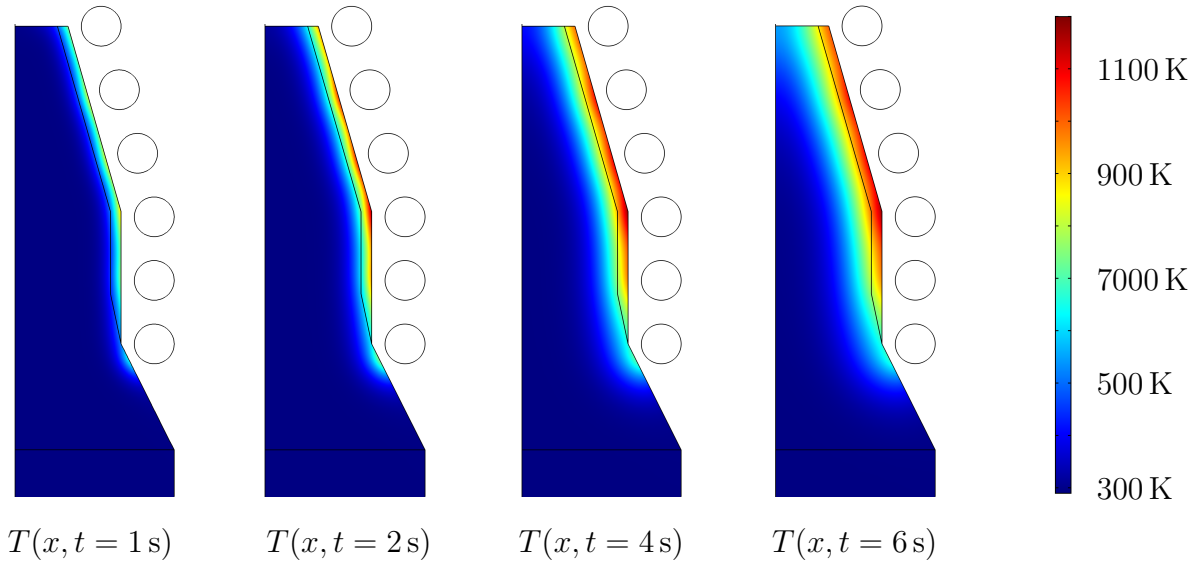

Figure 3.12: Temperature profiles T during the surface hardening process satisfying the state constraint despite the pronounced end and edge effects leading to local hot spots.

domains of the workpiece is less pronounced and does not appear significantly until the very end of the heat-up process. The local hot spots of the temperature at the end and edge area of the surface layer are permanently kept in the range of the state constraint, also see Figure 3.11. This clarifies the optimal control strategy to heat up the surface layer as fast as possible.

In conclusion, the optimization framework from Section 3.5.2 provides optimal trajectories for the surface hardening process by taking the formulated state and input constraints into account. The 2D model in cylindrical coordinates allows for a numerical efficient solution of the associated optimization problem, whereby the canonical equations are discretized by $2.74 \cdot 10^5$ degrees of freedom within the region of interest Ω, cf. Figure 3.10b. The average required CPU time for one gradient iteration is approximately 20 min.

3.6.3 Microwave ablation for interstitial hyperthermia therapy

The optimization-based trajectory planning approach is also demonstrated for interstitial hyperthermia therapy. The simulation scenario in the following lines concerns MWA for a tumor Ω_t that is located in the region of the liver Ω_h, cf. Figure 3.2a and 3.13a. A serious damage of the tumor due to temperature-dependent necrosis effects is enforced by the electromagnetic heat source arising from an electrode with spatial domain Ω_c. The degree of freedom for the trajectory planning is the boundary controlled voltage source u of the electrode. The problem settings of hyperthermia therapy correspond to [99, 112]. Numerical results for the optimal trajectory planning in the case of RFA are presented in [112].

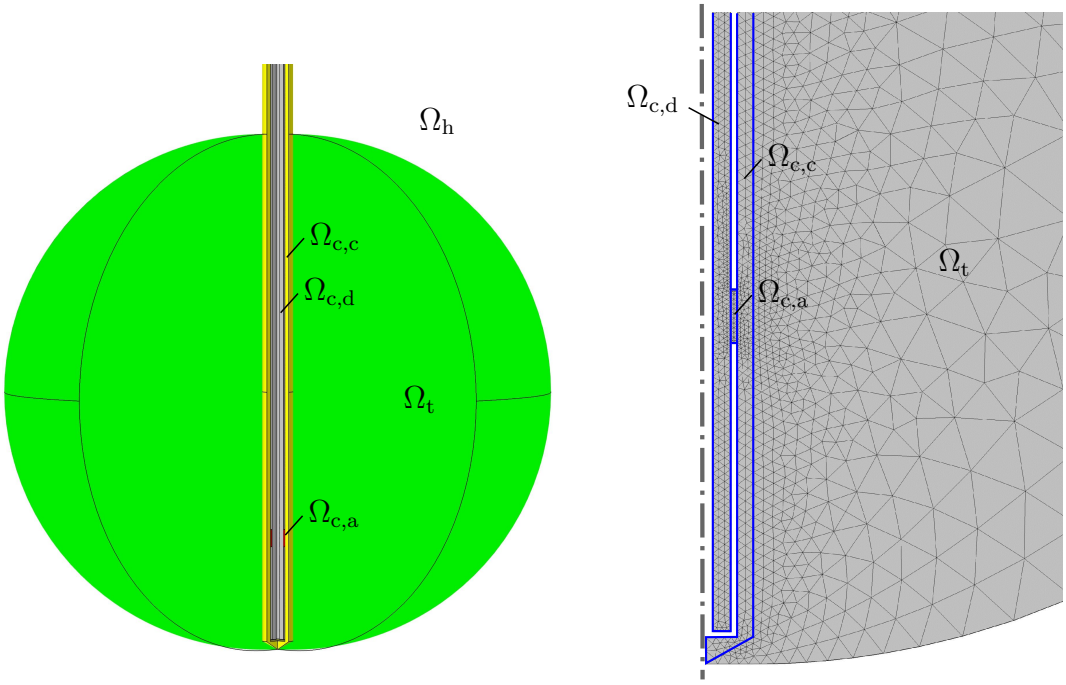

(a) Tumor with electrode (b) Detail view of tumor and electrode

Figure 3.13: MWA setup with tumor Ω_t and liver Ω_h. The electrode for generating the heat source consists of the dielectric $\Omega_{c,d}$, the catheter $\Omega_{c,c}$, and the air gap $\Omega_{c,a}$.

The electromagnetic and thermal phenomena of MWA are taken into account in the spatial domain $\Omega = \Omega_t \cup \Omega_h$. A sufficiently precise prediction of the system dynamics is obtained by means of the PDE system (3.10) and the material parameters shown in Table 3.5. The differential operators defined in Section 3.3.1 are used to formulate the corresponding optimization problem. The angular frequency of MWA is set to $\omega = 2\pi \cdot 2.45\,\mathrm{GHz}$, see, e. g., [44]. The control trajectory u is bounded by $[0\,\mathrm{V}, 40\,\mathrm{V}]$.

Table 3.5: Material parameters of the thermal and electromagnetic subsystem of MWA.

	dielectric $\Omega_{c,d}$	air gap $\Omega_{c,a}$	catheter $\Omega_{c,c}$	tumor, liver $\Omega_t \cup \Omega_h$	
rel. magnetic permeability μ_r	1	1	1	1	-
rel. electric permittivity ϵ_r	2.03	1	2.6	43.03	-
electrical conductivity σ	0	1	0	1.69	S/m
density (of blood) ρ/ρ_b	-	-	-	$1.1/1.0 \cdot 10^3$	$\mathrm{kg/m^3}$
heat capacity (of blood) C/C_b	-	-	-	$3.5/3.6 \cdot 10^3$	$\mathrm{J/(kg\,K)}$
thermal conductivity k	-	-	-	0.56	$\mathrm{W/(m\,K)}$
perfusion rate ω_b	-	-	-	$3.6 \cdot 10^{-3}$	1/s

The axisymmetrical setup of MWA is shown in Figure 3.13a. The electrode is sticked directly into the spatial domain of the tumor assuming spherical shape and a diameter of 3 cm. The discretization of the spatial domain around the air gap of the electrode by finite elements is shown in Figure 3.13b. The fineness of the mesh ensures an accurate representation of the propagation effects of the electromagnetic field in the electrode and of the electromagnetic heat source in the tumor.

To achieve a complete destruction of the tumor, its temperature has to exceed $T_\mathrm{d} = 333\,\mathrm{K}$ for a certain time interval [43].[15] For medical safety reasons, however, the temperature of the tumor and healthy tissue must not exceed $T^+ = 373\,\mathrm{K}$, cf., e. g., [38, 43]. A suitable representation of the objective of heating up the tumor within optimization problem (3.17) is achieved by a set-point transition from the initial temperature T_0 to a stationary temperature profile that minimizes the quadratic error $(T - T_\mathrm{d})^2$ within the tumor.[16] To this end, the quadratic error is penalized in the Lagrange term $l(T)$ and Mayer term $V(T(\cdot, t_\mathrm{f}))$ of cost functional (3.14). The corresponding weights are $q_1 = 10^8$ and $q_2 = 10^8$. The temperature constraint is taken into account by means of the outer penalty function in the Lagrange term $l(T)$. The corresponding weight is set to $q_3 = 10^9$, cf. Equation (3.14). Table 3.6 shows the weights of the Mayer and Lagrange terms (3.14).

To be able to perform the cancer treatment for any time periods, the trajectory planning approach for MWA identifies in a first step appropriate stationary set points $(u_\mathrm{d}, T_\mathrm{d}(x))$. To this end, the stationary version of optimization problem (3.17) is numerically solved using the cost functional

$$J(u) = \int_\Omega \frac{q_2}{2}\chi_{\Omega_\mathrm{t}} \left(T - T_\mathrm{d}\right)^2 + \frac{q_3}{2}\chi_{\Omega_\mathrm{o}} \max\left(0, T - T^+\right)^2 \,\mathrm{d}x \tag{3.59}$$

representing the objectives of the trajectory planning as discussed above.[17] Accordingly, the numerical solution of this optimization problem reveals optimal stationary set points $(u_\mathrm{d}, T_\mathrm{d}(x))$ that can be used in a second step to specify cost functional (3.14) for solving the instationary problem (3.17).

Table 3.6: Weights of the Mayer and Lagrange terms (3.14) for hyperthermia therapy.

weight	objective
$q_1 = 10^8$	minimiz. of state error $(T - T_\mathrm{d})^2$ in tumor Ω_t (Mayer term)
$q_2 = 10^8$	minimiz. of state error $(T - T_\mathrm{d})^2$ in tumor Ω_t (Lagrange term)
$q_3 = 10^9$	violation of state constraint $T \leq T^+$ in Ω_o (Lagrange term)
$q_4 = 10^2$	penalization of control action $(u - u_\mathrm{d})^2$ on Γ_c (Lagrange term)

[15] The treatment time of MWA varies according to whether metastases may be present or not. Generally speaking, the oncologist estimates the treatment time as a rule of thumb.

[16] The initial temperature of the tumor and healthy tissue is the temperature of blood $T_\mathrm{b} = 310\,\mathrm{K}$.

[17] Note that the temperature T does not depend on time t but only on the spatial coordinate x due to the stationary formulation of the associated optimization problem.

Both the stationary and instationary version of optimization problem (3.17) are numerically solved by means of the optimization framework from Section 3.5. Similar to Section 3.6.2, the optimization framework uses the adaptive line search strategy for updating the control trajectory u in each gradient iteration. The gradient method of Algorithm 3.1 is terminated after fulfilling condition (3.56) with $\epsilon_J = 10^{-6}$.

The control trajectory u resulting from the numerical solution of the instationary version of optimization problem (3.17) leads to an optimal heat-up behavior of the tumor as shown in Figure 3.14. The control trajectory exhibits an identical structure as the one in the case of induction heating and can be divided into three phases. During the first minute, the control trajectory u maximizes the intensity of the electromagnetic heat source by remaining at its upper bound u^+. Subsequently, the control trajectory decreases continuously within the time interval $(1\,\text{min}, 6\,\text{min})$ to generate only as much heat as is permissible to comply with the state constraint $T \leq T^+$ with bound $T^+ = 373\,\text{K}$, cf. the trajectories of the minimum $T_{\min}(t)$, average $T_{\text{avg}}(t)$, and maximum temperature $T_{\max}(t)$ of the tumor in Figure 3.14.

The temperature profiles at the time instants $t \in \{1\,\text{min}, 2\,\text{min}, 8\,\text{min}\}$ in Figure 3.15 demonstrate the optimal heat-up behavior of the tumor to the desired temperature profile $T_{\text{d}}(x)$. Since the electromagnetic heat source is mainly confined to the region around the air gap of the electrode, the rather slow heat transfer due to diffusion is required to heat-up the outer region of the tumor. This fact is also reflected in the sharp decrease of the control trajectory u after $t = 1\,\text{min}$ and in the moderate increase of the average and minimum temperature in contrast to the rapid increase of the maximum one, cf. Figure 3.14.

The therapeutic success of MWA can be assessed by means of the temperature of ablation $T_{\text{abl}} = 315\,\text{K}$. Instead of requiring that the tumor is heated up to $T_{\text{d}} = 333\,\text{K}$ in total, the necrosis effects that seriously damage the tumor also arise if the tumor temperature exceeds the threshold T_{abl}, see, e. g., [43]. To guarantee a sufficiently large destruction of

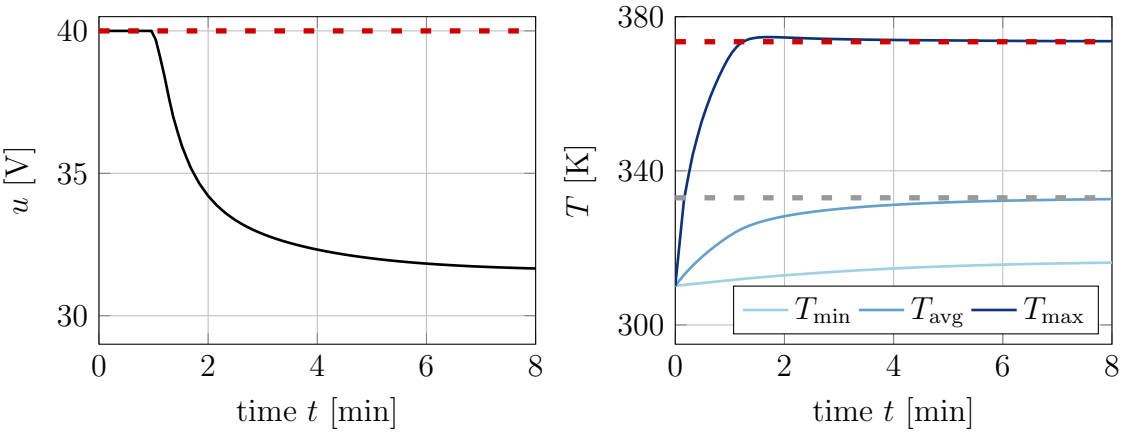

Figure 3.14: Optimal control trajectory u to heat up the tumor to the desired set-point $T_{\text{d}}(x)$. The minimum $T_{\min}$, average T_{avg}, and maximum temperature $T_{\max}$ of the tumor minimize their distance to $T_{\text{d}}(x)$ but do not significantly exceed the constraint T^+.

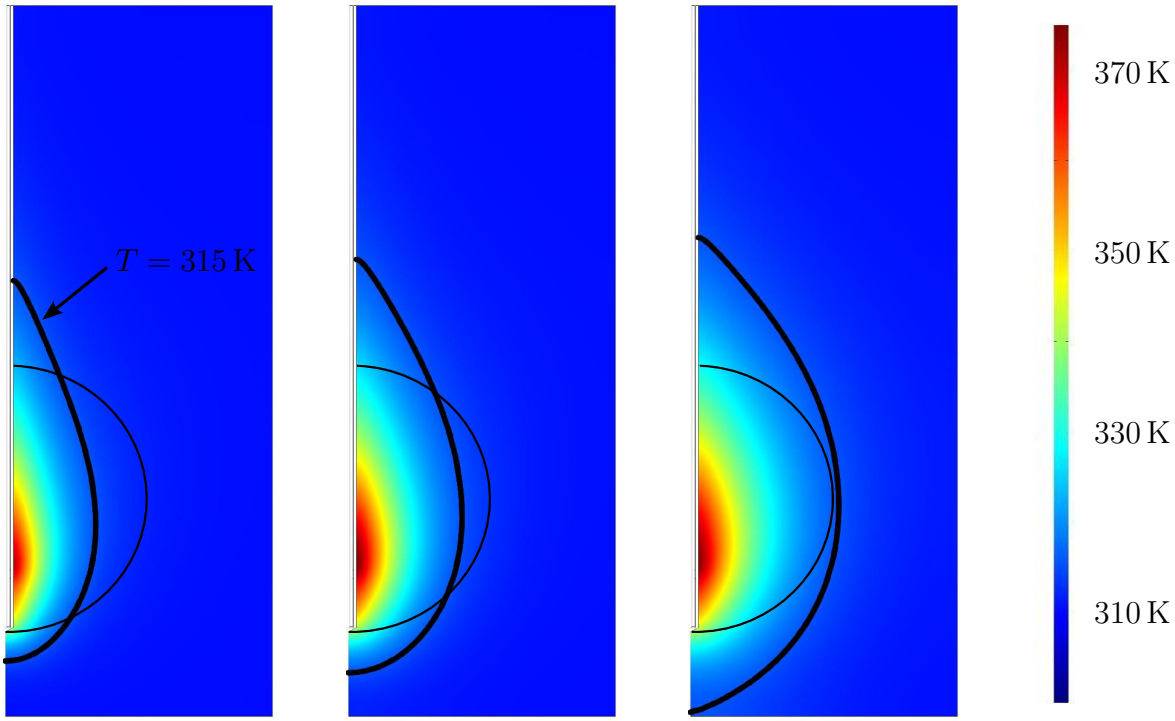

Figure 3.15: Temperature profiles of the tumor and surrounding liver T with isoline $T = 315\,\mathrm{K}$ at the time instants $t \in \{1\,\mathrm{min}, 2\,\mathrm{min}, 8\,\mathrm{min}\}$.

the tumor for $T_{\mathrm{abl}} \ll T_{\mathrm{d}}$, the treatment time t_{f} has to be increased. The successful cancer therapy becomes clear by considering the stationary temperature profile at $t = 8\,\mathrm{min}$ and the isoline $T_{\mathrm{abl}} = 315\,\mathrm{K}$ that completely encloses the tumor in Figure 3.15.

3.7 Conclusions

This chapter discusses the formulation and numerical solution of optimization problems for planning trajectories of various kinds of electromagnetic heating systems. The control tasks of typical application examples such as induction heating and hyperthermia therapy are represented by cost functionals which are minimized subject to the electromagnetic and thermal subsystems from Chapter 2. The optimality conditions are derived by the formal Lagrangian technique in terms of an FOTD approach.

Special emphasis is paid to adapt the trajectory planning approach to general electromagnetic heating systems. To this end, use is made of the structure of the optimality conditions that possess unconstrained state and adjoint state variables, as well as canonical equations with separated initial and final time conditions. Keeping in mind that the gradient algorithm relies on simple forward and backward integrations of the canonical equations, the incorpo-

ration of FEM software for the trajectory planning is favorable. An optimization framework is developed that picks up this idea and closely couples optimization algorithms in MATLAB and FEM-based solution techniques from the software package COMSOL MULTIPHYSICS. This offers an elegant way to separate the methodological and numerical issues from each other when optimizing the excitation of electromagnetic actuators. The applicability and accuracy of the trajectory planning approach is illustrated for induction heating processes and hyperthermia therapy.

Chapter 4

Optimal position and shape of actuators

Besides the adjustment of the intensity of the electromagnetic heat source by means of impressed currents or voltages within the actuator as addressed in the previous chapter, the position and shape of the actuator constitute further important degrees of freedom with respect to an optimal trajectory planning. The specific choice of the actuator configuration (e. g. inductor shape or electrode position) allows one to influence the spatial distribution of the heat source within the object to be heated. The control performance of electromagnetic heating systems can benefit from this additional degree of freedom and, for instance, the workpiece or tumor from the previous chapter can be heated up more homogeneously.

As the optimal actuator configuration depends on its electrical excitation, a simultaneous treatment of both problems is essential. The extended trajectory planning approach proposed in this chapter attacks the coupled problem by considering a joined optimization problem. The optimality conditions are derived by means of the adjoint-based sensitivity analysis in conjunction with the formal Lagrangian technique. Analogous to Chapter 3, the optimality conditions are numerically solved by considering a close interaction of state-of-the-art FEM software and a tailored gradient method.

4.1 Problem formulation

The optimization of the actuator configuration is used to tailor the spatial distribution of the heat source to the desired heat-up behavior of the object to be heated. This means that the diverse objectives of electromagnetic heating applications such as homogeneous heating of a gear wheel or local overheating of a tumor can be taken more effectively into account by the trajectory planning. In this thesis, the optimization of the actuator configuration is exemplified for the surface hardening processes shown in Figure 4.1 and introduced in Chapter 3. The problem of an optimal positioning of N inductors is illustrated in Figure 4.1a, whereas Figure 4.1b addresses the problem of optimizing the inductor shape. The primary objective of both scenarios is to heat up the surface layer $\tilde{\Omega}_\mathrm{o}$ as homogeneously as possible to the desired temperature T_d. Further objectives concern the prevention of an excessive heat-up of inner domains of the workpiece and the compliance of temperature constraints to suppress undesired metallurgical effects during the heat-up process [32].

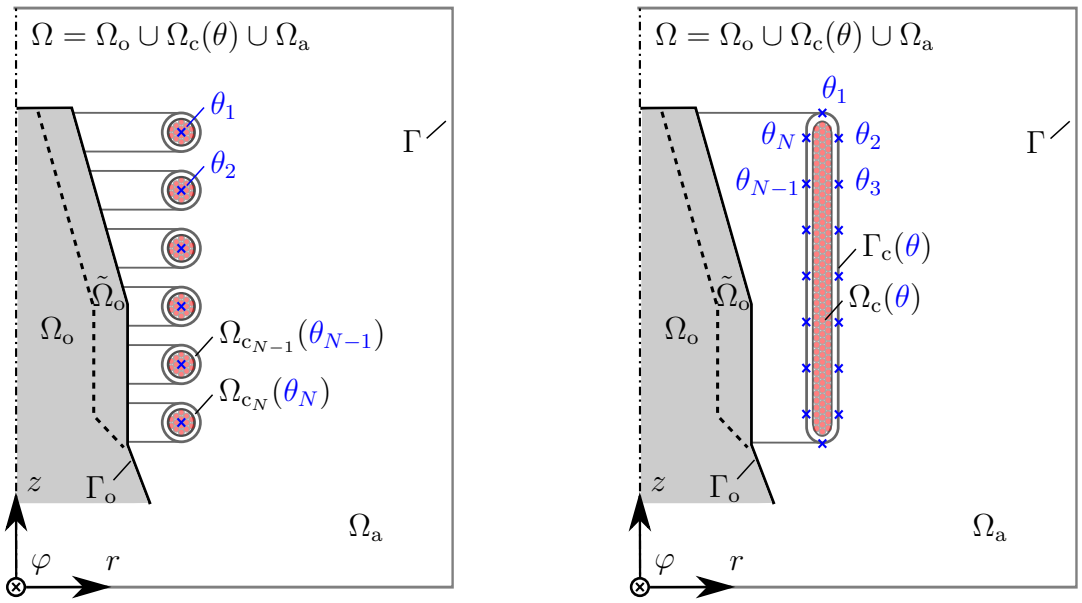

(a) Scenario for optimal inductor positions

(b) Scenario for optimal inductor shape

Figure 4.1: Geometrical setup for optimizing a) the position of N inductors and b) the shape of an inductor (not to scale). The degrees of freedom to manipulate the actuator configuration are the tuples $\theta_j = (\theta_{j,r}, \theta_{j,z})^\mathsf{T},\ j \in \{1, 2, \ldots, N\}$.

4.1.1 Governing equations

The surface hardening processes from Figure 4.1 are mathematically described using the coupled PDE system (3.2). The state variables are the temperature T and the magnetic vector potential A. The corresponding geometrical setups are of axisymmetrical type with spatial coordinates $x = [r, \varphi, z]^\mathsf{T}$, whereby the region of interest $\Omega = \Omega_o \cup \Omega_c(\theta) \cup \Omega_a$ encompasses the workpiece Ω_o, the inductor $\Omega_c(\theta)$, and the ambient air Ω_a. The surface layer to be hardened is denoted by $\tilde{\Omega}_o \subset \Omega_o$.

To obtain the degrees of freedom for optimizing the actuator configuration, the spatial domain of the inductor is defined as a function of the parameter vector $\theta = [\theta_1^\mathsf{T}, \theta_2^\mathsf{T}, \ldots, \theta_N^\mathsf{T}]^\mathsf{T}$ including the tuples

$$\theta_j = \begin{pmatrix} \theta_{j,r} \\ \theta_{j,z} \end{pmatrix}, \quad j \in \{1, 2, \ldots, N\}\ . \tag{4.1}$$

A second degree of freedom for the trajectory planning is the time-dependent control trajectory u, which allows to adjust besides the spatial distribution of the electromagnetic heat source also its intensity. Thus, the phasor for modeling the impressed inductor currents

$$J_{\mathrm{imp}}(u;\theta) = \tfrac{N_c}{A_c} u \chi_{\Omega_c(\theta)} e_\varphi \qquad \text{in } \Omega \times (0, t_f) \tag{4.2}$$

includes both optimization variables u and θ. The phasor $J_{\mathrm{imp}}(u;\theta)$ explicitly depends on the control trajectory u and implicitly on the parameter vector θ in view of the parametrization of the actuator configuration with spatial domain $\Omega_c(\theta)$.

4.1.2 Parametrization of the position and shape of the actuator

This section presents suitable parametrization techniques to provide the optimization variables for optimizing the position and shape of electromagnetic actuators.[1] The optimization variables related to the positions of the N inductors from Figure 4.1a are the parameters

$$\theta = [\theta_1, \theta_2, \ldots, \theta_N]^\mathsf{T} \ . \tag{4.3}$$

Further variables of the actuator configuration such as the diameter of inductors or the number of coil windings can be optimized by extending the parameter vector θ.

The actuator configuration of the second scenario where the inductor shape is optimized is specified as follows. Suitable parametrization techniques are applied to mathematically describe the inductor contour $\Gamma_\mathrm{c}(\theta)$, as shown in Figure 4.1b. The so-called discrete approach is one possible option and linearly interpolates between two consecutive tuples (θ_j, θ_{j+1}), cf. Equation (4.1). In this case, the optimization variables are all elements of the tuples. While this parametrization technique is easy to implement, the required number of optimization variables is generally large to achieve a smooth contour $\Gamma_\mathrm{c}(\theta)$. This is especially true for segments of $\Gamma_\mathrm{c}(\theta)$ involving sharp edges or curvatures [104].

A more appropriate approach for parameterizing the inductor contour $\Gamma_\mathrm{c}(\theta)$ relies on piecewise polynomial functions [121]. To this end, the contour of the inductor is covered by n connected subintervals

$$\Gamma_\mathrm{c}(\theta) = \sum_{j=0}^{n} N_{j,p}(\xi) \begin{pmatrix} \theta_{j,r} \\ \theta_{j,z} \end{pmatrix} \ , \qquad a \leq \xi \leq b \ , \tag{4.4}$$

whereby the basis functions $N_{j,p}(\xi)$ of degree p ensure a smooth parametrization.[2] The j-th basis function is defined on the subinterval $[\xi_j, \xi_{j+1})$ with knots ξ_j, non-periodic knot vector

$$X = [\xi_0 = a,\, \xi_1, \ldots,\, \xi_j, \ldots,\, \xi_m = b]^\mathsf{T} \ , \tag{4.5}$$

and $m \geq n$. The tuples θ_j, also referred to as control points, have a local influence on the inductor contour $\Gamma_\mathrm{c}(\theta)$. In order to reduce the number of control points, respectively the number of optimization variables, the length of the n subintervals can be varied depending on both its expected and required smoothness.

In literature, there are many methods such as spline interpolation, Bézier approximation, or B-spline techniques to define the basis functions $N_{j,p}(\xi)$, also see [121, 104]. For a sufficiently smooth parametrization of the inductor contour $\Gamma_\mathrm{c}(\theta)$, a B-spline approximation with the basis functions defined by the recursive formula

$$N_{j,0}(\xi) = \begin{cases} 1 & \text{if } \xi_j \leq \xi \leq \xi_{j+1} \\ 0 & \text{else} \end{cases} \tag{4.6a}$$

$$N_{j,p}(\xi) = \frac{\xi - \xi_j}{\xi_{j+p} - \xi_j} N_{j,p-1}(\xi) + \frac{\xi_{j+p+1} - \xi}{\xi_{j+p+1} - \xi_{j+1}} N_{j,p-1}(\xi) \tag{4.6b}$$

[1] The parametrization techniques are universally applicable but are directly applied to the surface hardening processes from Figure 4.1.

[2] The tuple θ_0 is used to close the curve $\Gamma_\mathrm{c}(\theta)$ by setting $\theta_0 = \theta_1$.

is proposed. The degree of the basis functions p allows to influence the smoothness of the inductor contour $\Gamma_\mathrm{c}(\theta)$ as it has continuous derivatives up to the order of $p-1$, cf. Equation (4.4) and (4.6). A more detailed discussion of B-spline parametrization techniques including modified approaches such as non-uniform rational B-splines (NURBS – *Non-Uniform Rational B-Splines*) can be found, for instance, in [121, 104].

Similar to the optimization of the inductor positions, the parameter vector (4.3) summarizes the optimization variables for optimizing the inductor shape. Generally, the optimization variables θ comprise all control points $(\theta_{j,r}, \theta_{j,z})$ that affect the B-spline basis functions $N_{j,p}(\xi)$, cf. Equation (4.4). In order to reduce the number of optimization variables, some of the control points can be assumed to be constant.

4.1.3 Formulation of a coupled optimization problem

The trajectory planning approach uses the optimization variables (u, θ) to adjust the intensity and spatial distribution of the electromagnetic heat source. Thereby, the constraints

$$u(t) \in \mathcal{U}_\mathrm{ad} := \{u(t) \in \mathbb{R} \,|\, u^- \leq u(t) \leq u^+\} \tag{4.7a}$$

$$\theta \in \theta_\mathrm{ad} := \{\theta \in \mathbb{R}^N \,|\, \theta^- \leq \theta \leq \theta^+\} \tag{4.7b}$$

with the minimal and maximal allowable inductor currents (u^-, u^+) and the admissible distance between actuator and object specified by (θ^-, θ^+) have to be taken into account. The temperature constraint

$$T(x,t) - T^+ \leq 0 \qquad \text{in } \Omega_\mathrm{o} \times (0, t_\mathrm{f}) \tag{4.8}$$

prevents transformation processes of the crystalline structure of the object.

The cost functional for incorporating the objectives of the surface hardening processes reads

$$J(u;\theta) = \int_\Omega V(T(\cdot, t_\mathrm{f}))\, \mathrm{d}x + \iint_{\Omega\times(0,t_\mathrm{f})} l(T,u;\theta)\, \mathrm{d}x\, \mathrm{d}t \tag{4.9}$$

and exhibits a similar structure to its counterpart in Section 3.1, cf. Equation (3.6). The Mayer term $V(T(\cdot, t_\mathrm{f}))$ and the Lagrange term $l(T,u;\theta)$ are specified as follows

$$V(T(\cdot, t_\mathrm{f})) = \frac{q_1}{2}\chi_{\Omega_\mathrm{d}} \left(T(\cdot, t_\mathrm{f}) - T_\mathrm{d}\right)^2 \tag{4.10a}$$

$$\begin{aligned} l(T,u;\theta) = {} & \frac{q_2}{2}\chi_{\Omega_\mathrm{d}} \left(T - T_\mathrm{d}\right)^2 + \frac{q_3}{2}\chi_{\Omega_\mathrm{o}} \max\left(0, T - T^+\right)^2 + \frac{q_4}{2}\chi_{\Omega_\mathrm{c}(\theta)} u^2 \\ & + \frac{q_5}{2}\chi_{\Omega_\mathrm{i}} \left(T - T_0\right)^2 \end{aligned} \tag{4.10b}$$

and penalize the quadratic error $(T - T_\mathrm{d})^2$ with weights $(q_1, q_2) \geq 0$ on the surface $\Omega_\mathrm{d} = \tilde{\Omega}_\mathrm{o}$. The Lagrange term (4.10b) is also used to weakly incorporate the state constraint (4.8) in terms of an outer penalty function approach. The severity of this part is influenced by the weight $q_3 \geq 0$ and allows to specify the tolerable violation of the state constraint compared

to the primary objectives with weights (q_1, q_2). The third part of the Lagrange term weights the control action u^2 with the parameter $q_4 \geq 0$. A more detailed discussion about the Mayer term and the above-mentioned parts of the Lagrange term follows from Section 3.1.3.

The last part of the Lagrange term (4.10b) accounts for the objective of a surface hardening process to prevent the heat-up of inner domains of the workpiece. To this end, the parameter $q_5 \geq 0$ weights the quadratic error $(T - T_0)^2$ on the spatial domain

$$\Omega_\mathrm{i} = \Omega_\mathrm{o} \setminus \tilde{\Omega}_\mathrm{o} \tag{4.11}$$

encompassing the workpiece Ω_o but not the surface layer $\tilde{\Omega}_\mathrm{o}$. The degree of freedom to adapt the spatial distribution of the electromagnetic heat source by the actuator configuration facilitates to realize the objective of preventing the heat-up of inner domains of the workpiece. Note that this is hardly viable for scenarios where only the electrical excitation of the actuator constitutes the optimization variable. However, the weight q_5 has to be chosen sufficiently small compared to q_1 and q_2 to ensure that the primary objective of heating up the surface layer dominates the overall cost functional.

The cost functional (4.9) and the Mayer and Lagrange terms (4.10) are used to formulate the PDE constrained optimization problem

$$\min_{\substack{u(\cdot)\in\mathcal{U}_\mathrm{ad}\\ \theta\in\theta_\mathrm{ad}}} J(u;\theta) = \int_\Omega V(T(\cdot,t_\mathrm{f}))\,\mathrm{d}x + \iint_{\Omega\times(0,t_\mathrm{f})} l(T,u;\theta)\,\mathrm{d}x\,\mathrm{d}t \tag{4.12a}$$

$$\begin{aligned}
\text{s.t.}\quad & e_{\nabla,t}\left(\rho C, T\right) - e_\Delta\left(k, T\right) = f_{\Omega_\mathrm{o}}(T, K) && \text{in } \Omega_\mathrm{o}\times(0,t_\mathrm{f}) && (4.12\mathrm{b})\\
& e_{\nabla,x}\left(k, T\right) = f_{\Gamma_{\mathrm{o,N}}}(T) && \text{on } \Gamma_{\mathrm{o,N}}\times(0,t_\mathrm{f}) && (4.12\mathrm{c})\\
& T = f_{\Gamma_{\mathrm{o,D}}} && \text{on } \Gamma_{\mathrm{o,D}}\times(0,t_\mathrm{f}) && (4.12\mathrm{d})\\
& T(\cdot,0) = T_0 && \text{in } \Omega_\mathrm{o} \text{ at } t=0 && (4.12\mathrm{e})\\
& e_{\nabla\times,\nabla\times}\left(\mu^{-1}, K\right) = f_\Omega(K,u;\theta) && \text{in } \Omega\times(0,t_\mathrm{f}) && (4.12\mathrm{f})\\
& e_{\nabla\times}\left(\mu^{-1}, K\right) = f_{\Gamma_\mathrm{N}}(K,u) && \text{on } \Gamma_\mathrm{N}\times(0,t_\mathrm{f}) && (4.12\mathrm{g})\\
& e_\times\left(K\right) = f_{\Gamma_\mathrm{D}}(u) && \text{on } \Gamma_\mathrm{D}\times(0,t_\mathrm{f}) && (4.12\mathrm{h})
\end{aligned}$$

to cope with the simultaneous optimization of the actuator configuration and electrical excitation. The optimization problem is formulated using the differential operators (3.15)–(3.16) and the state variable of the electromagnetic subsystem $K \in \{A, E\}$ to address various kinds of electromagnetic heating systems. The right hand sides of the thermal and electromagnetic subsystem (4.12b)–(4.12e) and (4.12f)–(4.12h) allows one to specify the system dynamics of a particular problem. The problem considered in these lines is described by

$$\begin{aligned}
f_{\Omega_\mathrm{o}}(T,A) &= \tfrac{\sigma\omega^2}{2}|A|^2 && \text{in } \Omega_\mathrm{o}\times(0,t_\mathrm{f}) && (4.13\mathrm{a})\\
f_{\Gamma_{\mathrm{o,N}}}(T) &= \alpha\left(T_\mathrm{a} - T\right) + \epsilon\sigma_\mathrm{SB}\left(T_\mathrm{a}^4 - T^4\right) && \text{on } \Gamma_{\mathrm{o,N}}\times(0,t_\mathrm{f}) && (4.13\mathrm{b})\\
f_\Omega(A,u;\theta) &= \tfrac{N_\mathrm{c}}{A_\mathrm{c}} u \chi_{\Omega_\mathrm{c}(\theta)} e_\varphi - j\omega\sigma A && \text{in } \Omega\times(0,t_\mathrm{f}) && (4.13\mathrm{c})\\
f_{\Gamma_\mathrm{D}}(u) &= 0 && \text{on } \Gamma_\mathrm{D}\times(0,t_\mathrm{f})\ , && (4.13\mathrm{d})
\end{aligned}$$

also see Section 3.3.

4.2 Approach for handling the coupled optimization problem

The optimality conditions of optimization problem (4.12) rely on the analysis of the Lagrangian $\mathcal{L} := \mathcal{L}(T, K, u, p, \Lambda; \theta)$. Its definition is based on the cost functional (4.12a) and the adjoined PDE system (4.12b)–(4.12h) and reads as

$$\begin{aligned}\mathcal{L} = &\int_{\Omega} V(T(\cdot, t_\mathrm{f}))\ \mathrm{d}x + \iint_{\Omega\times(0,t_\mathrm{f})} l(T, u; \theta)\ \mathrm{d}x\,\mathrm{d}t \\ &+ \iint_{\Omega_\mathrm{o}\times(0,t_\mathrm{f})} p\left[e_{\nabla,\,t}\left(\rho C, T\right) - e_{\Delta}\left(k, T\right) - f_{\Omega_\mathrm{o}}(T, K)\right]\ \mathrm{d}x\,\mathrm{d}t \\ &+ \iint_{\Gamma_{\mathrm{o,N}}\times(0,t_\mathrm{f})} p\left[e_{\nabla,\,x}\left(k, T\right) - f_{\Gamma_{\mathrm{o,N}}}(T)\right]\ \mathrm{d}x\,\mathrm{d}t + \iint_{\Gamma_{\mathrm{o,D}}\times(0,t_\mathrm{f})} p\left[T - f_{\Gamma_{\mathrm{o,D}}}\right]\ \mathrm{d}x\,\mathrm{d}t \\ &+ \iint_{\Omega\times(0,t_\mathrm{f})} \Lambda\cdot\left[e_{\nabla\times,\nabla\times}\left(\mu^{-1}, K\right) - f_{\Omega}(K, u; \theta)\right]\ \mathrm{d}x\,\mathrm{d}t \\ &+ \iint_{\Gamma_\mathrm{N}\times(0,t_\mathrm{f})} \Lambda\cdot\left[f_{\Gamma_\mathrm{N}}(K, u) - e_{\nabla\times}\left(\mu^{-1}, K\right)\right]\ \mathrm{d}x\,\mathrm{d}t + \iint_{\Gamma_\mathrm{D}\times(0,t_\mathrm{f})} \Lambda\cdot\left[e_{\times}\left(K\right) - f_{\Gamma_\mathrm{D}}(u)\right]\ \mathrm{d}x\,\mathrm{d}t \end{aligned} \tag{4.14}$$

with the adjoint states $p(x,t)$ and $\Lambda(x;t)$, cf. Section 3.4. The optimization variables θ only arise implicitly within the Lagrangian $\mathcal{L}$ in view of its influence on the position and shape of the actuator $\Omega_\mathrm{c}(\theta)$. The implicit time dependency of the adjoint state $\Lambda(x;t)$ is due to the time-harmonic formulation of the electromagnetic subsystem (4.12f)–(4.12h).

The optimality conditions of optimization problem (4.12) are derived separately for optimizing the actuator configuration and excitation. In a first step, the adjoint-based sensitivity analysis is applied to optimization problem (4.12). Thereby, the variational inequality

$$\nabla_{\theta_j}\mathcal{L} := \left.\frac{\mathrm{d}\mathcal{L}}{\mathrm{d}\theta_j}\right|_{y^*}\left(\theta_j - \theta_j^*\right) \geq 0 \qquad \forall\theta_j \in \theta_\mathrm{ad} \tag{4.15}$$

is interpreted as a necessary optimality condition, whereby $y^* = (T^*, K^*, u^*, \theta^*, p^*, \Lambda^*)$ denotes the optimal solution, see Section 4.3. The second problem, i. e., the optimal excitation of the actuator, relies on the definition of the directional derivatives

$$\left.\frac{\partial\mathcal{L}}{\partial T}\right|_{y^*} h_T = 0 \qquad \forall h_T \tag{4.16a}$$

$$\left.\frac{\partial\mathcal{L}}{\partial K}\right|_{y^*}\cdot H_K = 0 \qquad \forall H_K \tag{4.16b}$$

$$\left.\frac{\partial\mathcal{L}}{\partial u}\right|_{y^*} h_u \geq 0 \qquad \forall u \in \mathcal{U}_\mathrm{ad}\ , \tag{4.16c}$$

which are analyzed in Section 4.4 by means of the formal Lagrangian technique as discussed in detail in Chapter 3. The optimality systems deduced from Equation (4.15) and (4.16) are combined in Section 4.5 to facilitate a holistic optimization approach.

4.3 Optimality conditions for optimal actuator configuration

The adjoint-based sensitivity analysis, see, for instance, [79, 128, 18, 86], relates an optimal actuator configuration to the variational inequality (4.15), whereby the total differential

$$\nabla_{\theta_j}\mathcal{L} = \left.\frac{\mathrm{d}\mathcal{L}}{\mathrm{d}\theta_j}\right|_{y^*} , \qquad j \in \{1, 2, \ldots, N\} \tag{4.17}$$

reflect the influence of an optimization variable θ_j on both the cost functional (4.12a) and the systems dynamics (4.12b)–(4.12h). In combination with the geometrical meaning of an optimization variable θ_j in terms of its direction in the spatial coordinate r or z, Equation (4.17) constitutes geometrical gradients of the cost functional with respect to θ.

The crucial point of a solely implicit dependency of the Lagrangian $\mathcal{L}$ with respect to the optimization variables θ is tackled by means of the state sensitivities

$$T_{\theta_j} = \frac{\partial T(x,t;\theta)}{\partial \theta_j} \tag{4.18a}$$

$$K_{\theta_j} = \frac{\partial K(x;t,\theta)}{\partial \theta_j} , \qquad j \in \{1, 2, \ldots, N\} . \tag{4.18b}$$

The state sensitivities $T_{\theta_j} := T_{\theta_j}(x,t)$ and $K_{\theta_j} := K_{\theta_j}(x;t)$ represent the impact of a variation of the optimization variable θ_j on the state variables (T, K). In what follows, the evaluation of the variational inequality (4.15) and its subsequent analysis is presented. It is shown that the formulation of an optimality system comprising an adjoint PDE system, an adjoint ODE system, and a gradient condition ensures the validity of the variational inequality (4.17).

4.3.1 Adjoint PDE system

The handling of temporal and spatial operators involved in the Lagrangian (4.14) constitutes a major challenge when analysing the gradients (4.17). However, this problem can be tackled according to the formal Lagrangian technique by treating temporal and spatial operators formally, cf. the discussion in Section 1.3.3. After substituting the Lagrangian (4.14) into (4.15), the evaluation of the total differential yields

$$\begin{aligned}
\nabla_{\theta_j}\mathcal{L} = {} & \int_{\Omega} \partial_T V(T(\cdot,t_\mathrm{f}))\big|_{y^*}\, T_{\theta_j}(\cdot,t_\mathrm{f})\,\mathrm{d}x + \iint_{\Omega\times(0,t_\mathrm{f})} \partial_T l(T,u;\theta)\big|_{y^*}\, T_{\theta_j} + \partial_{\theta_j} l(T,u;\theta)\big|_{y^*}\,\mathrm{d}x\,\mathrm{d}t \\
& + \iint_{\Omega_\mathrm{o}\times(0,t_\mathrm{f})} p^* \Big[e_{\nabla,t}\left(\rho C, T_{\theta_j}\right) - e_{\Delta}\left(k, T_{\theta_j}\right) - \partial_T f_{\Omega_\mathrm{o}}(T,K)\big|_{y^*}\, T_{\theta_j} - \partial_K f_{\Omega_\mathrm{o}}(T,K)\big|_{y^*}\cdot K_{\theta_j} \Big]\,\mathrm{d}x\,\mathrm{d}t \\
& + \iint_{\Gamma_{\mathrm{o,N}}\times(0,t_\mathrm{f})} p^* \Big[e_{\nabla,x}\left(k, T_{\theta_j}\right) - \partial_T f_{\Gamma_{\mathrm{o,N}}}(T)\big|_{y^*}\, T_{\theta_j} \Big]\,\mathrm{d}x\,\mathrm{d}t + \iint_{\Gamma_{\mathrm{o,D}}\times(0,t_\mathrm{f})} p^* T_{\theta_j}\,\mathrm{d}x\,\mathrm{d}t
\end{aligned}$$

$$+ \iint\limits_{\Omega\times(0,t_\mathrm{f})} \Lambda^* \cdot \Big[e_{\nabla\times,\nabla\times}\left(\mu^{-1}, K_{\theta_j}\right) - \partial_K f_\Omega(K,u;\theta)\big|_{y^*} \cdot K_{\theta_j} - \partial_{\theta_j} f_\Omega(K,u;\theta)\big|_{y^*} \Big] \,\mathrm{d}x\,\mathrm{d}t$$
$$+ \iint\limits_{\Gamma_\mathrm{N}\times(0,t_\mathrm{f})} \Lambda^* \cdot \Big[\partial_K f_{\Gamma_\mathrm{N}}(K,u)\big|_{y^*} \cdot K_{\theta_j} - e_{\nabla\times}\left(\mu^{-1}, K_{\theta_j}\right) \Big] \,\mathrm{d}x\,\mathrm{d}t + \iint\limits_{\Gamma_\mathrm{D}\times(0,t_\mathrm{f})} \Lambda^* \cdot e_\times\left(K_{\theta_j}\right) \,\mathrm{d}x\,\mathrm{d}t \ . \tag{4.19}$$

Thereby, the arguments of the temporal and spatial operators swap from the state variables (T, K) to the state sensitivities $(T_{\theta_j}, K_{\theta_j})$, see Equation (3.25) and (3.31) for handling the partial derivatives of the temporal and spatial operators (3.15)–(3.16) with respect to the optimization variables θ. The state sensitivities (4.18) are used to deal with the total differential of the variational inequality (4.15) with respect to θ.

Reformulation of the gradient equation

The gradients (4.19) depend on both the unknown state sensitives $(T_{\theta_j}, K_{\theta_j})$ and the yet unknown adjoint states (p, Λ). Analogously to the formal Lagrangian technique in Chapter 3, the parts of (4.19) with sensitivities $(T_{\theta_j}, K_{\theta_j})$ that are subject to temporal or spatial derivatives are reformulated by means of integral identities. The basis for this reformulation step is provided in Section 3.4.1–3.4.2. The temporal derivative of the state sensitivity T_{θ_j} in the first part of the second line of Equation (4.19) can be shifted to the adjoint state p using the formula of partial integration (3.26). The application of Green's second identity (3.27) to the second part of the second line of (4.19) shifts the Laplacian from the state sensitivity T_{θ_j} to the adjoint state p. This also cancels out the first part of the third line of (4.19).

To shift the double curl operator from the state sensitivity K_{θ_j} to the adjoint state Λ within the first part of the fourth line of (4.19), the vector analogue of Green's second identity (3.34) is applied. In summary, the integral identities (3.26), (3.27), and (3.34) provide a suitable basis to reformulate Equation (4.19) as the equivalent counterpart

$$\begin{aligned}
\nabla_{\theta_j}\mathcal{L} = &\iint\limits_{\Omega\times(0,t_\mathrm{f})} \partial_{\theta_j} l(T,u;\theta)\big|_{y^*} - \partial_{\theta_j} f_\Omega(K,u;\theta)\big|_{y^*} \cdot \Lambda^* \,\mathrm{d}x\,\mathrm{d}t \\
&+ \iint\limits_{\Omega_\mathrm{o}\times(0,t_\mathrm{f})} \Big[-e_{\nabla,t}\left(\rho C, p^*\right) - e_\Delta\left(k, p^*\right) - \partial_T f_{\Omega_\mathrm{o}}(T,K)\big|_{y^*} p^* + \partial_T l(T,u;\theta)\big|_{y^*} \Big] T_{\theta_j} \,\mathrm{d}x\,\mathrm{d}t \\
&\quad + \iint\limits_{\Gamma_{\mathrm{o,N}}\times(0,t_\mathrm{f})} \Big[e_{\nabla,x}\left(k, p^*\right) - \partial_T f_{\Gamma_{\mathrm{o,N}}}(T)\big|_{y^*} p^* \Big] T_{\theta_j} \,\mathrm{d}x\,\mathrm{d}t + \iint\limits_{\Gamma_{\mathrm{o,D}}\times(0,t_\mathrm{f})} p^* T_{\theta_j} \,\mathrm{d}x\,\mathrm{d}t \\
&\qquad + \int\limits_{\Omega_\mathrm{o}} \Big[\rho C p^*(\cdot,t_\mathrm{f}) + \partial_T V(T(\cdot,t_\mathrm{f}))\big|_{y^*} \Big] T_{\theta_j}(\cdot,t_\mathrm{f}) \,\mathrm{d}x
\end{aligned}$$

$$+ \iint\limits_{\Omega\times(0,t_\mathrm{f})} \Big[e_{\nabla\times,\nabla\times}\left(\mu^{-1},\Lambda^*\right) - \partial_K f_\Omega(K,u;\theta)\big|_{y^*}\cdot\Lambda^* - \chi_{\Omega_\mathrm{o}} p^*\, \partial_K f_{\Omega_\mathrm{o}}(T,K)\big|_{y^*}\Big]\cdot K_{\theta_j}\,\mathrm{d}x\,\mathrm{d}t$$
$$+ \iint\limits_{\Gamma_\mathrm{N}\times(0,t_\mathrm{f})} \Big[\partial_K f_{\Gamma_\mathrm{N}}(K,u)\big|_{y^*}\cdot\Lambda^* - e_{\nabla\times}\left(\mu^{-1},\Lambda^*\right)\Big]\cdot K_{\theta_j}\,\mathrm{d}x\,\mathrm{d}t - \iint\limits_{\Gamma_\mathrm{D}\times(0,t_\mathrm{f})} e_\times\left(\Lambda^*\right)\cdot K_{\theta_j}\,\mathrm{d}x\,\mathrm{d}t\ . \tag{4.20}$$

Formulation of an adjoint PDE system

The variational inequality (4.15) with the reformulated gradients (4.20) contains state sensitivities $(T_{\theta_j}, K_{\theta_j})$ that are separated from the adjoint states (p,Λ). This allows one to formulate the coupled PDE system

$$e_{\nabla,t}\left(\rho C,p^*\right) + e_\Delta\left(k,p^*\right) = \partial_T l(T,u;\theta)\big|_{y^*} - \partial_T f_{\Omega_\mathrm{o}}(T,K)\big|_{y^*}\, p^* \qquad \text{in } \Omega_\mathrm{o}\times(0,t_\mathrm{f}) \tag{4.21a}$$
$$e_{\nabla,x}\left(k,p^*\right) = \partial_T f_{\Gamma_{\mathrm{o,N}}}(T)\big|_{y^*}\, p^* \qquad \text{on } \Gamma_{\mathrm{o,N}}\times(0,t_\mathrm{f}) \tag{4.21b}$$
$$p^* = 0 \qquad \text{on } \Gamma_{\mathrm{o,D}}\times(0,t_\mathrm{f}) \tag{4.21c}$$
$$\rho C p^*(\cdot,t_\mathrm{f}) = -\,\partial_T V(T(\cdot,t_\mathrm{f}))\big|_{y^*} \qquad \text{in } \Omega_\mathrm{o} \text{ at } t=t_\mathrm{f} \tag{4.21d}$$

$$e_{\nabla\times,\nabla\times}\left(\mu^{-1},\Lambda^*\right) - \partial_K f_\Omega(K,u;\theta)\big|_{y^*}\cdot\Lambda^* = \chi_{\Omega_\mathrm{o}} p^*\,\partial_K f_{\Omega_\mathrm{o}}(T,K)\big|_{y^*} \qquad \text{in } \Omega\times(0,t_\mathrm{f}) \tag{4.21e}$$
$$e_{\nabla\times}\left(\mu^{-1},\Lambda^*\right) = \partial_K f_{\Gamma_\mathrm{N}}(K,u)\big|_{y^*}\cdot\Lambda^* \qquad \text{on } \Gamma_\mathrm{N}\times(0,t_\mathrm{f}) \tag{4.21f}$$
$$e_\times\left(\Lambda^*\right) = 0 \qquad \text{on } \Gamma_\mathrm{D}\times(0,t_\mathrm{f})\ . \tag{4.21g}$$

It is postulated that an optimal solution y^* complies with the adjoint dynamics (4.21) to get rid of the state sensitivities $(T_{\theta_j}, K_{\theta_j})$ within the variational inequality (4.15), respectively within the gradients (4.20). The adjoint subsystem (4.21a)–(4.21d) ensures that the second, third, and fourth line of the gradient equation (4.20) vanish in a distributional manner. The last two lines are eliminated by the adjoint subsystem (4.21e)–(4.21g). Note that the adjoint PDE system (4.21) avoids the necessity to calculate the state sensitivities $(T_{\theta_j}, K_{\theta_j})$ for each optimization parameter θ_j using finite difference schemes.

4.3.2 Adjoint ODE system

The formulation of the adjoint PDE system (4.21) simplifies Equation (4.20) to

$$\nabla_{\theta_j}\mathcal{L} = \iint\limits_{\Omega\times(0,t_\mathrm{f})} \partial_{\theta_j} l(T,u;\theta)\big|_{y^*} - \partial_{\theta_j} f_\Omega(K,u;\theta)\big|_{y^*}\cdot\Lambda^*\,\mathrm{d}x\,\mathrm{d}t \tag{4.22}$$

that can be used for evaluating the gradients $\nabla_{\theta_j}\mathcal{L}$ without numerically solving the state sensitivities $(T_{\theta_j}, K_{\theta_j})$, cf. Equation (4.20). The integral equation (4.22) can also be stated as the adjoint ODE system

$$\dot{s}^*_{\theta_j} = \int_\Omega \partial_{\theta_j} f_\Omega(K,u;\theta)\big|_{y^*}\cdot\Lambda^* - \partial_{\theta_j} l(T,u;\theta)\big|_{y^*}\,\mathrm{d}x\ , \qquad s^*_{\theta_j}(t_\mathrm{f}) = 0\ , \tag{4.23}$$

also referred to as sensitivity ODEs, whereby the sensitivities $s_{\theta_j} := s_{\theta_j}(t)$ are the state variables.[3] The evaluation of the sensitivity s_{θ_j} at $t = 0$ specifies the gradient $\nabla_{\theta_j}\mathcal{L}$ and reveals the impact of an optimization variable θ_j on optimization problem (4.12).

In order to cope with the partial derivative of the terms $f_\Omega(K, u; \theta)$ and $l(T, u; \theta)$ with respect to the optimization variables θ, the finite difference schemes

$$\partial_{\theta_j} f(\alpha; \theta) \approx \frac{f(\alpha; \theta_j + \epsilon) - f(\alpha; \theta_j - \epsilon)}{2\epsilon} , \qquad f(\alpha; \theta) \in \{f_\Omega(K, u; \theta), l(T, u; \theta)\} \tag{4.24}$$

are considered. The finite difference schemes approximately solve the term $\partial_{\theta_j} f(\alpha; \theta)$ using the admissible geometrical perturbation in the direction of θ_j, i. e., $\theta_j \pm \epsilon \in \theta_{\text{ad}}$. As the implicit dependency is caused by the spatial domain of the actuator $\Omega_{\text{c}}(\theta)$, the function $f(\alpha; \theta_j \pm \epsilon)$ can be evaluated with relative ease.

4.3.3 Gradient condition for optimal actuator configuration

The adjoint ODE system (4.23) provides a suitable basis to optimize the actuator configuration in terms of the first-order optimality condition (4.15). On the basis of Equation (4.15) and (4.23), it can be concluded that an optimal actuator configuration correlates with

$$s^*_{\theta_j}(0) \begin{cases} > 0 & \text{if } \theta_j^* = \theta_j^- \\ = 0 & \text{if } \theta_j^* \in (\theta_j^-, \theta_j^+) \\ < 0 & \text{if } \theta_j^* = \theta_j^+ \end{cases} . \tag{4.25}$$

The conditional character (4.25) follows from the variational inequality (4.15) and takes the constraints of the optimization variables (4.7b) into account. For a more compact notation, the sensitivities $s(t) = [s_{\theta_1}(t), s_{\theta_2}(t), \ldots, s_{\theta_N}(t)]^\mathsf{T}$ evaluated at the time instant $t = 0\,\text{s}$ are summarized by the gradient vector

$$g_\theta = [s_{\theta_1}(0), s_{\theta_2}(0), \ldots, s_{\theta_N}(0)]^\mathsf{T} . \tag{4.26}$$

In conclusion, the adjoint-based sensitivity analysis forms a basis to determine an optimal actuator configuration by appropriately solving the adjoint PDE system (4.21), the adjoint ODE system (4.23), and the gradient condition (4.25).

4.4 Optimality conditions for optimal control trajectory

The approach for handling the coupled optimization problem (4.12) applies the formal Lagrangian technique to derive the optimality conditions for optimal inductor currents u, cf. Section 4.2. The following lines only summarize the resulting optimality system comprising an adjoint PDE system and a gradient condition. A detailed discussion on handling this problem can be found in Chapter 3.

[3] The fundamental theorem of calculus is used to transform the integral equation (4.22) to the final value problem (4.23).

Adjoint PDE system

The analysis of the directional derivatives (4.16a)–(4.16b) eventually results in the adjoint PDE system (4.21), cf. the discussion in Section 3.4.1 and 3.4.2. Consequently, the optimality conditions with respect to both an optimal actuator configuration and excitation relies on an identical adjoint PDE system.

Gradient condition for optimal control trajectory

In order to optimize the control trajectory u, the directional derivative (4.16c) is considered yielding the reduced gradient

$$g_u = \int_\Omega \partial_u l(T,u;\theta)|_{y^*} - \Lambda^* \cdot \partial_u f_\Omega(K,u;\theta)|_{y^*} \; \mathrm{d}x + \int_\Gamma \Lambda^* \cdot \left(\chi_{\Gamma_\mathrm{N}} \, \partial_u f_{\Gamma_\mathrm{N}}(K,u)|_{y^*} - \chi_{\Gamma_\mathrm{D}} \, \partial_u f_{\Gamma_\mathrm{D}}(u)|_{y^*} \right) \mathrm{d}x \; , \quad (4.27)$$

also see Section 3.4.3. The reduced gradient $g_u := g_u(T,K,u;\theta)$ depends on the numerical solution of the adjoint PDE system (4.21). The conditional expression (3.40) takes the input constraints (4.7a) into account.

4.5 Numerical solution of the optimality conditions

The solution of optimization problem (4.12) follows the idea from Chapter 3 to combine optimization algorithms in MATLAB with FEM software. To this end, the gradient method in Algorithm 3.1 and the optimization framework shown in Figure 3.5 are adapted to the problem of optimizing the actuator configuration. The MATLAB environment is extended by a module that deals with the parametrization of the actuator configuration as illustrated in Figure 4.2. The interface between MATLAB and COMSOL MULTIPHYSICS not only facilitates to outsource the numerical issues related with multiphysics problems to the FEM software but also to manipulate the actuator position and shape during the gradient iterations.

The tailored gradient method shown in Algorithm 4.1 copes with the simultaneous optimization of the actuator configuration and excitation by taking advantage of the fact that both problems are linked to the adjoint PDE system (4.21). The gradient method starts with initial optimization variables $(u^{(1)},\theta^{(1)})$ to integrate the system dynamics $e_\mathrm{sys}(T,K,u^{(j)};\theta^{(j)}) = 0$, i. e., the PDE system (4.12b)–(4.12h), forwards in time, cf. step II.i) of Algorithm 4.1. The trajectories of the state variables $(T^{(j)},K^{(j)})$ obtained by this step allows one to numerically solve the adjoint dynamics $e_\mathrm{adj}(p,\Lambda,T^{(j)},K^{(j)},u^{(j)};\theta^{(j)}) = 0$ and $e_\mathrm{adj,ODE}(s,\Lambda^{(j)},T^{(j)},K^{(j)},u^{(j)};\theta^{(j)}) = 0$ specified by the PDE system (4.21) and the ODE system (4.23), cf. step II.ii). The adjoint systems are integrated backward in time and result in the trajectories of the adjoint state variables $(p^{(j)},\Lambda^{(j)},s^{(j)})$.

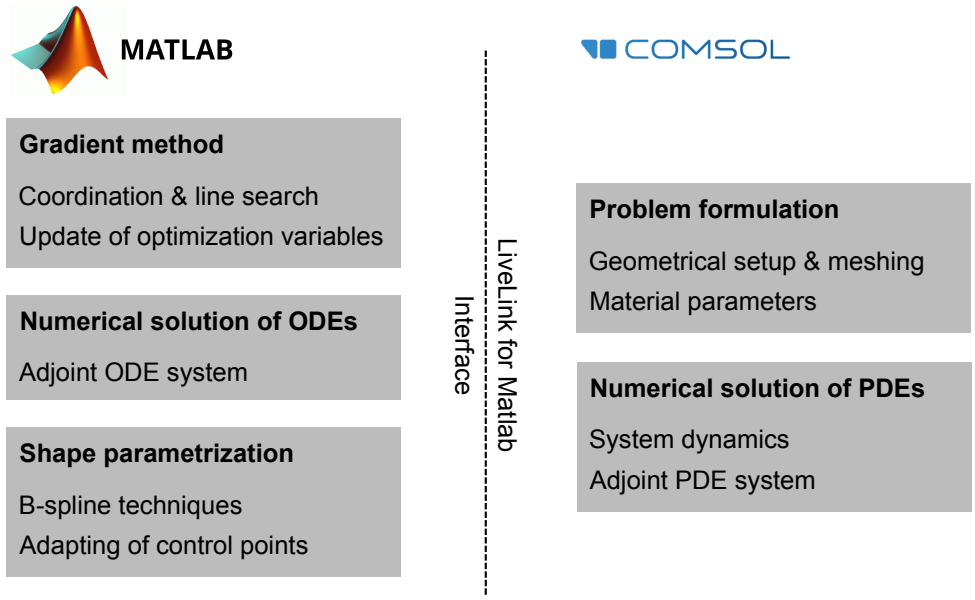

Figure 4.2: Optimization framework for solving optimization problem (4.12).

The canonical equations $e_{\text{sys}}(T, K, u^{(j)}; \theta^{(j)}) = 0$ and $e_{\text{adj}}(p, \Lambda, T^{(j)}, K^{(j)}, u^{(j)}; \theta^{(j)}) = 0$ are numerically solved by means of the FEM software COMSOL MULTIPHYSICS. Thereby, the separated initial and final time conditions (4.12e) and (4.21d) as well as the fact that the PDE systems comprise unconstrained state variables allows one to numerically solve them by means of simple forward and backward integrations in time. The adjoint ODE system $e_{\text{adj,ODE}}(s, \Lambda^{(j)}, T^{(j)}, K^{(j)}, u^{(j)}; \theta^{(j)}) = 0$ is numerically solved in MATLAB as illustrated in Figure 4.2, cf. step II.ii) of Algorithm 4.1.

The steps II.iii)–II.v) of Algorithm 4.1 are concerned with the update of the optimization variables $(u^{(j)}, \theta^{(j)})$. The current optimization variables and the gradients (4.26) and (4.27) are used to formulate the joint line search problem (4.28). The numerical solution of the line search problem provides the step size $\alpha^{(j)}$ and ensures the optimality of the interaction of the optimization variables u and θ.[4] Consequently, the update step (4.29) leads to improved optimization variables $(u^{(j+1)}, \theta^{(j+1)})$ in the sense of cost reduction.

For numerical reasons, the line search problem (4.28) and the update of the actuator configuration (4.29a) involve a scaling factor $\gamma > 0$ that adapts the different temporal and spatial scales of the optimization variables u and θ, see, e. g., [16]. The projection function

$$\psi_\beta(\beta) = \begin{cases} \beta^- & \text{if } \beta < \beta^- \\ \beta^+ & \text{if } \beta > \beta^+ \\ \beta & \text{else} \end{cases} \qquad \beta \in \{\theta, u\} \tag{4.30}$$

takes the conditional expressions of the reduced gradients (4.25) and (3.40) into account. Thus, the optimization variables $(\theta^{(j+1)}, u^{(j+1)})$ comply with the constraints (4.7) during the gradient iterations. The termination criterion (3.56) is used to quit Algorithm 4.1.

[4] A discussion about line search strategies to approximately solve (4.28) can be found in Section 3.5.1.

Algorithm 4.1 Gradient method for solving optimization problem (4.12).

I. **Initialization**

i) Choice of initial optimization variables $(\theta^{(1)}, u^{(1)})$.

ii) Select suitable termination criterion such as (3.56) with threshold $\epsilon_J > 0$.

II. **Gradient iteration $j = 1, 2, \ldots$**

i) Forward integration of system dynamics $e_{\text{sys}}(T, K, u^{(j)}; \theta^{(j)}) = 0$ specified by the PDE system (4.12b)–(4.12h) to obtain state trajectories $(T^{(j)}, K^{(j)})$.

ii) Backward integration of adjoint dynamics

- Solution of PDE system $e_{\text{adj}}(p, \Lambda, T^{(j)}, K^{(j)}, u^{(j)}; \theta^{(j)}) = 0$ specified by Equation (4.21) to obtain adjoint state trajectories $(p^{(j)}, \Lambda^{(j)})$.
- Solution of ODE system $e_{\text{adj,ODE}}(s, \Lambda^{(j)}, T^{(j)}, K^{(j)}, u^{(j)}; \theta^{(j)}) = 0$ specified by Equation (4.23) to obtain adjoint state trajectory $s^{(j)}$.

iii) Evaluation of the gradients (4.26) and (4.27) to obtain the current directions of steepest descent $-(g_\theta^{(j)}, g_u^{(j)})$.

iv) Numerical solution of line search problem

$$\alpha^{(j)} = \underset{\alpha>0}{\arg\min}\, J\left(\psi_u(u^{(j)} - \alpha g_u^{(j)}); \psi_\theta(\theta^{(j)} - \gamma\alpha g_\theta^{(j)})\right) \tag{4.28}$$

with projection function ψ_β, cf. Equation (4.30).

v) Update of optimization variables

$$\theta^{(j+1)} = \psi_\theta(\theta^{(j)} - \gamma\alpha^{(j)} g_\theta^{(j)}) \tag{4.29a}$$
$$u^{(j+1)} = \psi_u(u^{(j)} - \alpha^{(j)} g_u^{(j)}) \tag{4.29b}$$

following a steepest descent approach.

vi) Quit gradient method, if termination criterion (3.56) is fulfilled. Otherwise, set $j \leftarrow j + 1$ and return to step II.i).

4.6 Numerical results

In the following, the simultaneous optimization of the actuator configuration and excitation is presented for the surface hardening processes from Figure 4.1. To this end, the optimization problem (4.12) and the parametrization techniques from Section 4.1.2 are adapted to the individual heat-up scenarios. The numerical solution of the optimality conditions is provided by the optimization framework illustrated in Figure 4.2.

4.6.1 Surface hardening process with optimal inductor positions

The first simulation scenario optimizes the positions of $N = 6$ inductors of a surface hardening process, also see [109, 110]. The geometrical setup of the heat-up scenario is identical to Section 3.6.2 with the exception that the inductor positions are part of the optimal solution. The workpiece is made of steel with the material parameters shown in Table 4.1. The objective is to heat up the surface layer $\tilde{\Omega}_\mathrm{o}$ from $T_0 = 773\,\mathrm{K}$ to $T_\mathrm{d} = 1023\,\mathrm{K}$.[5] The time interval of the heat-up cycle $t \in (0, t_\mathrm{f})$ is specified by the final time $t_\mathrm{f} = 10\,\mathrm{s}$.

Table 4.1: Material parameters of the surface hardening process.

	workpiece Ω_o	inductor $\Omega_\mathrm{c}(\theta)$	air Ω_a	
rel. magnetic permeability μ_r	3	1	1	$[-]$
electrical conductivity σ	$4 \cdot 10^6$	0	0	[S/m]
density ρ	$7.9 \cdot 10^3$	-	-	$[\mathrm{kg/m^3}]$
heat capacity C	475	-	-	$[\mathrm{J/(kg\,K)}]$
thermal conductivity k	44.5	-	-	$[\mathrm{W/(m\,K)}]$
heat transfer coefficient α	1.54	-	-	$[\mathrm{W/(m^2\,K)}]$
emissivity of the surface ϵ	0.7	-	-	$[-]$

The optimization problem (4.12) with the Mayer and Lagrange terms (4.10) serves as the basis for the trajectory planning. The right hand sides of the thermal and electromagnetic subsystem (4.12b)–(4.12e) and (4.12f)–(4.12h) are specified by Equation (3.57). The inductor positions $\theta_{j,r}$ are subject to some constraints which stem from the requirement of a minimal air gap between the boundary of the inductors and the workpiece of $r_\mathrm{ag} = 5\,\mathrm{mm}$.[6] The control trajectory u is bounded by the interval $[0\,\mathrm{A}, 30\,\mathrm{A}]$. The angular frequency of the impressed currents is set to $\omega = 50\,\mathrm{kHz}$. During the heat-up process, the workpiece temperature must not exceed $T^+ = 1103\,\mathrm{K}$.

Table 4.2: Weights of cost functional (4.12a) for optimizing the inductor positions.

weight	objective
$q_1 = 10^1$	minimization of state error $(T - T_\mathrm{d})^2$ in surface layer $\tilde{\Omega}_\mathrm{o}$ (Mayer term)
$q_2 = 10^4$	minimization of state error $(T - T_\mathrm{d})^2$ in surface layer $\tilde{\Omega}_\mathrm{o}$ (Lagrange term)
$q_3 = 10^8$	violation of state constraint $T \leq T^+$ in workpiece Ω_o (Lagrange term)
$q_4 = 10^{-2}$	penalization of control action u^2 in $\Omega_\mathrm{c}(\theta)$ (Lagrange term)
$q_5 = 0$	minimization of state error $(T - T_0)^2$ in inner domains Ω_i (Lagrange term)

[5] The prior heat-up of the workpiece from the ambient temperature $T_\mathrm{a} = 293\,\mathrm{K}$ to the initial temperature $T_0 = 773\,\mathrm{K}$ can be tackled by means of the findings of Chapter 3.

[6] Equidistantly distributed inductors are assumed in the direction of z. The optimization of the inductor positions in the direction of r and z is presented in [111] for a similar heat-up problem.

The solution of optimization problem (4.12) with the weights shown in Table 4.2 is provided by the optimization framework from Section 4.5. Algorithm 4.1 approximately solves the line search problem (4.28) using the adaptive line search strategy. At the end of each gradient iteration j, the current inductor positions $\theta^{(j+1)}$ are used to update the actuator configuration within COMSOL MULTIPHYSICS. For this purpose, the capabilities of the interface between the software packages MATLAB and COMSOL MULTIPHYSICS are utilized. The termination criterion of Algorithm 4.1 is specified by Equation (3.56) with bound $\epsilon_J = 10^{-6}$.

The solid lines in Figure 4.3 shows the numerical solution of the coupled problem of optimizing the inductor positions and its electrical excitation. The optimal control trajectory u energizes the inductors in a way that the surface layer of the workpiece $\tilde{\Omega}_\mathrm{o}$ is heated up as homogeneously as possible to the desired temperature $T_\mathrm{d} = 1023\,\mathrm{K}$. The optimal heat-up behavior of the surface layer is illustrated by means of the trajectories of the minimum $\tilde{T}_\mathrm{min}(t)$, average $\tilde{T}_\mathrm{avg}(t)$, and maximum temperature $\tilde{T}_\mathrm{max}(t)$.

In order to assess the impact of optimizing the actuator configuration on the control performance, an auxiliary optimization problem is considered with a fixed distance of $r_\mathrm{ag} = 5\,\mathrm{mm}$ between the boundary of inductors and workpiece.[7] The dotted lines in Figure 4.3 are

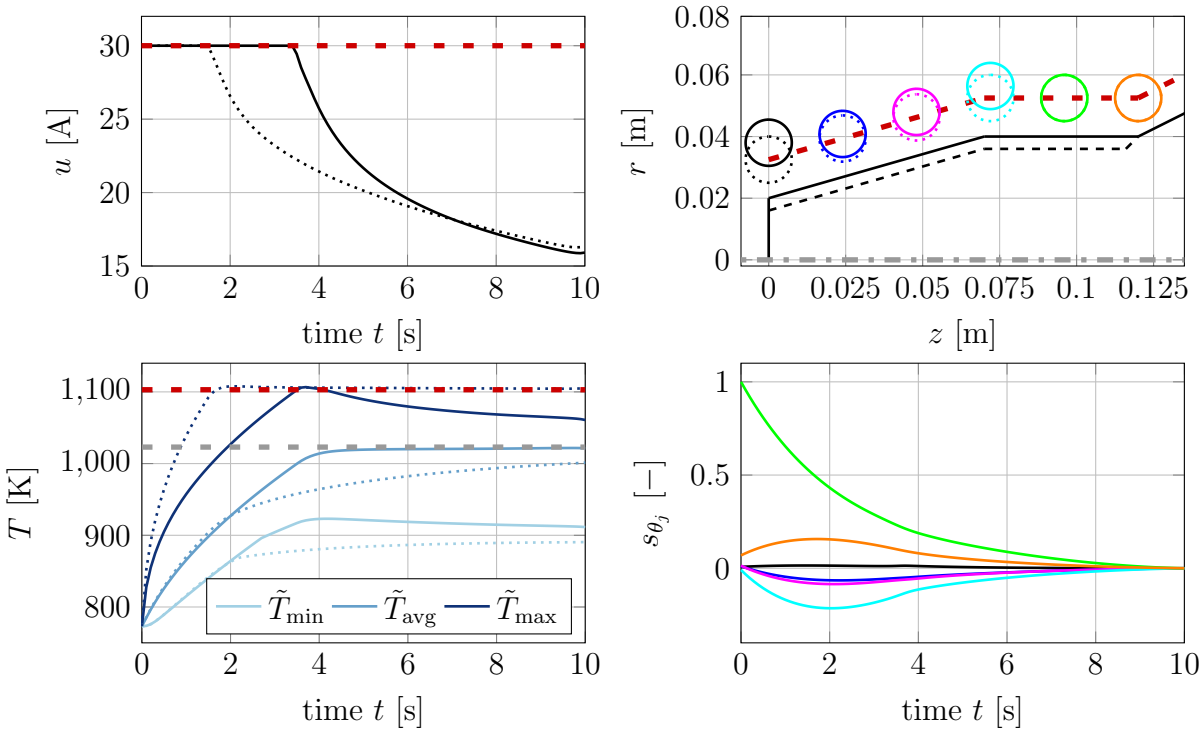

Figure 4.3: Optimized control trajectory u and actuator configuration θ (solid lines) leading to the minimum $\tilde{T}_\mathrm{min}$, average $\tilde{T}_\mathrm{avg}$, and maximum temperature $\tilde{T}_\mathrm{max}$ within the surface layer. The sensitivities $s_{\theta_j}(0)$ reflect the optimality of the actuator configuration. Results with fixed inductor positions are shown as dotted lines.

[7] Up to the fixed inductor positions and the material parameters shown in Table 4.1, the problem setting and numerical solution of optimization problem (4.12) is the same as the one described in Section 3.6.2.

related to the solution of this problem formulation. The significantly lower temperature range $\Delta T(t) = \tilde{T}_{\max}(t) - \tilde{T}_{\min}(t)$ in the case of optimized inductor positions compared to the case of fixed inductor positions is achieved on the basis of a much more homogeneous spatial distribution of the heat source within the surface layer.

The optimization of the actuator configuration makes it possible that the maximum temperature $\tilde{T}_{\max}(t)$ no longer has to be in the range of the state constraint $T^+ = 1103\,\mathrm{K}$ during the whole heat-up cycle, cf. Figure 4.3. The trajectory of the maximum surface temperature $\tilde{T}_{\max}(t)$ touches the temperature constraint (4.8) only for a short time interval and the average temperature $\tilde{T}_{\mathrm{avg}}(t)$ reaches the desired temperature $T_{\mathrm{d}} = 1023\,\mathrm{K}$ at the time instant $t = 5\,\mathrm{s}$ already. Consequently, the final time of the heat-up process t_{f} can be halved with a simultaneous increase of control performance.

The optimized actuator configuration shown in Figure 4.3 compensates the end and edge effects in contrast to the scenario with fixed inductor positions as good as possible. Especially the leftmost inductor (——) and the fourth one from the left (——) are placed farther away from the workpiece to weaken the end and edge effects. The second and third inductor (——,——) are slightly displaced with respect to the default position to counteract an increased accumulation of heat at the head of the workpiece. The fifth and sixth inductor (——,——) are placed as close as possible to the workpiece since the right part of the surface layer prones to stay below the desired temperature $T_{\mathrm{d}} = 1023\,\mathrm{K}$ due to a significantly lower intensity of the heat source in this region and heat conduction effects.

The sensitivities $s^*_{\theta_j}(t)$ in Figure 4.3 reflect the optimality of the actuator configuration. The trajectories relate to the last gradient iteration and clearly show that the gradients for optimizing the actuator configuration $g_\theta = [s^*_{\theta_1}(0), s^*_{\theta_2}(0), \ldots, s^*_{\theta_N}(0)]^{\mathsf{T}}$ are almost zero. Apart from the sensitivity of the fifth and sixth inductor (——,——), the inductor positions are in the allowable region and do not require to touch the constraints (4.7b) with respect to an optimal solution. Consequently, the sensitivities $s^*_{\theta_j}(t)$ of the first four inductors from the left are zero. In contrast to this, the two inductors on the right hand side are placed to the surface layer of the workpiece as close as possible to ensure that there is a sufficient heat source in this area. The exploitation of the constraints prevents the corresponding sensitivities from becoming zero, cf. Figure 4.3, also see Equation (4.25).

The convergence behavior of the inductor positions θ to their optimal solution is shown in Figure 4.4 during the gradient iterations. Figure 4.4 also shows the decrease of the normalized cost functional J_{n} both for the coupled optimization problem (solid lines) and for the problem with fixed inductor positions (dotted lines), cf. Equation (3.58) for a definition of the normalized cost functional. Although the convergence behavior of the coupled problem is somewhat slower, the optimization of the actuator configuration makes it possible to achieve a greater reduction of the cost functional. The decreased value of the cost functional is due to the optimal adaptation of the spatial distribution of the electromagnetic heat source to the heat-up behavior of the surface layer, as already discussed on the basis of the varying temperature range $\Delta T(t) = \tilde{T}_{\max}(t) - \tilde{T}_{\min}(t)$ in the case of optimized inductor positions and fixed inductor positions, cf. Figure 4.3.

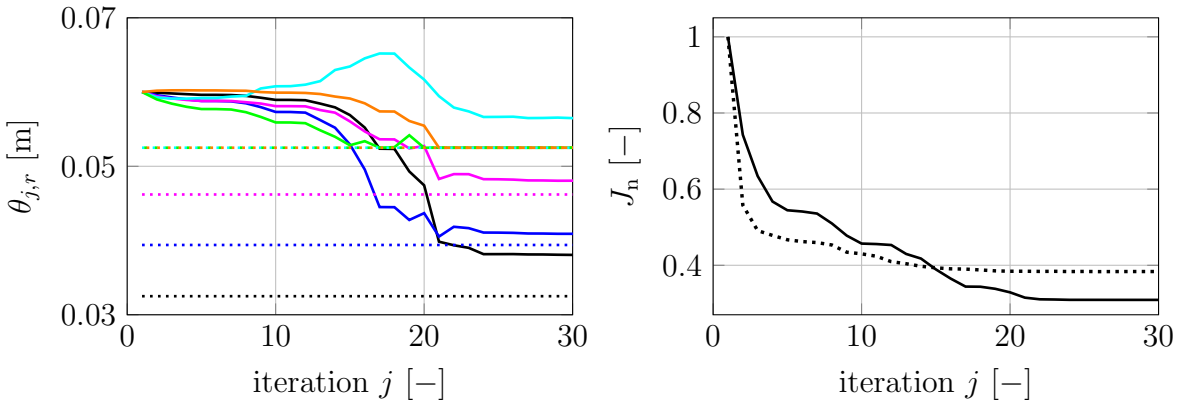

Figure 4.4: Convergence of the inductor positions $\theta_{j,r}$ to optimal solution and normalized cost functional J_n. Results with fixed inductor positions are shown as dotted lines.

The temperature profiles T in Figure 4.5 at the time instants $t \in \{1\,\mathrm{s}, 2\,\mathrm{s}, 4\,\mathrm{s}, 10\,\mathrm{s}\}$ illustrate the optimal heat-up behavior of the surface layer for the case of fixed inductor positions (upper row) and for an optimal actuator configuration (lower row). The end and edge effects are present even in the case of an optimal actuator configuration but are significantly weakened. Thus, the surface layer can be heated up more homogeneously and the surface hardening process is not restricted by local hot spots of the workpiece temperature in the end and edge layer due to the formulated temperature constraint (4.8).

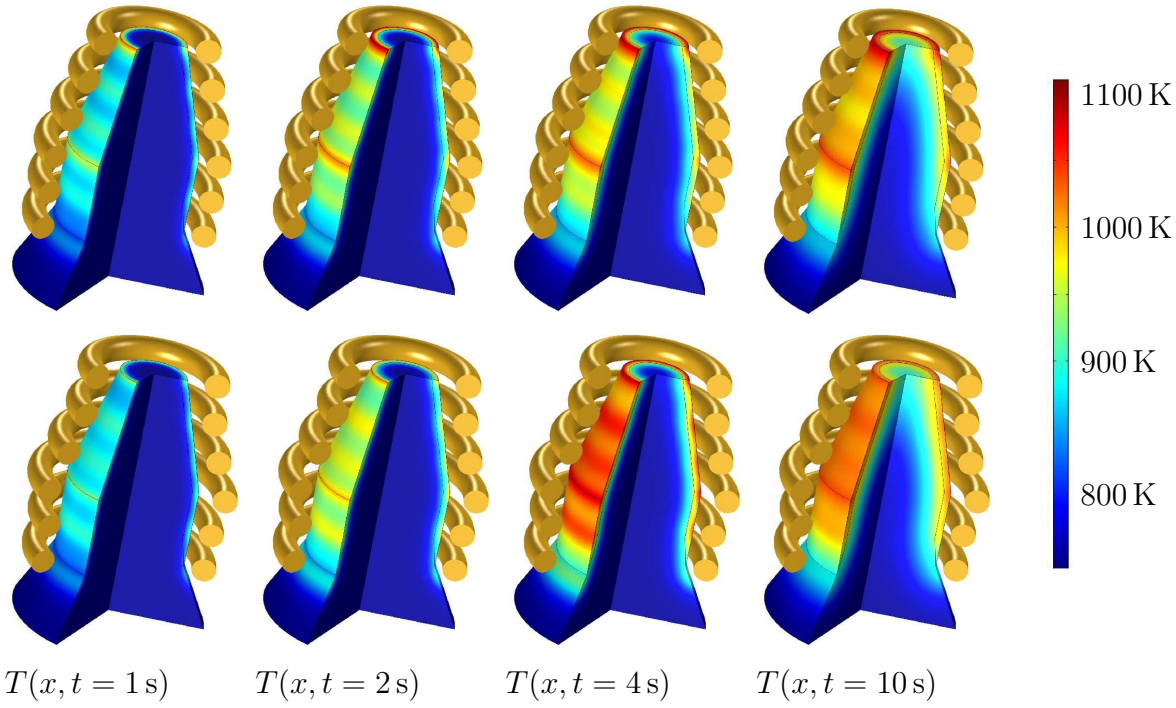

Figure 4.5: Temperature profiles T for fixed inductor positions (upper row) and optimized inductor positions (lower row).

4.6.2 Surface hardening process with optimal inductor shape

The second simulation scenario deals with the optimal actuator design for electromagnetic heating systems. For this purpose, the surface hardening process shown in Figure 4.1b is considered. To provide the optimization variables θ for the trajectory planning, the parametrization technique from Section 4.1.2 is applied to the inductor shape. The implementation of the B-spline parametrization technique is carried out in MATLAB, whereby the interface of the optimization framework shown in Figure 4.2 is used to adapt the geometrical setup for numerically solving the PDE systems $e_{\text{sys}}(T, K, u^{(j)}; \theta^{(j)}) = 0$ and $e_{\text{adj}}(p, \Lambda, T^{(j)}, K^{(j)}, u^{(j)}; \theta^{(j)}) = 0$ in COMSOL MULTIPHYSICS. Thus, the optimization problem (4.12) can be solved in each gradient iteration on the basis of the current actuator configuration.

The optimization problem (4.12) is numerically solved for different degrees of the basis functions p to be able to influence the smoothness of the inductor contour $\Gamma_{\text{c}}(\theta)$. A first case study deals with the objective to achieve optimal control performance, whereby significant deformations of the inductor contour will be accepted.[8] A second case study is presented with the purpose of obtaining a smooth inductor contour. The problem settings of the two case studies are identical to those in Section 4.6.1, also see [126, 111]. Table 4.3 shows the weights of the Mayer and Lagrange terms (4.10).

Table 4.3: Weights of cost functional (4.12a) for optimizing the inductor shape.

weight	objective
$q_1 = 10^1$	minimization of state error $(T - T_{\text{d}})^2$ in surface layer $\tilde{\Omega}_{\text{o}}$ (Mayer term)
$q_2 = 10^4$	minimization of state error $(T - T_{\text{d}})^2$ in surface layer $\tilde{\Omega}_{\text{o}}$ (Lagrange term)
$q_3 = 10^8$	violation of state constraint $T \leq T^+$ in workpiece Ω_{o} (Lagrange term)
$q_4 = 10^{-2}$	penalization of control action u^2 in $\Omega_{\text{c}}(\theta)$ (Lagrange term)
$q_5 = 10^2$	minimization of state error $(T - T_0)^2$ in inner domains Ω_{i} (Lagrange term)

Case study I

Figure 4.6 shows the parametrized inductor contour $\Gamma_{\text{c}}(\theta)$ using B-splines with $n = 24$ subintervals and tuples $\theta_j = [\theta_{j,r}, \theta_{j,z}]^{\mathsf{T}}$. The degree of the basis functions (4.6) is set to $p = 3$. This ensures that the numerical solution of optimization problem (4.12) results in an inductor contour which is locally adapted to end and edge effects within the surface layer. However, only the elements in the direction of r of the tuples $\{\theta_1, \theta_2, \ldots, \theta_{11}\}$ and the element in the direction of z of tuple θ_{12} are used to optimize the inductor shape. In order to obtain an inductor shape with uniform width in the direction of r, the spatial coordinates of the remaining elements of the tuples are a function of the optimization variables.

[8] The manufacturing of electromagnetic actuators by means of additive techniques, also referred to as 3D printing, is an active topic of research, see, e. g., [94, 47].

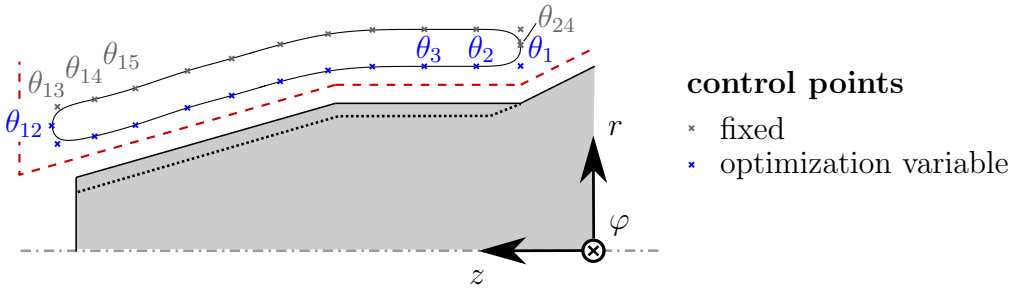

Figure 4.6: Parametrization of the inductor shape.

The parameter vector for shape optimization is specified by

$$\theta = [\theta_{1,r}, \theta_{2,r}, \ldots, \theta_{11,r}, \theta_{12,z}]^{\mathsf{T}}, \qquad \theta \in \mathbb{R}^{12} \tag{4.31}$$

and allows one to adapt important characteristics of the inductor shape such as the distance between outer boundary of the workpiece and inner inductor contour, as well as the inductor length. Geometrical constraints of the inductor shape are shown in Figure 4.6, which prevent a placement of the inductor too close to the workpiece, respectively limit its length.

The numerical solution of optimization problem (4.12) results in the sequence of inductor shapes shown in Figure 4.7. Optimization variable $\theta_{12,z}$ increases the inductor length by which a sufficiently large spatial domain of the upper region of the surface layer is exposed to the electromagnetic heat source. In addition, the distance between workpiece and inductor is increased in this region by optimization variable $\theta_{11,r}$ to mitigate the end effect. The combination of the increased inductor length and the mitigation of the end effect makes it possible to heat up the upper region of the surface layer as homogeneously as possible.

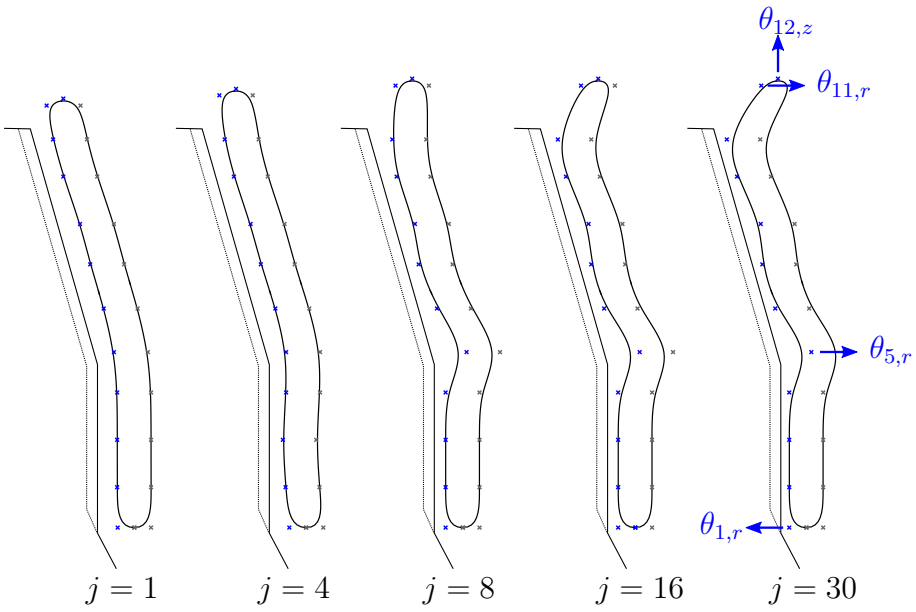

Figure 4.7: Sequence of inductor shapes for the gradient iterations $j = \{1, 4, 8, 16, 30\}$.

Similar to the adaptation of the inductor shape in the upper region, the edge effect is weakened by increasing the air gap between workpiece and inductor in the middle region by means of optimization variable $\theta_{5,r}$, cf. Figure 4.7. The optimization variables $(\theta_{6,r}, \theta_{7,r}, \ldots, \theta_{10,r})$ constitute a trade-off between a sufficiently large generation of the electromagnetic heat source in the upper region of the surface layer and a prevention of a too high accumulation of heat during the heat-up cycle. In order to heat up the lower region of the surface layer to the desired temperature as good as possible, the remaining optimization variables $(\theta_{1,r}, \theta_{2,r}, \ldots, \theta_{4,r})$ place the inductor as close as possible to the workpiece.

The numerical solution of optimization problem (4.12) also provides the optimal control trajectory u shown in Figure 4.8. Eventually, the simultaneous optimization of the actuator shape and excitation results in the trajectories of the minimum $\tilde{T}_{\min}(t)$, average $\tilde{T}_{\text{avg}}(t)$, and maximum temperature $\tilde{T}_{\max}(t)$ within the surface layer, cf. Figure 4.8. An important characteristic of the heat-up behavior is that the temperature constraint is not touched during the whole time interval. Actually, the optimized inductor shape provides a sufficiently homogeneous heat source within the surface layer by which it is not necessary to hit the constraint, also see Figure 4.9.

The advantage of optimizing the inductor shape over optimizing only its position as discussed in Section 4.6.1 can be observed in Figure 4.9 by means of the temperature profiles of both scenarios. In the case of an optimized inductor shape, the heat-up behavior of the surface layer benefits from the precise adjustment of the spatial distribution of the electromagnetic heat source (lower row). The major spatial domain of the surface layer is heated up closely to the desired temperature at the final time instant $t_{\text{f}} = 10\,\text{s}$. It can also be observed that the end and edge effects are further weakened compared to the case of optimized inductor positions (upper row). The mitigation of the distortion effects is particularly apparent for the temperature profiles of the workpiece at the time instants $t = 2\,\text{s}$ and $t = 4\,\text{s}$ in Figure 4.9 and is the main reason for the improved control performance.

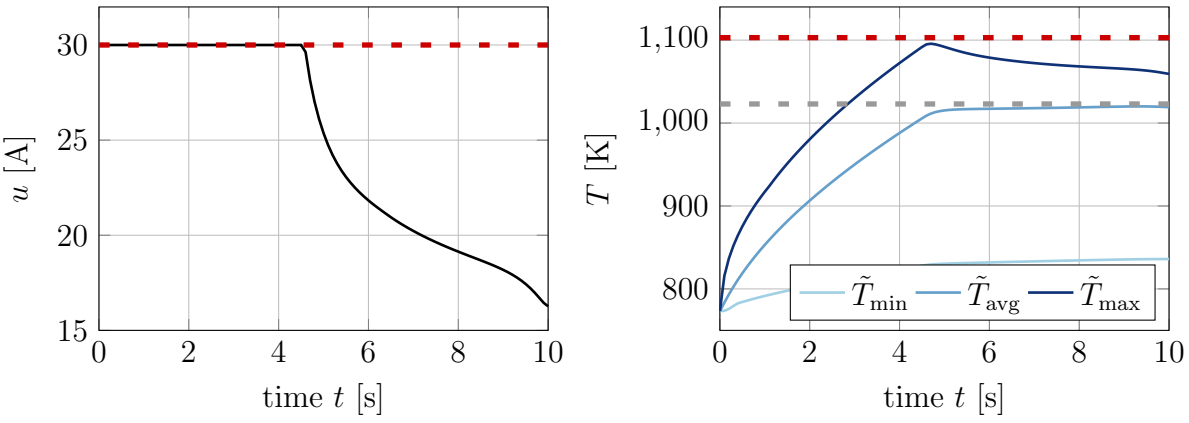

Figure 4.8: Control trajectory u and minimum $\tilde{T}_{\min}$, average $\tilde{T}_{\text{avg}}$, and maximum temperature $\tilde{T}_{\max}$ of the surface layer obtained with an optimal inductor shape.

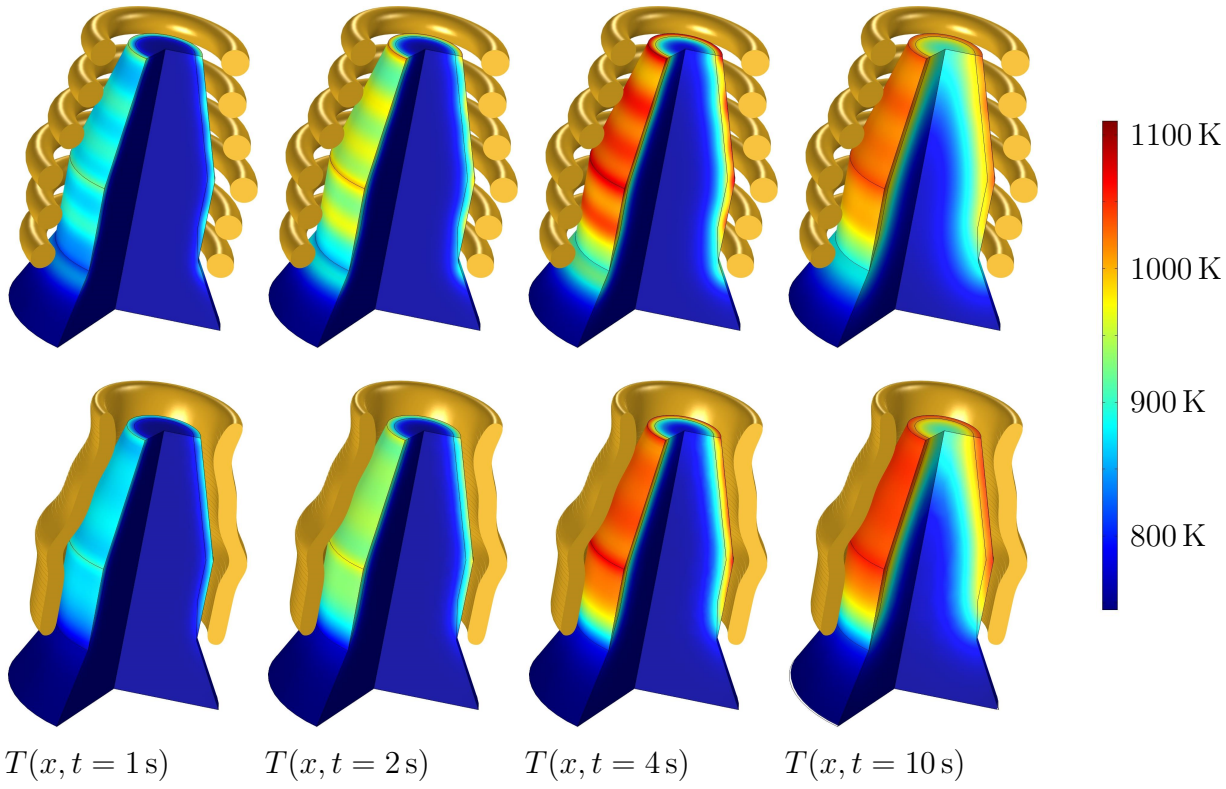

Figure 4.9: Temperature profiles of the workpiece T in the case of optimized inductor positions (upper row) and optimized inductor shape (lower row).

Case study II

For practical reasons (e. g. costs and efforts regarding the manufacturing of the inductor), there is often the demand for smooth contours of the inductor. The second case study deals with this problem by increasing the degree of the basis functions to $p = 8$. Consequently, the inductor contour $\Gamma_c(\theta)$ involves continuous derivatives up to the order of seven and the solution of optimization problem (4.12) naturally results in a smooth inductor contour. Beyond this modification, the problem settings correspond to the former case study.

Figure 4.10b shows the optimized inductor shape for the B-spline parametrization (4.4) with degree $p = 8$. For the sake of comparison, the inductor shape from the previous case study with $p = 3$ is illustrated in Figure 4.10a. The increase of the degree of the basis function p results in a smooth inductor contour $\Gamma_c(\theta)$. Only the middle region of the inductor is significantly adapted to cope with the predominant edge effect, cf. the discussion in Section 4.6.1. The relatively high degree of the basis functions $p = 8$ suppresses further spatial variations of the inductor contour.

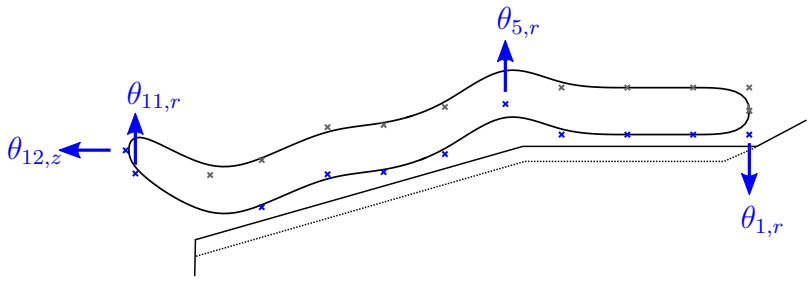

(a) Optimal inductor shape for a B-spline parametrization (4.4) with degree $p = 3$

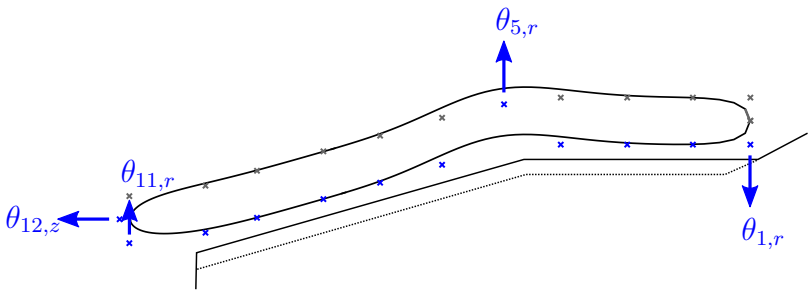

(b) Optimal inductor shape for a B-spline parametrization (4.4) with degree $p = 8$

Figure 4.10: Optimal inductor shapes with different degrees of smoothness of the contour $\Gamma_c(\theta)$. The major change of the smooth inductor shape with $p = 8$ is based on optimization variable $\theta_{5,r}$ to cope with the edge effect in a similar manner to the case $p = 3$.

Similar to the case $p = 3$, the inductor length is increased by optimization variable $\theta_{12,z}$, cf. Figure 4.10b. However, the distance between the left end of the workpiece and the inductor is only slightly increased by the optimization of parameter $\theta_{11,r}$. Moreover, the end effect is weakened but the small oscillations of the inductor contour $\Gamma_c(\theta)$ are not present as in the previous case, cf. Figure 4.10a. Note that the extension of the parameter vector (4.31) by optimization variable $\theta_{24,z}$ could be used to adapt the inductor length at the lower region of the surface layer to improve the heat-up behavior in this region, cf. Figure 4.9.

Further improvements of permitting uneven inductor contours can not be observed in the control trajectory u and the heat-up behavior of the surface layer with minimum $\tilde{T}_{\min}(t)$, average $\tilde{T}_{\text{avg}}(t)$, and maximum temperature $\tilde{T}_{\max}(t)$, as shown in Figure 4.11. The control u and the trajectories of the surface temperature differ only slightly for the cases of a smooth inductor contour (solid lines) and an uneven one (dotted lines). However, the secondary objective of the surface hardening process to prevent the heat-up of inner domains of the workpiece can be attacked superiorly by means of the uneven inductor contour.

As can be observed in Figure 4.11, the part of the cost functional (4.10) that penalizes the heat-up of inner domains of the workpiece

$$J_{T_0,\mathrm{n}} = \iint\limits_{\Omega\times(0,t_\mathrm{f})} \frac{q_5}{2}\chi_{\Omega_\mathrm{i}}\,(T-T_0)^2 \;\mathrm{d}x\,\mathrm{d}t / J^{(1)} \tag{4.32}$$

results in a smaller value in the case of the uneven inductor contour (dotted lines) compared to the smooth inductor contour (solid lines). On the contrary, the overall control performance is not significantly affected by the different inductor shapes as can be observed by the normalized cost functional J_n in Figure 4.11, cf. Equation (3.58). Note that the penalization of the quadratic error $(T-T_0)^2$ has a strong influence on optimization problem (4.12) which is why the corresponding weight is chosen relatively small and results in the low value of $J_{T_0,\mathrm{n}}$ as a part of the normalized cost functional J_n. In summary, both the smooth and uneven inductor contour lead to an optimal heat-up behavior of the surface hardening process.

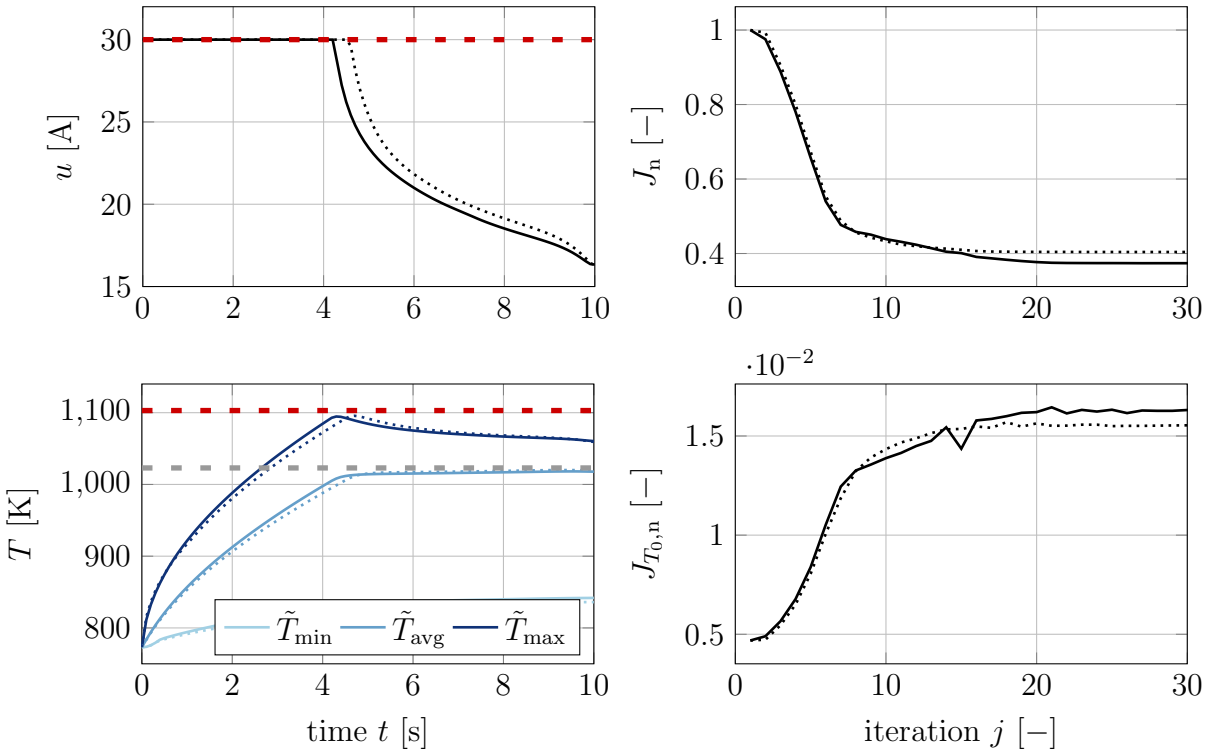

Figure 4.11: Numerical results of shape optimization with smooth (solid lines) and uneven inductor contour (dotted lines). In both cases, the optimal control trajectory u results in an almost identical heat-up behavior of the surface layer with minimum $\tilde{T}_\mathrm{min}$, average $\tilde{T}_\mathrm{avg}$, and maximum temperature $\tilde{T}_\mathrm{max}$. The normalized cost functionals J_n and $J_{T_0,\mathrm{n}}$ reveal that the uneven inductor contour has a beneficial impact on suppressing the heat-up of inner domains but not significantly affects the overall control performance.

4.7 Conclusions

This chapter extends the trajectory planning from Chapter 3 to account for the optimization of the actuator configurations of electromagnetic heating applications. The design of optimal actuator positions and shapes relies on suitable parametrization techniques to provide the degrees of freedom for spatially adapting the electromagnetic heat source. A PDE constrained optimization problem is considered for a simultaneous optimization of the actuator configuration and excitation.

The optimality conditions of the optimization problem are derived separately for optimizing the actuator configuration and excitation by applying the adjoint-based sensitivity analysis and the formal Lagrangian technique. The optimality conditions of both problems utilize the same adjoint PDE system and a simultaneous solution of the coupled problem can be carried out. The optimization of the actuator configuration involves only a further adjoint ODE system compared to the case of optimizing the actuator excitation. An extended version of the optimization framework from Chapter 3 is presented to cope with the coupled problem. The applicability and accuracy of the trajectory planning approach is illustrated for surface hardening processes involving different actuator configurations.

Chapter 5

State constrained trajectory planning

The trajectory planning approaches presented so far handle state constraints as soft constraints by penalty functions within the cost functional. This procedure has the shortcoming that the modified problem formulation reflects a trade-off between the original control tasks and the compliance of the state constraints. Thereby, the parametrization of the cost functional with penalty term is associated with trial-and-error tests to ensure that the influence of the individual parts of the cost functional is well balanced. The convergence behavior of the gradient method also becomes worse with increasing weights of the penalty term.

This chapter discusses an augmented Lagrangian method to deal with state constraints of electromagnetic heating systems such as constraints on the temperature. The appropriate formulation of an optimization problem and the derivation of its optimality conditions is one focus of this chapter. The derived optimality conditions are then numerically solved using an extended version of the optimization framework from Chapter 3. Two simulation studies demonstrate the applicability and accuracy of the state constrained trajectory planning.

5.1 Problem formulation

A problem formulation similar to that in Chapter 3 and 4 is considered to discuss the state constrained trajectory planning. At this current stage, the electromagnetic heating system is subject to the temperature constraint

$$h(T) = T(x,t) - T^{+} \leq 0 \qquad \text{in } \Omega_{\mathrm{o}} \times (0, t_{\mathrm{f}}) \tag{5.1}$$

with bound $T^{+} > 0$.[1] An application example concerns the induction heating processes from Chapter 3. To simplify the discussion about handling state constraints, the problem formulation includes an optimization of the control trajectory u, but ignores an optimization of the actuator configuration. Thus, only the constrained control trajectory

$$u(t) \in \mathcal{U}_{\mathrm{ad}} := \{u(t) \in \mathbb{R} \,|\, u^{-} \leq u(t) \leq u^{+}\} \tag{5.2}$$

serves as a degree of freedom for the trajectory planning.[2]

[1] The handling of constraints on the temperature gradient is discussed in Section 5.5.2.

[2] The simultaneous optimization of the actuator excitation and configuration by taking state constraints into account is presented in [111].

A suitable optimization problem for the state constrained trajectory planning reads

$$\min_{u(\cdot)\in\mathcal{U}_{\mathrm{ad}}} J(u) = \int_{\Omega} V(T(\cdot,t_{\mathrm{f}}))\,\mathrm{d}x + \iint_{\Omega\times(0,t_{\mathrm{f}})} l(T,u)\,\mathrm{d}x\,\mathrm{d}t \tag{5.3a}$$

$$\begin{aligned}
\text{s.t.}\quad & e_{\nabla,t}\left(\rho C,T\right) - e_{\Delta}\left(k,T\right) = f_{\Omega_{\mathrm{o}}}(T,K) && \text{in } \Omega_{\mathrm{o}}\times(0,t_{\mathrm{f}}) && (5.3b)\\
& e_{\nabla,x}\left(k,T\right) = f_{\Gamma_{\mathrm{o,N}}}(T) && \text{on } \Gamma_{\mathrm{o,N}}\times(0,t_{\mathrm{f}}) && (5.3c)\\
& T = f_{\Gamma_{\mathrm{o,D}}} && \text{on } \Gamma_{\mathrm{o,D}}\times(0,t_{\mathrm{f}}) && (5.3d)\\
& T(\cdot,0) = T_0 && \text{in } \Omega_{\mathrm{o}} \text{ at } t=0 && (5.3e)\\
& e_{\nabla\times,\nabla\times}\left(\mu^{-1},K\right) = f_{\Omega}(K,u) && \text{in } \Omega\times(0,t_{\mathrm{f}}) && (5.3f)\\
& e_{\nabla\times}\left(\mu^{-1},K\right) = f_{\Gamma_{\mathrm{N}}}(K,u) && \text{on } \Gamma_{\mathrm{N}}\times(0,t_{\mathrm{f}}) && (5.3g)\\
& e_{\times}\left(K\right) = f_{\Gamma_{\mathrm{D}}}(u) && \text{on } \Gamma_{\mathrm{D}}\times(0,t_{\mathrm{f}}) && (5.3h)\\
& h(T) \leq 0 && \text{on } \Omega_{\mathrm{o}}\times(0,t_{\mathrm{f}})\ . && (5.3i)
\end{aligned}$$

For the sake of transferability of the trajectory planning to other problems of electromagnetic heating, the governing equations of the thermal and electromagnetic subsystem (5.3b)–(5.3e) and (5.3f)–(5.3h) are formulated using the differential operators (3.15)–(3.16) and the generic right hand sides (3.18)–(3.19). A description of the thermal and electromagnetic phenomena with state variables (T,K) can be found in Chapter 2.

The cost functional to be minimized (5.3a) involves a Mayer term $V(T(\cdot,t_{\mathrm{f}}))$ and a Lagrange term $l(T,u)$ that are specified as follows

$$V(T(\cdot,t_{\mathrm{f}})) = \frac{q_1}{2}\chi_{\Omega_{\mathrm{d}}}\left(T(\cdot,t_{\mathrm{f}}) - T_{\mathrm{d}}\right)^2 \tag{5.4a}$$

$$l(T,u) = \frac{q_2}{2}\chi_{\Omega_{\mathrm{d}}}\left(T - T_{\mathrm{d}}\right)^2 + \frac{q_3}{2}\chi_{\Omega_{\mathrm{c}}}u^2\ . \tag{5.4b}$$

The characteristic function $\chi_{\Omega_{\mathrm{d}}}$ is used to penalize the quadratic between the temperature T and the desired temperature T_{d} on the spatial domain that should be heated up, also see Section 3.1.3. The characteristic function $\chi_{\Omega_{\mathrm{c}}}$ ensures to weight the control action u^2 only on the spatial domain of the actuator.

5.2 Augmented Lagrangian method

The augmented Lagrangian method reformulates the state constrained optimization problem (5.3) as a max-min problem for which optimality conditions can be derived in a straightforward manner. Moreover, the max-min problem is considerably easier to solve because it is no longer subject to state constraints. The maximization and minimization step can be performed separately from each other, what is particularly interesting from an algorithmic point of view, see, e. g., [16, 12, 69]. The formulation and numerical solution of the max-min problem is discussed in the following sections.

5.2.1 Formulation of a max-min problem

A commonly used approach in augmented Lagrangian theory is to transform the state constraint (5.3i) into the equality constraint

$$g(T,z) = h(T) + z = 0 \qquad \text{in } \Omega_\mathrm{o} \times (0, t_\mathrm{f}) \tag{5.5}$$

with slack variable $z := z(x,t) \geq 0$. This allows one to define the augmented cost functional

$$J_\beta(u,z,\mu) = J(u) + \iint\limits_{\Omega_\mathrm{o}\times(0,t_\mathrm{f})} \mu g(T,z) + \frac{\beta}{2} g(T,z)^2 \,\mathrm{d}x\,\mathrm{d}t \tag{5.6}$$

with Lagrange multiplier $\mu := \mu(x,t)$, also referred to as dual variable, and penalty parameter $\beta \geq 0$, see, e. g., [16]. The augmented cost functional $J_\beta(u,z,\mu)$ couples the equality constraint $g(T,z) = 0$ to the cost functional (5.3a) with the additional penalty term $g(T,z)^2$ for regularization purposes [16].

The augmented cost functional (5.6) must be minimized with respect to the primal variables (u,z) and maximized with respect to the dual variable μ. However, the minimization with respect to z can be solved analytically yielding $z^* = \max(0, -\mu/\beta - h(T))$, whereby the operator $\max(\cdot,\cdot)$ accounts for the constraint of the slack variable $z \geq 0$. This motivates the definition of the auxiliary function

$$\tilde{g}(T,\mu) = \max\left(h(T), -\mu/\beta\right) \qquad \text{in } \Omega_\mathrm{o} \times (0, t_\mathrm{f}) \;, \tag{5.7}$$

which facilitates the formulation of the augmented cost functional (5.6) in the absence of the slack variable z. The modified formulation of the augmented cost functional reads

$$J_\beta(u,\mu) = J(u) + \iint\limits_{\Omega_\mathrm{o}\times(0,t_\mathrm{f})} \mu\tilde{g}(T,\mu) + \frac{\beta}{2}\tilde{g}(T,\mu)^2 \,\mathrm{d}x\,\mathrm{d}t \;, \tag{5.8}$$

but consistency between Equation (5.6) and (5.8) can be shown by some straightforward manipulations, see, e. g., [16, 68].

On the basis of the augmented cost functional (5.8), the max-min problem

$$\max_{\mu(\cdot)} \min_{u(\cdot)\in\mathcal{U}_\mathrm{ad}} J_\beta(u,\mu) = J(u) + \iint\limits_{\Omega_\mathrm{o}\times(0,t_\mathrm{f})} \mu\tilde{g}(T,\mu) + \frac{\beta}{2}\tilde{g}(T,\mu)^2 \,\mathrm{d}x\,\mathrm{d}t \tag{5.9a}$$

$$\begin{aligned}
\text{s.t.} \quad & e_{\nabla,t}\left(\rho C, T\right) - e_\Delta\left(k, T\right) = f_{\Omega_\mathrm{o}}(T,K) && \text{in } \Omega_\mathrm{o} \times (0,t_\mathrm{f}) && \text{(5.9b)}\\
& e_{\nabla,x}\left(k, T\right) = f_{\Gamma_{\mathrm{o,N}}}(T) && \text{on } \Gamma_{\mathrm{o,N}} \times (0,t_\mathrm{f}) && \text{(5.9c)}\\
& T = f_{\Gamma_{\mathrm{o,D}}} && \text{on } \Gamma_{\mathrm{o,D}} \times (0,t_\mathrm{f}) && \text{(5.9d)}\\
& T(\cdot,0) = T_0 && \text{in } \Omega_\mathrm{o} \text{ at } t = 0 && \text{(5.9e)}\\
& e_{\nabla\times,\nabla\times}\left(\mu^{-1}, K\right) = f_\Omega(K,u) && \text{in } \Omega \times (0,t_\mathrm{f}) && \text{(5.9f)}\\
& e_{\nabla\times}\left(\mu^{-1}, K\right) = f_{\Gamma_\mathrm{N}}(K,u) && \text{on } \Gamma_\mathrm{N} \times (0,t_\mathrm{f}) && \text{(5.9g)}\\
& e_\times\left(K\right) = f_{\Gamma_\mathrm{D}}(u) && \text{on } \Gamma_\mathrm{D} \times (0,t_\mathrm{f}) && \text{(5.9h)}
\end{aligned}$$

is formulated, whereby the max-min problem without penalty term $\tilde{g}(T,\mu)^2$ is the dual formulation of the original primal problem (5.3). Note that both the minimization and the maximization of the augmented cost functional $J_\beta(u,\mu)$ with respect to the primal and dual variables u and μ is not affected by state constraints. Consequently, the max-min problem offers a promising alternative solution approach for the original problem.

5.2.2 Numerical solution of the max-min problem

Under the assumption of strong duality and existence of an optimal solution of the max-min problem (5.9), the saddle-point condition

$$J_\beta(u^*,\mu) \leq J_\beta(u^*,\mu^*) \leq J_\beta(u,\mu^*) \qquad \forall u \in \mathcal{U}_{\text{ad}}, \mu \tag{5.10}$$

holds for optimal primal and dual variables (u^*,μ^*), see, e. g., [142, 12, 69]. Roughly speaking, the assumption of strong duality allows one to approach the optimal saddle-point (u^*,μ^*) from "both sides" by alternately minimizing and maximizing the augmented cost functional (5.9a) in terms of steepest descent and ascent approaches. As shown in Algorithm 5.1, the minimization of the augmented cost functional $J_\beta(u,\mu)$ in step II.i) is separated from its maximization in step II.ii).

Minimization of the augmented cost functional

At the beginning of each iteration i of Algorithm 5.1, the augmented cost functional (5.9a) is minimized. The minimization step is considered for a fixed value of the dual variable $\mu^{(i)}$ and accounts for the system dynamics $e_{\text{sys}}(T,K,u)=0$, i. e., the PDE system (5.9b)–(5.9g). Eventually, the numerical solution of the PDE constrained optimization problem (5.11) provides the new primal variable $u^{(i+1)}$ as a function of the current dual variable $\mu^{(i)}$. A detailed discussion about handling this problem is the subject of Section 5.3 and 5.4.

Update of the dual variable

Step II.ii) of Algorithm 5.1 describes a steepest ascent approach to maximize the augmented cost functional (5.9a). To this end, the directional derivative

$$\left.\frac{\partial J_\beta(u,\mu)}{\partial \mu}\right|_{y^{(i+1)}} h_\mu = 0 \qquad \forall h_\mu \tag{5.15}$$

is analyzed to derive the direction of steepest ascent $g_\mu^{(i)} := g_\mu^{(i)}(x,t)$, whereby h_μ denotes the admissible directions of the dual variable μ and $y^{(i+1)} = (T^{(i+1)}, K^{(i+1)}, u^{(i+1)}, p^{(i+1)}, \Lambda^{(i+1)})$ the solution of minimization step II.i). To account for the fact that the state constraint (5.1) is defined on the spatial domain Ω_{o}, the directional derivative (5.15) is used to define the reduced gradient

$$g_\mu^{(i)} = \max\left(h(T^{(i+1)}), -\mu^{(i)}/\beta^{(i)}\right) \qquad \text{in } \Omega_{\text{o}} \times (0,t_{\text{f}}) \ . \tag{5.16}$$

Algorithm 5.1 Augmented Lagrangian method for solving max-min problem (5.9).

I. **Initialization**

i) Choice of initial primal and dual variables $(u^{(1)}, \mu^{(1)})$ and penalty parameter $\beta^{(1)}$.

ii) Set thresholds $(\epsilon_u, \epsilon_{T^+}) > 0$ of termination criterion (5.14).

II. **Augmented Lagrangian step $i = 1, 2, \ldots$**

i) Numerical solution of minimization problem

$$u^{(i+1)} = \underset{u(\cdot)\in\mathcal{U}_{\text{ad}}}{\arg\min}\ J_\beta(u, \mu^{(i)}) \tag{5.11a}$$

$$\text{s.t.}\ \ e_{\text{sys}}(T, K, u) = 0 \tag{5.11b}$$

following a steepest descent approach, cf. Algorithm 5.2.

ii) Update of dual variable by means of steepest ascent approach

$$\mu^{(i+1)} = \mu^{(i)} + \beta^{(i)} g_\mu^{(i)} \qquad \text{in } \Omega_{\text{o}} \times (0, t_{\text{f}}) \tag{5.12}$$

with gradient $g_\mu^{(i)}$ defined by Equation (5.16) and step size $\beta^{(i)}$.

iii) Update of penalty parameter

$$\beta^{(i+1)} = \begin{cases} \gamma_1 \beta^{(i)} & \text{if } \left\|\tilde{g}(T^{(i+1)}, \mu^{(i+1)})\right\|^2_{L_2(Q_{\text{o}})} > \kappa \left\|\tilde{g}(T^{(i)}, \mu^{(i)})\right\|^2_{L_2(Q_{\text{o}})} \\ \gamma_2 \beta^{(i)} & \text{if } \left\|\tilde{g}(T^{(i+1)}, \mu^{(i+1)})\right\|^2_{L_2(Q_{\text{o}})} \leq \epsilon_{T^+} \\ \beta^{(i)} & \text{else} \end{cases} \tag{5.13}$$

with norm (5.18), constant $\kappa \geq 0$, and adaptation factors $\gamma_1 \geq 1$ and $0 < \gamma_2 \leq 1$.

iv) Quit augmented Lagrangian method, if termination criterion

$$\frac{\left\|u^{(i+1)} - u^{(i)}\right\|^2_{L_2(0,t_{\text{f}})}}{\left\|u^{(1)}\right\|^2_{L_2(0,t_{\text{f}})}} \leq \epsilon_u \quad \wedge \quad \left\|\max\left(0, h(T^{(i+1)})\right)\right\|^2_{L_2(Q_{\text{o}})} \leq \epsilon_{T^+} \tag{5.14}$$

with thresholds $(\epsilon_u, \epsilon_{T^+}) > 0$ and norms (3.48) and (5.18) is fulfilled. Otherwise, set $i \leftarrow i + 1$ and return to step II.i).

This allows one to consider the steepest ascent approach (5.12) in step II.ii) of Algorithm 5.1, whereby the update of the dual variable (5.12) can also be formulated as

$$\mu^{(i+1)} = \max\left(0, \mu^{(i)} + \beta^{(i)} h(T^{(i+1)})\right) \qquad \text{in } \Omega_{\text{o}} \times (0, t_{\text{f}})\ . \tag{5.17}$$

As the step size in the direction of steepest ascent $g_\mu^{(i)}$, the penalty parameter $\beta^{(i)}$ is used, which is adapted after each maximization step using the heuristic (5.13). The step size $\beta^{(i)}$

is increased by the factor $\gamma_1 \geq 1$ if insufficient progress in improving the compliance with the inequality constraint $h(T) \leq 0$ is made compared to the previous augmented Lagrangian step. The step size is decreased by the factor $0 < \gamma_2 \leq 1$ if the constraint is sufficiently satisfied, also see [98]. The norm of the heuristic (5.13) is defined by

$$\|a\|^2_{L_2(Q_\mathrm{o})} := \iint\limits_{\Omega_\mathrm{o}\times(0,t_\mathrm{f})} a^2 \,\mathrm{d}x\,\mathrm{d}t \tag{5.18}$$

with $a := a(x,t)$. Note that a large adaptation factor γ_1 generally results in a fast convergence behavior of Algorithm 5.1. However, the max-min problem will be ill-conditioned for large dual variables $\mu^{(i)}$, so the increase of $\beta^{(i)}$ must be limited. A reference value for the adaptation factors is $\gamma_1 \in (4, 10)$ and $\gamma_2 = 0.9$ to achieve a good balance between fast convergence and a well-conditioned problem, also see [39, 111].

Termination of the augmented Lagrangian method

The augmented Lagrangian method is terminated if the minimization step II.i) results in no further improvement of the control trajectory $u^{(i+1)}$ and the state constraint $h(T^{(i+1)}) \leq 0$ is fulfilled with sufficient accuracy. To this end, step II.iv) of Algorithm 5.1 evaluates the termination criterion (5.14) with thresholds $(\epsilon_u, \epsilon_{T^+}) > 0$ and norms (3.48) and (5.18).

5.3 Optimality conditions for minimization step

The formal Lagrangian technique constitutes a promising approach to derive the optimality conditions of the PDE constrained optimization problem (5.11), whereby its similar structure to optimization problem (3.17) facilitates to recycle the results of Section 3.4 for deriving the optimality conditions. For minimizing the augmented cost functional (5.11a), the stationarity of the Lagrangian

$$\begin{aligned}
\mathcal{L} = &\int\limits_{\Omega} V(T(\cdot,t_\mathrm{f}))\,\mathrm{d}x + \iint\limits_{\Omega\times(0,t_\mathrm{f})} l(T,u)\,\mathrm{d}x\,\mathrm{d}t + \iint\limits_{\Omega_\mathrm{o}\times(0,t_\mathrm{f})} \mu^{(i)}\tilde{g}(T,\mu^{(i)}) + \frac{\beta^{(i)}}{2}\tilde{g}(T,\mu^{(i)})^2\,\mathrm{d}x\,\mathrm{d}t \\
&+ \iint\limits_{\Omega_\mathrm{o}\times(0,t_\mathrm{f})} p\left[e_{\nabla,t}\left(\rho C, T\right) - e_{\Delta}\left(k,T\right) - f_{\Omega_\mathrm{o}}(T,K)\right]\,\mathrm{d}x\,\mathrm{d}t \\
&+ \iint\limits_{\Gamma_{\mathrm{o,N}}\times(0,t_\mathrm{f})} p\left[e_{\nabla,x}\left(k,T\right) - f_{\Gamma_{\mathrm{o,N}}}(T)\right]\,\mathrm{d}x\,\mathrm{d}t + \iint\limits_{\Gamma_{\mathrm{o,D}}\times(0,t_\mathrm{f})} p\left[T - f_{\Gamma_{\mathrm{o,D}}}\right]\,\mathrm{d}x\,\mathrm{d}t \\
&+ \iint\limits_{\Omega\times(0,t_\mathrm{f})} \Lambda\cdot\left[e_{\nabla\times,\nabla\times}\left(\mu^{-1},K\right) - f_{\Omega}(K,u)\right]\,\mathrm{d}x\,\mathrm{d}t \\
&+ \iint\limits_{\Gamma_\mathrm{N}\times(0,t_\mathrm{f})} \Lambda\cdot\left[f_{\Gamma_\mathrm{N}}(K,u) - e_{\nabla\times}\left(\mu^{-1},K\right)\right]\,\mathrm{d}x\,\mathrm{d}t + \iint\limits_{\Gamma_\mathrm{D}\times(0,t_\mathrm{f})} \Lambda\cdot\left[e_{\times}\left(K\right) - f_{\Gamma_\mathrm{D}}(u)\right]\,\mathrm{d}x\,\mathrm{d}t
\end{aligned} \tag{5.19}$$

is analysed. The Lagrangian $\mathcal{L} := \mathcal{L}(T, K, u, \mu^{(i)}, p, \Lambda)$ couples the system dynamics (5.9b)–(5.9h) to the augmented cost functional (5.11a) using the adjoint states $p(x,t)$ and $\Lambda(x;t)$. Thus, the minimization of the augmented cost functional with respect to u can be reduced to the conditions of directional derivatives

$$\left.\frac{\partial \mathcal{L}}{\partial T}\right|_{y^*} h_T = 0 \qquad \forall h_T \tag{5.20a}$$

$$\left.\frac{\partial \mathcal{L}}{\partial K}\right|_{y^*} \cdot H_K = 0 \qquad \forall H_K \tag{5.20b}$$

$$\left.\frac{\partial \mathcal{L}}{\partial u}\right|_{y^*} h_u \geq 0 \qquad \forall u \in \mathcal{U}_{\mathrm{ad}} \ , \tag{5.20c}$$

also see Section 3.4. For the purpose of utilizing the directional derivatives within step II.i) of Algorithm 5.1, an adjoint PDE system and a gradient condition is formulated.

5.3.1 Adjoint PDE system

According to the findings of Section 3.4, the directional derivatives (5.20a)–(5.20b) will be fulfilled by formulating the adjoint PDE system

$$\begin{aligned}
e_{\nabla,t}\left(\rho C, p^*\right) + e_{\Delta}\left(k, p^*\right) &= g_{\Omega_\mathrm{o}}(T^*, K^*, u^*, \mu^{(i)}, p^*) && \text{in } \Omega_\mathrm{o} \times (0, t_\mathrm{f}) && (5.21a)\\
e_{\nabla,x}\left(k, p^*\right) &= g_{\Gamma_{\mathrm{o,N}}}(T^*, p^*) && \text{on } \Gamma_{\mathrm{o,N}} \times (0, t_\mathrm{f}) && (5.21b)\\
p^* &= 0 && \text{on } \Gamma_{\mathrm{o,D}} \times (0, t_\mathrm{f}) && (5.21c)\\
\rho C p^*(\cdot, t_\mathrm{f}) &= -\left.\partial_T V(T(\cdot, t_\mathrm{f}))\right|_{y^*} && \text{in } \Omega_\mathrm{o} \text{ at } t = t_\mathrm{f} && (5.21d)
\end{aligned}$$

$$\begin{aligned}
e_{\nabla\times,\nabla\times}\left(\mu^{-1}, \Lambda^*\right) - \left.\partial_K f_\Omega(K,u)\right|_{y^*} \cdot \Lambda^* &= g_\Omega(T^*, K^*, p^*) && \text{in } \Omega \times (0, t_\mathrm{f}) && (5.21e)\\
e_{\nabla\times}\left(\mu^{-1}, \Lambda^*\right) &= g_{\Gamma_\mathrm{N}}(K^*, u^*, \Lambda^*) && \text{on } \Gamma_\mathrm{N} \times (0, t_\mathrm{f}) && (5.21f)\\
e_{\times}\left(\Lambda^*\right) &= 0 && \text{on } \Gamma_\mathrm{D} \times (0, t_\mathrm{f}) \ , && (5.21g)
\end{aligned}$$

whereby the coupled subsystems (5.21a)–(5.21d) and (5.21e)–(5.21g) reflect the impact of the thermal and electromagnetic phenomena on the augmented cost functional (5.11a). Thereby, the right hand sides of the adjoint PDE system

$$\begin{aligned}
g_{\Omega_\mathrm{o}}(T^*, K^*, u^*, \mu^{(i)}, p^*) = {} & \left.\partial_T l(T,u)\right|_{y^*} - \left.\partial_T f_{\Omega_\mathrm{o}}(T,K)\right|_{y^*} p^* \\
& + \left.\partial_T \tilde{g}(T, \mu^{(i)})\right|_{y^*} \left(\mu^{(i)} + \beta^{(i)} \tilde{g}(T^*, \mu^{(i)})\right) \quad \text{in } \Omega_\mathrm{o} \times (0, t_\mathrm{f}) \qquad (5.22a)\\
g_{\Gamma_{\mathrm{o,N}}}(T^*, p^*) = {} & \left.\partial_T f_{\Gamma_{\mathrm{o,N}}}(T)\right|_{y^*} p^* \quad \text{on } \Gamma_{\mathrm{o,N}} \times (0, t_\mathrm{f}) \qquad (5.22b)
\end{aligned}$$

$$\begin{aligned}
g_\Omega(T^*, K^*, p^*) &= \chi_{\Omega_\mathrm{o}} p^* \left.\partial_K f_{\Omega_\mathrm{o}}(T,K)\right|_{y^*} && \text{in } \Omega \times (0, t_\mathrm{f}) && (5.22c)\\
g_{\Gamma_\mathrm{N}}(K^*, u^*, \Lambda^*) &= \left.\partial_K f_{\Gamma_\mathrm{N}}(K,u)\right|_{y^*} \cdot \Lambda^* && \text{on } \Gamma_\mathrm{N} \times (0, t_\mathrm{f}) && (5.22d)
\end{aligned}$$

reveal a similar structure as the adjoint PDE system in Chapter 3, where an outer penalty function approach is used to cope with state constraints, cf. Equation (3.29) and (3.37). A

difference to the case where no augmented Lagrangian method is applied is the right hand side of the adjoint subsystem (5.21a), cf. Equation (5.22a). The function $g_{\Omega_\mathrm{o}}(T^*, K^*, u^*, \mu^{(i)}, p^*)$ comprises the new part $\partial_T \tilde{g}(T, \mu^{(i)})\big|_{y^*} \left(\mu^{(i)} + \beta^{(i)} \tilde{g}(T^*, \mu^{(i)})\right)$.

The dual variable $\mu^{(i)}$ on the right hand side of the adjoint dynamics (5.21a) affects the optimality system in a way that an optimal solution complies with the state constraint (5.1) in terms of the augmented Lagrangian method. Furthermore, the part $\beta^{(i)} \tilde{g}(T^*, \mu^{(i)})$ mitigates the impact of the dual variable on the adjoint dynamics due to the regularization of the max-min problem by means of the penalty parameter $\beta^{(i)}$. The partial derivative of the function $\tilde{g}(T^*, \mu^{(i)})$ with respect to T reads as

$$\partial_T \tilde{g}(T, \mu^{(i)})\big|_{y^*} = \begin{cases} 1 & \text{if } h(T^*) > -\mu^{(i)}/\beta^{(i)} \\ 0 & \text{else} \end{cases} \qquad \text{in } \Omega_\mathrm{o} \times (0, t_\mathrm{f}) \tag{5.23}$$

and ensures, roughly speaking, that the parts $\mu^{(i)}$ and $\beta^{(i)} \tilde{g}(T^*, \mu^{(i)})$ affect the optimality system only if the state constraint (5.1) is violated.

5.3.2 Gradient condition for optimal primal variable

The directional derivative (5.20c) is used to formulate the gradient condition with respect to an optimal primal variable u. Similar to Section 3.4.3, the reduced gradient

$$g_u = \int_\Omega \partial_u l(T, u)\big|_{y^*} - \Lambda^* \cdot \partial_u f_\Omega(K, u)\big|_{y^*} \, \mathrm{d}x + \int_\Gamma \Lambda^* \cdot \left(\chi_{\Gamma_\mathrm{N}} \, \partial_u f_{\Gamma_\mathrm{N}}(K, u)\big|_{y^*} - \chi_{\Gamma_\mathrm{D}} \, \partial_u f_{\Gamma_\mathrm{D}}(u)\big|_{y^*}\right) \mathrm{d}x \tag{5.24}$$

is defined, whereby the negative gradient $-g_u$ is the direction of steepest descent and allows one to minimize the augmented cost functional (5.11a). To take the input constraints (5.2) into account, the conditional expression (3.40) is used.

5.3.3 Summary of the optimality conditions

The optimality conditions of minimization problem (5.11) comprise the canonical equations $e_\mathrm{sys}(T, K, u) = 0$ and $e_\mathrm{adj}(p, \Lambda, \mu^{(i)}, T, K, u) = 0$ specified by the PDE systems (5.9b)–(5.9h) and (5.21), respectively. The reduced gradient (5.24) represents the information of the adjoint dynamics with respect to minimize the augmented cost functional (5.11a).

5.4 Numerical solution of the minimization step

This section presents the numerical solution of minimization problem (5.11) for the sequence of dual variables $\mu^{(i)}$ provided by Algorithm 5.1. The optimality conditions from the previous section are numerically solved by means of a tailored gradient method and an extended version of the optimization framework from Chapter 3.

5.4.1 Tailored gradient method

The tailored gradient method shown in Algorithm 5.2 solves minimization problem (5.11) using the current primal and dual variables from Algorithm 5.1. After this initialization step, the first gradient iteration j starts with the numerical solution of the canonical equations $e_{\mathrm{sys}}(T, K, u^{(i,j)}) = 0$ and $e_{\mathrm{adj}}(p, \Lambda, \mu^{(i)}, T^{(i,j)}, K^{(i,j)}, u^{(i,j)}) = 0$. The canonical equations are integrated forwards and backwards in time and result in the trajectories of the current state variables $(T^{(i,j)}, K^{(i,j)})$ and adjoint state variables $(p^{(i,j)}, \Lambda^{(i,j)})$, cf. step II.i)–II.ii).

Algorithm 5.2 Gradient method for solving minimization problem (5.11).

I. **Initialization**

i) Initialize gradient method with primal variable $u^{(i,1)} = u^{(i)}$ from Algorithm 5.1.

ii) Get current dual variable $\mu^{(i)}$ from Algorithm 5.1.

iii) Get thresholds $(\epsilon_u, \epsilon_{T^+}) > 0$ of termination criterion (5.27) from Algorithm 5.1.

II. **Gradient iteration $j = 1, 2, \ldots$**

i) Integration of system dynamics $e_{\mathrm{sys}}(T, K, u^{(i,j)}) = 0$ forwards in time to obtain state trajectories $(T^{(i,j)}, K^{(i,j)})$.

ii) Integration of adjoint dynamics $e_{\mathrm{adj}}(p, \Lambda, \mu^{(i)}, T^{(i,j)}, K^{(i,j)}, u^{(i,j)}) = 0$ backwards in time to obtain adjoint state trajectories $(p^{(i,j)}, \Lambda^{(i,j)})$.

iii) Evaluation of gradient (5.24) to obtain direction of steepest descent $-g_u^{(i,j)}$.

iv) Numerical solution of line search problem

$$\alpha^{(i,j)} = \arg\min_{\alpha>0} J_\beta(\psi_u\left(u^{(i,j)} - \alpha g_u^{(i,j)}\right), \mu^{(i)}) \tag{5.25}$$

with projection function ψ_u, cf. Equation (3.44).

v) Update of primal variable

$$u^{(i,j+1)} = \psi_u\left(u^{(i,j)} - \alpha^{(i,j)} g_u^{(i,j)}\right) \tag{5.26}$$

following a steepest descent approach.

vi) Quit gradient method and set primal variable $u^{(i+1)} = u^{(i,j+1)}$ in Algorithm 5.1, if termination criterion

$$\frac{\left\|u^{(i,j+1)} - u^{(i,j)}\right\|^2_{L_2(0,t_\mathrm{f})}}{\left\|u^{(i,1)}\right\|^2_{L_2(0,t_\mathrm{f})}} \leq \epsilon_u \quad \vee \quad \left\|\max\left(0, h(T^{(i,j+1)})\right)\right\|^2_{L_2(Q_\mathrm{o})} > \gamma_3\, \epsilon_{T^+} \tag{5.27}$$

with $\gamma_3 > 1$ is fulfilled, whereby at least $N_{\min} > 2$ gradient iterations are considered. Otherwise, set $j \leftarrow j + 1$ and return to step II.i).

The steps II.iii)–II.v) of Algorithm 5.2 deal with the update of the primal variable $u^{(i,j)}$ following a steepest descent approach. To this end, the negative gradient $-g_u^{(j)}$ is determined using Equation (5.24). The step size in the direction of steepest descent $\alpha^{(i,j)}$ follows from the numerical solution of line search problem (5.25). This allows one to update the control trajectory (5.26), whereby the projection function ψ_u takes the input constraints (5.2) into account, cf. Equation (3.44).

If either the sequence of primal variables $u^{(i,j)}$ converges to at least a local optimum or the violation of the state constraint $h(T^{(i,j+1)}) \leq 0$ exceeds a critical threshold, the minimization of the augmented cost functional is interrupted, cf. step II.vi) of Algorithm 5.2. Instead, the augmented Lagrangian step from Algorithm 5.1 is carried out. The switchover from the minimization to the maximization step is described by termination criterion (5.27) with the thresholds $(\epsilon_u, \epsilon_{T^+})$, the constant $\gamma_3 > 1$, and the norms (3.48) and (5.18). The minimization step is not interrupted until at least $N_{\min} > 2$ gradient iterations are carried out. To achieve a good and robust convergence behavior, the reference value $N_{\min} \in (3, 6)$ is proposed.

5.4.2 Extended optimization framework

The numerical solution of the max-min problem (5.9) is tackled by means of the optimization framework shown in Figure 5.1. The augmented Lagrangian method and the tailored gradient method from Algorithm 5.1 and 5.2 are implemented in MATLAB, whereby an interface to the FEM-based simulation software COMSOL MULTIPHYSICS is used to separate the numerical issues of the state constrained trajectory planning from the algorithmic ones, also see the discussion in Section 3.5.

The sequence control of Algorithm 5.2 in MATLAB corresponds to Algorithm 3.1, but is extended by the augmented Lagrangian step described in Algorithm 5.1. The numerical solution of the canonical equations $e_{\text{sys}}(T, K, u^{(i,j)}) = 0$ and $e_{\text{adj}}(p, \Lambda, \mu^{(i)}, T^{(i,j)}, K^{(i,j)}, u^{(i,j)}) = 0$ is outsourced to the FEM software COMSOL MULTIPHYSICS. The corresponding simulation

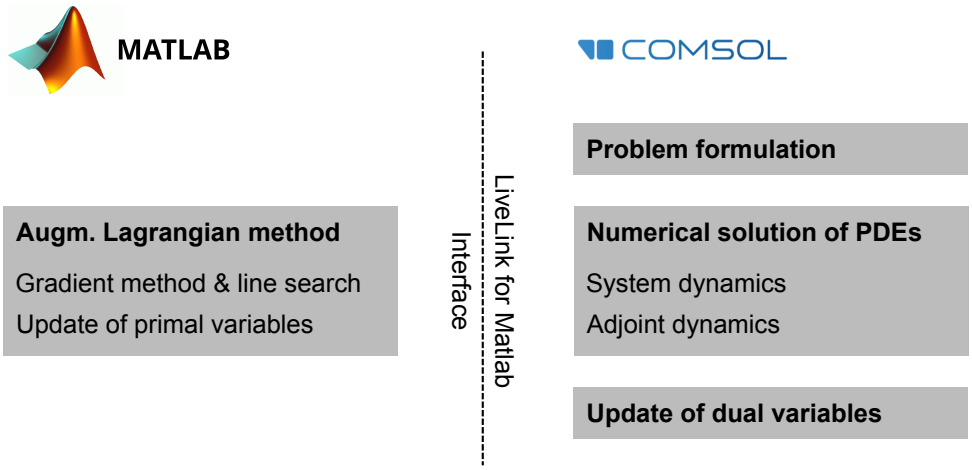

Figure 5.1: Extended optimization framework for solving max-min problem (5.9).

results are provided MATLAB to cope with the update of the primal variable $u^{(i,j)}$ in the steps II.iii)–II.v) of Algorithm 5.2. The update of the dual variable $\mu^{(i)}$ in the step II.ii) of Algorithm 5.1 is carried out in COMSOL MULTIPHYSICS. This allows one to outsource the memory management for the dual variable $\mu^{(i)}$ to the FEM software, which is especially advantageous for problems with state constraints defined on complex spatial domains.

5.5 Numerical results

This section presents numerical results of the state constrained trajectory planning. The optimization framework from the previous section is applied to a surface hardening and a constant heat-up process including constraints on the temperature and temperature gradient. The simulation scenarios reveal the capability of the optimization-based approach to plan trajectories that accurately satisfy state constraints.

5.5.1 Surface hardening process with temperature constraint

The first simulation study deals with the state constrained trajectory planning of a surface hardening process. The problem formulation is similar to Section 3.6.2. Figure 3.10 shows the geometrical setup of the surface hardening process encompassing six inductors Ω_{c_j} and the axisymmetrical workpiece Ω_{o} with surface layer $\tilde{\Omega}_{\mathrm{o}}$.

The control task consists in heating up the surface layer from the initial temperature $T_0 = 773\,\mathrm{K}$ to the desired temperature $T_{\mathrm{d}} = 1023\,\mathrm{K}$. The temperature constraint (5.1) is specified by the bound $T^+ = 1078\,\mathrm{K}$, which is significantly lower than in the problem formulation from Chapter 3 to demonstrate the accuracy of the augmented Lagrangian method. The input constraints (5.2) are specified by the interval $[0\,\mathrm{A}, 30\,\mathrm{A}]$, whereby the angular frequency of the impressed currents is set to $\omega = 50\,\mathrm{kHz}$. For the state constrained trajectory planning, an optimal actuator configuration is considered. To this end, the optimization framework from Chapter 4 is applied but not discussed in what follows.

The max-min problem (5.9) is numerically solved with the weights of the Mayer and Lagrange terms (5.4) as specified by Table 5.1. The initial penalty parameter is set to $\beta^{(1)} = 10^2$. The update law of the penalty parameter (5.13) uses the adaptation factors $\gamma_1 = 4$ and $\gamma_2 = 0.8$ as well as the factor $\kappa = 1.8$. The termination criteria (5.14) and (5.27) are evaluated with the bounds $\epsilon_u = 10^{-8}$ and $\epsilon_{T^+} = 10^{-5}$ and the constant $\gamma_3 = 10^3$.

Table 5.1: Weights of the Mayer and Lagrange terms (5.4) for the surface hardening process.

weight	objective
$q_1 = 10^1$	minimization of state error $(T - T_{\mathrm{d}})^2$ in surface layer $\tilde{\Omega}_{\mathrm{o}}$ (Mayer term)
$q_2 = 10^4$	minimization of state error $(T - T_{\mathrm{d}})^2$ in surface layer $\tilde{\Omega}_{\mathrm{o}}$ (Lagrange term)
$q_3 = 10^{-2}$	penalization of control action u^2 in Ω_{c} (Lagrange term)

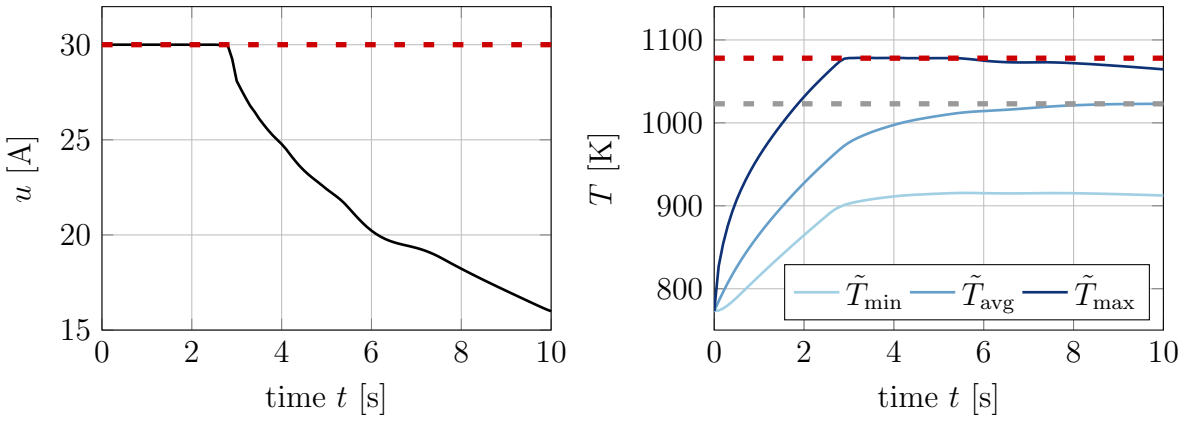

Figure 5.2: Control trajectory u leading to an optimal heat-up behavior of the surface layer with minimal, average, and maximum temperature $\tilde{T}_i$, $i \in \{\min, \text{avg}, \max\}$.

Figure 5.2 shows the optimized control trajectory u and the trajectories of the minimum, average, and maximum surface temperature $\tilde{T}_i(t)$, $i \in \{\min, \text{avg}, \max\}$. The temperature constraint $T \leq T^+$ with bound $T^+ = 1078\,\text{K}$ is well exploited by the trajectory $\tilde{T}_{\max}(t)$, making it possible to heat up the surface layer as fast as possible to the desired temperature $T_\text{d} = 1023\,\text{K}$. To comply with the temperature constraint, the optimization variable u adapts the electromagnetic heat source to the heat-up behavior of the workpiece.

5.5.2 Heat-up process with temperature gradient constraint

The second simulation scenario is concerned with heating a cylindrical workpiece from the initial temperature $T_0 = 293\,\text{K}$ to the desired temperature $T_\text{d} = 773\,\text{K}$ on the time interval $t \in (0, t_\text{f})$ with final time $t_\text{f} = 100\,\text{s}$. The absolute value of the temperature gradient must not exceed $|\nabla T^+| = 9 \cdot 10^3\,\text{K/m}$ during the heat-up process, what is a typical requirement to confine mechanical stresses of the workpiece [118]. The inductor currents are subject to the input constraints $u(t) \in [0\,\text{A}, 200\,\text{A}]$. The angular frequency is set to $\omega = 1\,\text{kHz}$.

The geometrical setup of the heat-up process comprises a workpiece made of aluminium alloy with radius $r = 0.06\,\text{m}$ and height $h = 0.2\,\text{m}$, three inductors with cross section surface $A_\text{c} = 7.5^2\,\pi\,10^{-6}\,\text{m}^2$ and coil windings $N_\text{c} = 100$, and the ambient air, cf. Figure 5.3. The air gap between inductor and workpiece is set to $r_\text{ag} = 10\,\text{mm}$. Table 5.2 shows the material parameters of the system dynamics.

To apply the augmented Lagrangian method to the problem considered in these lines, the inequality constraint $h(\nabla T)$ and the function $\tilde{g}(\nabla T, \mu)$ are defined as follows

$$h(\nabla T) = |\nabla T|^2 - |\nabla T^+|^2 \leq 0 \qquad \text{in } \Omega_\text{o} \times (0, t_\text{f}) \tag{5.28a}$$

$$\tilde{g}(\nabla T, \mu) = \max\left(h(\nabla T), -\mu/\beta\right) \qquad \text{in } \Omega_\text{o} \times (0, t_\text{f}) \tag{5.28b}$$

with $|\nabla T|^2 = \nabla T \cdot \nabla T$, cf. Equation (5.1) and (5.7). Thus, a max-min problem similar to the formulation (5.9) can be considered for handling the optimal trajectory planning problem including constraints on the temperature gradient.

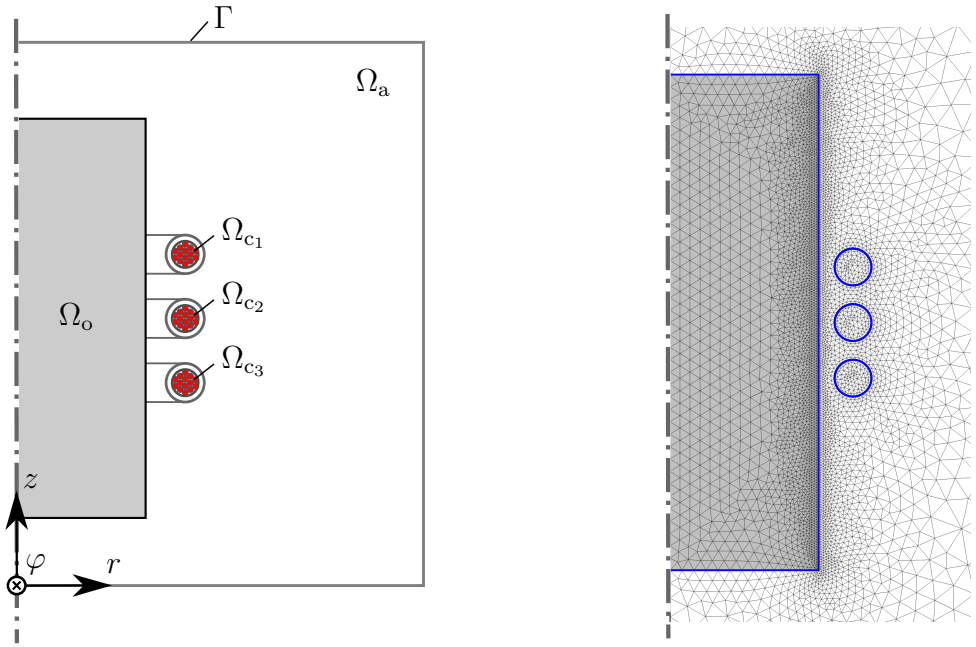

(a) Geometrical setup (not to scale) (b) Meshed spatial domain (detail view)

Figure 5.3: Geometrical setup and meshed spatial domain of the heat-up process.

The optimality conditions of the new max-min problem correspond to those from Section 5.3. The replacement of the constraint (5.1) and function (5.7) by Equation (5.28), however, lead to modified versions of the right hand sides of the adjoint subsystem (5.22a)–(5.22b). For the problem considered in these lines, the right hand sides are defined as follows

$$\begin{aligned} g_{\Omega_\mathrm{o}}(T^*, K^*, u^*, \mu, p^*) = {} & \partial_T l(T,u)\big|_{y^*} - \partial_T f_{\Omega_\mathrm{o}}(T,K)\big|_{y^*}\, p^* \\ & + \tilde{f}_{\Omega_\mathrm{o}}(\Delta T^*)\left(\mu^{(i)} + \beta^{(i)} \tilde{g}(\nabla T^*, \mu^{(i)})\right) \quad \text{in } \Omega_\mathrm{o} \times (0, t_\mathrm{f}) \qquad (5.29a) \\ g_{\Gamma_{\mathrm{o,N}}}(T^*, p^*) = {} & \tilde{f}_{\Gamma_{\mathrm{o},N}}(\nabla T^*) + \partial_T f_{\Gamma_{\mathrm{o,N}}}(T)\big|_{y^*}\, p^* \quad \text{on } \Gamma_{\mathrm{o,N}} \times (0, t_\mathrm{f})\ , \qquad (5.29b) \end{aligned}$$

whereby the new functions $\tilde{f}_{\Omega_\mathrm{o}}(\Delta T)$ and $\tilde{f}_{\Gamma_\mathrm{o}}(\nabla T)$ read as

$$\tilde{f}_{\Omega_\mathrm{o}}(\Delta T) = \begin{cases} -2\, e_\Delta\,(1, T^*) & \text{if } h(\nabla T^*) > -\mu^{(i)}/\beta^{(i)} \\ 0 & \text{else} \end{cases} \quad \text{in } \Omega_\mathrm{o} \times (0, t_\mathrm{f}) \qquad (5.30a)$$

$$\tilde{f}_{\Gamma_{\mathrm{o},N}}(\nabla T) = \begin{cases} 2\, e_{\nabla,x}\,(1, T^*) & \text{if } h(\nabla T^*) > -\mu^{(i)}/\beta^{(i)} \\ 0 & \text{else} \end{cases} \quad \text{on } \Gamma_{\mathrm{o,N}} \times (0, t_\mathrm{f})\ . \qquad (5.30b)$$

The functions (5.30) result from the part $\tilde{g}(\nabla T, \mu)$ when carrying out the directional derivative (5.20a). In this regard, Green's second identity (3.27) is used to shift the spatial operator ∇T from the admissible directions h_T to the state variable T.

The max-min problem specified above is solved with the weights of the Mayer and Lagrange terms (5.4) from Table 5.3. The initial penalty parameter is $\beta^{(1)} = 10^2$, whereby the update step (5.13) uses the constants $\gamma_1 = 4$, $\gamma_2 = 0.8$, and $\kappa = 2.5$. The stopping criteria (5.14) and (5.27) uses the bounds $\epsilon_u = 10^{-8}$ and $\epsilon_{T^+} = 10^{-5}$ as well as the constant $\gamma_3 = 10^3$.

Table 5.2: Material parameters of the heat-up process.

	workpiece Ω_o	inductor Ω_c	air Ω_a	
rel. magnetic permeability μ_r	1	1	1	[–]
electrical conductivity σ	$3.77 \cdot 10^7$	0	0	[S/m]
density ρ	$2.7 \cdot 10^3$	-	-	[kg/m^3]
heat capacity C	900	-	-	[J/(kg K)]
thermal conductivity k	238	-	-	[W/(m K)]
heat transfer coefficient α	6.8	-	-	[W/(m^2 K)]
emissivity of the surface ϵ	0.060	-	-	[–]

Table 5.3: Weights of the Mayer and Lagrange terms (5.4) for the heat-up process.

weight	objective
$q_1 = 10^5$	minimization of state error $(T - T_d)^2$ in workpiece Ω_o (Mayer term)
$q_2 = 10^3$	minimization of state error $(T - T_d)^2$ in workpiece Ω_o (Lagrange term)
$q_3 = 10^{-2}$	penalization of control action u^2 in Ω_c (Lagrange term)

The numerical results provided by the optimization framework are shown in Figure 5.4. The solution of the state constrained problem is compared to those of the unconstrained counterpart (dotted lines). In the former case, it can be seen that the control trajectory u hits its upper bound only initially and decreases afterwards to ensure that the absolute value of the maximum temperature gradient $|\nabla T|_{\max}(t)$ does not exceed $|\nabla T^+| = 9 \cdot 10^3$ K/m.

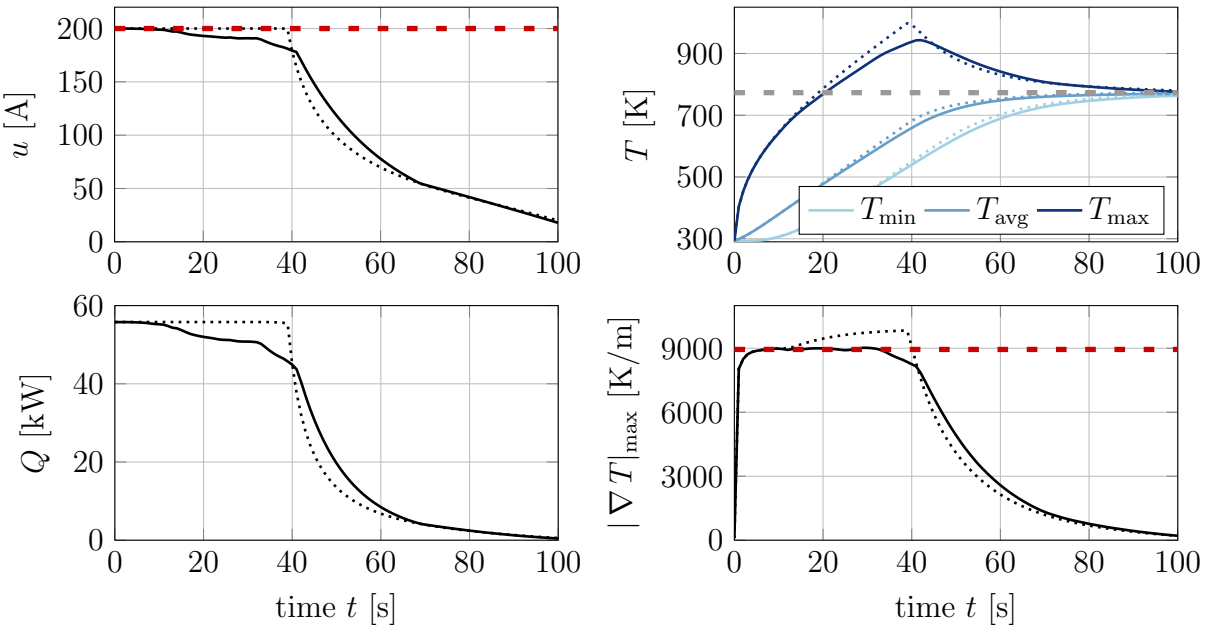

Figure 5.4: Optimal trajectories of the heat-up process with constraints on the temperature gradient (solid lines) and without constraints (dotted lines).

For both the scenario with and without temperature gradient constraints, the control trajectory u appropriately adjusts the power over the time interval $t \in (0, 100\,\mathrm{s})$ that is induced within the workpiece

$$Q(t) = \int_{\Omega_\mathrm{o}} \tfrac{\sigma\omega^2}{2} |A|^2 \, \mathrm{d}x \ , \tag{5.31}$$

cf. Figure 5.4. However, the control trajectory is increased for a short period of time after $t = 40\,\mathrm{s}$ in the case of a constrained temperature gradient (solid lines) compared to the unconstrained scenario (dotted lines). This compensates in the scenario with constraints the reduced power at the beginning of the heat-up process, what is necessary to comply with the temperature gradient constraint (5.28a). In both cases, the trajectories of the minimum $T_\mathrm{min}(t)$, average $T_\mathrm{avg}(t)$, and maximum workpiece temperature $T_\mathrm{max}(t)$ are harmonized with the desired temperature $T_\mathrm{d} = 773\,\mathrm{K}$ at the end of the heat-up process.

The spatial profiles of the absolute value of the temperature gradient $|\nabla T|$ are shown in Figure 5.5 for different time instants of the heat-up process with constraints on the temperature gradient. Due to an accumulation of heat at regions of the workpiece close to the inductors, individual areas occur where the temperature gradient increases rapidly, cf. the profiles at $t = 2\,\mathrm{s}$ and $t = 4\,\mathrm{s}$. These hot spots can be interpreted as equipotential surfaces which are especially pronounced during the time interval $t \in (10\,\mathrm{s}, 30\,\mathrm{s})$, where the optimized trajectories hit the state constraint $|\nabla T| \leq 9 \cdot 10^3\,\mathrm{K/m}$, cf. the profile of Figure 5.5 at $t = 10\,\mathrm{s}$ and the trajectory of the absolute value of the maximum gradient of the temperature $|\nabla T|_\mathrm{max}(t)$ in Figure 5.4.

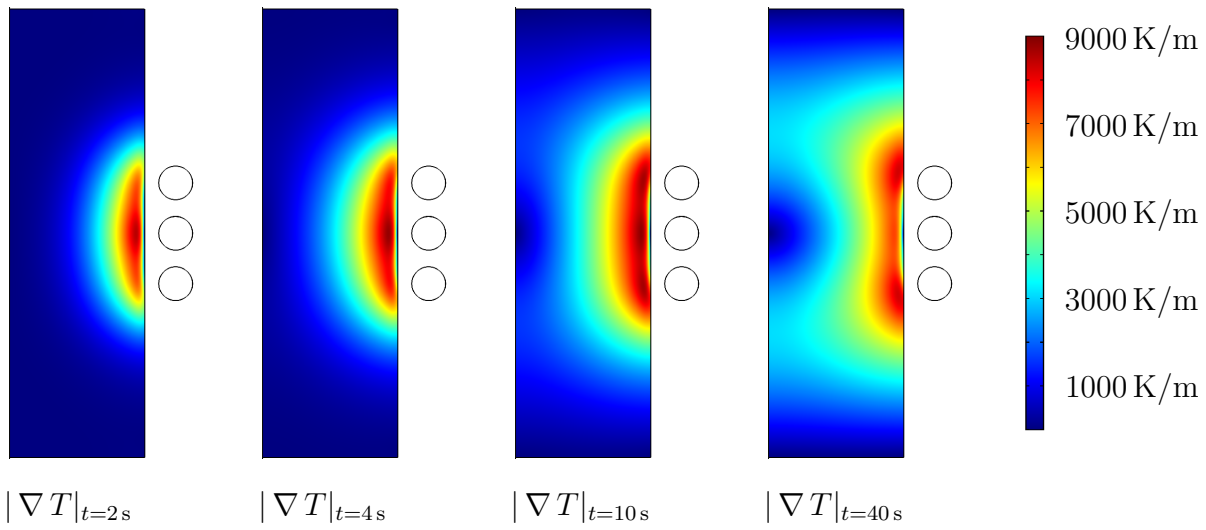

Figure 5.5: Absolute value of the temperature gradient $|\nabla T|$.

5.6 Conclusions

The optimization frameworks from Chapter 3 and 4 have been extended to account for state constraints in a more systematic manner compared to the outer penalty function approach. An augmented Lagrangian method is presented to replace the original problem by a max-min problem that can be numerically solved considerably easier, since the mutual minimization and maximization of the augmented cost functional are problem formulations that comprise no state constraints.

The augmented Lagrangian method is illustrated for a surface hardening process and a constant heat-up process including constraints on the temperature and the gradient of the temperature. The optimized trajectories of the electromagnetic heating systems exploit the state constraints highly accurate and lead to an optimal heat-up behavior.

Chapter 6

Conclusions and outlook

The trajectory planning of electromagnetic heating systems constitutes a multiphysics problem including electromagnetic and thermal phenomena. Generally speaking, the objective is to heat up specific spatial domains of an electrically conductive object. An important aspect of the trajectory planning concerns the proper electrical excitation of the actuator in order to achieve a desired heat-up behavior. Another important point concerns the spatial actuator design itself. Both degrees of freedom can be utilized to manipulate the intensity and spatial distribution of the electromagnetic heat source. The compliance of state constraints such as a constraints on the temperature or temperature gradient are typical requirements for electromagnetic heating applications.

In this thesis, the optimal trajectory planning of electromagnetic heating systems is tackled by formulating and numerically solving a PDE constrained optimization problem. The optimization of the electrical excitation and spatial configuration of the actuator relies on the formal Lagrangian technique and the adjoint-based sensitivity analysis. The corresponding optimality conditions are derived in the function space of the original problem formulation following a FOTD approach to ensure that not only the system dynamics but rather the whole optimality system can be numerically solved by means of FEM-based simulation software. The solution approach is characterized by its generality to deal with typical problems of electromagnetic heating. This means that different excitation strategies for the actuator, geometrical setups with arbitrary complexity, and various application examples such as induction heating processes or hyperthermia therapy can be handled with relative ease.

In order to account for state constraints, an outer penalty function approach and augmented Lagrangian method are presented.[1] The augmented Lagrangian method attacks the state constrained trajectory planning problem from an algorithmic point of view and circumvents the crucial point of manually choosing suitable weights for the outer penalty function. An important side effect is that the algorithmic implementation of the augmented Lagrangian method can be incorporated into the optimization frameworks already used for optimizing the excitation and spatial configuration of the actuator.

[1] Appendix A presents a transformation approach to deal with state constraints more analytically.

The three main components of this thesis, i. e., the optimal excitation of the actuator, its optimal spatial configuration, and the incorporation of state constraints for the trajectory planning, are tackled by an optimization framework that closely couples FEM software and optimization algorithms. The state-of-the-art FEM software COMSOL MULTIPHYSICS and the software package MATLAB are combined to cope with the trajectory planning problem. The algorithmic level of the optimization framework in MATLAB consists of a gradient method, respectively an augmented Lagrangian method, to solve the optimality conditions. The numerical effort that is associated with the trajectory planning, however, is outsourced to COMSOL MULTIPHYSICS. An interface between MATLAB and COMSOL MULTIPHYSICS ensures the interaction of the algorithmic and numerical level.

The primary benefit of the optimization framework lies in the usage of well known algorithms and solvers to numerically solve the canonical equations of the multiphysics problems. Furthermore, the integrated CAD tools of the FEM software allow to handle the description of the geometrical setup of the trajectory planning problems with relative ease. Another important characteristic of the optimization framework concerns the automated meshing of the domain of interest for which the canonical equations are numerically solved. This is particularly advantageous if complex geometries are involved and in the context of shape optimization since different candidates of actuator shapes are relatively easy to handle during the gradient iterations.

The trajectory planning approach is exemplified for various types of electromagnetic heating, as they typically arise in induction heating processes and hyperthermia therapy. The geometrical setups considered in this thesis range from two-dimensional spatial domains in the course of hyperthermia therapy over axisymmetrical setups of surface hardening processes to complex spatial domains of induction heat-up processes of a gear wheel. The presented simulation studies demonstrate the generality of the solution approach as well as the accuracy and general applicability of the optimization-based trajectory planning.

There are several promising extensions of the optimization framework. The numerical findings of the state constrained trajectory planning can be applied to real processes of induction heating or hyperthermia scenarios after suitable parameter identification techniques have been applied to estimate the material parameters of the electromagnetic and thermal subsystems. Another interesting extension of the optimization framework is to consider additional multiphysics phenomena such as metallurgical effects or thermo-mechanical strains and stresses. The integration of such physical phenomena into the mathematical model of the system dynamics improves the accuracy of the trajectory planning, but makes it more difficult to validate the mathematical model. It also remains to show that the optimality conditions of the new problem formulation can be derived and incorporated into the optimization framework.

Appendix A

Transformation approach for constraint handling

A transformation approach is discussed to cope with state constraints in a more analytic way compared to the outer penalty function approach in Chapter 3 and 4 as well as the augmented Lagrangian method in Chapter 5. The proposed approach makes use of an analytic preprocessing step relying on a constraint transformation technique.

The idea of the transformation approach goes back to optimal control problems governed by ODEs [53, 52, 71]. In a first step, the state constraints are substituted on the basis of saturation functions. As a result, the constrained state and input variables can be mapped onto new unconstrained counterparts. This reformulation step facilitates to transform the constrained system dynamics into an unconstrained one with the new variables serving as the states and inputs. The transformation approach eventually results in a new optimization problem, which inherently complies with the state constraints. The advantage of this state constraint handling is based on established optimization methods that can be used to numerically solve the new problem.

The following lines address how the transformation technique can be modified to cope with state constraints in the context of PDE constrained optimization. The modified approach preserves the structure of the optimality conditions from the previous chapters and allows to outsource its numerical solution to the respective optimization frameworks.

A.1 Transformation of state constrained optimization problems

The transformation approach is exemplified for optimization problem (5.3). However, the state constraints are handled in a more general way by replacing (5.3i) by the two-sided inequality constraint

$$T^- \leq T(x,t) \leq T^+ \qquad \text{in } \Omega_\mathrm{o} \times (0, t_\mathrm{f}) \ . \tag{A.1}$$

The upper and lower bounds $T^\pm$ are assumed to be symmetric.[1]

[1] To simplify matters, the notation $(\cdot)^\pm$ is used to address both symbols $(\cdot)^+$ and $(\cdot)^-$.

A.1.1 Saturation function approach and transformation instructions

The transformation approach substitutes the constrained state variable $T \in [T^-, T^+]$ by an equivalent unconstrained counterpart. In order to realize such a coordinate transformation, the saturation function

$$\Psi(\xi) = T^+ - \frac{T^+ - T^-}{1 + \mathrm{e}^{s\xi}} \qquad \text{in } \Omega_\mathrm{o} \times (0, t_\mathrm{f}) \tag{A.2}$$

is introduced with $\xi := \xi(x, t)$ serving as a new state variable. The parameter s is chosen as

$$s = \frac{4}{T^+ - T^-} \tag{A.3}$$

in order to normalize the slope of the saturation function (A.2) at $\xi = 0$ to $\partial_\xi \Psi(\xi) = 1$, also see [52]. Figure A.1 shows the characteristic of the saturation function $\Psi(\xi)$ of mapping the feasible interval (T^-, T^+) onto the unconstrained interval $(-\infty, \infty)$.

The saturation function approach (A.2) allows one to express the constrained state variable T within the new unconstrained coordinates of ξ. The applicability of this interchange of coordinates is due to the characteristic of the saturation function (A.2) to be asymptotic with respect to ξ, i. e.,

$$\lim_{\xi \to \pm\infty} \Psi(\xi) = T^\pm \qquad \text{in } \Omega_\mathrm{o} \times (0, t_\mathrm{f}) \ . \tag{A.4}$$

Thus, the bounds $T^\pm$ are only approached in the limit $\xi \to \pm\infty$, cf. Figure A.1. Another important characteristic of the saturation function $\Psi(\xi)$ is its behavior to be strictly monotonically increasing on the whole interval $\xi \in (-\infty, \infty)$ resulting in

$$\partial_\xi \Psi(\xi) > 0 \qquad \forall \xi \qquad \text{in } \Omega_\mathrm{o} \times (0, t_\mathrm{f}) \ , \tag{A.5}$$

as shown in Figure A.1.

Both the transformation of the constrained state variable T to its unconstrained counterpart ξ and the corresponding inverse transformation are formally defined by

$$T = \Psi(\xi) \ , \qquad \Psi : (-\infty, \infty) \to (T^-, T^+) \qquad \text{in } \Omega_\mathrm{o} \times (0, t_\mathrm{f}) \tag{A.6a}$$

$$\xi = \Psi^{-1}(T) \ , \qquad \Psi^{-1} : (T^-, T^+) \to (-\infty, \infty) \qquad \text{in } \Omega_\mathrm{o} \times (0, t_\mathrm{f}) \ , \tag{A.6b}$$

also see [137]. Thereby, the inverse of the saturation function

$$\Psi^-(T) = \frac{1}{s} \ln\left(\frac{T - T^-}{T^+ - T}\right) \qquad \text{in } \Omega_\mathrm{o} \times (0, t_\mathrm{f}) \tag{A.7}$$

follows from Equation (A.2).

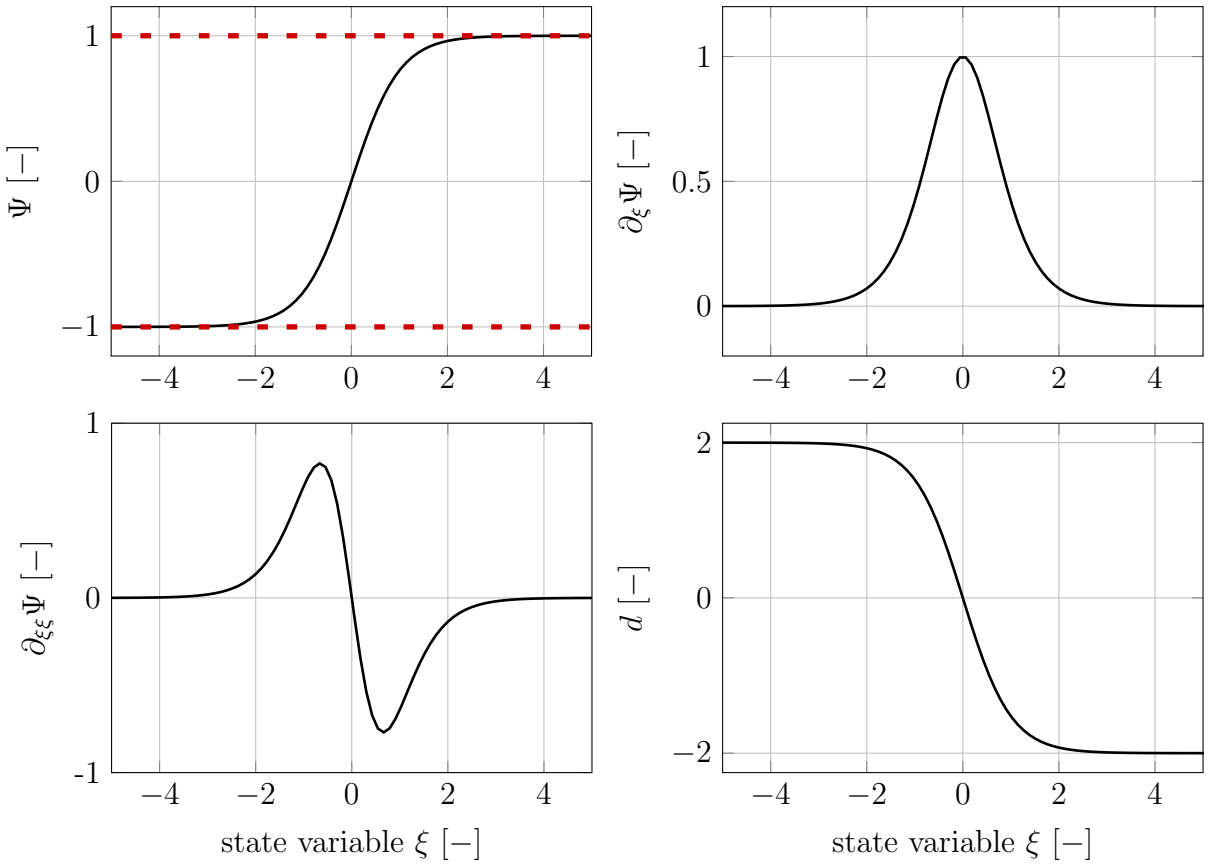

Figure A.1: Saturation function $\Psi(\xi)$ with bounds $T^{\pm} = \pm 1$ with partial derivatives of first and second order with respect to ξ, and function $d(\xi) = k\,\partial_{\xi\xi}\Psi/\partial_{\xi}\Psi$, cf. Equation (A.12).

The transformation (A.6a) can directly be applied to parts of optimization problem (5.3) that neither involve temporal nor spatial operators, whereby the transformation of the cost functional (5.3a) results in the transformed Mayer and Lagrange terms

$$\tilde{V}(\xi(\cdot, t_\mathrm{f})) = \frac{q_1}{2}\chi_{\Omega_\mathrm{d}} \left(\Psi(\xi(\cdot, t_\mathrm{f})) - T_\mathrm{d}\right)^2 \tag{A.8a}$$

$$\tilde{l}(\xi, u) = \frac{q_2}{2}\chi_{\Omega_\mathrm{d}} \left(\Psi(\xi) - T_\mathrm{d}\right)^2 + \frac{q_3}{2}\chi_{\Omega_\mathrm{c}} u^2 \ . \tag{A.8b}$$

The transformation (A.6a) is also applicable to the right hand sides of (5.3b)–(5.3c) yielding

$$\tilde{f}_{\Omega_\mathrm{o}}(\xi, K) = f_{\Omega_\mathrm{o}}(\Psi(\xi), K) \qquad \text{in } \Omega_\mathrm{o} \times (0, t_\mathrm{f}) \tag{A.9a}$$

$$\tilde{f}_{\Gamma_{\mathrm{o,N}}}(\xi) = f_{\Gamma_{\mathrm{o,N}}}(\Psi(\xi)) \qquad \text{on } \Gamma_{\mathrm{o,N}} \times (0, t_\mathrm{f}) \ . \tag{A.9b}$$

However, the transformation (A.6a) is not immediately applicable to temporal and spatial operators of the thermal subsystem (5.3b)–(5.3c). Note that the inverse transformation (A.6b) allows one to transform the Dirichlet boundary condition (5.3d) and initial the condition (5.3e) into the coordinates of ξ.

A.1.2 Transformation of the thermal dynamics

For a transformation of parts of optimization problem (5.3) involving temporal or spatial operators with T as an argument, the transformation instructions

$$\partial_t T = \Psi'(\xi)\,\partial_t \xi \qquad \text{in } \Omega_\mathrm{o} \times (0, t_\mathrm{f}) \tag{A.10a}$$

$$\nabla T = \Psi'(\xi)\;\nabla \xi \qquad \text{in } \Omega_\mathrm{o} \times (0, t_\mathrm{f}) \tag{A.10b}$$

$$\nabla\cdot (k\,\nabla T) = k\,\Psi''(\xi)\;\nabla \xi\cdot\;\nabla \xi + \Psi'(\xi)\,\nabla\cdot (k\,\nabla \xi) \qquad \text{in } \Omega_\mathrm{o} \times (0, t_\mathrm{f}) \tag{A.10c}$$

are introduced. They are obtained by successively differentiating the left and right hands side of Equation (A.6a) with respect to the time variable t and the spatial coordinate x, respectively.[2] Using the transformation instructions (A.9) and (A.10), the thermal subsystem (5.3b)–(5.3e) can be transformed to the equivalent unconstrained counterpart

$$\Psi'(\xi)\,[e_{\nabla,\,t}\,(\rho C, \xi) - e_\Delta\,(k, \xi) - d(\xi)\,\nabla \xi\cdot\;\nabla \xi] = \tilde{f}_{\Omega_\mathrm{o}}(\xi, K) \qquad \text{in } \Omega_\mathrm{o} \times (0, t_\mathrm{f}) \tag{A.11a}$$

$$\Psi'(\xi)\,[e_{\nabla,\,x}\,(k, \xi)] = \tilde{f}_{\Gamma_{\mathrm{o,N}}}(\xi) \qquad \text{on } \Gamma_{\mathrm{o,N}} \times (0, t_\mathrm{f}) \tag{A.11b}$$

$$\xi = \Psi^{-1}(f_{\Gamma_{\mathrm{o,D}}}) \qquad \text{on } \Gamma_{\mathrm{o,D}} \times (0, t_\mathrm{f}) \tag{A.11c}$$

$$\xi(\cdot, 0) = \Psi^{-1}(T_0) \qquad \text{in } \Omega_\mathrm{o} \text{ at } t = 0 \tag{A.11d}$$

that inherently satisfies the state constraints (A.1), also see [113]. A more suitable structure of the transformed thermal subsystem (A.11) can be derived by introducing the relation

$$d(\xi) = k\frac{\Psi''(\xi)}{\Psi'(\xi)} \qquad \text{in } \Omega_\mathrm{o} \times (0, t_\mathrm{f})\ , \tag{A.12}$$

whereby it is guaranteed that $d(\xi)$ remains bounded for all ξ, cf. Figure A.1.

The structure of the transformed thermal subsystem (A.11) is almost identical to its constrained counterpart (5.3b)–(5.3e). The transformed thermal subsystem (A.11) only includes the additional function $d(\xi)\,\nabla \xi\cdot\;\nabla \xi$ and the partial derivative of the saturation function with respect to ξ, i. e., $\Psi'(\xi)$. Note that the function $\Psi'(\xi)$ asymptotically approaches zero for $\xi \to \pm\infty$. Consequently, the subsystem (A.11a)–(A.11b) degenerates to the set of algebraic constraints

$$0 = \tilde{f}_{\Omega_\mathrm{o}}(\xi, K) \qquad \text{in } \Omega_\mathrm{o} \times (t_1, t_2) \tag{A.13a}$$

$$0 = \tilde{f}_{\Gamma_{\mathrm{o,N}}}(\xi) \qquad \text{on } \Gamma_{\mathrm{o,N}} \times (t_1, t_2) \tag{A.13b}$$

with $t \in (t_1, t_2)$ denoting time intervals where $\xi \to \pm\infty$. At these time intervals, the original state variable T approaches its bounds $T^{\pm}$.

In order to cope with the degenerated subsystem (A.13), the control variable $v := v(x, t)$ is introduced and related to the left and right hand sides of (A.11a) as follows

$$e_{\nabla,\,t}\,(\rho C, \xi) - e_\Delta\,(k, \xi) - d(\xi)\,\nabla \xi\cdot\;\nabla \xi = v \qquad \text{in } \Omega_\mathrm{o} \times (0, t_\mathrm{f}) \tag{A.14a}$$

$$\Psi'(\xi) v = \tilde{f}_{\Omega_\mathrm{o}}(\xi, K) \qquad \text{in } \Omega_\mathrm{o} \times (0, t_\mathrm{f})\ . \tag{A.14b}$$

[2] For the sake of brevity, the partial derivatives of the saturation function $\Psi(\xi)$ with respect to ξ of first and second order are denoted by $\Psi'(\xi)$ and $\Psi''(\xi)$.

As shown in the following lines, this alternative description of the system dynamics allows the formulation of an optimization problem in such a way that the left hand side of Equation (A.14a) is well-defined even if the state constraints are approached, which implies $\xi \to \pm\infty$. In such cases, the control variable v tends to peak in view of the algebraic constraint (A.14b) that is used to achieve consistency between the formulations (A.11a) and (A.14a). Consequently, a quadratic penalization of the control variable v allows one to prevent the crucial point that the state variable ξ becomes unbounded, also see [52].

It is worth to mention that the right hand side of Equation (A.14a) is specified using the control variable v instead of setting directly

$$v = \frac{\tilde{f}_{\Omega_\mathrm{o}}(\xi, K)}{\Psi'(\xi)} \qquad \text{in } \Omega_\mathrm{o} \times (0, t_\mathrm{f}) \ . \tag{A.15}$$

At a first glance, this is an identical formulation to Equation (A.14b). However, formulation (A.15) would result in both a nonlinear and state-dependent transformation of the state variable of the electromagnetic subsystem K and therefore to an inconsistency between the assumed distribution of the electromagnetic heat source in the coordinates of ξ and the true physical conditions. The inconsistency is caused by the temporal and spatial dynamics of the state variable ξ which do not reflect the original situation. The correct spatial distribution of the electromagnetic heat source depends on the dynamics of the electromagnetic system (5.3f)–(5.3h). For this reason, the algebraic constraint (A.14b) is considered, which can be interpreted as an equality constraint for v.

To achieve a well-defined formulation of the thermal dynamics in the coordinates of ξ, the transformed PDE system

$$\begin{aligned}
e_{\nabla,\,t}\left(\rho C, \xi\right) - e_{\Delta}\left(k, \xi\right) - d(\xi)\,\nabla\xi \cdot \nabla\xi &= v && \text{in } \Omega_\mathrm{o} \times (0, t_\mathrm{f}) && \text{(A.16a)}\\
e_{\nabla,\,x}\left(k, \xi\right) &= \tilde{f}_{\Gamma_{\mathrm{o,N}}}(\xi)/\Psi'(\xi) && \text{on } \Gamma_{\mathrm{o,N}} \times (0, t_\mathrm{f}) && \text{(A.16b)}\\
\xi &= \Psi^{-1}(f_{\Gamma_{\mathrm{o,D}}}) && \text{on } \Gamma_{\mathrm{o,D}} \times (0, t_\mathrm{f}) && \text{(A.16c)}\\
\xi(\cdot, 0) &= \Psi^{-1}(T_0) && \text{in } \Omega_\mathrm{o} \text{ at } t = 0 && \text{(A.16d)}\\
\Psi'(\xi) v &= \tilde{f}_{\Omega_\mathrm{o}}(\xi, K) && \text{in } \Omega_\mathrm{o} \times (0, t_\mathrm{f}) && \text{(A.16e)}
\end{aligned}$$

is introduced. The control variable v actuates the transformed thermal subsystem (A.16a)–(A.16d), whereby the algebraic constraint (A.16e) ensures that the spatial distribution of the electromagnetic heat source is reflected correctly.

A.1.3 Optimization problem with unconstrained state variables

The transformed cost functional (A.8) and subsystem (A.16) is used to formulate the optimization problem

$$\min_{\substack{u(\cdot)\in\mathcal{U}_{\mathrm{ad}}\\ v(\cdot)}} J_\epsilon(u,v) = \int_\Omega \tilde{V}(\xi(\cdot,t_\mathrm{f}))\,\mathrm{d}x + \iint_{\Omega\times(0,t_\mathrm{f})} \tilde{l}(\xi,u) + p_\epsilon(v)\,\mathrm{d}x\,\mathrm{d}t \tag{A.17a}$$

$$\begin{aligned}
\text{s.t.}\quad & e_{\nabla,t}\left(\rho C,\xi\right) - e_\Delta\left(k,\xi\right) - d(\xi)\,\nabla\xi\cdot\nabla\xi = v && \text{in } \Omega_\mathrm{o}\times(0,t_\mathrm{f}) && \text{(A.17b)}\\
& e_{\nabla,x}\left(k,\xi\right) = \tilde{f}_{\Gamma_{\mathrm{o,N}}}(\xi)/\Psi'(\xi) && \text{on } \Gamma_{\mathrm{o,N}}\times(0,t_\mathrm{f}) && \text{(A.17c)}\\
& \xi = \Psi^{-1}(f_{\Gamma_{\mathrm{o,D}}}) && \text{on } \Gamma_{\mathrm{o,D}}\times(0,t_\mathrm{f}) && \text{(A.17d)}\\
& \xi(\cdot,0) = \Psi^{-1}(T_0) && \text{in } \Omega_\mathrm{o} \text{ at } t=0 && \text{(A.17e)}\\
& e_{\nabla\times,\nabla\times}\left(\mu^{-1},K\right) = f_\Omega(K,u) && \text{in } \Omega\times(0,t_\mathrm{f}) && \text{(A.17f)}\\
& e_{\nabla\times}\left(\mu^{-1},K\right) = f_{\Gamma_\mathrm{N}}(K,u) && \text{on } \Gamma_\mathrm{N}\times(0,t_\mathrm{f}) && \text{(A.17g)}\\
& e_\times\left(K\right) = f_{\Gamma_\mathrm{D}}(u) && \text{on } \Gamma_\mathrm{D}\times(0,t_\mathrm{f}) && \text{(A.17h)}\\
& g(\xi,K,v) = \Psi'(\xi)v - \tilde{f}_{\Omega_\mathrm{o}}(\xi,K) = 0 && \text{in } \Omega_\mathrm{o}\times(0,t_\mathrm{f})\ , && \text{(A.17i)}
\end{aligned}$$

whereby the unconstrained state variable ξ allows one to overcome the demanding task of a direct handling of the state constraint (5.3i) when numerically solving the optimization problem. The control trajectory u is subject to the constraints (5.2) and serves as one of two optimization variables. The control variable v serves as a further optimization variable, which has to comply with (A.17i) for reasons of consistency, cf. Appendix A.1.2.

The cost functional to be minimized (A.17a) is amended by the penalty term

$$p_\epsilon(v) = \chi_{\Omega_\mathrm{o}}\frac{\epsilon}{2}v^2 \qquad \text{in } \Omega\times(0,t_\mathrm{f}) \tag{A.18}$$

with $\epsilon > 0$ as the penalty parameter. In order to interpret the penalty term, the cost functional $J_\epsilon(u,v)$ is transformed back into the original control and state variables (u,T) using the inverse transformation (A.6b). The back transformation of the Mayer and Lagrange terms $\tilde{V}(\xi(\cdot,t_\mathrm{f}))$ and $\tilde{l}(\xi,u)$ leads to its original counterparts $V(T(\cdot,t_\mathrm{f}))$ and $l(T,u)$. For achieving a change of coordinates for the penalty term $p_\epsilon(v)$, the control variable v is replaced according to Equation (A.15), which eventually results in

$$p_\epsilon^{-1}(T,K) = \frac{\epsilon}{2}\left(\frac{1}{4}\frac{\left(T^- - T^+\right)^2}{\left(T^- - T\right)\left(T^+ - T\right)}\right)^2 f_{\Omega_\mathrm{o}}(T,K)^2 \qquad \text{in } \Omega_\mathrm{o}\times(0,t_\mathrm{f})\ . \tag{A.19}$$

Thus, the inverse of the penalty term $p_\epsilon^{-1}(T,K)$ becomes unbounded as soon as the temperature T approaches its bounds $T^\pm$, also see [52, 137].

The discussion above reveals that the incorporation of the penalty term (A.18) into the cost functional $J_\epsilon(u,v)$ can be interpreted as an interior barrier function that is capable to cope with state constraints on the basis of the original problem formulation (5.3). In the

coordinates of the transformed unconstrained problem (A.17), the term (A.18) penalizes large values of the state variable ξ in order to circumvent the critical case of unbounded state variables ξ implying

$$\Psi(\xi) \to T^{\pm} \quad \Leftrightarrow \quad \Psi'(\xi) \to 0 \qquad \text{in } \Omega_\mathrm{o} \times (0, t_\mathrm{f}) \; . \tag{A.20}$$

The convergence behavior of the new optimization problem (A.17) for a successively reduced penalty parameter ϵ is investigated in [52].

A.2 Numerical solution of the transformed optimization problem

This section applies an augmented Lagrangian method to numerically solve optimization problem (A.17). The equality constrained problem is first reformulated as a max-min problem. Subsequently, the optimality conditions of the new problem formulation are derived and numerically solved as discussed in Chapter 5.

A.2.1 Formulation and numerical solution of a max-min problem

The augmented Lagrangian method from Chapter 5 allows one to reformulate the equality constrained optimization problem (A.17) as the max-min problem

$$\max_{\mu(\cdot)} \quad \min_{\substack{u(\cdot)\in\mathcal{U}_\mathrm{ad} \\ v(\cdot)}} \; J_\beta(u,v,\mu) = J_\epsilon(u,v) + \iint\limits_{\Omega_\mathrm{o}\times(0,t_\mathrm{f})} \mu g(\xi,K,v) + \frac{\beta}{2} g(\xi,K,v)^2 \,\mathrm{d}x\,\mathrm{d}t \tag{A.21a}$$

$$\begin{aligned}
\text{s.t.} \quad & e_{\nabla,\,t}\left(\rho C,\xi\right) - e_\Delta\left(k,\xi\right) - d(\xi)\,\nabla\xi\cdot\nabla\xi = v && \text{in } \Omega_\mathrm{o}\times(0,t_\mathrm{f}) && \text{(A.21b)}\\
& e_{\nabla,\,x}\left(k,\xi\right) = \tilde{f}_{\Gamma_\mathrm{o,N}}(\xi)/\Psi'(\xi) && \text{on } \Gamma_\mathrm{o,N}\times(0,t_\mathrm{f}) && \text{(A.21c)}\\
& \xi = \Psi^{-1}(f_{\Gamma_\mathrm{o,D}}) && \text{on } \Gamma_\mathrm{o,D}\times(0,t_\mathrm{f}) && \text{(A.21d)}\\
& \xi(\cdot,0) = \Psi^{-1}(T_0) && \text{in } \Omega_\mathrm{o} \text{ at } t=0 && \text{(A.21e)}\\
& e_{\nabla\times,\nabla\times}\left(\mu^{-1},K\right) = f_\Omega(K,u) && \text{in } \Omega\times(0,t_\mathrm{f}) && \text{(A.21f)}\\
& e_{\nabla\times}\left(\mu^{-1},K\right) = f_{\Gamma_\mathrm{N}}(K,u) && \text{on } \Gamma_\mathrm{N}\times(0,t_\mathrm{f}) && \text{(A.21g)}\\
& e_{\times}\left(K\right) = f_{\Gamma_\mathrm{D}}(u) && \text{on } \Gamma_\mathrm{D}\times(0,t_\mathrm{f}) \; , && \text{(A.21h)}
\end{aligned}$$

whereby the augmented cost functional (A.21a) couples the equality constraint $g(\xi,K,v)=0$ to the cost functional (A.17a) using the dual variable $\mu(x,t)$. In addition, the augmented cost functional includes a regularization term with penalty parameter $\beta > 0$. Comparing the max-min problem (A.21) with the formulation in original state variables (5.9), it can be concluded that Algorithm 5.1 is suitable to cope with both problems. The max-min problem (A.21) can be numerically solved by alternately minimizing and maximizing the augmented cost functional $J_\beta(u,v,\mu)$ with respect to the primal variables (u,v) and dual variable μ.

In order to minimize the augmented cost functional (A.21a) in step II.i) of Algorithm 5.1, the optimality conditions are derived in Appendix A.2.2. The maximization of the augmented cost functional in step II.ii) is tackled by means of the directional derivative

$$\left.\frac{\partial J_\beta(u,v,\mu)}{\partial \mu}\right|_{y^{(i+1)}} h_\mu = 0 \qquad \forall h_\mu \tag{A.22}$$

with h_μ denoting the admissible directions of the dual variable μ. The directional derivative (A.22) is evaluated for the solution $y^{(i+1)}$ of the prior minimization step, cf. Algorithm 5.1. The directional derivative allows the formulation of the reduced gradient

$$g_\mu^{(i)} = g(\xi^{(i)}, K^{(i)}, v^{(i)}) \qquad \text{in } \Omega_\mathrm{o} \times (0, t_\mathrm{f}) \ , \tag{A.23}$$

whereby $g_\mu(x,t)$ is interpreted as the direction of steepest ascent with respect to maximizing the augmented cost functional $J_\beta(u,v,\mu)$ in the augmented Lagrangian step i.

A.2.2 Optimality conditions for minimization step

The optimality conditions for minimizing the augmented cost functional (A.21a) in step II.i) of Algorithm 5.1 are derived by applying the formal Lagrangian technique. As the structure of the max-min problem (A.21) is similar to that in Chapter 5, the following discussion is restricted to the specifics of the transformation approach. The transformed thermal dynamics (A.21b)–(A.21e) encompass the same temporal and spatial operators up to the part $d(\xi)\,\nabla\xi\cdot\nabla\xi$ as its constrained counterpart (5.9b)–(5.9e). Accordingly, the application of the formal Lagrangian technique will result in optimality conditions that are similar to those in Section 5.3.

First of all, the Lagrangian $\mathcal{L} := \mathcal{L}(\xi, K, u, v, \mu^{(i)}, p, \Lambda)$ is defined as

$$\begin{aligned}
\mathcal{L} = {} & \int_\Omega \tilde{V}(\xi(\cdot,t_\mathrm{f}))\,\mathrm{d}x + \iint_{\Omega\times(0,t_\mathrm{f})} \tilde{l}(\xi,u) + p_\epsilon(v)\,\mathrm{d}x\,\mathrm{d}t + \iint_{\Omega_\mathrm{o}\times(0,t_\mathrm{f})} \mu^{(i)} g(\xi,K,v) + \frac{\beta^{(i)}}{2} g(\xi,K,v)^2\,\mathrm{d}x\,\mathrm{d}t \\
& + \iint_{\Omega_\mathrm{o}\times(0,t_\mathrm{f})} p\left[e_{\nabla,t}\left(\rho C,\xi\right) - e_\Delta\left(k,\xi\right) - d(\xi)\,\nabla\xi\cdot\nabla\xi - v\right]\,\mathrm{d}x\,\mathrm{d}t \\
& + \iint_{\Gamma_{\mathrm{o,N}}\times(0,t_\mathrm{f})} p\left[e_{\nabla,x}\left(k,\xi\right) - \tilde{f}_{\Gamma_{\mathrm{o,N}}}(\xi)/\Psi'(\xi)\right]\,\mathrm{d}x\,\mathrm{d}t + \iint_{\Gamma_{\mathrm{o,D}}\times(0,t_\mathrm{f})} p\left[\xi - \Psi^{-1}(f_{\Gamma_{\mathrm{o,D}}})\right]\,\mathrm{d}x\,\mathrm{d}t \\
& + \iint_{\Omega\times(0,t_\mathrm{f})} \Lambda\cdot\left[e_{\nabla\times,\nabla\times}\left(\mu^{-1},K\right) - f_\Omega(K,u)\right]\,\mathrm{d}x\,\mathrm{d}t \\
& + \iint_{\Gamma_\mathrm{N}\times(0,t_\mathrm{f})} \Lambda\cdot\left[f_{\Gamma_\mathrm{N}}(K,u) - e_{\nabla\times}\left(\mu^{-1},K\right)\right]\,\mathrm{d}x\,\mathrm{d}t + \iint_{\Gamma_\mathrm{D}\times(0,t_\mathrm{f})} \Lambda\cdot\left[e_\times\left(K\right) - f_{\Gamma_\mathrm{D}}(u)\right]\,\mathrm{d}x\,\mathrm{d}t
\end{aligned} \tag{A.24}$$

coupling the transformed thermal subsystem (A.21b)–(A.21d) and the electromagnetic subsystem (A.21f)–(A.21h) to the augmented cost functional $J_\beta(u,v,\mu^{(i)})$ using the adjoint states $p(x,t)$ and $\Lambda(x;t)$. Note that the augmented cost functional is minimized for a fixed value of the dual variable μ, cf. the discussion in Section 5.2.

The optimality conditions for a minimization of the augmented cost functional (A.21a) are derived by analyzing the directional derivatives

$$\left.\frac{\partial \mathcal{L}}{\partial \xi}\right|_{y^*} h_\xi = 0 \qquad \forall h_\xi \tag{A.25a}$$

$$\left.\frac{\partial \mathcal{L}}{\partial K}\right|_{y^*} \cdot H_K = 0 \qquad \forall H_K \tag{A.25b}$$

$$\left.\frac{\partial \mathcal{L}}{\partial u}\right|_{y^*} h_u \geq 0 \qquad \forall u \in \mathcal{U}_{\mathrm{ad}} \tag{A.25c}$$

$$\left.\frac{\partial \mathcal{L}}{\partial v}\right|_{y^*} h_v = 0 \qquad \forall v \ . \tag{A.25d}$$

The conditions of vanishing directional derivatives (A.25a)–(A.25b) are used to formulate an adjoint PDE system with respect to the thermal subsystem (A.21b)–(A.21e) and the electromagnetic subsystem (A.21f)–(A.21h). The directional derivatives (A.25c)–(A.25d) allows one to formulate gradient conditions for the primal variables (u, v).

To achieve a more compact notation, the left and right hand sides of the adjoint PDE system are derived separately from each other. To this end, the knowledge about how the individual parts of the Lagrangian (A.24) affect the structure of the adjoint PDE system is utilized. By bearing in mind that the dynamics of the adjoint PDE subsystems stem from parts of the Lagrangian $\mathcal{L}$ that contain temporal or spatial operators, the left hand sides can be specified. Furthermore, it is known that the right hand sides of the adjoint dynamics reflect parts that originate from the augmented cost functional $J_\beta(u, v, \mu^{(i)})$ and right hand sides of the system dynamics (A.21b)–(A.21h).

Adjoint dynamics of the transformed thermal subsystem

The following lines evaluate the directional derivative (A.25a) to define the adjoint dynamics of the transformed thermal subsystem (A.21b)–(A.21e). The left hand side of the adjoint subsystem can to a large extent be inferred from the results of Section 5.3 by keeping in mind the similar structure of the transformed thermal subsystem and its original counterpart (5.3b)–(5.3e). The analysis of optimization problem (5.11) in Section 5.3 has revealed how the temporal and spatial operators (3.15) will be reflected within the adjoint dynamics due to an interchange of the state variable T to the adjoint state p.

It remains to show how the part $d(\xi)\,\nabla\,\xi\cdot\nabla\,\xi$ can be incorporated into the left hand side of the adjoint thermal subsystem. To this end, its associated part of the directional derivative (A.25a) is analyzed

$$\iint\limits_{\Omega_\mathrm{o}\times(0,t_\mathrm{f})} \left.\frac{\partial}{\partial \xi}\left(p d(\xi)\,\nabla\,\xi\cdot\nabla\,\xi\right)\right|_{y^*} h_\xi \,\mathrm{d}x\,\mathrm{d}t =$$

$$\iint\limits_{\Omega_\mathrm{o}\times(0,t_\mathrm{f})} p^* d'(\xi^*)\,\nabla\,\xi^*\cdot\nabla\,\xi^* h_\xi + 2p^* d(\xi^*)\,\nabla\,\xi^*\cdot\nabla\,h_\xi \,\mathrm{d}x\,\mathrm{d}t \tag{A.26}$$

with $d'(\xi)$ as the partial derivative of first order of $d(\xi)$ with respect to ξ. In order to evaluate the overall directional derivative (A.25a), the function $2p^*d(\xi^*)\,\nabla\,\xi^*\cdot\,\nabla\,h_\xi$ on the right hand side of Equation (A.26) is transformed into an equivalent form where the admissible directions h_ξ are not subject to spatial derivatives. A suitable integral identity to put this into practice can be deduced from the formula of partial integration and reads as

$$\iint\limits_{\Omega_\mathrm{o}\times(0,t_\mathrm{f})} 2p^*d(\xi^*)\,\nabla\,\xi^*\cdot\,\nabla\,h_\xi\;\mathrm{d}x\,\mathrm{d}t = \iint\limits_{\Gamma_\mathrm{o}\times(0,t_\mathrm{f})} \left[n\cdot(2p^*d(\xi^*)\,\nabla\,\xi^*)\right] h_\xi\;\mathrm{d}x\,\mathrm{d}t - \iint\limits_{\Omega_\mathrm{o}\times(0,t_\mathrm{f})} \left[2p^*d(\xi^*)\Delta\,\xi^* + 2p^*d'(\xi^*)\,\nabla\,\xi^*\cdot\,\nabla\,\xi^* + 2d(\xi^*)\,\nabla\,p^*\cdot\,\nabla\,\xi^*\right] h_\xi\;\mathrm{d}x\,\mathrm{d}t\;, \quad \text{(A.27)}$$

cf., e. g., [2].

By substituting the integral identity (A.27) into Equation (A.26), the relation

$$\iint\limits_{\Omega_\mathrm{o}\times(0,t_\mathrm{f})} \frac{\partial}{\partial\xi}\left(pd(\xi)\,\nabla\,\xi\cdot\,\nabla\,\xi\right)\Big|_{y^*} h_\xi\;\mathrm{d}x\,\mathrm{d}t = \iint\limits_{\Gamma_\mathrm{o}\times(0,t_\mathrm{f})} \left[n\cdot(2p^*d(\xi^*)\,\nabla\,\xi^*)\right] h_\xi\;\mathrm{d}x\,\mathrm{d}t - \iint\limits_{\Omega_\mathrm{o}\times(0,t_\mathrm{f})} \left[2p^*d(\xi^*)\Delta\,\xi^* + p^*d'(\xi^*)\,\nabla\,\xi^*\cdot\,\nabla\,\xi^* + 2d(\xi^*)\,\nabla\,p^*\cdot\,\nabla\,\xi^*\right] h_\xi\;\mathrm{d}x\,\mathrm{d}t \quad \text{(A.28)}$$

is obtained, which no longer contains any derivatives of the admissible directions h_ξ. For the sake of compactness, the functions

$$g_{l,\Omega_\mathrm{o}} = -2pd(\xi)\Delta\,\xi - pd'(\xi)\,\nabla\,\xi\cdot\,\nabla\,\xi - 2d(\xi)\,\nabla\,p\cdot\,\nabla\,\xi \qquad \text{in } \Omega_\mathrm{o}\times(0,t_\mathrm{f}) \qquad \text{(A.29a)}$$

$$g_{l,\Gamma_{\mathrm{o,N}}} = n\cdot(2pd(\xi)\,\nabla\,\xi) \qquad \text{on } \Gamma_{\mathrm{o,N}}\times(0,t_\mathrm{f}) \qquad \text{(A.29b)}$$

are introduced with $g_{l,\Omega_\mathrm{o}} := g_{l,\Omega_\mathrm{o}}(\xi,p)$ and $g_{l,\Gamma_{\mathrm{o,N}}} := g_{l,\Gamma_{\mathrm{o,N}}}(\xi,p)$ summarizing the terms of (A.28) on the space-time cylinders $\Omega_\mathrm{o}\times(0,t_\mathrm{f})$ and $\Gamma_\mathrm{o}\times(0,t_\mathrm{f})$ by neglecting the factors of the admissible directions h_ξ.

The parts of the directional derivative (A.25a) that originate from the augmented cost functional (A.21a) and the right hand sides of the transformed subsystem (A.21b)–(A.21e) read

$$g_{r,\Omega_\mathrm{o}} = \partial_\xi\tilde{l}(\xi,u)\Big|_{y^*} + \partial_\xi g(\xi,K,v)|_{y^*}\left(\mu^{(i)} + \beta^{(i)}g(\xi^*,K^*,v^*)\right) \qquad \text{in } \Omega_\mathrm{o}\times(0,t_\mathrm{f}) \qquad \text{(A.30a)}$$

$$g_{r,\Gamma_{\mathrm{o,N}}} = \partial_\xi\tilde{f}_{\Gamma_{\mathrm{o,N}}}(\xi)/\Psi'(\xi)\Big|_{y^*} p^* \qquad \text{on } \Gamma_{\mathrm{o,N}}\times(0,t_\mathrm{f}) \qquad \text{(A.30b)}$$

$$g_{r,\Gamma_{\mathrm{o,D}}} = 0 \qquad \text{on } \Gamma_{\mathrm{o,D}}\times(0,t_\mathrm{f}) \qquad \text{(A.30c)}$$

$$g_{r,\Omega_{\mathrm{o},t_\mathrm{f}}} = \partial_\xi\tilde{V}(\xi(\cdot,t_\mathrm{f}))\Big|_{y^*} \qquad \text{in } \Omega_\mathrm{o} \text{ at } t=t_\mathrm{f} \qquad \text{(A.30d)}$$

with the functions $g_{r,\Omega_\mathrm{o}} := g_{r,\Omega_\mathrm{o}}(\xi,K,v,\mu^{(i)})$, $g_{r,\Gamma_{\mathrm{o,N}}} := g_{r,\Gamma_{\mathrm{o,N}}}(\xi,p)$, and $g_{r,\Omega_{\mathrm{o},t_\mathrm{f}}} := g_{r,\Omega_{\mathrm{o},t_\mathrm{f}}}(\xi)$, respectively. The functions will define the sources of the adjoint dynamics related to the transformed thermal subsystem. Using the integral identities (3.26), (3.27), and (A.28), the

adjoint PDE system of the transformed thermal subsystem can be defined

$$
\begin{aligned}
e_{\nabla,t}\left(\rho C, p^*\right) + e_{\Delta}\left(k, p^*\right) + g_{l,\Omega_\mathrm{o}}(\xi^*, p^*) &= g_{r,\Omega_\mathrm{o}}(\xi^*, K^*, v^*, \mu^{(i)}) && \text{in } \Omega_\mathrm{o} \times (0, t_\mathrm{f}) && \text{(A.31a)}\\
e_{\nabla,x}\left(k, p^*\right) + g_{l,\Gamma_{\mathrm{o,N}}}(\xi^*, p^*) &= g_{r,\Gamma_{\mathrm{o,N}}}(\xi^*, p^*) && \text{on } \Gamma_{\mathrm{o,N}} \times (0, t_\mathrm{f}) && \text{(A.31b)}\\
p^* &= g_{r,\Gamma_{\mathrm{o,D}}} && \text{on } \Gamma_{\mathrm{o,D}} \times (0, t_\mathrm{f}) && \text{(A.31c)}\\
-\rho C p^*(\cdot, t_\mathrm{f}) &= g_{r,\Omega_{\mathrm{o},t_\mathrm{f}}}(\xi^*) && \text{in } \Omega_\mathrm{o} \text{ at } t = t_\mathrm{f}\ . && \text{(A.31d)}
\end{aligned}
$$

Adjoint dynamics of the electromagnetic subsystem

The condition of a vanishing directional derivative (A.25b) is used to formulate a further adjoint PDE system. However, the analysis of the directional derivative is similar to that in Chapter 3 since the transformation approach affects only the thermal subsystem but not the electromagnetic subsystem, cf. Appendix A.1.3. The analysis of the directional derivative (A.25b) eventually results in the adjoint PDE system (3.37).

Gradient conditions for optimal primal variables

The minimization of the augmented cost functional (A.21a) relies on the gradients

$$
\begin{aligned}
g_u = &\int_\Omega \partial_u \tilde{l}(\xi, u)\Big|_{y^*} - \Lambda^* \cdot \partial_u f_\Omega(K, u)|_{y^*}\ \mathrm{d}x\\
&+ \int_\Gamma \Lambda^* \cdot \left(\chi_{\Gamma_\mathrm{N}}\, \partial_u f_{\Gamma_\mathrm{N}}(K, u)|_{y^*} - \chi_{\Gamma_\mathrm{D}}\, \partial_u f_{\Gamma_\mathrm{D}}(u)|_{y^*}\right)\ \mathrm{d}x && \text{(A.32a)}\\
g_v = &\ \partial_v p_\epsilon(v)|_{y^*} + \partial_v g(\xi, K, v)|_{y^*}\left(\mu + \beta g(\xi^*, K^*, v^*)\right) - p^* && \text{in } \Omega_\mathrm{o} \times (0, t_\mathrm{f}) && \text{(A.32b)}
\end{aligned}
$$

with $g_u := g_u(t)$ and $g_v := g_v(x, t)$, which result from the directional derivatives (A.25c)–(A.25d). In combination with the canonical equations comprising the system dynamics (A.21b)–(A.21h) and the adjoint PDE systems (A.31) and (3.37), the reduced gradients complete the optimality system for the minimization step II.i) of Algorithm 5.1. Thereby, the gradient (A.32a) is subject to the conditional expression (3.40) to take the input constraints (5.2) into account.

A.3 Numerical results for a heat-up process

The discussion so far shows that the transformation approach essentially affects the thermal subsystem for which the state constraint is formulated. The electromagnetic subsystem is only indirectly influenced by the control variable v and the equality constraint $g(\xi, K, v) = 0$ used to obtain a well-defined problem formulation, cf. Equation (A.17) and (A.17i) as well as the discussion in Appendix A.1.2. This structural property is evident for the application example of surface hardening where the electromagnetic subsystem (A.17f)–(A.17h) remains unaffected from the transformation approach.

The transformation approach and its advantages regarding the numerical solution of state constrained optimization problems is demonstrated for a heat-up process. The boundary control u represents the heat source on the right hand side of a slab and serves as the optimization variable. The corresponding problem formulation reads

$$\min_{u(\cdot)\in\mathcal{U}_{\mathrm{ad}}} J(u) = \iint\limits_{\Omega\times(0,t_{\mathrm{f}})} \frac{q_1}{2}\,(T-T_{\mathrm{d}})^2 \;\mathrm{d}x\,\mathrm{d}t + \iint\limits_{\Gamma_1\times(0,t_{\mathrm{f}})} \frac{q_2}{2}u^2 \;\mathrm{d}x\,\mathrm{d}t \tag{A.33a}$$

$$\begin{aligned}
\text{s.t.}\quad & e_{\nabla,t}\,(\rho C,T) - e_{\Delta}\,(k,T) = 0 && \text{in } \Omega\times(0,t_{\mathrm{f}}) && \text{(A.33b)}\\
& e_{\nabla,x}\,(k,T) = 0 && \text{on } \Gamma_0\times(0,t_{\mathrm{f}}) && \text{(A.33c)}\\
& e_{\nabla,x}\,(k,T) = u && \text{on } \Gamma_1\times(0,t_{\mathrm{f}}) && \text{(A.33d)}\\
& T(\cdot,0) = T_0 && \text{in } \Omega \text{ at } t=0 && \text{(A.33e)}\\
& T^- \le T \le T^+ && \text{in } \Omega\times(0,t_{\mathrm{f}})\ . && \text{(A.33f)}
\end{aligned}$$

The focus of the simulation study is to show that the transformation approach leads to a well-defined problem formulation that can be numerically solved by the optimization framework from Chapter 5, also see [113, 137, 136].

The control task to be carried out consists in the transition from the initial temperature $T_0 = 0$ to the desired temperature $T_{\mathrm{d}} = 1$.[3] The bounds of the temperature constraint (A.33f) are set to $T^{\pm} = \pm 1.2$. The control trajectory is bounded by $u^{\pm} = \pm 2$. The system dynamics (A.33b)–(A.33e) is defined on a one-dimensional slab with spatial domain Ω and boundary $\Gamma = \Gamma_0 \cup \Gamma_1$ with $\Gamma_0 = 0$ and $\Gamma_1 = 1$. The spatial coordinate is denoted by $x \in (0,1)$.

The state constrained system dynamics (A.33b)–(A.33f) is represented for the trajectory planning by an unconstrained one using the transformation approach from Appendix A.1. The transformation approach results in the transformed PDE system

$$\begin{aligned}
e_{\nabla,t}\,(\rho C,\xi) - e_{\Delta}\,(k,\xi) - d(\xi)\,\nabla\xi\cdot\nabla\xi = 0 \qquad & \text{in } \Omega\times(0,t_{\mathrm{f}}) && \text{(A.34a)}\\
n\cdot(k\,\nabla\xi) = 0 \qquad & \text{on } \Gamma_0\times(0,t_{\mathrm{f}}) && \text{(A.34b)}\\
n\cdot(k\,\nabla\xi) = w \qquad & \text{on } \Gamma_1\times(0,t_{\mathrm{f}}) && \text{(A.34c)}\\
\xi(\cdot,0) = \Psi^{-1}(T_0) \qquad & \text{in } \Omega \text{ at } t=0\ , && \text{(A.34d)}
\end{aligned}$$

where the constrained input and state variables (u,T) are replaced by the unconstrained counterparts (w,ξ). The interchange of the state variables is described by (A.6), whereas the change of coordinates of the input variable is based on the substitution

$$w = \frac{u}{\Psi'(\xi)} \qquad \text{on } \Gamma_1\times(0,t_{\mathrm{f}}) \tag{A.35}$$

and follows from the transformation approach, cf. Equation (A.15). The corresponding inverse transformation is defined by

$$u = \Psi'(\xi)w \qquad \text{on } \Gamma_1\times(0,t_{\mathrm{f}})\ . \tag{A.36}$$

[3] The problem formulation (A.33) is based on a normalized system dynamics by setting the diffusion parameter k, the density ρ, and the heat capacity C to one.

The new optimization variable $w := w(t)$ is related to the original one by means of the inequality constraint[4]

$$u^- \leq \Psi' w \leq u^+ \qquad \text{on } \Gamma_1 \times (0, t_\mathrm{f}) \tag{A.37}$$

to account for the input constraints (5.2).

Following the augmented Lagrangian method from Chapter 5, the augmented cost functional $J_\beta(w, \mu)$ is defined as follows

$$\begin{aligned} J_\beta(w,\mu) = \iint\limits_{\Omega\times(0,t_\mathrm{f})} \frac{q_1}{2}\left(\Psi(\xi) - T_\mathrm{d}\right)^2 \,\mathrm{d}x\,\mathrm{d}t + \iint\limits_{\Gamma_1\times(0,t_\mathrm{f})} \frac{q_2}{2}\left(\Psi'(\xi)w\right)^2 + \frac{\epsilon}{2}w^2 \,\mathrm{d}x\,\mathrm{d}t \\ + \iint\limits_{\Gamma_1\times(0,t_\mathrm{f})} \mu^\mathsf{T}\tilde{g}(\xi,w,\mu) + \frac{\beta}{2}\tilde{g}(\xi,w,\mu)^\mathsf{T}\tilde{g}(\xi,w,\mu) \,\mathrm{d}x\,\mathrm{d}t\ . \end{aligned} \tag{A.38}$$

The first two integrals reflect the transformed cost functional (A.33a) that is amended by a penalty term as discussed in Appendix A.1.3. The corresponding penalty parameter is $\epsilon \geq 0$, cf. Equation (A.18). The integral in the second line of Equation (A.38) accounts for the inequality constraints (A.37) by means of the Lagrange multiplier $\mu = [\mu_1, \mu_2]^\mathsf{T}$ and the function $\tilde{g}(\xi, w, \mu) = [\tilde{g}_1(\xi, w, \mu_1), \tilde{g}_2(\xi, w, \mu_2)]^\mathsf{T}$ with elements

$$\tilde{g}_1(\xi, w, \mu_1) = \max\left(\Psi' w - u^+, -\mu_1/\beta\right) \qquad \text{on } \Gamma_1 \times (0, t_\mathrm{f}) \tag{A.39a}$$

$$\tilde{g}_2(\xi, w, \mu_2) = \max\left(u^- - \Psi' w, -\mu_2/\beta\right) \qquad \text{on } \Gamma_1 \times (0, t_\mathrm{f})\ . \tag{A.39b}$$

Thereby, the penalty parameter $\beta \geq 0$ is used to achieve a regularization of the associated max-min problem.

The minimization and maximization of the augmented cost functional (A.38) with respect to the primal variable w and dual variable μ is carried out by the optimization framework from Section 5.4, also see Algorithm 5.1. The weights of the augmented cost functional (A.38) are shown in Table A.1. The initial value of the penalty parameter is chosen as $\beta^{(1)} = 10^2$, whereby its update law (5.13) is specified by $\gamma_1 = 6$, $\gamma_2 = 0.8$, and $\kappa = 1.8$.

Table A.1: Weights of the augmented cost functional (A.38).

weight	objective
$q_1 = 10^4$	minimization of state error $\left(\Psi(\xi) - T_\mathrm{d}\right)^2$ in Ω
$q_2 = 10^{-3}$	penalization of control action u^2 on Γ_1
$\epsilon = 10^{-4}$	penalization of optimization variable w^2 on Γ_1, cf. penalty term (A.18)

The upper row of Figure A.2 shows the numerical solution of the max-min problem in form of the trajectories of the unconstrained input variable w and state variable $\xi|_{x'}$ evaluated at the spatial coordinates $x' \in \{0, 0.25, 0.5, 0.75, 1\}$. The trajectories of the constrained

[4] Alternatively, the input constraints can be substituted by a further saturation function [113].

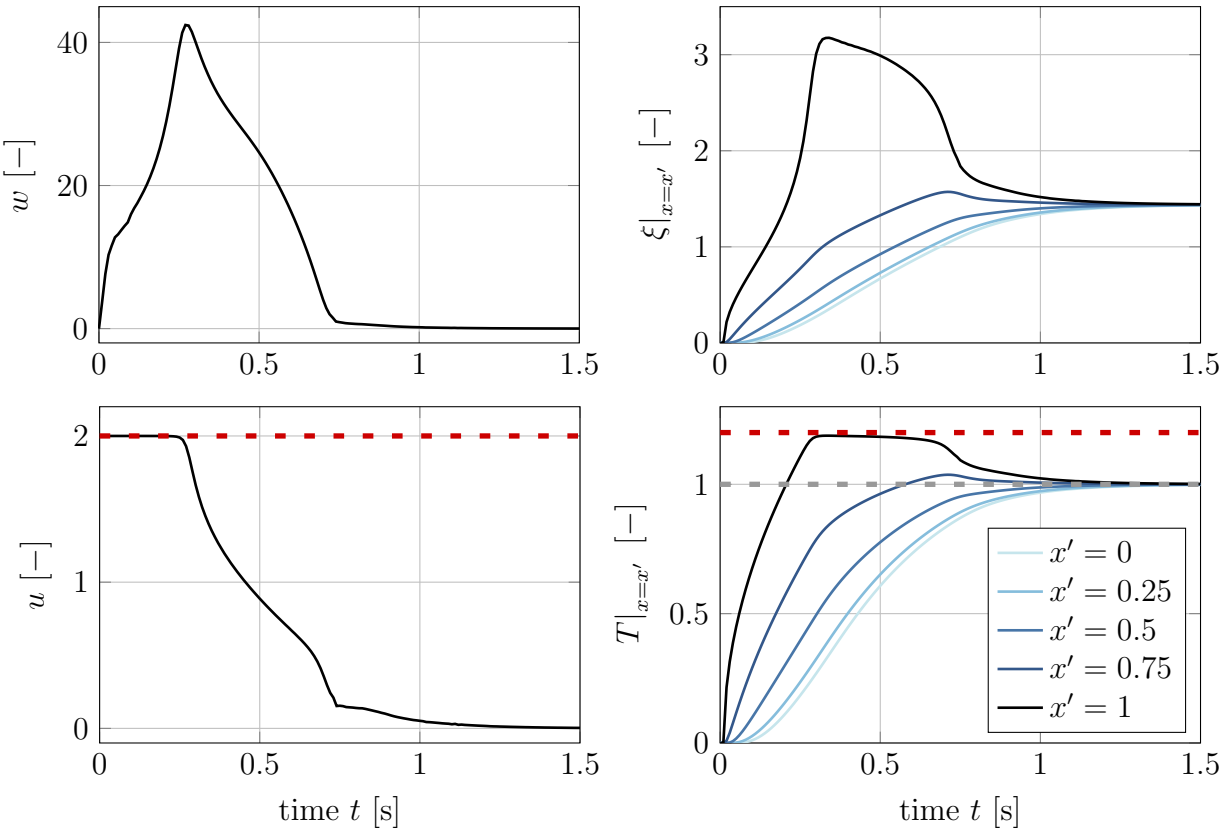

Figure A.2: Trajectories of the unconstrained input and state variables (w, ξ) and its transformed constrained counterparts (u, T).

counterparts (u, T) are obtained by applying the inverse transformations (A.36) and (A.6b) and are shown in the bottom row of Figure A.2. In order to exploit the bounds $u^{\pm} = \pm 2$ and $T^{\pm} = \pm 1.2$ of the original input and state variable (u, T), the input variable w, and state variable $\xi|_{x=1}$ assume rather large values. Note that his characteristic is due to the saturation function approach (A.2).

The approach of the bounds $T^{\pm} = \pm 1.2$ in the original variables (u, T) leads to large values in the unconstrained state variable ξ, also see Figure A.1. At the same time, the approach of the state constraints causes the characteristic of peaking values of w since in this case the function $\Psi'(\xi)$ asymptotically approaches zero, cf. Equation (A.35) and Figure A.1. However, the regularization of the unconstrained input variable w within the augmented cost functional (A.38) ensures a well-defined problem formulation and prevents the degeneration of the thermal dynamics into an algebraic constraint as discussed in Appendix A.1.2.

The good exploitation of the input and state constraints leads to an optimal heat-up behavior of the slab as illustrated in Figure A.2. At the beginning, the control variable u heats up the slab by means of the maximum allowable intensity of heat. After this initial period, the intensity of the heat source is adapted to the state constraint and the thermal dynamics to hold the state trajectory $T|_{x=1}$ at its upper bound T^{+}. Finally, the slab is heated up in total to the desired temperature $T_{\mathrm{d}} = 1$.

A.4 Conclusions

The basic idea of the transformation approach is to reformulate constrained input and state variables by means of a saturation function to obtain an equivalent problem formulation in unconstrained coordinates. This reformulation step facilitates to deal with the state constrained trajectory planning from a more analytical point of view compared to the outer penalty function or augmented Lagrangian method in Chapter 3–5. The applicability of the transformation approach is illustrated for a heat-up process.

Appendix B

List of symbols

The following lists only contain abbreviations, functions, and variables that are used continuously throughout the text. Local quantities are not listed.

B.1 Abbreviations

$(\cdot)\vert_{a^*}$	compact notation for $(\cdot)\vert_{a=a^*}$
$(\cdot)^{\pm}$	compact notation for constraints $(\cdot)^{+}$ and $(\cdot)^{-}$
CAD	computer-aided design
FDTO	first discretize then optimize
FEM	finite element method
FOTD	first optimize then discretize
MRI	magnetic resonance imaging
MWA	micro-wave ablation
NURBS	non-uniform rational B-splines
ODE	ordinary differential equation
PDE	partial differential equation
PEC	perfect electric conductor
PMC	perfect magnetic conductor
RFA	radio frequency ablation
s.t.	subject to
TEM	transverse electromagnetic

B.2 Functions

$e_{\mathrm{sys}}(\cdot)$	system dynamics
$e_{\mathrm{adj}}(\cdot)$	adjoint PDE system
$e_{\mathrm{adj,ODE}}(\cdot)$	adjoint ODE system
$E_{\mathrm{imp}}(\cdot)$	electric field intensity on the boundary of the actuator
$g(\cdot)$	equality constraint
$\tilde{g}(\cdot)$	function of transformed equality constraint
$g_u(\cdot)$	gradient for optimal control trajectory u, $g_u := g_u(t)$
$g_v(\cdot)$	gradient for optimal control variable v, $g_v := g_v(x,t)$
$g_w(\cdot)$	gradient for optimization variable w, $g_w := g_w(t)$
$g_\theta(\cdot)$	gradient vector for optimal actuator configuration
$g_\mu(\cdot)$	direction of steepest ascent for dual variable μ, $g_\mu := g_\mu(x,t)$
$G(\cdot)$	control-to-state operator
$h(\cdot)$	inequality constraint
$J(\cdot)/J_{\mathrm{n}}(\cdot)$	cost functional / normalized cost functional
$J_\beta(\cdot)$	augmented cost functional
$\mathcal{J}_{\mathrm{imp}}(\cdot)/J_{\mathrm{imp}}(\cdot)$	externally impressed current density (instantaneous quantity / phasor)
$l(\cdot)$	Lagrange term
$\mathcal{L}(\cdot)$	Lagrangian
$N_{j,p}(\cdot)$	j-th basis function of degree p
$p_\epsilon(\cdot)$	penalty term
$V(\cdot)$	Mayer term
$\chi(\cdot)$	characteristic function
$\Psi(\cdot)$	projection function or saturation function

B.3 Variables

A	magnetic vector potential (phasor $A := A(x;t)$)
A_c	cross section surface of the actuator
$\mathcal{B}/B$	magnetic flux density (instantaneous quantity / phasor)
C/C_b	heat capacity / heat capacity of blood
$\mathcal{D}/D$	electric flux density (instantaneous quantity / phasor)
e_r/e_φ	unit vector in the direction of r and φ
$\mathcal{E}/E$	electric field intensity (instantaneous quantity $\mathcal{E}(x,t)$ / phasor $E(x;t)$)
E_out	outgoing wave (phasor)
$\mathcal{H}/H$	magnetic field intensity (instantaneous quantity / phasor)
h_T, H_K, h_u	admissible directions of state and input variables
i	current source or iteration index of augmented Lagrangian method
j	imaginary unit or iteration index of gradient method
$\mathcal{J}$	current density (instantaneous quantity)
$\mathcal{J}_\mathrm{ind}/J_\mathrm{ind}$	induced current density (instantaneous quantity / phasor)
k	thermal conductivity
K	state of electromagnetic subsystem (phasor $K := K(x;t)$, $K \in \{A, E\}$)
n	outward unit normal vector or number of subintervals
N	dimension of parameter vector θ
N_c	coil windings
p	adjoint state of thermal subsystem $p := p(x,t)$ or degree of basis function
q_i	weights of cost functional
$\mathcal{Q}/Q$	electromagnetic heat source (instantaneous quantity / phasor (averaged over one time period))
s	sensitivity vector of the cost functional w.r.t. the parameters θ, $s := s(t)$
t	time coordinate
t_f	final time of heat-up cycle
T	state of thermal subsystem (temperature $T := T(x,t)$)

$T_{\min}/\tilde{T}_{\min}$	trajectory of the minimum temperature within object / surface layer
$T_{\text{avg}}/\tilde{T}_{\text{avg}}$	trajectory of the average temperature within object / surface layer
$T_{\max}/\tilde{T}_{\max}$	trajectory of the maximum temperature within object / surface layer
T_0	initial temperature
T_{a}	temperature of ambient air
T_{d}	desired temperature profile
$T_{\theta_j}/K_{\theta_j}$	state sensitivity w.r.t. states T and K ($T_{\theta_j} := T_{\theta_j}(x,t)$, $K_{\theta_j} := K_{\theta_j}(x;t)$)
u	control trajectory (current or voltage source $u := u(t)$)
u_{d}	set point for control trajectory
v	voltage source or control variable $v := v(x,t)$
w	optimization variable $w := w(t)$
X	Banach space or knot vector
x	spatial coordinates ($x = [x_1, x_2, x_3]^{\mathsf{T}}$ or $x = [r, \varphi, z]^{\mathsf{T}}$)
y^*	optimal solution
α	step size of gradient method or heat transfer coefficient
β	penalty parameter
γ	scaling factor
γ_i	adaptation factors for updating the penalty parameter β or constant of termination criterion
Γ	boundary of the region of interest Ω, also see Appendix B.4
Γ_{D}	boundary segment with Dirichlet boundary condition
Γ_{N}	boundary segment with Neumann boundary condition
Γ_{i}	boundary segment that is subject to a current source
Γ_{v}	boundary segment that is subject to a voltage source
ϵ	electrical permittivity, emissivity of the surface, or weight of penalty term
ϵ_0	permittivity of free space
ϵ_{r}	relative electric permittivity
$\epsilon_J/\epsilon_{T^+}/\epsilon_u$	thresholds of termination criteria

θ	parameter vector for manipulating the actuator configuration
κ	adaptation factor of adaptive line search strategy or constant of the update law for the penalty parameter
Λ	adjoint state of electromagnetic subsystem (phasor $\Lambda := \Lambda(x;t)$)
μ	Lagrange multiplier $\mu := \mu(x,t)$ or magnetic permeability
μ_0	permeability of free space
μ_r	relative magnetic permeability
ξ	knot of B-spline or transformed state variable $\xi := \xi(x,t)$
ρ/ρ_b	density / density of blood or electrical charge density
σ	electrical conductivity
σ_SB	Stefan-Boltzmann constant
ω	angular frequency of the electrical excitation of the actuator
ω_b	perfusion rate
Ω	region of interest, also see Appendix B.4

B.4 Subscripts of spatial domains

a	ambient air
b	bones, dorsal vertebra
c	coil or electrode (actuator)
c, a	air gap of the electrode
c, c	catheter of the electrode
c, d	dielectric of the electrode
d	spatial subdomain that should be heated up
h	healthy tissue such as breast or liver
i	spatial subdomain that should not be heated up
o	object to be heated (workpiece, human tissue)
s	spinal canal
t	tumor

B.5 Mathematical operators

$\cdot$	scalar product
$\times$	cross product
$\partial_a(\cdot)$	partial derivative with respect to $a \in \{t, \theta_j, \xi\}$
$\nabla(\cdot)$	gradient
$\nabla\cdot(\cdot)$	divergence
$\Delta(\cdot)$	Laplacian
$\nabla\times(\cdot)$	curl
$\mathrm{Re}\{\cdot\}$	real part

Bibliography

[1] G. Allaire. *Numerical Analysis and Optimization: An Introduction to Mathematical Modelling and Numerical Simulation*. Numerical Mathematics and Scientific Computation. Oxford University Press, Oxford, UK, 2007.

[2] H. W. Alt. *Lineare Funktionalanalysis* (in German). Springer, Heidelberg, Germany, 2011.

[3] I. Altrogge. *Optimization of the Probe Placement for Radiofrequency Ablation*. PhD thesis, Universität Bremen, Germany, 2009.

[4] C. Amrouche, C. Bernardi, M. Dauge, and V. Girault. Vector potentials in three-dimensional non-smooth domains. *Mathematical Methods in the Applied Sciences*, 21(9):823–864, 1998.

[5] ANSYS. Webpage. `http://ansys.com`. Accessed 5-October-2017.

[6] F. Assous. Improving the absorbing boundary condition in a 3D Maxwell's equation solver. *Piers Online*, 5(8):701–705, 2009.

[7] F. Assous, P. Degond, E. Heintze, P. Raviart, and J. Segre. On a finite-element method for solving the three-dimensional Maxwell equations. *Journal of Computational Physics*, 109(2):222–237, 1993.

[8] H. Attouch, G. Buttazzo, and G. Michaille. *Variational Analysis in Sobolev and BV Spaces: Applications to PDEs and Optimization*. Society for Industrial and Applied Mathematics (SIAM), Philadelphia, USA, 2014.

[9] G. Baronzio and E. Hager. *Hyperthermia in Cancer Treatment: A Primer*. Springer, New York, USA, 2008.

[10] J. Barzilai and J. M. Borwein. Two-point step size gradient methods. *Journal of Numerical Analysis (IMA)*, 8(1):141–148, 1988.

[11] F. Bay, V. Labbé, Y. Favennec, and J. L. Chenot. A numerical model for induction heating processes coupling electromagnetism and thermomechanics. *International Journal for Numerical Methods in Engineering*, 58(6):839–867, 2003.

[12] M. Benzi, G. H. Golub, and J. Liesen. Numerical solution of saddle point problems. *Acta Numerica*, 14(2005):1–137, 2005.

[13] M. Bergounioux and K. Kunisch. On the structure of Lagrange multipliers for state-constrained optimal control problems. *System & Control Letters*, 48(3–4):160–176, 2002.

[14] M. Bergounioux and K. Kunisch. Primal-dual strategy for state-constrained optimal control problems. *Computational Optimization and Applications*, 22(2):193–224, 2002.

[15] E. Berjano. Theoretical modeling for radiofrequency ablation: State-of-the-art and challenges for the future. *Biomedical Engineering*, 5(1):24, 2006.

[16] D. P. Bertsekas. *Constrained Optimization and Lagrange Multiplier Methods*. Athena Scientific, Belmont, USA, 1996.

[17] O. Bodart, A.-V. Boureau, and R. Touzani. Numerical investigation of optimal control of induction heating processes. *Applied Mathematical Modelling*, 25(8):697–712, 2001.

[18] J. Borggaard and J. Burns. A PDE sensitivity equation method for optimal aerodynamic design. *Journal of Computational Physics*, 136(2):366–384, 1997.

[19] A. Borzì and V. Schulz. *Computational Optimization of Systems Governed by Partial Differential Equations*. Society for Industrial and Applied Mathematics (SIAM), Philadelphia, USA, 2012.

[20] S. Brill and D. M. Schibisch. A comparison between inductive hardening and case hardening (in German). *Elektrowärme International*, 3:76–75, 2014.

[21] A. E. Bryson. *Dynamic Optimization*. Addison-Wesley-Longman, Menlo Park, USA, 1999.

[22] A. E. Bryson and Y.-C. Ho. *Applied Optimal Control*. Blaisdell, New York, USA, 1969.

[23] R. Canters. *Optimization and Control in Deep Hyperthermia: Clinical Implementation of Hyperthermia Treatment Planning in Cervical Cancer Treatment to Obtain a Higher Treatment Quality*. PhD thesis, Erasmus University Rotterdam, Netherlands, 2013.

[24] M. A. Carrizales, L. W. Lake, and R. T. Johns. Production improvement of heavy-oil recovery by using electromagnetic heating. In *SPE Annual Technical Conference and Exhibition*. Society of Petroleum Engineers, 2008.

[25] E. Casas. Pontryagin's principle for state-constrained boundary control problems of semilinear parabolic equations. *SIAM Journal on Control and Optimization*, 35(4):1297–1327, 1997.

[26] S. Chen, H. Peng, J. Chang, and W. Jong. Simulations and verifications of induction heating on a mold plate. *International Communications in Heat and Mass Transfer*, 31(7):971–980, 2004.

[27] P. D. Christofides. *Nonlinear and Robust Control of PDE Systems*. Birkhäuser, Boston, USA, 2001.

[28] COMSOL Multiphysics. Webpage. `https://comsol.com`. Accessed 5-October-2017.

[29] S. Dappen and F. Amiri. Procedural aspects of induction hardening (in German). *Elektrowärme International*, 3(2015):89–98, 2015.

[30] A. J. Davies. *The Finite Element Method: An Introduction With Partial Differential Equations*. Oxford University Press, Oxford, UK, 2011.

[31] J. Davies. *Conduction and Induction Heating*. P. Peregrinus Limited, London, UK, 1990.

[32] J. R. Davis. *Surface Hardening of Steels: Understanding the Basics*. ASM International, Ohio, USA, 2002.

[33] J. de Los Reyes, P. Merino, J. Rehberg, and F. Tröltzsch. Optimality conditions for state-constrained PDE control problems with time-dependent controls. *Control and Cybernetics*, 37(1):5–38, 2008.

[34] C. De Wagter. Optimization of simulated two-dimensional temperature distributions induced by multiple electromagnetic applicators. *IEEE Transactions on Microwave Theory and Techniques*, 34(5):589–596, 1986.

[35] K. Deb, A. Pratap, S. Agarwal, and T. Meyarivan. A fast and elitist multiobjective genetic algorithm: NSGA-II. *IEEE Transactions on Evolutionary Computation*, 6(2):182–197, 2002.

[36] P. Di Barba, A. Savini, F. Dughiero, and S. Lupi. Optimal shape design of devices and systems for induction-heating: Methodologies and applications. *International Journal of Computation and Mathematics and Electronic Engineering*, 22(1):111–122, 2003.

[37] P.-É. Druet, O. Klein, J. Sprekels, F. Tröltzsch, and I. Yousept. Optimal control of three-dimensional state-constrained induction heating problems with nonlocal radiation effects. *SIAM Journal on Control and Optimization*, 49(4):1707–1736, 2011.

[38] M. Ebrahimi. On the temperature control in self-controlling hyperthermia therapy. *Journal of Magnetism and Magnetic Materials*, 416(2016):134–140, 2016.

[39] T. Englert, S. Grüner, and K. Graichen. Model predictive torque control of permanent magnet synchronous machines. In *Proceedings of the 20th IFAC World Congress*, pages 781–786, Toulouse, France, 2017.

[40] H. O. Fattorini. *Infinite Dimensional Optimization and Control Theory*. Cambridge University Press, Cambridge, UK, 1999.

[41] Y. Favennec, V. Labbé, and F. Bay. Induction heating processes optimization a general optimal control approach. *Journal of Computational Physics*, 187(1):68–94, 2003.

[42] J. Fuhrmann and D. Hömberg. Numerical simulation of the surface hardening of steel. *International Journal of Numerical Methods for Heat & Fluid Flow*, 9(6):705–724, 1999.

[43] P. Gas. Temperature distribution of human tissue in interstitial microwave hyperthermia. *Przeglad Elektrotechniczny*, 88(7a):144–146, 2012.

[44] P. Gas. Study on interstitial microwave hyperthermia with multi-slot coaxial antenna. *Revue Roumaine Sciences Techniques – Électrotechnique et Énergétique*, 59(2):215–224, 2014.

[45] P. Gas. Multi-frequency analysis for interstitial microwave hyperthermia using multi-slot coaxial antenna. *Journal of Electrical Engineering*, 66(1):26–33, 2015.

[46] A. Gasselhuber, M. R. Dreher, A. Negussie, B. J. Wood, F. Rattay, and D. Haemmerich. Mathematical spatio-temporal model of drug delivery from low temperature sensitive liposomes during radiofrequency tumour ablation. *International Journal of Hyperthermia*, 26(5):499–513, 2010.

[47] GH Induction. Webpage. `http://ghinduction.com`. Accessed 5-October-2017.

[48] P. E. Gill, W. Murray, and M. A. Saunders. Users guide for QPOPT 1.0: A Fortran package for quadratic programming. `http://sbsi-sol-optimize.com/asp/sol_product_qpopt.htm`, 1995. Accessed 5-October-2017.

[49] D. E. Goldberg. *Genetic Algorithms in Search, Optimization, and Machine Learning*. Addison-Wesley, Menlo Park, USA, 1989.

[50] K. Graichen, M. Egretzberger, and A. Kugi. A suboptimal approach to real-time model predictive control of nonlinear systems (in German). *at – Automatisierungstechnik*, 58(8):447–456, 2010.

[51] K. Graichen and B. Käpernick. A real-time gradient method for nonlinear model predictive control. In *Frontiers of Model Predictive Control*, pages 9–28. InTech, 2012. [Online]. Available: `http://intechopen.com/articles/show/title/a-real-time-gradient-method-for-nonlinear-model-predictive-control`.

[52] K. Graichen, A. Kugi, N. Petit, and F. Chaplais. Handling constraints in optimal control with saturation functions and system extension. *System & Control Letters*, 59(11):671–679, 2010.

[53] K. Graichen and N. Petit. Incorporating a class of constraints into the dynamics of optimal control problems. *Optimal Control Applications and Methods*, 30(6):537–561, 2009.

[54] GRAMPC. Webpage. `https://sourceforge.net/projects/grampc`. Accessed 5-October-2017.

[55] M. D. Gunzburger. *Perspectives in Flow Control and Optimization*. Society for Industrial and Applied Mathematics (SIAM), Philadelphia, USA, 2003.

[56] R. E. Haimbaugh. *Practical Induction Heat Treating*. ASM International, Materials Park, USA, 2001.

[57] R. F. Harrington. *Time-Harmonic Electromagnetic Fields*. John Wiley & Sons, Ltd., New York, USA, 2001.

[58] R. Herzog and K. Kunisch. Algorithms for PDE-constrained optimization. *GAMM-Mitteilungen*, 33(2):163–176, 2010.

[59] I. Hiltunen, A. Korpela, and R. Mikkonen. Solenoidal Bi-2223/Ag induction heater for aluminum and copper billets. *IEEE Transactions on Applied Superconductivity*, 15(2):2356–2359, 2005.

[60] M. Hintermüller and M. Hinze. Moreau-Yosida regularization in state constrained elliptic control problems: Error estimates and parameter adjustment. *SIAM Journal on Numerical Analysis*, 47(3):1666–1683, 2009.

[61] M. Hintermüller and K. Kunisch. PDE-constrained optimization subject to pointwise constraints on the control, the state, and its derivative. *SIAM Journal on Optimization*, 20(3):1133–1156, 2010.

[62] M. Hinze, R. Pinnau, M. Ulbrich, and S. Ulbrich. *Optimization With PDE Constraints*. Springer, New York, USA, 2009.

[63] M. Hinze and F. Tröltzsch. Discrete concepts versus error analysis in PDE-constrained optimization. *GAMM-Mitteilungen*, 33(2):148–162, 2010.

[64] D. Hömberg. A mathematical model for induction hardening including mechanical effects. *Nonlinear Analysis: Real World Applications*, 5(1):55–90, 2004.

[65] D. Hömberg and J. Sokolowski. Optimal shape design of inductor coils for surface hardening. *SIAM Journal on Control and Optimization*, 42(3):1087–1117, 2003.

[66] B. Houska, H. J. Ferreau, and M. Diehl. ACADO Toolkit – An open source framework for automatic control and dynamic optimization. *Optimal Control Applications and Methods*, 32(3):298–312, 2011.

[67] M. Ilic, S. Savic, and B. Notaros. First order absorbing boundary condition in large-domain finite element analysis of electromagnetic scatterers. In *Proceedings of the 10th International Conference on Telecommunication in Modern Satellite Cable and Broadcasting Services (TELSIKS)*, pages 424–427, Nis, Serbia, 2011.

[68] K. Ito and K. Kunisch. The augmented Lagrangian method for equality and inequality constraints in Hilbert spaces. *Mathematical Programming*, 46(3):341–360, 1990.

[69] K. Ito and K. Kunisch. *Lagrange Multiplier Approach to Variational Problems and Applications*. Society for Industrial and Applied Mathematics (SIAM), Philadelphia, USA, 2008.

[70] A. N. Iusem. On the convergence properties of the projected gradient method for convex optimization. *Computational and Applied Mathematics*, 22(1):37–52, 2003.

[71] B. Käpernick. *Gradient-Based Nonlinear Model Predictive Control With Constraint Transformation for Fast Dynamical Systems*. PhD thesis, Universität Ulm, Germany, 2016.

[72] B. Käpernick and K. Graichen. Model predictive control of an overhead crane using constraint substitution. In *Proceedings of the American Control Conference (ACC)*, pages 3973–3978, Washington D.C., USA, 2013.

[73] P. Keangin, P. Rattanadecho, and T. Wessapan. An analysis of heat transfer in liver tissue during microwave ablation using single and double slot antenna. *International Communications in Heat and Mass Transfer*, 38(6):757–766, 2011.

[74] C. T. Kelley. *Iterative Methods for Optimization*. Society for Industrial and Applied Mathematics (SIAM), Philadelphia, USA, 1999.

[75] A. Kermanpur, M. Jafari, and M. Vaghayenegar. Electromagnetic-thermal coupled simulation of levitation melting of metals. *Journal of Materials Processing Technology*, 211(2):222–229, 2011.

[76] D. E. Keyes, L. C. McInnes, C. Woodward, W. Gropp, and E. Myra. Multiphysics simulations: Challenges and opportunities. *International Journal of High Performance Computing Applications*, 27(1):4–83, 2013.

[77] Y. S. Kim, J. K. Byun, and I. H. Park. A level set method for shape optimization of electromagnetic systems. *IEEE Transactions on Magnetics*, 45(3):1466–1469, 2009.

[78] O. Klein and P. Philip. Transient numerical investigation of induction heating during sublimation growth of silicon carbide single crystals. *Journal of Crystal Growth*, 247(1):219–235, 2003.

[79] M. Koda, A. H. Dogru, and J. H. Seinfeld. Sensitivity analysis of partial differential equations with application to reaction and diffusion processes. *Journal of Computational Physics*, 30(2):259–282, 1979.

[80] T. Köhler, P. Maass, P. Wust, and M. Seebass. A fast algorithm to find optimal controls of multiantenna applicators in regional hyperthermia. *Physics in Medicine and Biology*, 46(9):2503–25014, 2001.

[81] T. Kozulina, S. Galunin, K. Blinov, and Y. Blinov. Numerical optimization of induction heating systems. In *2016 IEEE NW Russia Young Researchers in Electrical and Electronic Engineering Conference (EIConRusNW)*, pages 621–624, 2016.

[82] M. Kranjc and D. Miklav. Optimization of induction heating using numerical modeling and genetic algorithm. In *Industrial Electronics, 2009. IECON'09. 35th Annual Conference of IEEE*, pages 2104–2108, 2009.

[83] D. Labridis and P. Dokopoulos. Calculation of eddy current losses in nonlinear ferromagnetic materials. *IEEE Transactions on Magnetics*, 25(3):2665–2669, 1989.

[84] L. Lapidus and G. F. Pinder. *Numerical Solution of Partial Differential Equations in Science and Engineering*. John Wiley & Sons, Ltd., New York, USA, 2011.

[85] A. S. Lewis. The mathematics of eigenvalue optimization. *Mathematical Programming*, 97(1):155–176, 2003.

[86] S. Li and L. Petzold. Adjoint sensitivity analysis for time-dependent partial differential equations with adaptive mesh refinement. *Journal of Computational Physics*, 198(1):310–325, 2004.

[87] J. H. Lienhard. *A Heat Transfer Textbook*. Phlogiston Press, Cambridge, USA, 2004.

[88] J. L. Lions. *Optimal Control of Systems Governed by Partial Differential Equations*. Springer, Berlin, Germany, 1971.

[89] O. Lucía, P. Maussion, E. J. Dede, and J. M. Burdío. Induction heating technology and its applications: Past developments, current technology, and future challenges. *IEEE Transactions on Industrial Electronics*, 61(5):2509–2520, 2014.

[90] A. Masserey, J. Rappaz, R. Rozsnyo, and R. Touzani. Optimal control of an induction heating process for thixoforming. *IEEE Transactions on Magnetics*, 40(3):1664–1671, 2004.

[91] D. Miyagi, A. Saitou, N. Takahashi, N. Uchida, and K. Ozaki. Improvement of zone control induction heating equipment for high-speed processing of semiconductor devices. *IEEE Transactions on Magnetics*, 42(2):292–294, 2006.

[92] P. Monk. A finite element method for approximating the time-harmonic Maxwell equations. *Numerische Mathematik*, 63(1):243–261, 1992.

[93] P. Monk. *Finite Element Methods for Maxwell's Equations*. Oxford University Press, Oxford, UK, 2003.

[94] P. Moratalla. Additive manufacturing: A revolutionary manufacturing solution for hardening coils. *Heat Processing*, 13(3):61–66, 2015.

[95] R. Naar and F. Bay. Numerical optimisation for induction heat treatment processes. *Applied Mathematical Modelling*, 37(4):2074–2085, 2013.

[96] I. Neitzel. *Numerical Analysis of PDE-Constrained Optimal Control Problems With Pointwise Inequality Constraints on the State and the Control*. PhD thesis, Technische Universität Berlin, Germany, 2011.

[97] E. Neufeld. *High Resolution Hyperthermia Treatment Planning*. PhD thesis, ETH Zürich, Switzerland, 2008.

[98] J. Nocedal and S. J. Wright. *Numerical Optimization*. Springer, New York, USA, 2000.

[99] C. Oesterle. Vorsteuerungsentwurf für Hyperthermie-Vorgänge (in German). Master's thesis, University of Ulm, Germany, 2015.

[100] H. H. Pennes. Analysis of tissue and arterial blood temperatures in the resting human forearm. *Journal of Applied Physiology*, 1(2):93–122, 1948.

[101] H. J. Pesch. Optimal control of dynamical systems governed by partial differential equations: A perspective from real-life applications. *7th Vienna International Conference on Mathematical Modelling*, 45(2):1–12, 2012.

[102] T. Petzold. *Modelling, Analysis and Simulation of Multifrequency Induction Hardening*. PhD thesis, Technische Universität Berlin, Germany, 2014.

[103] H. N. Pham, H. Fujita, K. Ozaki, and N. Uchida. Estimating method of heat distribution using 3-D resistance matrix for zone-control induction heating systems. *IEEE Transactions on Power Electronics*, 27(7):3374–3382, 2012.

[104] L. Piegl and W. Tiller. *The NURBS Book*. Springer, Berlin, Germany, 2012.

[105] L. S. Pontryagin. *Mathematical Theory of Optimal Processes*. Taylor & Francis, New York, USA, 1987.

[106] A. Quarteroni and A. Valli. *Numerical Approximation of Partial Differential Equations*. Springer, Berlin, Germany, 1994.

[107] P. Rattanadecho and P. Keangin. Numerical study of heat transfer and blood flow in two-layered porous liver tissue during microwave ablation process using single and double slot antenna. *International Journal of Heat and Mass Transfer*, 58(1-2):457–470, 2013.

[108] S. Rhein and K. Graichen. Dynamic optimization of induction heat-up and surface hardening processes on complex spatial domains. In *Proceedings of the IEEE Conference on Control Application (CCA) Part of IEEE Multi-conference on Systems and Control (MSC)*, pages 1829–1834, Sydney, Australia, 2015.

[109] S. Rhein and K. Graichen. Coupled actuator placement and controller design for electromagnetic heating by means of dynamic optimization. In *Proceedings of the 55th IEEE Conference on Decision and Control*, pages 4809–4814, Las Vegas, USA, 2016.

[110] S. Rhein and K. Graichen. Optimale Ansteuerung und Aktorplatzierung bei elektromagnetisch-thermisch gekoppelten Systemen (in German). In *Proceedings of the GMA-Fachausschuss 1.40 "Theoretische Verfahren der Regelungstechnik"*, pages 275–289, Salzburg, Austria, 2016.

[111] S. Rhein and K. Graichen. Constrained trajectory planning and actuator design for electromagnetic heating systems. *Control Engineering Practice*, February 2018. Accepted for publication.

[112] S. Rhein, C. Oesterle, and K. Graichen. Optimal trajectory planning for interstitial hyperthermia processes. In *Proceedings of the 2nd IFAC Workshop on Control of Systems Governed by Partial Differential Equations*, pages 138–143, Bertinoro, Italy, 2016.

[113] S. Rhein, T. Utz, and K. Graichen. Efficient state constraint handling for MPC of the heat equation. In *Proceedings of the 10th International Conference on Control (UKACC)*, pages 656–661, Loughborough, UK, 2014.

[114] S. Rhein, T. Utz, and K. Graichen. Dynamic optimization of multiphysics problems applied to induction heating processes (in German). *at – Automatisierungstechnik*, 9(63):713–726, 2015.

[115] S. Rhein, T. Utz, and K. Graichen. Optimal control of induction heating processes using FEM software. In *Proceedings of the 14th European Control Conference (ECC)*, pages 515–520, Linz, Austria, 2015.

[116] A. A. Rodríguez and A. Valli. *Eddy Current Approximation of Maxwell Equations: Theory, Algorithms and Applications*. Springer, New York, USA, 2010.

[117] V. Rudnev. Induction hardening of gears and critical components. *Geartechnology*, 9(9–10):58–63, 2008.

[118] V. Rudnev, D. Loveless, R. L. Cook, and M. Black. *Handbook of Induction Heating*. Taylor & Francis, New York, USA, 2002.

[119] A. Rund, K. Chudej, J. Kerler, H. J. Pesch, and K. Sternberg. Optimal control of coupled multiphysics problems: Guidelines for real-life applications demonstrated for a complex fuel cell model. *GAMM-Mitteilungen*, 35(2):146–174, 2012.

[120] H. Sagan. *Introduction to the Calculus of Variations*. Dover Books on Mathematics, New York, USA, 1992.

[121] D. Salomon. *Curves and Surfaces for Computer Graphics*. Springer, Lakeside, USA, 2007.

[122] M. Sathe, O. Schenk, M. Christen, and H. Burkhart. A parallel PDE-constrained optimization framework for biomedical hyperthermia treatment planning. In *PARS-Mitteilungen*, Erlangen, Germany, 2009.

[123] A. Schiela. Barrier methods for optimal control problems with state constraints. *SIAM Journal on Optimization*, 20(2):1002–1031, 2009.

[124] W. E. Schiesser. *The Numerical Method of Lines*. Academic Press, San Diego, USA, 1991.

[125] A. Schönbohm. Flatness based inductive reheating of A356 billets into the semi-solid state. *Solid State Phenomena*, 116(2006):766–770, 2006.

[126] D. T. Seifert. Ansätze zur Geometrieoptimierung und Aktorplatzierung für örtlich verteilte Systeme (in German). Master's thesis, University of Ulm, Germany, 2016.

[127] P. G. Simpson. *Induction Heating: Coil and System Design*. McGraw-Hill, New York, USA, 1960.

[128] J. Sokołowski and J.-P. Zolésio. *Introduction to Shape Optimization: Shape Sensitivity Analysis*. Springer, New York, USA, 1992.

[129] P. R. Stauffer, T. C. Cetas, and R. C. Jones. Magnetic induction heating of ferromagnetic implants for inducing localized hyperthermia in deep-seated tumors. *IEEE Transactions on Biomedical Engineering*, 31(2):235–251, 1984.

[130] J. A. Stratton. *Electromagnetic Theory*. John Wiley & Sons, Ltd., New York, USA, 1941.

[131] J. W. Thomas. *Numerical Partial Differential Equations: Finite Difference Methods*. Springer, New York, USA, 1998.

[132] V. Thomée. *Galerkin Finite Element Methods for Parabolic Problems*. Springer, New York, USA, 2006.

[133] F. Tröltzsch. *Optimal Control of Partial Differential Equations: Theory, Methods, and Applications*. American Mathematical Society, Providence, USA, 2010.

[134] F. Tröltzsch and I. Yousept. A regularization method for the numerical solution of elliptic boundary control problems with pointwise state constraints. *Computational Optimization and Applications*, 42(1):43–66, 2009.

[135] F. Tröltzsch and I. Yousept. PDE-constrained optimization of time-dependent 3D electromagnetic induction heating by alternating voltages. *ESAIM: Mathematical Modelling and Numerical Analysis*, 46(4):709–729, 2012.

[136] T. Utz, S. Rhein, and K. Graichen. Constraint handling in optimization-based control of a heat-up problem using a transformation approach. *Proceedings in Applied Mathematics and Mechanics*, 14(1):909–910, 2014.

[137] T. Utz, S. Rhein, and K. Graichen. Transformation approach to constraint handling in optimal control of the heat equation. In *Proceedings of the 19th IFAC World Congress*, pages 9135–9140, Cape Town, South Africa, 2014.

[138] H. K. Versteeg and W. Malalasekera. *An Introduction to Computational Fluid Dynamics - The Finite Volume Method*. Addison-Wesley-Longman, Essex, UK, 1995.

[139] A. Wächter and C. Laird. IPOPT webpage. `https://projects.coin-or.org/Ipopt`. Accessed 5-October-2017.

[140] N. Werner. *Analysis and Automation of the Crucible-Free Floating Zone (FZ) Growth of Silicon Crystals*. PhD thesis, Leibniz Institute for Crystal Growth (IKZ), Berlin, Germany, 2014.

[141] D. V. Widder. *The Heat Equation*. Academic Press, New York, USA, 1976.

[142] D. A. Wismer. *Optimization Methods for Large-Scale Systems: With Applications*. McGraw-Hill, New York, USA, 1971.

[143] S. J. Wright. *Primal-Dual Interior-Point Methods*. Society for Industrial and Applied Mathematics (SIAM), Philadelphia, USA, 1997.

[144] P. Wust, B. Hildebrandt, G. Sreenivasa, B. Rau, J. Gellermann, H. Riess, R. Felix, and P. M. Schlag. Hyperthermia in combined treatment of cancer. *The Lancet Oncology*, 3(8):487–497, 2002.

[145] I. Yousept. Optimal control of a nonlinear coupled electromagnetic induction heating system with pointwise state constraints. *Mathematics and its Applications: Annals of the Academy of Romanian Scientists*, 2(1):45–77, 2010.

[146] O. C. Zienkiewicz and K. Morgan. *Finite Elements and Approximation*. Wiley, New York, USA, 1983.

[147] S. Zinn and S. Semiatin. *Elements of Induction Heating: Design, Control, and Applications*. ASM International, Ohio, USA, 1988.